MEMS-based Planar Optical Switching Solutions with Integrated Silicon Nitride Photonics for Telecommunication Applications

by

Suraj SHARMA

MANUSCRIPT-BASED THESIS PRESENTED TO ÉCOLE DE TECHNOLOGIE SUPÉRIEURE IN PARTIAL FULFILLEMENT FOR THE DEGREE OF DOCTOR OF PHILOSOPHY
Ph.D.

MONTREAL, JUNE 11, 2024

ECOLE DE TECHNOLOGIE SUPÉRIEURE
UNIVERSITÉ DU QUÉBEC

BOARD OF EXAMINERS (THESIS PH.D.)

THIS THESIS HAS BEEN EVALUATED

BY THE FOLLOWING BOARD OF EXAMINERS

Mr. Frédéric Nabki, Thesis Supervisor
Department of Electrical Engineering at École de technologie supérieure

Mr. Michaël Ménard, Thesis Co-supervisor
Department of Electrical Engineering at École de technologie supérieure

Mr. Éric David, President of the Board of Examiners
Department of Mechanical Engineering, at École de technologie supérieure

Mr. Vahé Nerguizian, Member of the jury
Department of Electrical Engineering, at École de technologie supérieure

Mr. David V. Plant, External Evaluator
Department of Electrical & Computer Engineering, at McGill University

THIS THESIS WAS PRENSENTED AND DEFENDED

IN THE PRESENCE OF A BOARD OF EXAMINERS AND THE PUBLIC

ON MAY 9, 2024

AT ÉCOLE DE TECHNOLOGIE SUPÉRIEURE

ACKNOWLEDGMENTS

First and foremost, I express my sincere gratitude to my Ph.D. supervisor, Professor Frederic Nabki, and co-supervisor, Professor Michaël Ménard, for allowing me to embark on this rigorous yet beautiful journey in 2015. I am grateful for their support during all these years with a well-funded Ph.D. project, where I never had to worry about scholarship and funds to support my research activities. Professor Nabki's enthusiasm towards technology and his knowledge about MEMS have inspired me throughout these years. He has always encouraged me to develop out-of-the-box thinking and a critical mindset to dissect a complex scientific research problem into tangible and simple challenges to ensure success. His attention to detail during our discussions and valuable insights into minute details of my research work ensured that I could come up with feasible ideas that worked upon pursual. I will always be grateful to him for showing me the way during times when I found this journey long and strenuous. Professor Ménard's relentless pursuit of excellence in writing has helped me immensely during these years. As a result, the quality of my work has improved substantially. His expertise in optics and attention to fundamentals have encouraged me to understand core concepts before jumping to conclusions. I will always be grateful to him for showing confidence in my abilities to present our group's research at prestigious international scientific conferences and demonstrate our prototype devices at various research competitions for students.

I extend my sincere gratitude to the members of the thesis committee, Professor David V. Plant from McGill University, and Professor Vahé Nerguizian and Professor Éric David from École de technologie supérieure for their time, encouragement, and insightful feedback for this thesis. I want to thank AEPONYX Inc. for the opportunity to realize my ideas through their technology. I would also like to thank CMC Microsystems for making it possible for researchers like me to pursue their MEMS ideas through various MUMPs technologies at a subsidized cost. I would also like to thank the Natural Sciences and Engineering Research

Council (NSERC) and the Microsystems Strategic Alliance of Quebec (ReSMiQ) for financially supporting this work.

I want to thank Anubha Gupta and Shivaram Arunachalam for encouraging me to apply for this research project and supporting me all these years. I am grateful to Mathieu Gratuze and Mohammed Saadati for their positive and helpful attitude that made it effortless to work in the lab. My colleagues in our research group, Niharika, Almur, Seyed, and Mohammad, have helped me towards the successful completion of my Ph.D. project. They were always up for a thoughtful scientific discussion, figuring out simulation bugs, and device testing at any hour of the day, apart from being there, for a quick Tim Horton's trip after each group meeting. My friends Devika, Divya, Michiel, Saurabh, Ranim, Navid, Julian, and Qader have made this journey joyful and memorable for me. I thank you all. My friends from The Art of Living, Ami, Aditya, Heena, Roshan, Kiran, Srikanth, Mikashmi, Haleh, Collin, and Sumit, have supported me immensely when things got tough. Thank you for always being there!

This Ph.D. thesis could not have been completed without my constant pillars of strength, my parents, Hemant Kumar Sharma, and Geeta Sharma, who have supported me unconditionally throughout these years during all my ups and downs. I am fortunate to have you in my life. Thank you! My brother, Arun Sharma, and sister-in-law, Himani Sharma, 's resilience in life inspires me to be humble and grateful for everything I have received. Thank you!

My best friend for life, and my wife, Anupriya Sharma has unconditionally supported me through this period. I have been fortunate to share this life with her. She has helped me grow as a person during these years with her love and care. I am grateful for the blessing that is you! I would also like to thank my father-in-law, Ashok Kumar, mother-in-law, Kailash Desore, and sister-in-law, Akshita Desore, for their love and support through this journey.

Finally, I would like to thank my beloved, Gurudev Sri Sri Ravi Shankar Ji for inspiring me to pursue this journey which has helped me learn to unlearn.

This thesis is dedicated to you, my Gurudev!

MEMS-based planar optical switching solutions with integrated silicon nitride photonics for telecommunication applications

Suraj SHARMA

RÉSUMÉ

La consommation d'énergie élevée et les procédures d'assemblage longues et complexes ont augmenté les coûts de production liés aux systèmes optiques utilisés dans les centres de données du monde entier. De tels systèmes reposent également sur une conversion optique-électrique-optique (OEO) pour commuter le signal optique dans le(s) canal(s) de télécommunication. La technologie de microfabrication peut faire des systèmes optiques complexes qui ne nécessitent pas de conversion OEO énergivore une réalité à faible coût. Dans le passé, des systèmes microélectromécaniques (MEMS) ont été intégrés à des composants photoniques en silicium (Si) pour des solutions de commutation optique de faible puissance. Une telle intégration offre une flexibilité limitée dans le contrôle des composants optiques à base de Si et de la couche MEMS mobile à base de Si, car les deux utilisent souvent la même couche de dispositif en Si dans une tranche de silicium sur isolant (SOI) classique. L'intégration de MEMS basés sur SOI avec des composants photoniques en nitrure de silicium (SiN) permet un contrôle indépendant des conceptions de composants optiques et de MEMS. Une perte de diffusion plus faible due à la rugosité des parois latérales, une moindre sensibilité aux variations de largeur et une large plage de longueurs d'onde de fonctionnement font du SiN une alternative prometteuse au Si. Les solutions de commutation optique actuelles avec SiN reposent sur le réglage thermique de composants optiques tels que l'interféromètre Mach-Zehnder (MZI) et les résonateurs à micro-anneaux. Ce type de commutation optique consomme beaucoup d'énergie et fonctionne à haute température. De plus, la plage de longueurs d'onde de fonctionnement est limitée par la conception du filtre optique. Dans cette thèse, nous proposons un projet de doctorat sur la conception, l'optimisation et l'intégration d'actionneurs MEMS basés sur SOI avec photonique SiN pour la commutation optique avec une large plage de longueurs d'onde de fonctionnement. La plate-forme développée au cours de ce projet intègre des actionneurs MEMS avec des guides d'ondes à canal SiN pour mettre en œuvre des commutateurs optiques 1 x 3 et 1 x 5 avec une perte de transmission optique minimale, une faible consommation d'énergie et une large plage de longueurs d'onde opérationnelles. Minimiser la perte optique dans un commutateur optique SiN basé sur MEMS nécessite une gestion des contraintes résiduelles et une ingénierie de conception précise. Le processus de fabrication commercial multi-utilisateurs PiezoMUMPs a été utilisé pour valider les conceptions MEMS avant l'intégration avec les guides d'ondes SiN. Divers aspects conduisant à une perte optique dans un commutateur optique SiN intégré MEMS ont été étudiés pour améliorer les performances. Le commutateur optique 1 x 5 réalisé a une plage de longueurs d'onde de fonctionnement de 1540 nm à 1625 nm avec une perte d'insertion moyenne minimale de 2,2 dB et une perte d'insertion moyenne maximale de 7,5 dB. Le commutateur optique 1 x 5 fonctionne à $\leq$ 90 V avec le mécanisme de réduction des pertes optiques fonctionnant à 120 V.

Mots-clés: MEMS, optique, photonique, nitrure de silicium, actionneur électrostatique, actionneur piézoélectrique, PiezoMUMPs

MEMS-based planar optical switching solutions with integrated silicon nitride photonics for telecommunication applications

Suraj SHARMA

ABSTRACT

High power consumption and long-and-complex assembly procedures have increased production costs related to optical systems used in data centers around the world. Such systems also rely upon optical-electrical-optical (OEO) conversion for switching optical signal in the telecommunication channel(s). Microfabrication technology can make complex optical systems which do not require the energy intensive OEO conversion a reality at low cost. Microelectromechanical systems (MEMS) have been integrated with silicon (Si) photonics components for low power optical switching solutions in the past. Such integration provides limited flexibility in the control over Si based optical components and Si based movable MEMS layer because both often use the same Si device layer in a conventional silicon-on-insulator (SOI) wafer. SOI-based MEMS integration with silicon nitride (SiN) photonics components enables independent control over optical component and MEMS designs. Lower scattering loss due to sidewall roughness, less sensitivity to width variations, and wide operating wavelength range make SiN a promising alternative to Si. Current optical switching solutions with SiN rely upon thermal tuning of optical components Mach-Zehnder interferometers (MZI) and micro-ring resonators. This kind of optical switching consumes high power and operates at high temperature. Also, the operating wavelength range is limited by the optical filter design. In this thesis, we propose a PhD project on the design, optimization, and integration of SOI-based MEMS actuators with SiN photonics for optical switching with wide operation wavelength range. The platform developed during this project integrates MEMS actuators with SiN channel waveguides to implement 1 x 3 and 1 x 5 optical switches with minimal optical transmission loss, low power consumption, and wide operational wavelength range. Minimizing the optical loss in a MEMS based SiN optical switch requires residual stress management and precise design engineering. Commercial multi-user fab process PiezoMUMPs was used to validate MEMS designs before integration with SiN waveguides. Various aspects leading to optical loss in a MEMS integrated SiN optical switch were investigated for performance improvement. The realized 1 x 5 optical switch has an operating wavelength range of 1540 nm to 1625 nm with a minimum average insertion loss of 2.2 dB and a maximum average insertion loss of 7.5 dB. The 1 x 5 optical switch operates at ≤ 90 V with the optical loss reduction mechanism working at 120 V.

Keywords: MEMS, optics, photonics, silicon nitride, electrostatic actuator, piezoelectric actuator, PiezoMUMPs

TABLE OF CONTENTS

Page

LIST OF TABLES

Page

LIST OF FIGURES

Page

XXVIII

LIST OF ABREVIATIONS

1-D	one-dimensional
2-D	two-dimensional
3-D	three-dimensional
AC	alternate current
AlN	aluminum nitride
Al	aluminum
AICu	aluminum cooper
AON	all-optical network
AVC	angular vertical comb
BOX	buried oxide
BSOI	bonded silicon on insulator
CMOS	complementary-metal-oxide-semiconductor
CTE	coefficient of thermal expansion
CVD	chemical vapor deposition
DC	direct current
DOF	degree of freedom
DRIE	deep reactive ion etching
DUT	device under test
E	electric vector
EME	Eigenmode expansion
ETS	École de Technologie Supérieure

FDTD	finite-difference time-domain
FEA	finite element analysis
FEM	finite element modeling
GC	gap closing
GUI	graphic user interface
H	magnetic vector
HG	Hermite-Gaussian
LPCVD	low pressure chemical vapor deposition
LSW	left switching
MEMS	micro-electro-mechanical systems
MOEMS	micro-opto-electro-mechanical systems
MUMPs	multi user MEMS processes
MZI	Mach-Zehnder interferometer
OADM	optical add-drop multiplexer
OEO	optical-electrical-optical
OSA	optical switching architecture
OXC	optical cross-connect
PCB	printed circuit board.
PDMS	polydimethylsiloxane
PECVD	plasma-enhanced chemical vapor deposition
PIC	photonics integrated circuit

PZT	lead zirconate titanate
RIE	reactive-ion etching
ROADM	reconfigurable optical add–drop multiplexer
RSW	right switching
SEM	scanning electron microscope
SGC	surface grating coupler
Si	silicon
SIMOX	separated by implanted oxygen
SiN	silicon nitride
SiO2	silicone dioxide
SOI	silicon-on-insulator
SONET	synchronous optical network
SW	switching
SVC	staggered vertical comb
TE	transverse electric
TEOS	tetraethyl orthosilicate
TM	transverse magnetic
UQAM	Université du Québec à Montréal

INTRODUCTION

In the opening remarks of his article in Electronics magazine, Moore (1965) famously predicted "With unit cost falling as the number of components per circuit rises, by 1975 economics dictate squeezing as many as 65,000 components on a single silicon chip." Even after 1975, technological advancement in the microfabrication industry kept up well with Moore's law's two-year revised cycles until 2012 (Clark, 2015). Over the last three decades, the diversification of integrated silicon technology into micro-electro-mechanical systems (MEMS) based sensors and actuators has enabled interactions between the chip and the outer world, thereby pushing semiconductor technological advancement into the "More-than-Moore" domain (Arden et al. 2010). This diversification of microtechnology has made possible applications of MEMS in cars (STMicroelectronics), mobile phones (Warren, 2010), cameras (Sachs et al., 2006), cell culturing (Pakazad et. Al, 2012, p. 817-820), and minimally invasive surgery (Mimoun et al. 2013) a reality today.

Micro devices with optical and MEMS components known as micro-opto-electromechanical systems (MOEMS) or optical MEMS have also been developed for use in laser scanners (Holmström et al., 2014) and digital micro mirror displays (Ben-Mrad et al., 2015). The development of these devices took several years following which the development of optical MEMS subsided due to the immaturity of the technology and the stock market recession around 2003 (Kaajakari, 2009). However, with the world moving towards optical fiber-based communication, MOEMS must be developed to meet the ever-growing demand for optical switching solutions that reduce power consumption in optical networks at a reduced cost. Such solutions should also have a wide operational wavelength range, high transmission efficiency, high port counts, and flexibility towards control over MEMS and optical component design. In this work, MEMS based optical switching solutions integrated with silicon nitride photonics were developed for telecommunication applications that provide control over MEMS and optical components, have a wide operational wavelength range with maximum transmission efficiency, and have no DC power consumption.

0.1 Motivation

Conventional electronic data centers are often associated with high cost, limited bandwidth capacity, cabling complexity and high energy-and-space consumption (Hammadi et. al., 2014). A recent report from an international environmental advocacy group suggests that the total power consumption by data centers in the U.S. alone has risen from 76.4 billion kWh/year in 2011 to 91 billion kWh/year in 2013 and could amount to 13 billion dollars annually to businesses across U.S. by 2020 (Delforge, 2014). These technological, environmental, and monetary constraints have paved the way for the development of hybrid optical data center designs such as Helios (Farrington et al., 2010) as shown in Figure 0.1 (a), and Optical Switching Architecture (OSA) (Chen et al., 2014) over the years. Such data centers often rely upon 3-D MEMS with out-of-plane rotating micro-mirrors for beam steering inside an optical cross connect switch (Kim et al., 2003) using piezoelectric actuation (Truex et al., 2003) or

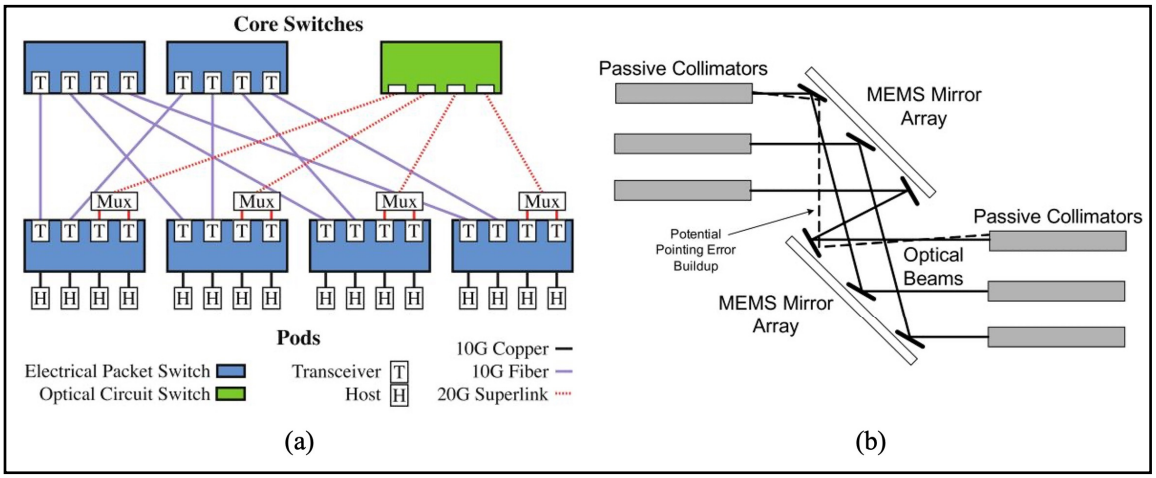

Figure 0.1 (a) Helios optical data center architecture
Taken from Farrington et al. (2010)
(b) 3-D MEMS mirror array for optical switching
Taken from Truex et al. (2003)

electrostatic actuation (Fernandez et al., 2004) as shown in Figure 0.1 (b).

While 3-D MEMS designs allow for a large number of ports to share the burden of data switching in optical telecommunication networks, the development of such systems often suffers from packaging constraints due to complex structures, wafer bonding processes involved, and alignment discrepancies between different components. The switching time for typical 3D optical MEMS switch fabrics is also slower in comparison to 2D optical MEMS switch fabrics (Yoo, 2022). Piezoelectric actuation mechanisms envisioned for these optical telecommunication networks provide fast and reliable actuation but often come with material compatibility constraints (Livermore, 2007), limiting integration with silicon photonics. Planar 2-D optical MEMS devices save space through simpler and smaller packaging with easier alignment between the optical fiber array and the chip.

SOI based MEMS technology has been integrated with Si waveguide photonics in the past. These devices use electrostatic actuation that consumes no DC power and could be designed and optimised for low actuation voltages (Bai et. al., 2010). Such MEMS integration into data centers reduces power consumption from 12.5 Watts per port for electronic switches to 0.24 Watts per port for optical switches, but with limited re-configurability that is restricted to a few milliseconds (Hammadi et al., 2014). However, SOI based MEMS and Si waveguide integration is possible through the use of the Si device layer in SOI wafers for both optical and MEMS components. An example of such planar optical MEMS device that integrates SOI-based MEMS with Si waveguides from the device layer is shown in Figure 0.2 (a). Such integration limits the design adaptability of MEMS and optical components for telecommunication applications. Alternatively, SiN waveguides can provide lower scattering loss due to sidewall roughness, less sensitivity to width variations, and transparency over a wide range of wavelengths in comparison to Si waveguides (Shaw et al., 2005, Blumenthal et al., 2018 and Gloria et al., 2018). The constraints associated with the existing Si photonics technology integration with MEMS, and the advantages of SiN photonics make MEMS-based optical switching with integrated SiN photonics a relevant research problem. Existing SiN based optical switching solutions use thermal tuning of optical filters such as MZI and ring

resonators as shown in Figure 0.2 (b). These solutions consume high power, generate heat, and have a limited operational wavelength range (Joo et al., 2018).

In this work, we developed SOI based MEMS optical switches integrated with SiN photonics. We address the key performance issues such as residual stress due to the integration of SiN over suspended MEMS layers, that can lead to vertical misalignment between suspended and fixed waveguides in the device during switching. We demonstrate a design approach for the actuator to close the air gaps between suspended and fixed waveguide without any device

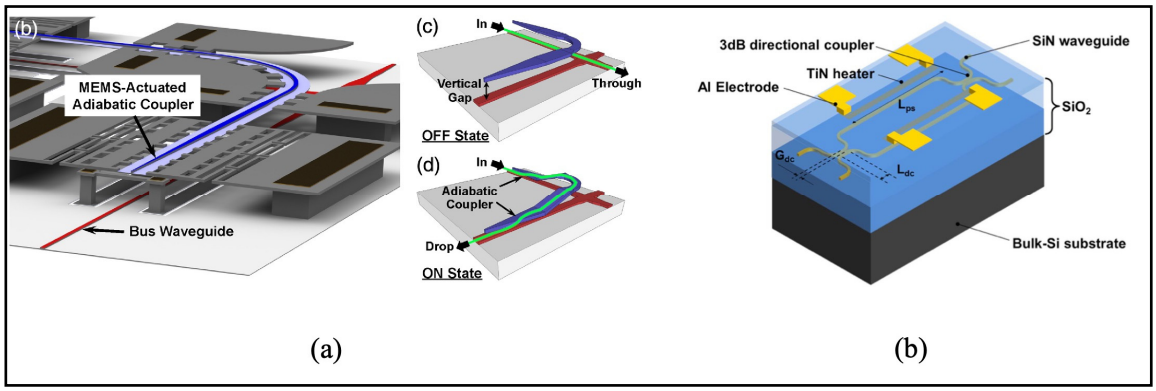

Figure 0.2 (a) Planar electrostatic MEMS actuator based optical switch with integrated Si waveguides
Taken from Seok et al. (2016)
(b) Thermally tuned MZI based SiN optical switch
Taken from Joo et al. (2018)

shorting as the suspended and fixed MEMS layers make contact. This approach greatly reduces the optical losses during switching between different ports. The MEMS actuation voltage, operational wavelength range and average insertion loss over the entire operational wavelength range are some of the key aspects we focus upon in this Ph.D. work. The optical switching technology developed can be useful for applications in next generation passive optical networks (NG-PON2) which require 4 to 8 switching channels.

0.2 Research Goals

Advancement in microfabrication technology over the years has made complex optical systems at the micron scale a reality. The platform developed in this PhD project combines SiN based optical components with SOI-based MEMS, which can significantly increase manufacturing volumes through batch processing, thereby reducing associated costs. Energy efficient optical switching solutions can be achieved using electrostatic and piezoelectric actuation for MEMS that consume zero DC power. These MEMS structures can provide compact and versatile systems capable of controlling light in a chip through SiN channel waveguide integration. The specific objectives envisioned to be achieved through this PhD project are listed below:

- The primary objective of this PhD thesis is to design, optimize and implement electrostatic MEMS actuators with low operation voltage (< 200 V). These actuators must be integrated with SiN waveguides for optical switching with minimum optical transmission loss caused due to MEMS design and fabrication constraints. This objective is explored in chapter 5 to chapter 8 of this thesis.

- To develop a novel MEMS device with a gap closing mechanism to minimize the optical loss due to air gaps between suspended and fixed optical components in a MEMS structure integrated with SiN channel waveguides. When MEMS is integrated with SiN photonics for planar optical switching, release of MEMS structures during the microfabrication process leaves air gap(s) between suspended and fixed optical components (Briere et. al., 2015). Such air gap(s) limit the functionality and use of these devices by increasing the overall optical loss. This objective is explored in chapter 5 and chapter 6 of this thesis.

- To minimize the impact of residual stress caused by integration of optical components with SOI-based MEMS using low-power actuation mechanisms and material specifications. Integration of an SiN channel waveguide with SOI-based MEMS leads to residual stress in the integrated structure that can cause deformation of the suspended structure critically leading to misalignment between different parts of the device. Such

misalignment can increase the overall optical loss in an integrated device. This objective is explored in chapter 7 and chapter 8 of this thesis.

- To achieve maximum displacement with the MEMS actuator designs based upon commercial PiezoMUMPs technology, and the custom microfabrication process flow developed by AEPONYX inc. A high fill factor through successful implementation of a multi-port SiN photonics switch is important to integrate multiple SiN waveguides for telecommunication applications. This is made easier by actuators that have larger travel ranges, enabling the addressing of multiple waveguides. This objective is explored in chapter 5 to chapter 8 of this thesis.

- To develop prototype MEMS actuators using commercial PiezoMUMPs technology that integrate electrostatic and piezoelectric actuation mechanisms for movement along multiple axes. This objective is explored in chapter 7 of this thesis.

- To develop fine alignment capability within a MEMS controlled SiN photonics switch to increase the transmission efficiency between two SiN waveguides during optical switching. This objective is explored in chapter 8 of this thesis.

- To identify key factors that impact the development of low-power broadband SiN optical switches that use MEMS for the switching action. This objective is explored in chapter 8 of this thesis.

0.3 Original Contributions

This research project has led to the following original contributions that are presented in this thesis:

- A new design of SOI-based MEMS actuator that can be integrated with SiN waveguides for digitally controlled planar optical switching. This design allows to completely close the air gaps at Si device layer level without device shorting. Details about the actuator and spring design are reported in chapter 5.

- The first demonstration of a 1 x 3 optical switch that integrates SOI-based MEMS with SiN waveguides for broadband optical switching with a wide operational wavelength range. The specifics of this optical switch along with the methodology used to minimize the impact of residual stress upon optical misalignment between suspended and fixed SiN waveguides are presented in chapter 6.
- The first demonstration of a hybrid actuator based upon the PiezoMUMPs (multi user MEMS processes) process that integrated multi-axial motion of SOI-based MEMS actuator with electrostatic and piezoelectric actuation. Details about the challenges associated with such hybrid actuation with its potential as a 1 x 5 optical switch through SiN waveguide integration are described in chapter 7.

- The first demonstration of an integrated 1 x 5 SiN photonics switch that combines analog control over 3 switching channels and digital control over 2 switching channels through low-power electrostatic actuation in a small device footprint. Chapter 8 describes the details about this optical switch.

The contributions from this research project led to publication or submission of four articles in four different peer-reviewed international journals in the field of MEMS and photonics. These articles are the basis for chapters 5 to 8 in this thesis in the order given below:

- Sharma, S., Kohli, N., Brière, J., Ménard, M., & Nabki, F. (2019). Translational MEMS Platform for Planar Optical Switching Fabrics. Micromachines, 10(7). doi: https://doi.org/10.3390/mi10070435. (**Published**)

- Sharma, S., Kohli, N., Brière, J., Nabki, F., & Ménard, M., (2022). Integrated 1 × 3 MEMS silicon nitride photonics switch. Optics Express, 30(12). doi: https://doi.org/10.1364/OE.460533 (**Published**)

- Sharma, S., Nabavi, S., Rabih, A. A. S., Ménard, M., & Nabki, F. (2023). Hybrid MEMS Actuator With 3 Degrees-of- Freedom for Efficient Planar Optical Switching. Journal of Microelectromechanical Systems, 32(6). doi: https://doi.org/10.1109/JMEMS.2023.3322223 (**Published**)

- An Integrated 1 x 5 MEMS Silicon Nitride Photonics Switch (**Accepted for Publication**)

These contributions also led to two publications in top international conferences in the field of photonics. These conference publications are reported in Appendix III and IV in the order given below:

- Sharma, S., Kohli, N., Brière, J., Nabki, F., & Ménard, M., (2022). Digitally Controlled Silicon Nitride Optical Switch. 2022 Optical Fiber Communications Conference and Exhibition (OFC) in San Diego, CA, USA. pp. 1-3. (**Published**)

- Sharma, S., Kohli, N., Ménard, M., & Nabki, F., (2022). 1 × 5 Silicon Nitride MEMS Optical Switch. 2022 European Conference on Optical Communication (ECOC) in Basel, Switzerland. pp. 1-4. (**Published**)

In addition, the following two patent applications related to MEMS integrated optics were also submitted during this research project:

- Structures and Methods for Stress and Gap Mitigation in Integrated Optics Microelectromechanical Systems. (**WO2020093136**)

- Integrated Optical Microelectronic Mechanical Systems Devices and Methods. (**WO2022006677**)

0.4 Thesis Organization

Chapter 1 provides an overview of MEMS technology covering various actuation methods that are key to MEMS actuator development. It also introduces readers to key fabrication technologies that were used during this research project for MEMS development prior to integration with SiN waveguides.

Chapter 2 gives an overview of optical waveguide theory along with an introduction to different types of waveguides. Various simulation methods used to design and optimize waveguides are discussed in this chapter. The edge coupling method, that is key to SiN waveguide integration with MEMS structures to realise an integrated optical switch, is also discussed in this chapter.

Chapter 3 introduces the readers to MEMS-based optical switches that have been developed in the past. Emphasis is laid on discussion about power-efficient optical MEMS switches based upon electrostatic actuation methods. Devices reported previously that utilize out-of-plane and in-plane motion provided by MEMS actuators have been reviewed in this chapter.

Chapter 4 discusses MEMS integration with SiN photonics. In this chapter, readers are introduced to the current photonics switching solutions that utilize thermal tuning of SiN-based optical components. Recent development in MEMS integration with SiN waveguides for power-efficient optical switching is also presented in this chapter. Details of the fabrication process used in this research project for SOI-based MEMS integration with SiN waveguides are given in this chapter along with the critical factors that affect device performance during such integration.

Chapter 5 presents a translational MEMS platform based upon SOI technology that was fabricated using the PiezoMUMPs process. Insights into designs challenges in achieving uniform bi-axial planar motion of the MEMS actuator without rotational behaviour are discussed in this chapter. Optical design considerations required for future integration of such platform with SiN waveguides is a key aspect of this chapter.

Chapter 6 describes a 1 x 3 MEMS silicon nitride photonics switch that integrates SOI-based MEMS based upon MEMS prototype development in the previous chapter. Microfabrication process followed to fabricate this device and details about the MEMS and optical characterization are discussed in this chapter in detail.

Chapter 7 introduces readers to a hybrid MEMS actuator device that utilizes low-power electrostatic and piezoelectric actuator. Details about the design development process key towards such integration along with characterization results of a prototype device fabricated using the PiezoMUMPs microfabrication process are given in this chapter.

Chapter 8 gives details about a 1 x 5 SiN photonics switch that is realized through integration of the actuator design of MEMS prototype presented in the previous chapter. Variation in optical performance of the photonics switch through analog and digital control in various switching positions of the fabricated device provides key insight into various factors that affect SiN waveguide integration with SOI-based MEMS actuators.

In conclusion, key findings from this thesis are identified along with highlighting of the contributions from this research project. Future work recommendations to further improve performance of optical devices that integrate SiN waveguides with MEMS actuators for power-efficient optical switching systems are provided at the end of this thesis.

CHAPTER 1

AN OVERVIEW OF MEMS TECHNOLOGY

1.1 Introduction

The ability of MEMS to convert various forms of input energy such as electrostatic (Song et al., 2012), electrothermal (Syms et al., 2004), piezoelectric (Truex et al., 2003), electromagnetic (Koh et al., 2012) etc. into precise mechanical motion at the micron scale can be used to manipulate light when integrated with optical components. These actuation mechanisms have their own merits and constraints which impact the design and function of a MOEMS device, and determine the degree of control, and ease of fabrication and packaging associated with it. In this chapter, we will primarily focus on electrostatic actuation and briefly discuss electrothermal and piezoelectric actuation mechanisms, which could also be used for out-of-plane actuation.

1.2 Electrostatic Actuation

The electrostatic actuation mechanism is based upon the motion caused due to the electrostatic force of attraction between two or more oppositely charged plates as shown in Figure 1.1. When a potential difference (V) is applied between two parallel plates of area (A) at a distance (d) from each other placed in a dielectric medium with permittivity (ϵ), the two plates acquire opposite charge. If one of these plates is movable and the other one is fixed, the electrostatic force of attraction (Fe) can generate a displacement which can be given as the rate of change of energy stored in the capacitor which written as

$$F_e = -\frac{dW_e}{dx} = \frac{V^2 dC}{2\,dx} = \frac{\epsilon A V^2}{2(d-x)^2} \tag{1.1}$$

where W_e is the potential energy stored in the capacitor is given as

$$W_e = \left(\frac{1}{2}\right) CV^2. \tag{1.2}$$

The movable plate is anchored through an elastic material of spring constant (k). If the actuator is displaced by a distance (x), the mechanical spring force (F_s) exerted on the movable plate can be given as

$$F_s = -kx. \tag{1.3}$$

The negative sign of the force is due the restoring nature of the mechanical spring force. Thus, the net force (F) acting on the electrode becomes a summation of the two forces which can be given as

$$F = F_e + F_s = \frac{\epsilon A V^2}{2(d-x)^2} - kx. \tag{1.4}$$

From these equations, we can tell that the actuator displacement is not only critically dependant on the electrode area, gap, and actuation voltage, but the spring design plays an important part in designing large force and large displacement electrostatic actuators. The electrostatic force

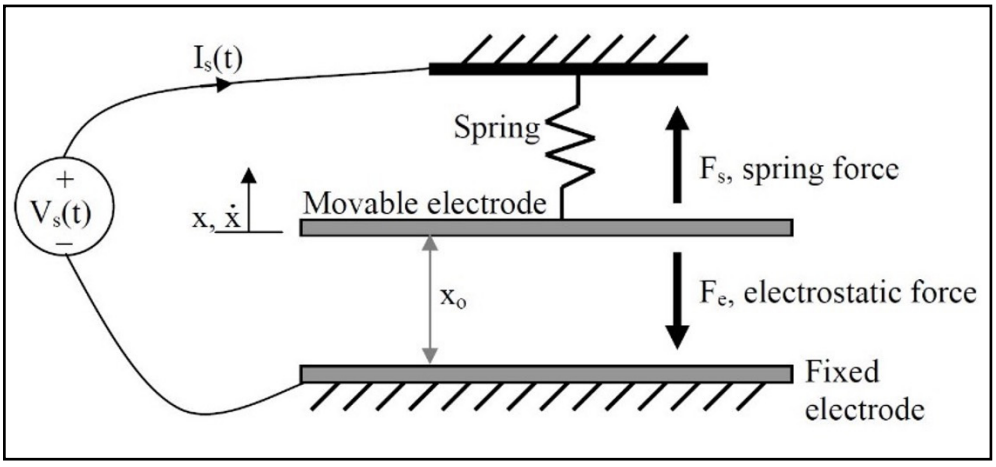

Figure 1.1 Attractive force between two parallel plates
Taken from Shakoor et al. (2010)

overcomes the restoring mechanical spring force and pull-in point of the actuator when it is pushed beyond its equilibrium point. The two electrodes snap with each other, and the actuator might be short circuited and damaged if not prevented through sensor designing physical isolation, dimpled structures, and grounding of the actuator at pull-in point. The pull-in voltage (V_p) and pull-in displacement (x_p) of a parallel plate actuator is given as

$$V_p = \sqrt{\frac{8kd^3}{27\varepsilon A}} \tag{1.5}$$

$$x_p = \frac{d}{3} \tag{1.6}$$

These two are perhaps the most important parameters when it comes to electrostatic actuation and are often used to predict the operational limits of the actuator. As we can see the pull-in displacement is 1/3rd of the gap between the electrodes and thus for larger displacement the gap between the electrodes needs to be on the higher side. However, increasing the gap without careful consideration of the other parameters will increase the actuation voltage required beyond the desired limits and will lead to system wide power consumption while making the high voltage actuator operation a cause of concern. Therefore, the spring mechanism supporting the electrostatic actuator becomes a key component in achieving large displacement at a low actuation voltage using parallel plate actuators.

The equations for a parallel plate actuator do not hold true for a longitudinal comb drive geometry where the gap between the electrodes remains constant and the actuator displacement is perpendicular to the gap direction, as shown in Figure 1.2 (b). Pull-in phenomena does exist in longitudinal comb drive designs and is dependent upon the complex fringe capacitance calculations. These calculations are based upon the non-overlapping parts of the actuator and can be accurately predicted through finite element modelling of the actuator using simulation software like ANSYS or COMSOL. The comb drive design consists of several electrode

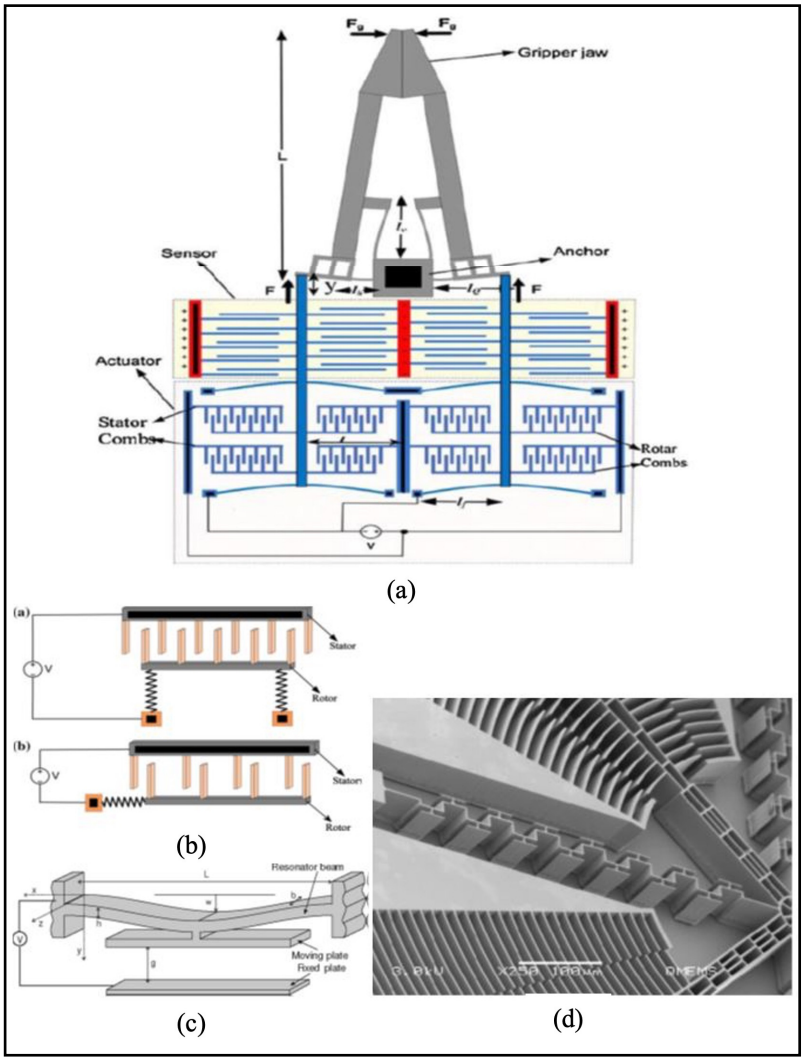

Figure 1.2 (a) Electrostatic microgripper
Taken from Bazaz et al. (2011)
(b) lateral and transverse comb drive
Taken from Khan et al. (2010)
(c) parallel plate electrostatic actuator
Taken from Marques et al. (2007)
(d) rotational comb drive
Taken from Yeh et al. (2005)

fingers designed to be parallel to each other like a parallel plate capacitor. However, in this design the area between the electrodes changes during actuation and produces motion of the movable comb fingers as shown in Figure 1.2 (b). For a comb drive actuator placed in dielectric

medium with permittivity (ε) with finger thickness (h), constant gap between fingers (d) and number of fingers overlapping (N) the electrostatic force (Fe) upon application of actuation voltage (V) is given as

$$F_e = \frac{N\epsilon h V^2}{2d}. \tag{1.7}$$

The comb drive actuator design offers linearity and large travel range when compared to parallel plate actuation although the net force through comb drive is lesser than that for a parallel plate actuator of a similar volume and capacitor gap making large voltage operation inevitable for large actuation forces. (Kaajakari, 2009). It is often used for translational in-plane motion (Bazaz et al., 2011) and in-plane rotational movement through curved comb drive design (Yeh et al., 2005) as shown in Figure 1.2 (a) and Figure 1.2 (d), respectively. However, through staggered and angular vertical comb drive design (Kim et al., 2006) it can be used for out of plane rotational movement and through differential comb drive thickness (Wang et al., 2012) and flexure beams (Gaspar et al., 2010), it can be used for out-of-plane vertical displacement as well.

In an electrostatic actuator, the parallel plates can be designed and fabricated with different shapes to produce linear (Legtenberg et al., 1996) and rotational (Rahim et al., 2013) movement or for the deformation (Hung et al., 1999) of suspended structures. In any of these designs, the MEMS consist of a stationary electrode as a plate / surface or stator combs and a movable electrode as a suspended structure or rotor combs, as shown in Figure 1.2. Over several years, researchers have carefully designed comb drives to rotate, pull and push adjoined components in-plane and out-of-plane. Comb drives enhance the degree of movement associated with MEMS because of their large number of electrostatically actuated fingers (large area of actuation). Although micro devices based on this mechanism operate at higher voltages and may suffer from stiction if not carefully designed, they operate at low power and provide fast response times with greater accuracy and control compared to electrothermal and

electromagnetic actuation. Also, they are easy to fabricate with fewer masks (Livermore, 2007).

1.3 Piezoelectric Actuation

Piezoelectric actuation involves the deformation of a thin film material upon application of an electric field, which causes the deflection of a suspended structure. A piezo material can be patterned onto a suspended silicon beam. The silicon beam could be anchored to the substrate in longitudinal and transverse configurations, as shown in Figure 1.3. The longitudinal configuration enables force generation in the direction of the applied electric field upon actuation, whereas the transverse configuration enables force generation perpendicular to the electric field. Different piezoelectric coefficients come into play with these two configurations.

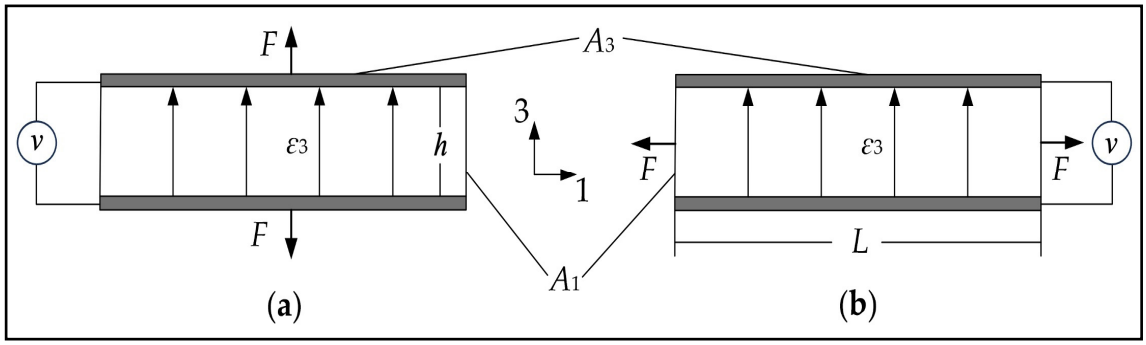

Figure 1.3 (a) Longitudinal and (b) transverse configurations of a piezoelectric actuator
Adapted from Wang et al. (2022)

Piezoelectric coefficients e_{33} and e_{31} come into play in longitudinal and transverse configurations, respectively (Kajaakari, 2009).

For a piezoelectric actuator in longitudinal configuration, the displacement (Δh) for an actuator of beam thickness (h), Young's modulus (E) and piezoelectric coefficient (e_{33}) upon application of an actuation voltage (v) is given as

$$\Delta h = \frac{e_{33} v}{E}. \tag{1.8}$$

For a piezoelectric actuator in transverse configuration, the displacement (ΔL) for an actuator of beam length (L), young's modulus (E), beam thickness (h) and piezoelectric coefficient (e31) upon application of an actuation voltage (v) is given as

$$\Delta L = \left(\frac{e_{31}L}{Eh}\right)v. \tag{1.9}$$

As we can see, for a transverse configuration the displacement is dependent upon the dimensions of the actuator. The higher the ratio between the length and thickness of the actuator the higher will be the displacement produced through actuation. If only one of the ends of the actuator beam is anchored to the substrate the piezoelectric effect can cause the bending of the beam in upward or downward direction depending upon the polarity of the potential applied (Sinha et al., 2009).

This actuation mechanism consumes no DC power and provides faster response with high forces compared to electrothermal actuation. The displacement produced through this actuation is relatively low at low voltages compared to electrostatic comb drives. Complex fabrication processes, environmental concerns due to use of lead in piezo materials such as PZT and packaging constraints limit the integrability of this actuation mechanism with other components (Mousharraf, 2012 and Livermore, 2007). However, with the introduction of commercially optimized Piezo MUMPs process from MEMSCAP (now known as Science) (Cowen et al., 2013) which uses aluminum nitride (AlN) as the piezoelectric material, this actuation mechanism could be potentially used for designing actuators for out-of-plane displacement which can be used for alignment of optical components within a die.

1.4 Electrothermal Actuation

Electrothermal actuation involves thermal expansion of a suspended structure upon application of heat through applied current. It works upon the principle of difference in coefficient of thermal expansion within a suspended structure due to different material properties or due to

the specific shape of the actuator which causes motion. When an electric current is passed through a beam with length (L) and coefficient of thermal expansion (α), it will cause a change in temperature (δT) as electrical energy is transformed to heat. The resulting change in length (δL) can be given as

$$\delta L = L\alpha\delta T. \tag{1.10}$$

For a cross sectional area denoted by (A), a beam with a Young's modulus (Y) can produce Force F upon thermal actuation, which can be given as

$$F = Y\, A\alpha\delta T \tag{1.11}$$

Electrothermal actuation can be used to produce large forces and higher displacements when compared to electrostatic actuation through various designs but suffers from high temperature generation, slow response and recovery times and high-power consumption compared to electrostatic actuation. A bimorph structure in an electrothermal actuator uses two thin film layers stacked together. The difference in the coefficient of thermal expansion between these films causes bending displacement perpendicular to the strain. Residual intrinsic stress is present within the structure after release during fabrication process. This stress along with extrinsic stress due to heat generation upon application of current in a bimorph causes actuation (Liu, 2013) as shown in Figure 1.4.

For a uniformly heated bimorph beam with thin film thickness (t_1) and (t_2) the tangential angle (θ) upon actuation where (l_b) is the length of the beam, (ρ) is the curvature of the bent beam, (β) is the parameter determined by biaxial elastic modulus and thickness of the two films and ($\Delta\varepsilon_{in}$) and ($\Delta\varepsilon_{th}$) represent initial residual strain and the strain mismatch due to joule heating respectively, can be given as

$$\theta = \frac{l_b}{\rho} = \frac{\beta l_b}{t_1 + t_2}(\Delta\varepsilon_{in} + \Delta\varepsilon_{th}) \tag{1.12}$$

Mostly such bimorph structures have been incorporated to electrothermally actuate, suspended structures vertically out-of-plane for large displacements. However, fabrication process for such MEMS structures with integrated optics can be complex due to multiple thin film processing involved. Shear force at the interface of these thin film layers could lead to delamination over time and thus decrease the reliability of these devices (Chen et al., 2003). Complex bimorph geometry and residual strain involved due to material mismatch makes this actuation mechanism undesirable for this thesis.

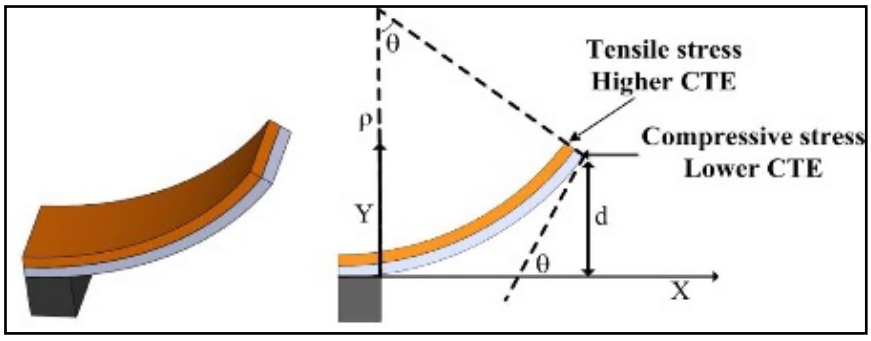

Figure 1.4 Structural view of bimorph cantilever
Taken from Liu (2013)

During this PhD project, electrostatic actuation remains the choice of actuation for in-plane MEMS because of low power consumption and ease of fabrication. The potential use of piezoelectric actuation along with electrostatic actuation to develop out-of-plane displacement

and hybrid motion MEMS as a part of reconfigurable silicon photonics solutions is also explored in this thesis.

1.5 Fabrication Technologies

Earliest lithography record to transfer a pattern date back to 1827 when Lemaitre made an etched copy of an engraving of Cardinal d'Amboise. It took more than 100 years when in 1961 photoetching a 5 μm transistor on silicon became a reality (Madou, 2018). Today, microfabrication processes such as lithography, thin film deposition, wafer bonding, wet and dry etching etc. are used for MEMS research and development throughout the world. These techniques have already been thoroughly researched and are undergoing constant development since as early as 1940s. With the development of photoresists, patterns could be transferred onto the substrate which enabled the fabrication of suspended movable structures at micron scale in 1960s (Nathanson, 1967). Different fabrication technologies such as bulk micromachining (Kovacs et al., 1998), surface micromachining (Bustillo et al., 1998) and metal micromachining (Wang et al., 2008) have been developed for MEMS fabrication over several years.

Bulk micromachining involves directly etching into the substrate to define structures within it. It is usually used to create v-grooves that can be used to place optical fibers in a MEMS integrable silicon photonics device (Hoffmann et al., 2002). Two bulk micromachined substrates can be adhered to each other using bonding techniques such as fusion bonding and anodic bonding to fabricate complex structures that are not possible with the bulk micromachining technique alone. Such bonding techniques often come with alignment and adhesion discrepancies.

Micromachining technique is one of the most preferred methods for MEMS fabrication. It involves microfabrication of suspended movable structures over a substrate material (mostly silicon) through subsequent deposition and selective removal of sacrificial and structural layers

of materials different from the substrate material (Bustillo et al., 1998). However, surface micromachined structures may suffer from stiction between suspended structures and the substrate due to unwanted capillary and van der Waals forces which can affect the reliability of micro devices (Tas et al., 1996). Also, the excellent elastic properties of silicon (Hopcroft, 2010) make it the preferred material for movable structures in MEMS. Researchers have developed MEMS devices by combining surface/bulk micromachining technique in which reactive ion etching (RIE) is used to etch structural patterns in silicon followed by sidewall passivation using oxide and undercutting of bulk silicon using alkaline etchants (Lee et al., 1999 and Park et al., 2002).

The development of silicon on insulator (SOI) technology has pushed the use of silicon as structural material in MEMS. The ease of MEMS fabrication using SOI technology due to inherently separate structural and device silicon layer along with commercially available fabrication processes to expedite MEMS development make it the choice of fabrication technology for this research project. Furthermore, we will discuss the silicon on insulator approach for MEMS device fabrication and a commercially available SOI-based MEMS microfabrication process that is used in this PhD project.

1.5.1 SOI Technology

SOI wafer is an engineered silicon substrate available worldwide. A typical SOI wafer consists of two silicon layers of varying thickness with an insulating buried oxide (BOX) layer sandwiched in between them as shown in Figure 1.5. SOI technology has enabled chips with high-voltage applications and a greater number of circuits than before due to the insulating properties provided by the built-in BOX layer which prevents power leakage (Celler et al., 2003). In MEMS, the top Si structural layer has been patterned and etched as an accelerometer (Su et al., 2005), a gyroscope (Alper et al., 2006) and an optical switch (Chu et al., 2002). These SOI wafers are developed using various techniques such Bonded Silicon on Insulator (BSOI), Smart Cut and Separated by Implanted Oxygen (SIMOX). In the Bonded Silicon on Insulator [BSOI] approach; low stress suspended silicon structures are fabricated. An oxidized silicon substrate is thermally bonded through annealing (1100°C for 2 hours) to another silicon wafer. The desired thickness of the bonded wafer can be realised through mechanical grinding, polishing and etching (Hak, 2005).

Ultra-thin single crystal layers can now be transferred from one substrate to another with the development of the Smart Cut Technology by Soitec. This technology makes use of wafer

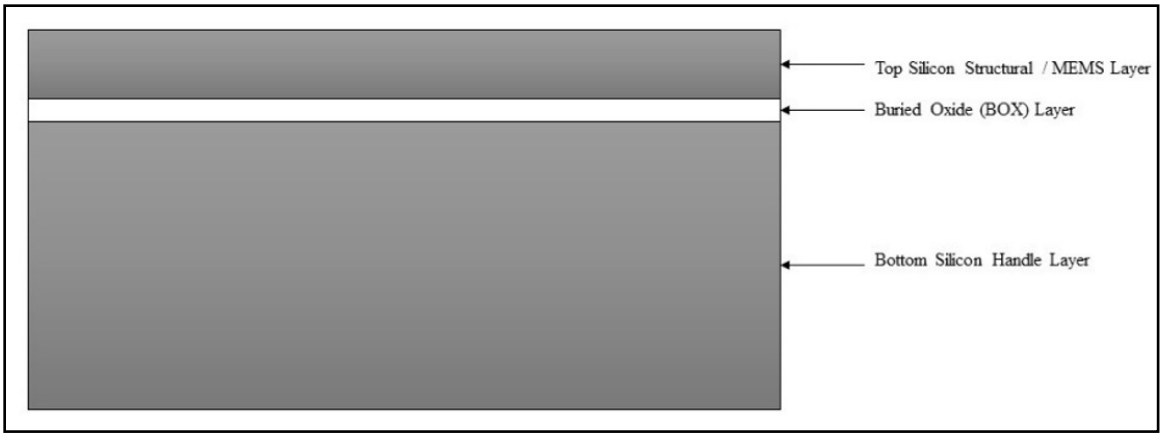

Figure 1.5 Silicon on insulator (SOI) wafer
Taken from Syms (2005)

bonding and ion implantation by implanting light elements such as hydrogen, helium, argon

etc. A layer of thermal oxide is grown on a silicon wafer followed by hydrogen implantation. The wafer is then bonded to another silicon wafer and then a part of the base silicon wafer is removed to obtain a SOI wafer for application in MOEMS. Uniform thickness, precision, large temperature range and reuse of the donor substrate are some advantages of this method (Celler et al., 2003).

In SIMOX, oxygen ions are implanted into a silicon wafer followed by annealing at 1300°C. Through varying annealing temperature and implant dose the thickness of BOX layer can be controlled. Additional epitaxial may also be grown over the structural silicon layer using CVD, if needed (Hak, 2005).

Typically, SOI micromachining involves spin coating a thick photoresist and patterning the MEMS structure in the top silicon layer using dry etching technique such as reactive ion etching (RIE) or deep reactive ion etching (DRIE) to etch away the top silicon layer selectively (Hak, 2005). Following which the buried oxide layer can be isotropically etched using buffered HF (Syms, 2005) or a backside silicon etching can be performed with the buried oxide layer acting as an etch stop, providing a suspended MEMS structure. Alternatively, a polymer layer can be spin coated and acts as an etch stop for backside etching of silicon and the buried oxide layer. The polymer layer can then be etched away to obtain suspended movable silicon structures at micron scale (Milanovic, 2004). Aluminum, aluminum-copper or gold can be patterned on top of the structural silicon layer as electrical contacts. Deposition and patterning of aluminum, aluminum nitride, PZT etc. can be done to obtain a variety of MEMS that function on different actuation mechanisms as discussed in section 1.2. MEMS fabrication using SOI technology is relatively simpler compared to surface micromachining or bulk micromachining, and requires a smaller number of masks, making it the technological choice for MEMS actuators in this thesis. Commercially available Piezo MUMPs process used for MEMS prototype device fabrication during this thesis. is briefly discussed in the next sub-section.

1.5.2 Piezo MUMPs Fabrication Process

The Piezo MUMPs process developed by MEMSCAP (now known as Science) (Cowen et al., 2013) uses SOI technology. A 10 µm silicon device sandwiches a 1 µm or 2 µm oxide layer between a 400 µm silicon substrate. The top silicon layer is patterned with piezoelectric material aluminum nitride (AlN) with a minimum thickness and minimum width of 0.5 µm and 10 µm respectively. The 0.2 µm thick and 5 µm wide oxide layer is patterned for electrical isolation of the piezoelectric material and the metal layers from silicon as shown in Figure 1.6.

The pad metal layer can be used to fabricate bond pads and electrical routes in order to achieve various forms of actuation. The process can be used to develop piezoelectric MEMS resonators

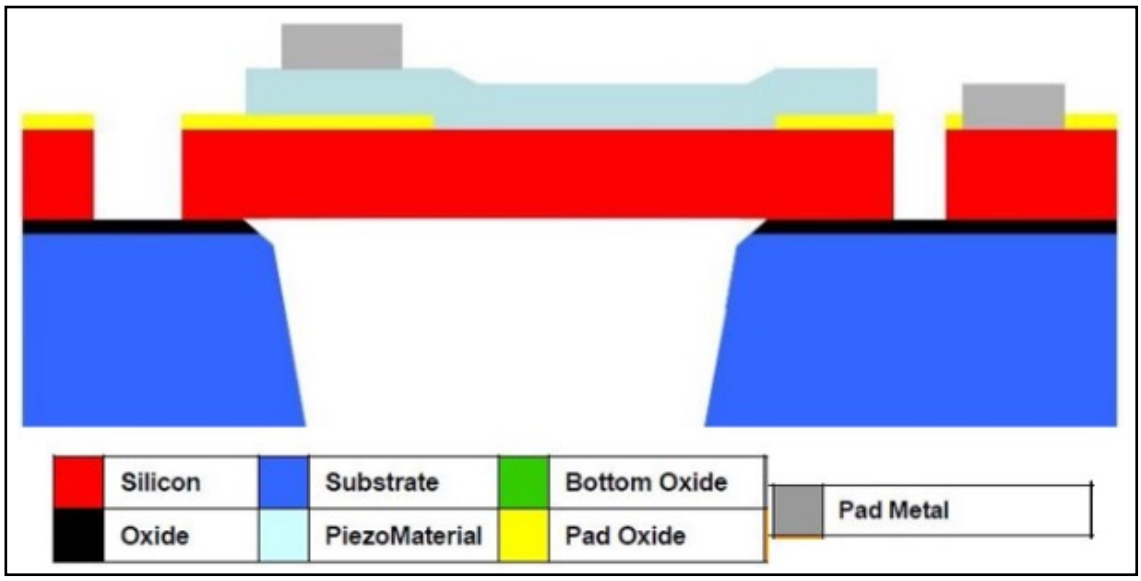

Figure 1.6 Cross sectional view of Piezo MUMPs process by MEMSCAP
Taken from Cowen et al. (2014)

(Tu et al., 2015 & Elsayed et al., 2016). The PiezoMUMPs process is mostly similar to the SOI MUMPs process barring the additional piezo material and pad oxide layers. The PiezoMUMPs and is only available with 10 µm device layer unlike the SOIMUMPs process which is available with 25 µm silicon device layer thicknesses. The SOI MUMPs has been used to develop electrostatic and electrothermal micro actuators before (Khan et al., 2010 & Guan et

al., 2010). Similarly, the Piezo MUMPs process can also be used to develop electrostatic and thermal actuators through complete removal of the piezo material and pad oxide layers. This process can also be used potentially to develop actuators with hybrid actuation mechanisms (electrostatic, electrothermal and piezoelectric).

1.6 Summary

This chapter discussed different mechanisms for converting input energy into mechanical motion of a suspended microstructure. We discussed the operating principle of electrostatic, piezoelectric, and electrothermal actuation in sections 1.2, 1.3 and 1.4. We discussed in detail the advantages and disadvantages associated with each actuation mechanism. We can conclude through this discussion that electrostatic and piezoelectric actuation mechanisms can be the most effective solutions for energy-efficient and fast MEMS devices. Different fabrication technologies used for MEMS fabrication were presented in section 1.5. SOI technology, widely used for MEMS device fabrication, was discussed in detail in section 1.5.1. Thus, the commercial microfabrication process that can be used to fabricate and test electrostatic and piezoelectric MEMS devices was discussed in section 1.5.2.

CHAPTER 2

AN OVERVIEW OF OPTICAL WAVEGUIDES

2.1 Introduction

Like signal transmission in optical fibers, optical signal can be transmitted at the chip level using photonic components called waveguides. These waveguides consist of a high refractive index core material surrounded by a lower refractive index cladding material, as shown in Figure 2.1. Total internal reflection at the waveguide core and cladding interface lets the optical signal propagate through the waveguide structure (Okamoto, 2021).

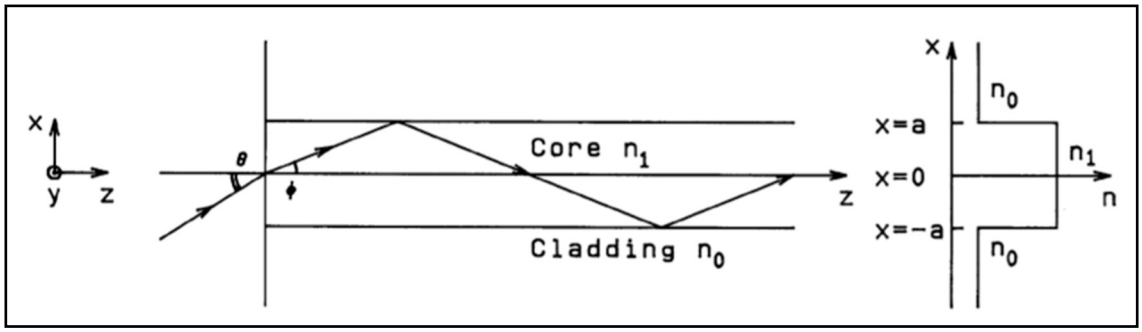

Figure 2.1 Schematic for an optical waveguide with core and cladding of different refractive index
Taken from Okamoto (2005)

Planar waveguides confine the optical signal in only one transverse direction since the waveguide core is limited in only direction between the cladding layers. Strip or ridge waveguides confine the optical signal in two-dimensions with the core surrounded by the cladding layers in all transverse directions (Liu, 2009). Figure 2.2 shows cross-sectional views

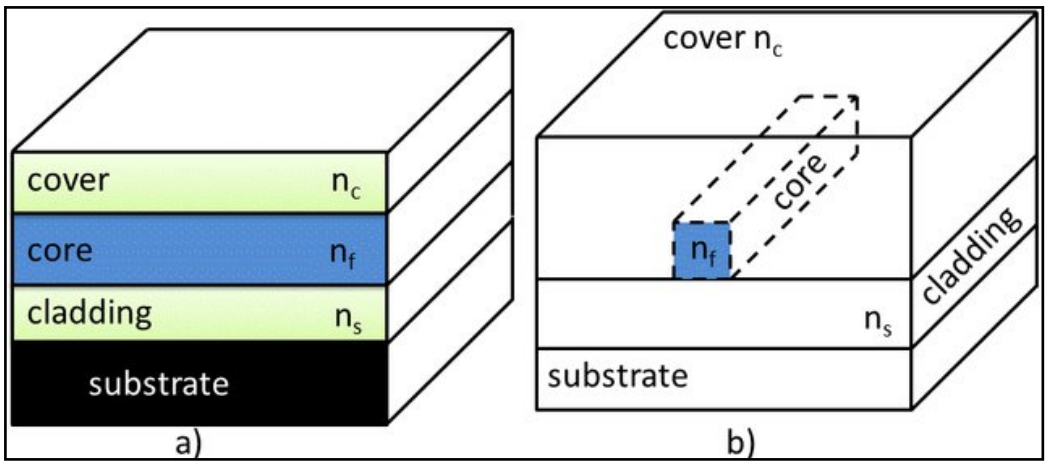

Figure 2.2 Cross-sectional view of a typical (a) planar waveguide and (b) non-planar waveguide
Taken from Prajzler et al. (2017)

of a typical planar and strip waveguide. Waveguides with an abrupt change of refractive index between the core and the cladding are referred to as step-index waveguides (Kress, 2014). Among these waveguides, buried and ridge waveguide structures are the most common non-planar channel waveguides used in photonic integrated circuits (PICs). Alternatively, smooth, and continuous change between the core and the cladding refractive index produces a refracted wave inside the waveguide core. Such waveguides are referred to as a graded-index waveguides (Kress, 2014). Various 2D channel waveguide structures are shown in Figure 2.3.

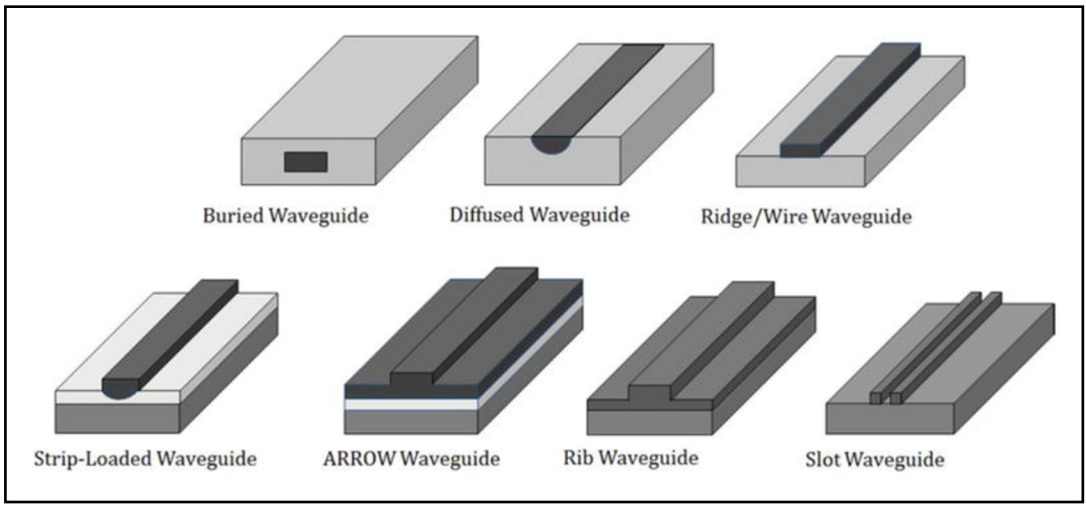

Figure 2.3 Various types of channel waveguides
Taken from You (2018)

As per the electromagnetic wave theory, optical signal propagates along the core of the waveguide as a transverse field distribution called a waveguide mode (Chrostowski & Hochberg, 2015). The electric and magnetic fields of a waveguide mode for an electromagnetic wave transmitting through a channel waveguide can be given as

$$E_v(r,t) = E_v(x,y)e^{i(\beta_v z - \omega t)} \tag{2.1}$$

$$H_v(r,t) = H_v(x,y)e^{i(\beta_v z - \omega t)} \tag{2.2}$$

where $E_v(x,y)$ and $H_v(x,y)$ are the mode field profiles, v is the mode index, ω is the angular frequency of the optical wave, and β_v is the mode propagation constant (Liu 2009). Here, the mode index v represents two mode numbers with integral m and n for the discrete guided modes in a channel waveguide. A propagating wave that is totally reflected at the interfaces of the waveguide core and the cladding results in guided modes inside a waveguide (Liu 2009). The transverse electric (TE) guided mode allows propagation of electromagnetic waves where the electric vector (E) is always perpendicular to the direction of light propagation. The transverse magnetic (TM) guided mode allows propagation of electromagnetic waves where the magnetic vector (H) is always perpendicular to the direction of light propagation. Mode profiles for different modes in channel waveguides with rectangular symmetry are referred to as Hermite-Gaussian (HG) modes (Uren 2019). The transverse intensity for different HG modes in a symmetric rectangular channel waveguide is shown in Figure 2.4.

In this chapter, we will further discuss the simulation methods and techniques used to understand wave propagation to design efficient waveguides. Edge coupling theory, to understand how optical signal is transmitted between two channel waveguides in an optical switch is discussed in the section 2.3 along with the critical factors for efficient edge coupling between waveguides.

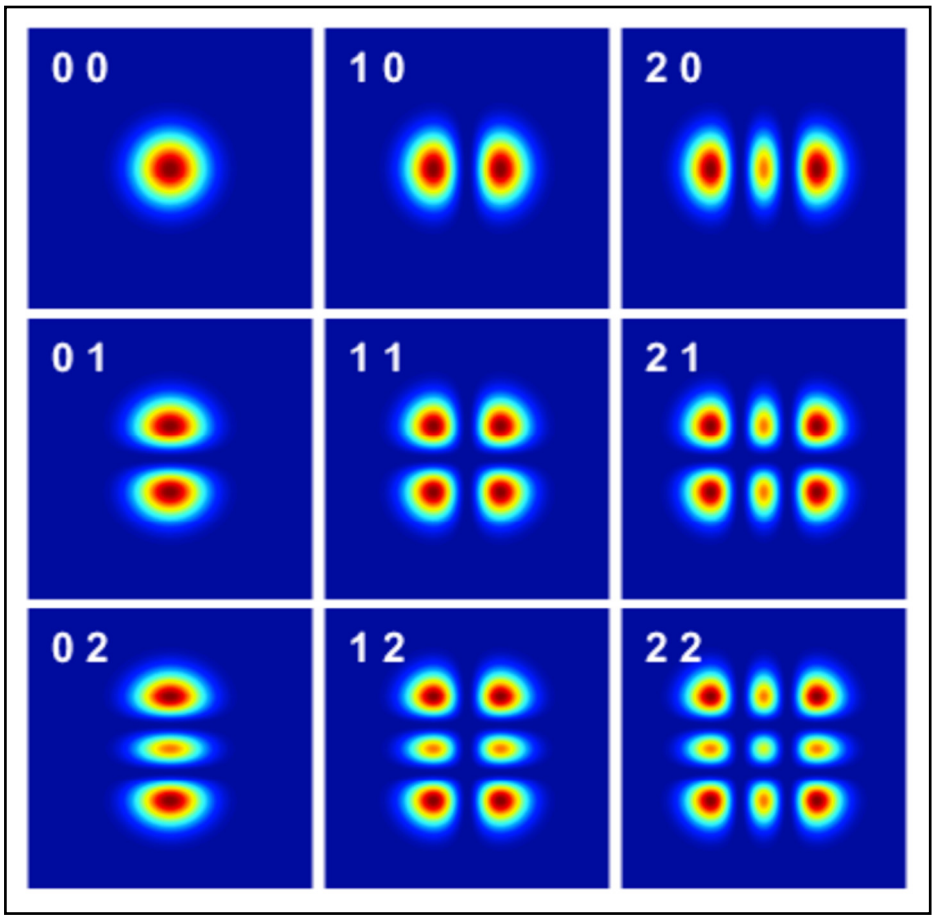

Figure 2.4 Mode intensity profile for different HG modes in a symmetric rectangular channel waveguide where the first number denotes order *m* and the second number denotes order *n* with 0 0 representing the fundamental HG mode
Taken from Uren (2019)

2.2 Waveguide Design

Typically, one-dimensional (1D) calculations (where the waveguide is considered a planar waveguide with restricted thickness as per the specification from the foundry used for microfabrication) are used to analyze the waveguide modes supported by a certain waveguide core thickness. Once the waveguide thickness is determined, the effective index method can

be used to find a suitable waveguide width to achieve single mode or multi-mode light propagation (Chrostowski & Hochberg, 2015).
Finite difference time domain (FDTD) and Eigenmode expansion (EME) methods are used in this thesis to design efficient single mode SiN channel waveguides. The dimensions are restricted as per the specifications determined by the industrial partner AEPONYX inc.

2.2.1 FDTD Method

The FDTD method is a numerical solution method used to solve 3D Maxwell equations to understand and analyze light interaction with complex waveguide structures. This method operates in the time domain, simulating the propagation of a brief light pulse (ranging from tens to hundreds of femtoseconds) containing a broad spectrum of wavelengths. The system response to this pulse correlates with the transmission spectrum through the Fourier transform, allowing a single simulation to capture the optical system response across a diverse range of wavelengths simultaneously. The following steps (as shown in Figure 2.5) are followed for a typical FDTD simulation (Chrostowski & Hochberg, 2015):

- Defining optical materials (e.g., silicon, silicon nitride) using the material from the library in the software tool for these simulations.

- Defining structures (waveguides, cladding) using a graphic user interface (GUI) or a script. Parameterization of the geometry can be helpful in design optimization while saving the computational time.

- Specifying simulation parameters such as mesh size and boundary conditions. Optimal mesh size is very important for simulation efficiency as the simulation time is proportional to $1/dx^4$, where dx is the mesh size. Similarly, metallic boundaries can be used as perfect reflectors in regions where no light absorption is expected to reduce the computation time.

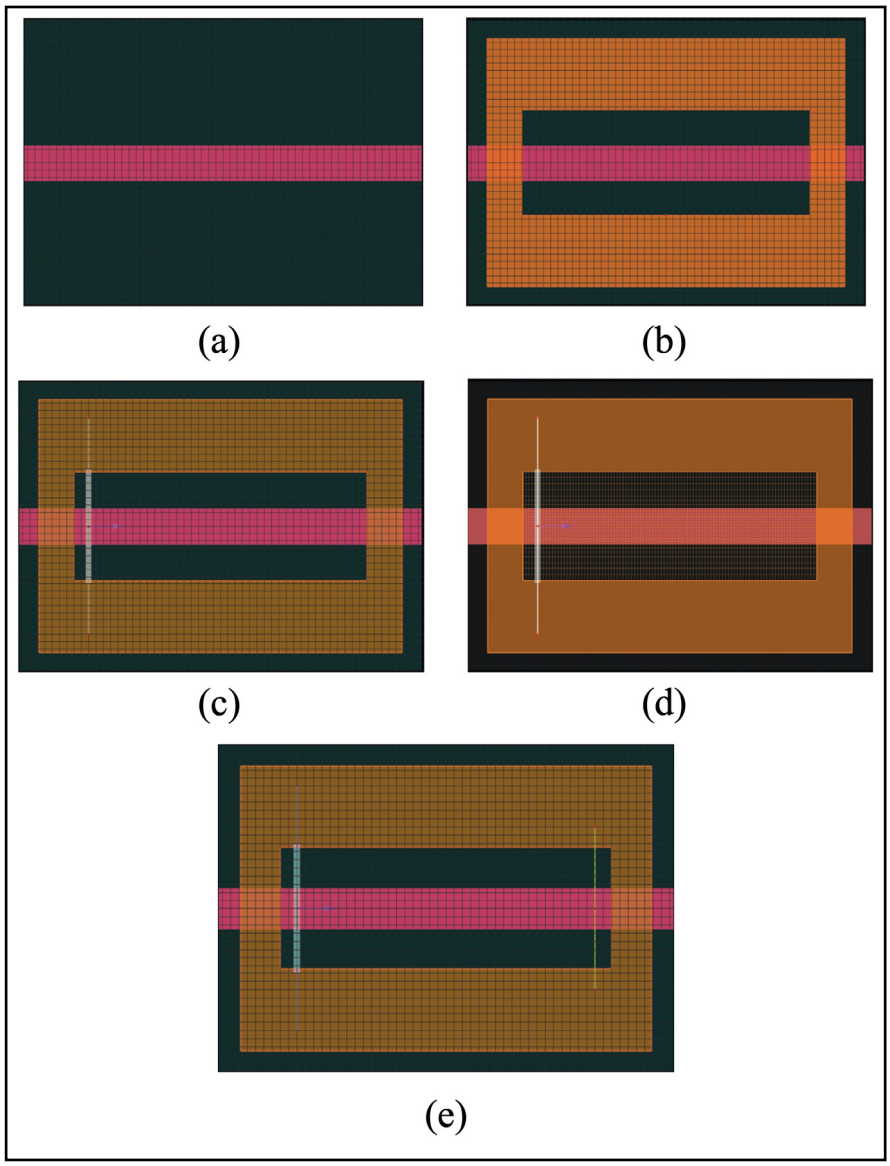

Figure 2.5 Typical steps for FDTD simulations where (a) materials and geometries are defined, (b) the simulation volume, mesh, and boundary conditions are defined, (c) the optical source is added to launch light into the waveguide, (d) the mesh is optimized to reduce simulation time, and (e) a profile monitor is added to measure the optical field quantities Adapted from Chrostowski & Hochberg (2015)

- Adding optical sources with the appropriate mode (e.g., fundamental TE mode) based upon mode calculations for the waveguide structure used in the simulation model. This

optical source needs to be placed 1-2 mesh points away from the boundary within the defined simulation volume.

- Adding monitors at specific locations to measure the optical field quantities, E and H, at these locations. These can be a point, a line, a plane, or a 3-D space. A field profile monitor can be used to generate the optical transmission spectrum of the waveguide.

- Sweeping parameters dependent upon waveguide geometry, wavelength, polarization etc. helps in design optimization to achieve waveguide structures with the desired figure of merit.

While the 3D FDTD technique is the most accurate in predicting the light propagation in a waveguide core, its main drawback is that it is computationally intensive, given the sub-femtosecond simulation time-step. Alternatively, the 2.5D FDTD or 2D FDTD approach can be used for planar photonic components. The effective index method (EIM) is used to convert the 3D structure to a simpler 2D set of effective indices. The main advantage of this approach is the fast computation time that helps in faster design optimization by simulation of many design parameters. Its main disadvantage is that it cannot be used for modeling devices such as polarization rotators because it does not consider coupling between the TE and TM modes (Chrostowski & Hochberg, 2015). In this thesis, both 3D FDTD and 2.5D FDTD methods have been used for waveguide design optimization.

2.2.2 EME Method

While the FDTD method allows accurate simulations in short waveguide structures, long structure simulations exhibit significantly longer simulation times. The EME method is ideal for simulating such long structures with efficient simulation times. The EME method is also used to solve Maxwell's equations to understand and analyze light interaction with complex

waveguide structures. However, it is a frequency domain method, unlike the FDTD method which is a time domain method.

In any waveguide, guided modes propagate light along the waveguide without loss while the radiation modes dissipate optical power away from the waveguide. These modes together form a complete basis set that can be used to express the solution of Maxwell's equations in any region of the waveguide in terms of a superposition of the forward and backward propagation modes (Gallagher et al., 2003). The EME method examines light propagation by breaking down the local field into position-specific modes referred to as "supermodes". Scattering parameters, also known as S-parameters, are used to connect each position-specific mode to the next section of the device (Chrostowski & Hochberg, 2015). This technique provides an effective approach to simulate mode propagation in waveguide tapers and bending regions (Gallagher et al., 2003).

Staircase approximation and first-order integration modeling approaches can be used to compute local modes at discrete positions along the waveguide taper using the EME technique. The first-order integration approach avoids the issue of non-physical reflections at the section interfaces that give rise to spurious resonances for long structures along with the overall improvement in computational efficiency in comparison to the staircase approximation approach. These approaches for mode propagation along with waveguide taper are shown in Figure 2.6. The EME framework allows a bend to be treated as a set of straight waveguides

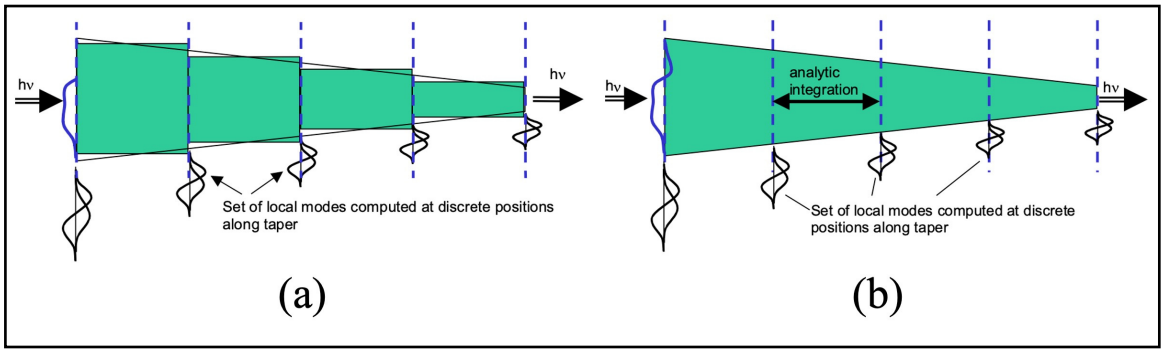

Figure 2.6 Different approaches for EME method-based computation of a waveguide taper using (a) staircase approximation and (b) first-order integration
Taken from Gallagher et al. (2003)

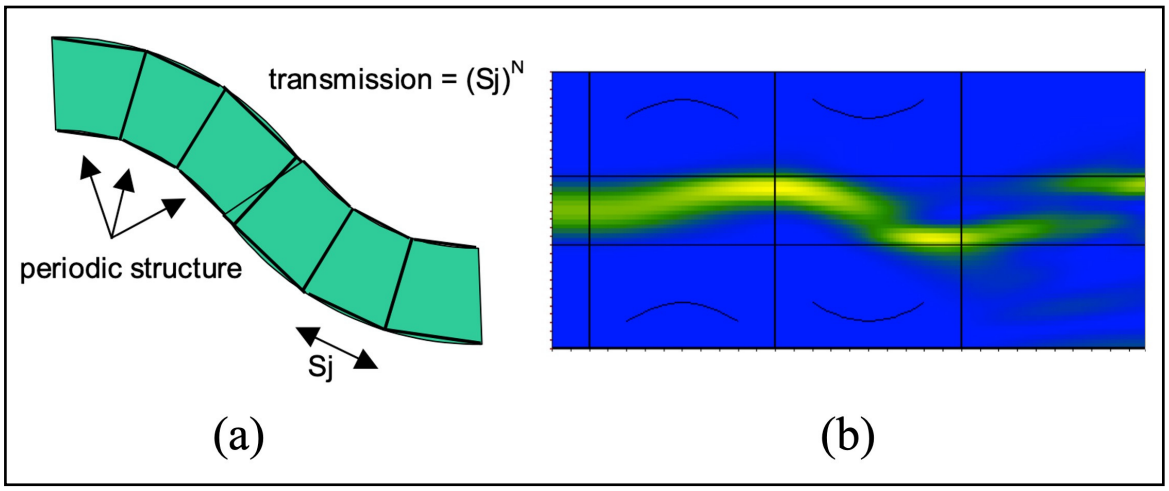

Figure 2.7 (a) EME computation approach using a periodic algorithm for a s-bend, and (b) simulation result showing light propagation through the s-bend
Taken from Gallagher et al. (2003)

with slight tilt between each section ash shown in Figure 2.7. This approach allows efficient computation of waveguide bends through the use of a periodic algorithm (Gallagher et al., 2003).

The EME method offers significant advantages based upon its rigorous solution of Maxwell's Equations. While an exact solution is achievable with an infinite number of modes, practical limitations limit the number of modes that can be used for numerical approximations. EME bi-directional algorithm, accounting for all reflections, and the S-matrix technique, can provide solutions for both TE and TM inputs simultaneously. EME wide-angle capability allows simulating light propagation at any angle. The method efficiency is notable, particularly for structures with relatively small cross-sections, where computation times are significantly shorter than other techniques. However, EME faces challenges with structures of large cross-sections due to cubic scaling of computational time with width. Also, complex algorithms often require meticulous attention to ensure comprehensive mode inclusion (Gallagher et al., 2003). In this thesis, the EME method has been used to design waveguide tapers, enhance coupling between waveguides, and to understand alignment tolerances for the improvement of MEMS designs.

2.3 Edge Coupling

Optical signal transfer from one optical component to another is referred to as “coupling” between components. Broadly coupling can be of two types, off-plane coupling and in-plane coupling (Mu et al., 2020). Grating couplers can be used to couple light between waveguides and optical fibers that are in different planes (off-plane coupling). Grating couplers prevent the key issues of mode mismatch, low alignment tolerance, and post-processing after fabrication, that are associated with the alternative in-plane coupling approach using edge couplers (Chrostowski & Hochberg, 2015). Edge couplers can couple light between a waveguide and an optical fiber that are in the same plane, or between two waveguides that are in the same plane (in-plane coupling). Broadband response, low insertion loss, and the ability to couple both TE and TM polarizations are the key advantages of edge couplers over grating couplers (Chrostowski & Hochberg, 2015). In this thesis, we use grating couplers to couple light between fiber array and SiN waveguides. However, we use edge coupling to couple light between suspended and fixed SiN waveguides to achieve an optical switch with minimum insertion loss.

The most basic form of an edge coupler relies on a standard single inverse taper, providing a straightforward solution for various types of edge couplers. However, when the thickness of the waveguide remains constant, it transforms into a taper, causing inadequate confinement of light within the narrow taper end. As the width gradually decreases, the mode is distributed in a larger area around the taper, contributing to an enlarged modal size. This taper profile is referred to as a linear profile. Although the linear profile is a common choice for its structural simplicity and ease of fabrication, it may not be the most suitable for achieving optimal performance due to its large size and limited coupling efficiency, especially when coupled with fibers with large spot sizes (Mu et al., 2020). However, it can work well when used for coupling with similar sized waveguides in an integrated optical switch, as intended in this thesis. Research studies have explored different taper profiles, such as multi-sectional (Fu et al.,

2014), parabolic (Hettrick et al., 2004), and exponential tapers (Ren et al., 2011), aiming to enhance performance in terms of a smaller footprint, lower propagation loss, and broader

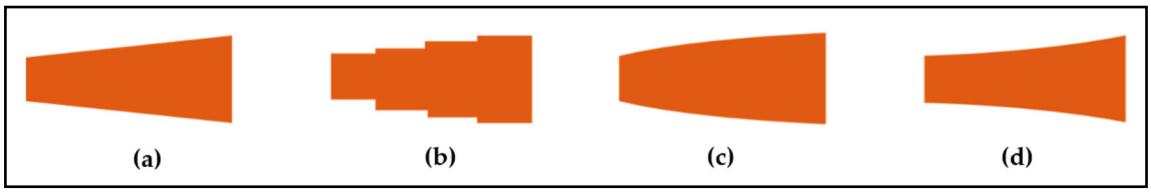

Figure 2.8 (a) Linear, (b) multi-sectional, (c) parabolic and (d) exponential inverse tapers
Taken from Mu et al. (2020)

bandwidth (Mu et al., 2020). These taper profiles are shown in Figure 2.8.

Coupling efficiency for an edge coupler can be estimated through analysis of the mode profile at the tip of the inverse taper. Usually, mode overlap calculations are performed to estimate the coupling efficiency between an edge coupler and an optical fiber. It is necessary that the mode profiles from the waveguide (shown in Figure 2.9) and the optical fiber match well to limit any mode-mismatch loss. Since we intend to use inverse taper edge couplers for coupling between waveguides of similar dimensions, mode-mismatch will not be as critical as in the case of fiber-to-chip edge coupling. However, such mode overlap calculations can help assess the impact of

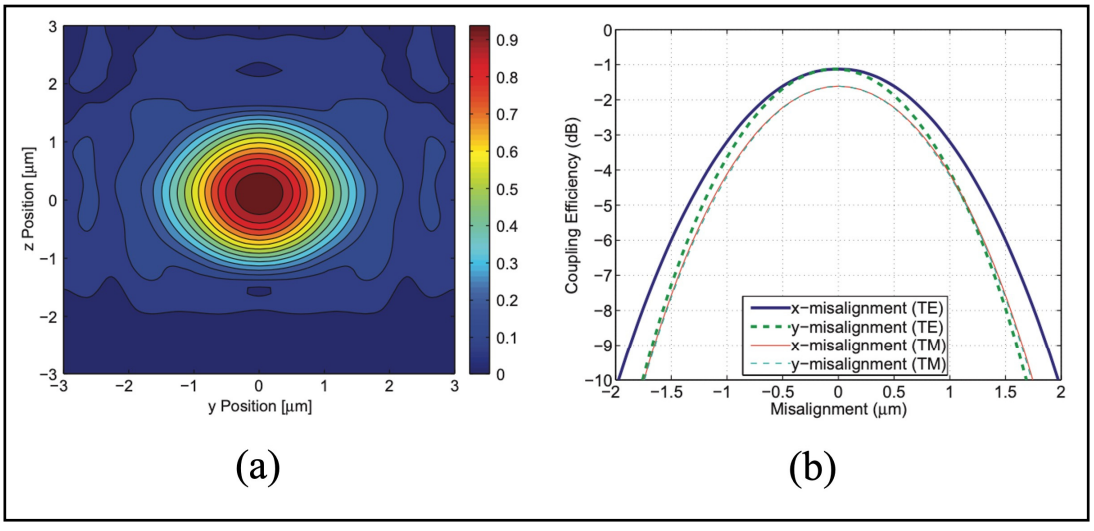

Figure 2.9 (a) FDTD simulation-based field profile at inverse taper output in air, and (b) misalignment impact upon coupling efficiency
Adapted from Chrostowski & Hochberg (2015)

misalignment upon edge coupling efficiency as shown in Figure 2.9 (Chrostowski & Hochberg, 2015).

2.4 Summary

This chapter discussed optical waveguide theory along with an overview of the different types of waveguides in section 2.1. Widely used simulation methods, FDTD and EME, were discussed in section 2.2 of this chapter, to understand their implementation in designing efficient waveguides. Steps and approaches associated with these methods along with their advantages and disadvantages were also presented in section 2.2. The edge coupling method, that is critical to understand the coupling between optical components that are in the same plane, was discussed in section 2.3.

CHAPTER 3

AN OVERVIEW OF OPTICAL MEMS SWITCHES

3.1 Introduction

The first generation of MEMS devices were introduced in 1960's (Nathanson, 1967). Through 1970s and 1980s MEMS evolved from pressure sensors (Johnston, 1974) and inkjet nozzles (Kurth, 1979) to the first MEMS mirror (Peterson, 1980) and rotary motor (Fan et al., 1988). It took nearly 15 years since the introduction of MEMS mirror for its use in telecommunication applications (Lin, 1994). Research in the past decade or two has moved towards the integration of mems with silicon photonics (Marxer et al., 1999, Zhang et al., 2007, Zandi et al., 2012 & Quack et al., 2016).

Conventional optical switching in telecommunication networks such as synchronous optical network (SONET) uses optical-electrical-optical (OEO) technology in network nodes. This technology requires conversion of the optical signal into the electrical signal for switching. The switched electrical signal is regenerated into the optical signal for further transmission (Maier, 2008). This OEO regeneration is expensive and energy intensive (Grubb et al., 2006 & Ji et al., 2014). The alternative approach for switching in telecommunication networks such as all-optical networks (AONs), uses optical add-drop multiplexers (OADMs) and optical cross-connects (OXCs) (Maier, 2008) in network nodes. In comparison to SONET, AONs can provide energy efficient all optical switching without the complexity of optical signal conversion and regeneration. MEMS integration in OADMs and OXCs can further reduce power consumption through use of electrostatic and piezoelectric actuators for switching in AONs (Robinson 2001).

MEMS based optical switching can be achieved in two configurations. It can be 3-D or out-of-plane configurations through reflection of the input optical signal over the mirror surface using

suspended MEMS-based mirrors. Alternatively, it can also be in 2-D or in-plane / planar configuration through in-plane movement of suspended waveguides or mirrors for optical switching (Han et al., 2015). Such integration allows all optical switching with low power consumption at a reduced cost in comparison to OEO technology (Seok et al., 2016). These optical MEMS switching solutions can meet the growing demand for all optical switching to overcome the OEO bottlenecking in an energy efficient way. MEMS integration with optics can provide wide operational wavelength range with minimum power consumption. It can provide functional optical devices based on industrial microfabrication processes that also enable all optical networks at low cost through batch processing.

In this chapter, we will discuss optical MEMS devices operating mainly using power efficient electrostatic actuation. Some piezoelectric and electrothermal actuators will be discussed as well. The two configurations of optical MEMS switches, out-of-plane and in-plane are discussed in separate sections of this chapter. Out-of-plane (z-direction or more than one plane) with vertical and rotational motion devices which also includes hybrid devices with more than one actuation mechanisms are discussed in section 3.2. Planar (x-y plane) devices with lateral and rotational motion for optical switching are discussed in section 3.3.

3.2 Out-of-Plane Optical MEMS

Electrostatic actuators have been incorporated in optics for many years as out-of-plane rotational mirrors. These have found applications as optical switches (Fernandez et al., 2004) and scanners (Zhou et al., 2006) for telecommunication applications. Mirrors with different geometries have been designed for out-of-plane rotation as shown in Figure 3.1. Researchers over the past decades have focussed on bringing down the operational voltage with enhanced displacement / rotation through development of staggered vertical comb drive (SVC) (Yunija et al., 2014) and angular vertical comb drive (AVC) (Kim et al., 2006). Through incorporation of different materials such as PDMS (Lee et al., 2011) and SU-8 for torsional springs, thick rotor layers and small lateral gap, SVCs can provide larger displacement / rotational motion

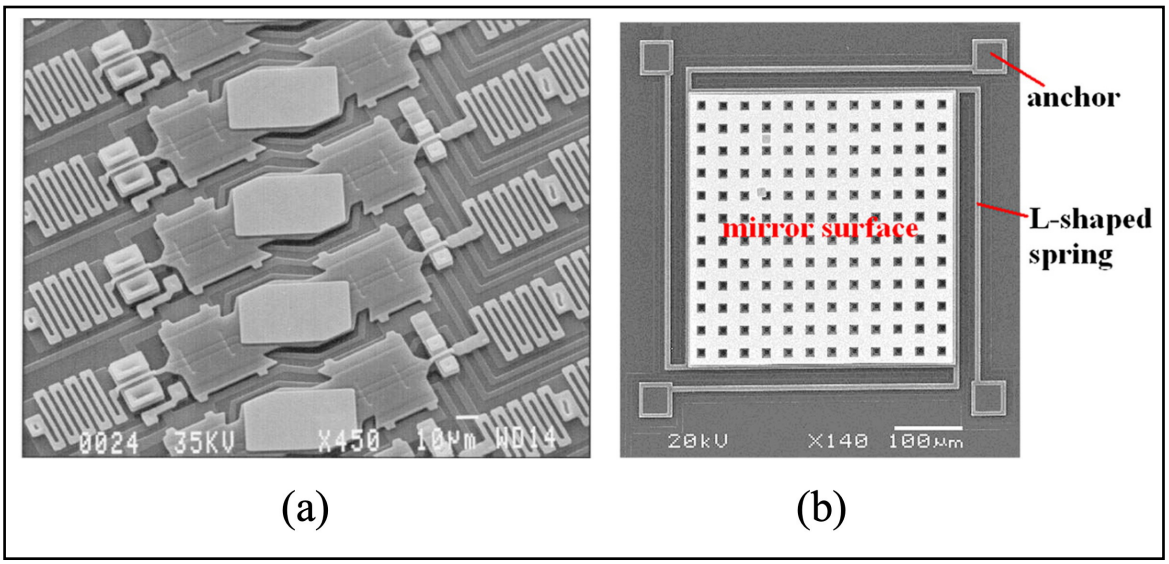

Figure 3.1 (a) Hexagonal MEMS mirror array
Taken from Ford et al. (1999)
(b) Square MEMS mirror array
Taken from Hu et al. (2010)

(Yunija et al., 2014). Gimbal frame design consisting of a mirror placed in the center connected to two separate frames through torsion beams that provide rotation about two axes using electrostatic actuation have been demonstrated by researchers using polysilicon MUMPs process (Toshiyoshi et al., 2001), SOI backside isolation process (Kwon et al., 2004) and combination of SOI and polysilicon for enhanced fill factor, mechanical strength, and electrical routing (Hung et al., 2015).

Electrostatic actuation used for such out-of-plane displacement often requires complex fabrication processes which involve bonding of multiple SOI wafers (Lee et al., 2004), or polysilicon with SOI (Quack et al., 2016), or commercially available MUMPs and Honeywell processes (Hung et al., 1999) for electrostatic pull down. Multiple SOI wafers have also been combined through the Micralyne's MicraGEM-Si fabrication process to achieve an out-of-plane upward displacement with rotational motion (Ba-Tis et al., 2015). However, it should be noted that this process would be relatively costly in comparison to Piezo MUMPs processes

available to us through CMC, and can come with the fabrication complexity, high number of masks and misalignment issues.

3.3 In-Plane Optical MEMS

Comb drive based electrostatic actuators have been designed to produce lateral actuation in MEMS devices. Each comb drive consists of interdigitated fingers of different materials, depending upon the fabrication process it can be doped polysilicon (Legtenber et al., 1996), metal (Marxer et al., 1999) or silicon (Almeida et al., 2006). These comb drives are electrostatically actuated to move a connected suspended structure which is anchored at one or more ends through beams or springs, usually of the same material. In recent years, silicon-based comb drives have become an important part of research and development of optical

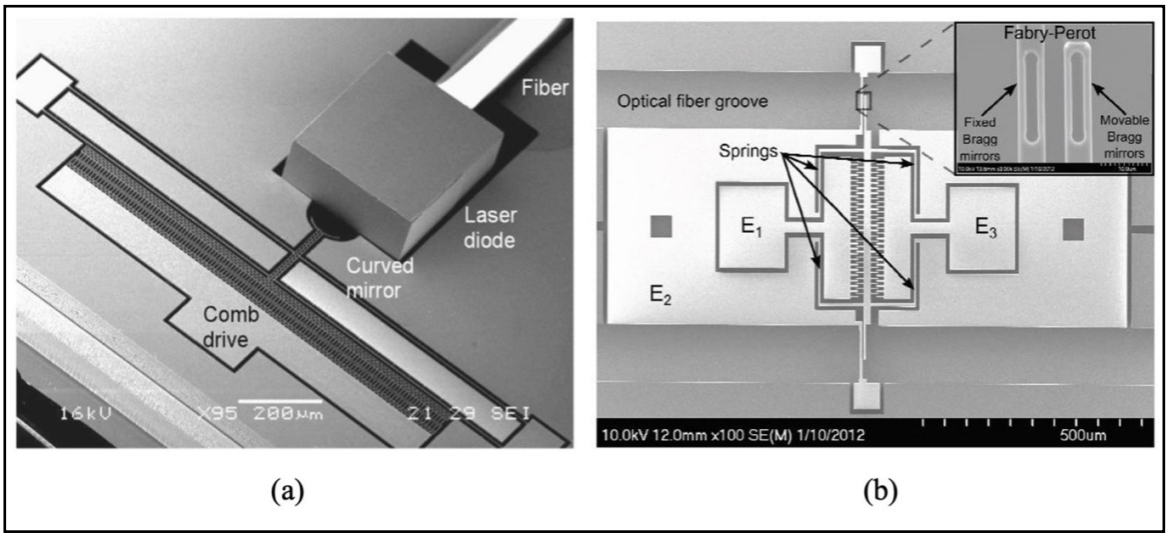

Figure 3.2 (a) Tunable laser with curved mirror
Taken from Zhang et al. (2004)
(b) in-plane MEMS tunable Fabry-Perot filter
Taken from Poulin et al. (2012)

MEMS devices. SOI technology where the top silicon layer is used for both optics and actuation has been demonstrated as shown in Figure 3.2.

Zhang (2004) designed a curved mirror instead of a flat one which when electrostatically actuated using comb drives provided a tuning range of 13 nm with low power consumption.

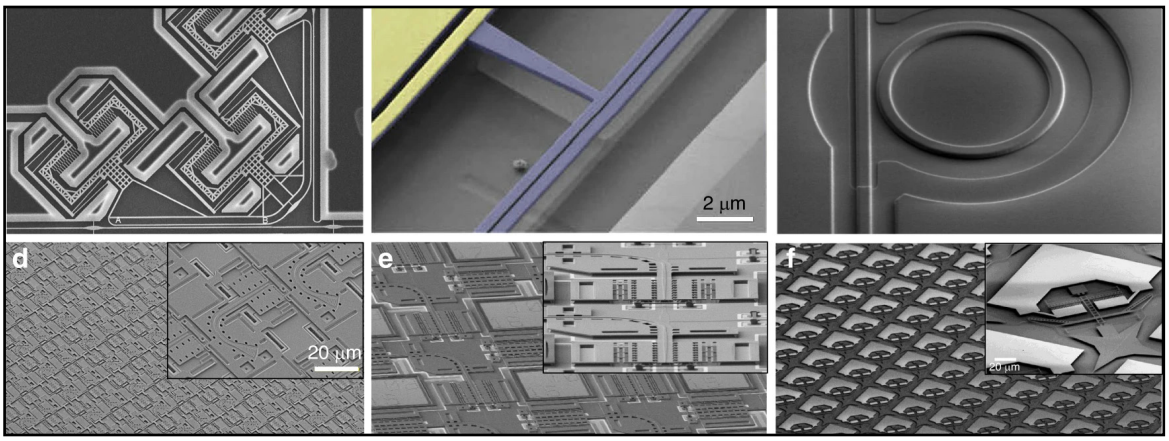

Figure 3.3 SOI-based recently demonstrated silicon photonics MEMS solutions: (a) tunable couplers, (b) phase shifters, (c) ultrasound sensors, (d) beam steering device, (e) (f) large-scale photonic switch matrix
Taken from Quack et al. (2023)

Poulin (2012) developed a MEMS based laser with linear behaviour through the integration of Fabry-Perot filter into the design. The linearity obtained was due to the push and pull electrostatic actuator design along the y-axis using comb drives. A 35 kHz natural resonance frequency with a small tuning range of 20 nm was achieved for the device. Biaxial gimbal structures have also been achieved using electrostatic actuation driven by comb drive structures to move a micromirror structure on a suspended silicon platform (Laszcyk et al., 2010). Such MEMS and photonic integration to combine complex optical systems has made significant progress. Si has been the leading material for such integration where the device layer of a SOI wafer works for both MEMS and optics as shown in recently developed devices in Figure 3.3 (Quack et al., 2023).

Usually, switching in MEMS integrated silicon PICs use directional couplers that rely upon evanescent field interactions to couple light between adjacent waveguides. Separation between waveguides and interaction is critical to the power coupled between waveguides during the switching action (Quack et al., 2023). A MEMS tunable ring resonator that uses electrostatic actuation to move suspended Si ring resonator alongside Si channel waveguides has been demonstrated as a add-drop filter (Errando-Herranz et al., 2015). Similarly, a directional

coupler that integrates Si channel waveguides and bi-directional Si-based MEMS actuators in the same SOI device layer has been used to demonstrate broadband operation over the wavelength range of 1520 nm to 1580 nm (Sattari et al., 2020). This device has been further implemented in a 6-port optical switch with 4-switching configurations with a low actuation voltage of 3.75 V (Sattari et al., 2021). A 50 x 50 Si photonics switch has also been demonstrated that uses Si-based MEMS cantilevers bent due to residual stress to switch light between Si waveguides. This switch also relies upon directional coupler design where switching is done through evanescent coupling between adjacent waveguides (Han et al., 2015). Only a few devices have been developed that use edge coupling between waveguides for optical switching. A 1 x 2 Si photonics switch that can move the suspended input Si channel waveguide towards any of the two output Si channel waveguides through MEMS-based b-directional motion of the input waveguide has been demonstrated with 1.5 dB insertion loss (Ollier, 2002). These devices have the constraint of using the same Si layer for both MEMS and photonics which limits independent control over the two key technologies. A 2 x 2 optical switch that integrated polymer waveguides with Si-based MEMS has been demonstrated with 3 dB insertion loss (Frank & Chollet, 2009). However, no broadband operation was reported for the polymer waveguides used in this optical switch.

In conclusion, the integration of MEMS with waveguides for photonics applications, particularly in silicon photonics, shows great promise in overcoming current limitations and advancing towards the realization of very large-scale PICs. While challenges remain, the combined effort of researchers and engineers is paving the way for the next generation of integrated photonic devices with enhanced performance and functionality.

3.4 Summary

In this chapter, the need for MEMS-based optical switching solutions along with the limitations of current OEO switching technology was discussed in section 3.1. Several existing optical switches that include MEMS for out-of-plane 3-D motion of suspended mirrors were discussed

in detail in section 3.2. We saw that such devices involve complex assembly of free space optics with MEMS-based suspended mirrors that consume space and include complex microfabrication process. These solutions are ideal for scanner and LiDAR applications. Planar MEMS-based optical switches can integrate MEMS with waveguides in a smally device footprint that requires a simpler fabrication and assembly process in comparison to out-of-plane 3-D optical MEMS systems. Recent development of such devices has also shown promising energy-efficient solutions as tunable couplers, phase shifters, ultrasound sensors, beam steering devices, and large-scale photonic switch matrix. However, completely SOI-based integrated optical systems that use Si device layer for both optics and MEMS components limit independent control over each component. This creates a demand for developing alternative planar optical MEMS solutions that can give control over the different aspects of the integrated device. With this view, MEMS integration with SiN photonics is discussed further in chapter 4 of this thesis.

CHAPTER 4

MEMS INTEGRATION WITH SIN PHOTONICS

4.1 Introduction

Early research in using SiN waveguides for optical signal transmission was to guide a 632-nm light through slab waveguides (Boyd et al., 1976; and Stutius & Streifer et al., 1977). Like silicon waveguides, SiN waveguides require top and bottom cladding structures to confine light within the waveguide core. In case of SiN waveguides, a silicon oxide cladding with thickness as much as 15 μm has been used to limit absorption of light in the silicon substrate (Bose et al., 2023). High power handling, low optical losses, and transparency over a broad wavelength range of 400 nm to 2350 nm have driven research in developing photonic components using SiN waveguides. Low propagation loss in the range of 0.3 dB/m to 1.0 dB/m over the wavelength range provided by SiN waveguides can enable linear and nonlinear optical functions (Blumenthal et al., 2018). Shorter wavelengths below 1.1 μm demonstrate high absorption losses for Si waveguides in comparison to SiN waveguides that are transparent in most of the visible range. SiN has been used to implement optical devices with on-chip spectroscopic sensing (Subramaniam et al., 2015).

Si waveguides can have losses of 1 to 2 dB/cm due to scattering losses caused by sidewall roughness. SiN waveguides can have losses as low as 1 dB/m at 1550 nm wavelength that is suitable for telecommunication applications (Bauters et al., 2011). Si waveguide refractive index of 3.5 at 1550 nm wavelength, in comparison to SiN waveguide's refractive index of 2 at 1550 nm wavelength, is significantly high. This provides a better index contrast for Si waveguides when cladded with SiO2 in comparison to SiN waveguides. This is useful for compact optical systems with high degree of light confinement. However, it also makes the waveguide sensitive to width variations which SiN waveguides can be less prone to width variations in comparison (Baets et al., 2016). Since SiN waveguides are fabricated on top of

Si device layer and are independent of the Si device layer of thickness in a SOI layer, these waveguides can be configured in single layer or multi-layer configurations as per the desired application.

In the last two decades, commercial foundries have developed SiN waveguides of three types depending upon waveguide core geometry as per the cross-sectional material stack representations shown in Figure 4.1. These can be single strip waveguide, multilayer waveguide with more than one layer of SiN waveguide core material, and buried waveguide

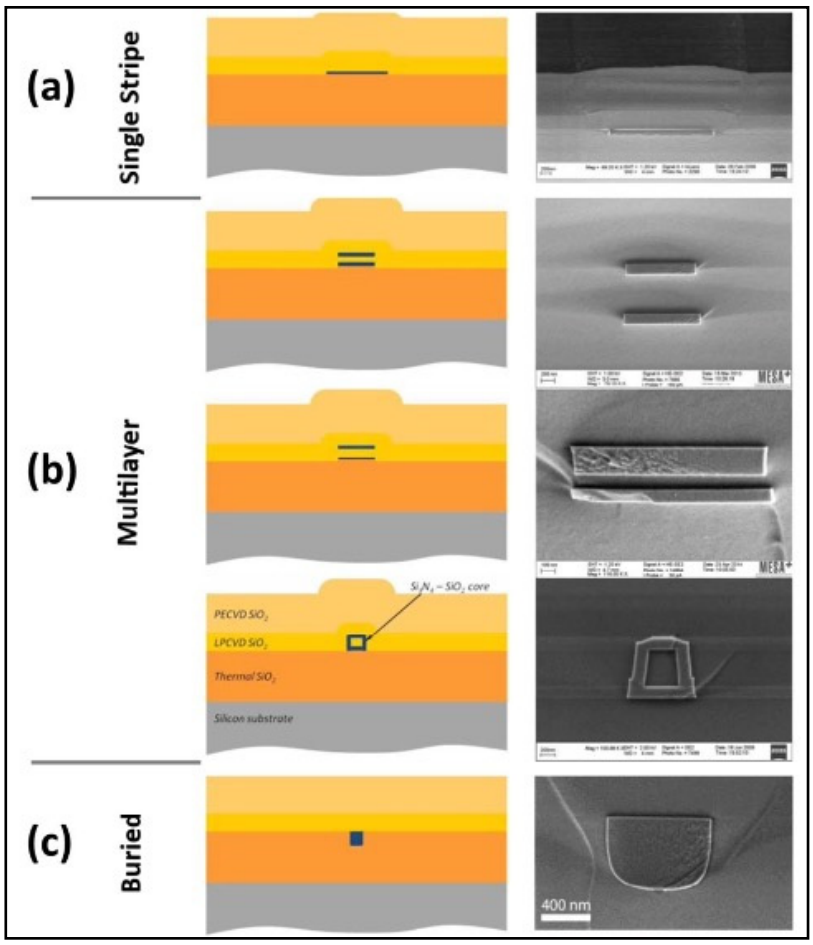

Figure 4.1 Cross-sectional and scanning electron microscope (SEM) images of three types of commercially available SiN waveguides, (a) single stripe waveguide, (b) multi-layer waveguide consisting of symmetrical, asymmetrical, and box configuration, and (c) buried waveguide
Taken from Blumenthal et al. (2018)

with SiN waveguide core buried inside the bottom cladding material. Single stripe waveguides show ultralow propagation losses with optimized fiber coupling (Huffman et al. 2018). Multi-layer waveguides have been designed with tight bends that can taper into single stripe (Worhoff et al., 2015). Box shaped multi-layer SiN waveguides can be polarization independent (Morichetti et al., 2007), and buried SiN waveguides have shown high confinement with non-linear optical properties (Epping et al., 2015). All these use bottom cladding of thermally grown silicon oxide (SiO2) material with low pressure chemical vapour deposition (LPCVD) and plasma enhanced chemical vapour deposition (PECVD) grown SiO2 as top cladding (Bluementhal et al., 2018). These commercial processes have enabled also nonlinear optics-based devices using SiN waveguide core (Pfeiffer et al., 2016).

In this chapter, we will briefly discuss the state-of-the-art silicon nitride waveguide-based photonics switching solutions. In section 4.2 we look at the recent development in thermal tuning of SiN optical components, and MEMS-based optical switching. The microfabrication technology developed by AEPONYX Inc. in collaboration with our research group at ETS is presented in section 4.3. Following this, we discuss the key factors for successful MEMS integration with SiN photonics that have been addressed in this Ph.D. thesis.

4.2 Thermally Tuned Silicon Nitride Photonics Switching

NGPON-2 optical distribution networks can benefit greatly by all optical switching solutions in the C and L band of the telecommunication spectrum between 1500 nm and 1630 nm wavelength range that can support up to 8 switching channels (Pinho et al., 2020). SiN photonics can provide such switching solutions due to its optical performance in the C and L bands. Most of the existing SiN photonics switching solutions use the thermo-optic effect to generate switching action between different MZI arms to in a simple on-off, 1 x 2 or a 2 x 2 optical switch configuration (Faneca et al., 2020; Mashayekh et al., 2021; Joo et al., 2018). A 4 x 4 polarization independent SiN photonics switch with MZI based optical switching has also been demonstrated recently that uses 580 nm thick SiN waveguide core (Sun et al., 2019).

A 1 x 4 SiN photonics switch has also been demonstrated that uses double strip SiN wavegiudes in an MZI-based architecture (Lin et al. 2022). However, the device is very large in size at

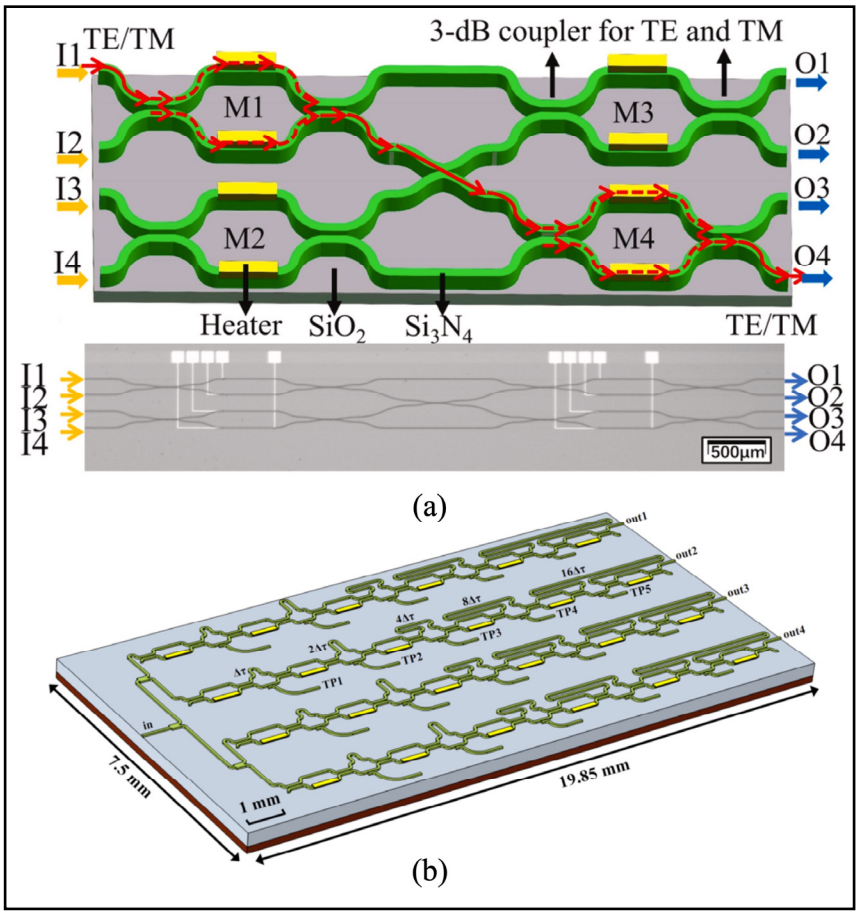

Figure 4.2 Schematic of (a) thermally tuned 4 x 4 polarization independent SiN photonics switch with microscopic image of the fabricated device
Taken from Sun et al. (2019)
(b) thermally tuned 1 x 4 microwave photonic beamforming device
Taken from Lin et al. (2022)

148.9 mm^2. Some of these optical switches are shown in Figure 4.2.

All of the conventional SiN photonics switching solutions discussed so far rely upon thermos-optic effect which consumes high power. One of the arms of the optical component such as MZI has to be heated to modify the refractive index. This consumes high power due to electric

current produced as well as generates heat in the device. The optical switching produced is also not truly broadband in nature and usually filters out different wavelengths or produces phase shift in the input optical signal. Heating of optical components for switching also leads to slow device performance. Some SiN photonic switches have been integrated with graphene layer to reduce the switching time significantly (Zhang et al., 2019, Qiu et al., 2021). However, these devices still consume large power up to 89.1 mW. There is a need for energy efficient SiN photonics switching solution that can provide true broadband switching. MEMS integration with SiN waveguides can provide such solutions which are discussed in the next section.

4.3 MEMS Integrated Silicon Nitride Photonics Switching

As discussed in the previous section, MEMS integration with SiN photonics can lead to power efficient switching solutions with broadband operation which can benefit NGPON-2 optical distribution networks. Only a few MEMS-based SiN photonics switching solutions exist. Most of them utilize low power electrostatic or piezoelectric actuation to tune the optical components fabricated using SiN waveguides. Electrostatic actuators have been used to tune a SiN ring resonator to filter out 3 wavelengths (Nielson et al. 2005). Although such MEMS integration achieves low power tuning of optical filters, it cannot achieve true broadband switching. Similarly, PZT-based piezoelectric actuation has been used to filter out multiple wavelengths from the input optical signal (Jin et al., 2018). PZT consists of lead which is not desired for commercial implementation due to its negative environmental effects.

Alternatively, AlN piezoelectric actuators have also been integrated with SiN waveguides to tune integrated ring resonators (Dong et al., 2018). This device cannot achieve broadband switching either as it only filters out certain wavelengths from the input optical signal. Recently, another low power electrostatically actuated MEMS-based SiN phase shifter has also been reported (McNulty et al., 2022). This device provides pi phase shift in the input optical signal at only 7 V but does not provide broadband switching in different physical outputs. Only

one MEMS-based SiN optical switch has been demonstrated so far that switches optical signal between multiple physical waveguides with no DC power consumption using electrostatic actuation (Briere et al., 2017). This device has only been able to demonstrate optical switching one wavelength of 1550 nm and is unable to close the air gap between suspended and fixed

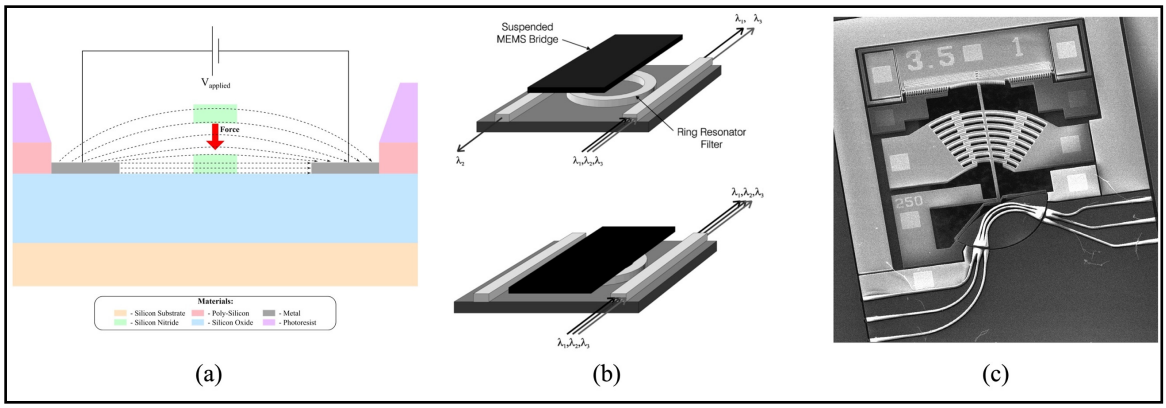

Figure 4.3 Design illustration for electrostatically actuated MEMS-based (a) SiN phase shifter
Taken from McNulty et al. (2022)
(b) SiN tunable ring resonator
Taken from Nielson et al. (2005)
(c) SEM image of fabricated MEMS-based crossbar switch with integrated SiN waveguides
Taken from Briere et al. (2017)

waveguide structures required for efficient optical switching. Design illustrations and SEM image of some of the devices where MEMS has been integrated with SiN photonics is shown in Figure 4.3.

There is a need for MEMS-based optical switching solution that consumes low power and provides wide operational wavelength range with broadband switching. The device also needs to address key issues related to MEMS integration with SiN waveguides such as residual stress, optical loss due to design challenges and misalignment between suspended waveguides. These factors are discussed further in this chapter along with the microfabrication process followed during this Ph.D. to fabricate these MEMS integrated SiN optical switches.

4.4 MEMS Integration with Silicon Nitride Photonics Process by AEPONYX

MEMS prototype device fabrication was done using the commercially available PiezoMUMPs process presented already in chapter 1. Integration of the MEMS actuator designs with SiN waveguides to obtain optical switches with wide operational wavelength range was done through a proprietary fabrication process developed by AEPONYX inc. in a commercial foundry (Sharma et al., 2017). This fabrication process uses a cavity-SOI (C-SOI) wafers with predefined cavities underneath the Si device layer. MEMS structure release at the end of the process becomes easier due to the predefined cavities. The process starts with deposition of a 3.2 μm thick SiO_2 layer using Tetra EthOxy Silane (TEOS) low pressure chemical vapor deposition (LPCVD) method. This SiO_2 layer acts as the bottom cladding for the SiN waveguide structures. Following deposition of the bottom cladding layer, SiN waveguide core layer with 435 nm thickness is deposited using LPCVD method. The waveguide core is patterned through photolithography using a stepper tool. Dry etching of SiN waveguide core is performed to obtain waveguide core structures. This waveguide core layer is then covered with a SiO_2 layer of 3.2 μm thickness using TEOS plasma enhanced chemical vapor deposition (PECVD) method. This layer of SiO_2 acts as the top cladding required to confine optical signal withing the SiN waveguide core.

We can refer to this combination of bottom cladding, waveguide core, and top cladding layers as the optical stack of the final MEMS integrated SiN photonics device. The optical stack is then patterned using photolithography to obtain the cladded waveguide patterns over the entire device as per the mask layout used. The openings in the etched optical stack expose the Si device layer underneath where a 1 µm thick aluminum cooper (AlCu) alloy is coated through sputtering and patterned through photolithography. This AlCu layer is used to form metal bonding pads that can be used to actuate the MEMS structure. The MEMS structure is obtained through photolithography and deep reactive ion etching (DRIE) of the Si device layer using a chromium hard mask. MEMS structures are released during the DRIE step as they are fabricated over cavities in a C-SOI wafer. A cross sectional view of the MEMS structure with integrated SiN waveguides over suspended Si and fixed Si is shown in Figure 4.4.

4.5 Critical Factors in MEMS Integration with Silicon Nitride Photonics

There are several factors that can affect MEMS integration with SiN waveguides for optical switching. These factors that are briefly discussed in this section have been addressed in this

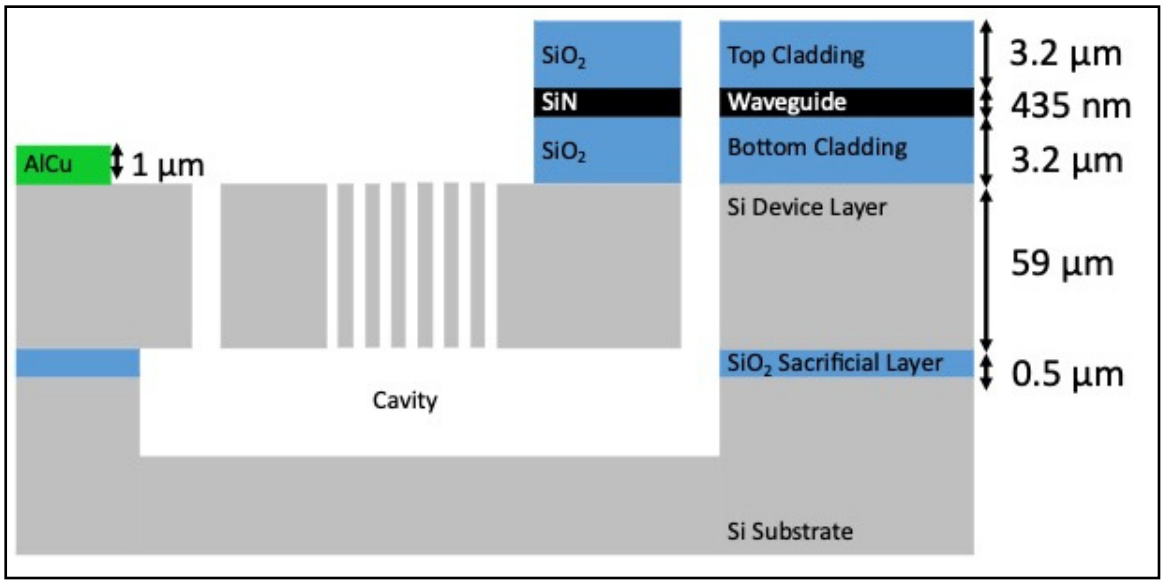

Figure 4.4 Design illustration with a cross-sectional view of the MEMS integrated with SiN waveguides over suspended and fixed Si structures as per the proprietary AEPONYX microfabrication process
Taken from Sharma et al. (2022)

Ph.D. research for successful implementation of multiple optical switches that integrate MEMS-based switching motion with SiN photonics.

4.5.1 Residual Stress

SiN and SiO_2 thin films have been known to produce residual stress when fabricated over suspended microstructures (Sharma et al., 2022). In the MEMS integrated optical system shown in the previous section of this chapter, we saw that the optical stack consisting of SiO_2 and SiN thin film layers can be fabricated over suspended Si MEMS structures. Such integration can lead to stress related deformation. Since, fabrication of the optical stack over suspended structures is required to form an optical switch that can switch optical signal between multiple waveguides, it is critical to mitigate this limitation that can lead to misalignment between suspended and fixed optical waveguides. Use of a thick Si device layer in a C-SOI wafer can help minimize such misalignment due to residual stress as shown in Figure 4.5. This has been discussed in detail in chapter 6 and chapter 8 of this thesis.

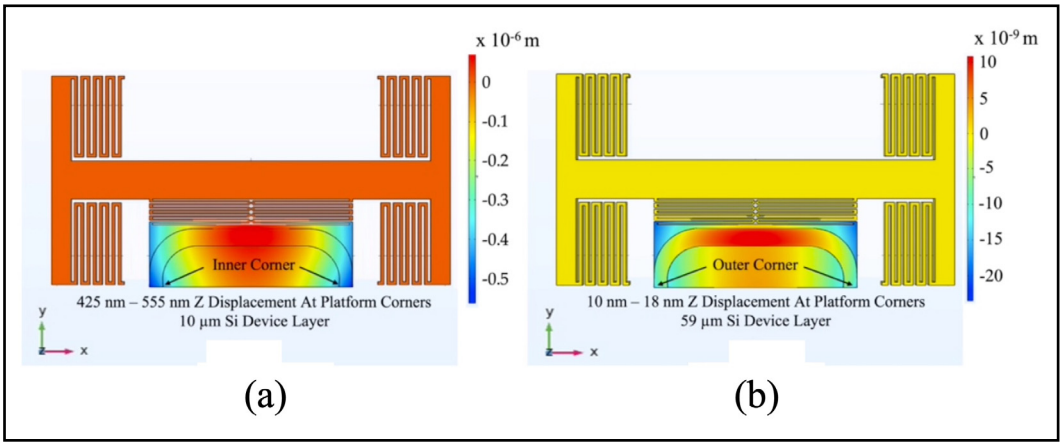

Figure 4.5 Simulation based deformation heat map due to residual stress of the SiO2-SiN-SiO2 optical stack upon MEMS integration with Si device layer thickness of (a) 10 µm, and (b) 59 µm
Taken from Sharma et al. (2022)

4.5.2 Air Gap

MEMS integration of SiN waveguides for optical switching requires suspended and fixed SiN waveguide structures along with the release of the MEMS structure in the Si device layer as shown in the previous section. This release of the MEMS structure leads to an intrinsic air gap between suspended and fixed waveguides that can lead to high optical losses (Briere et al., 2017). It is important to design a bi-axial MEMS actuator that can not only provide the necessary motion to switch between multiple waveguides, but also provides the motion to minimize the air gap between suspended and fixed waveguide structures for efficient optical switching. This issue affecting the optical switch device performance has been addressed in this thesis. Detailed discussion about the design approach used to mitigate this limitation is given in chapter 6 and chapter 8 of this thesis.

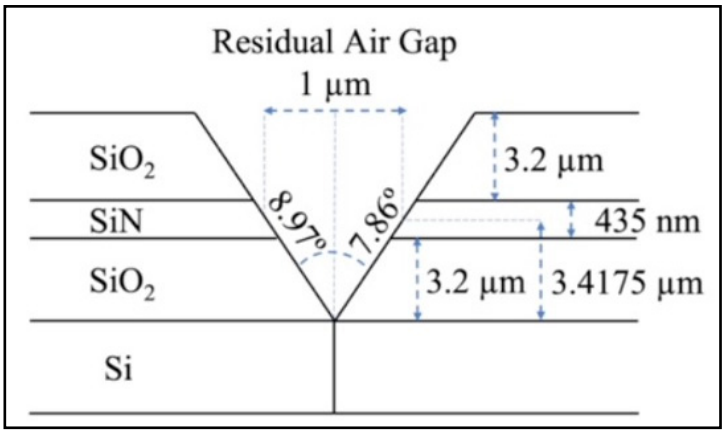

Figure 4.6 Residual air gap illustration for an optical stack with etch profile angles of 8.97º and 7.86º with zero gap between the Si layer underneath Taken from Sharma et al. (2022)

4.5.3 Etch Profile

Dry etching of all material layers such as SiN, SiO_2, and Si involved in any microfabrication process always include some etch profile angle for the fabricated device along the edge where etching is performed (Rangelow, 2001). When this factor is considered for the interface between the suspended and fixed SiN waveguides structures shown in Figure 4.4, the edge in the air gap region will always have a etch profile that can lead to a residual air gap between suspended and fixed waveguides even when the air gap between the Si layer underneath is closed completely through MEMS actuation (Sharma et al., 2022). A design illustration of this factor is shown in Figure 4.6. This residual air gap will always lead to some optical loss during the optical coupling between waveguides in a MEMS integrated SiN optical switch. Such losses can only be mitigated through process flow improvements to minimize the etch profile angle during dry etching of critical optical components. This factor is further discussed in detail in chapter 6 and chapter 8 of this thesis.

4.5.4 Optical Coupling Between Waveguides

Optical coupling between suspended and fixed waveguides is critical to transmission efficiency of any optical switch. While MEMS integration with SiN waveguides can lead to a residual air gap between waveguides in the previous sections, it is crucial to minimize the effect of such optical loss by waveguide design. Inverted tapers can be used to minimize such optical loss between butt-coupled waveguides as shown in the simulation results in Figure 4.7 from Sharma et al., 2019. There is a clear advantage in using waveguides with inverted tapers near the coupling region. Such tapering allows the possibility to have some residual air gap between two waveguide structures in case of MEMS integration discussed earlier in this section. The length of the inverted taper used and the width to which the waveguide is narrowed down near the interface of the suspended and fixed waveguides is important for efficient optical coupling. Dimensions of the inverted tapers used in this work along with the relevant simulation results are discussed in chapter 5 of this thesis.

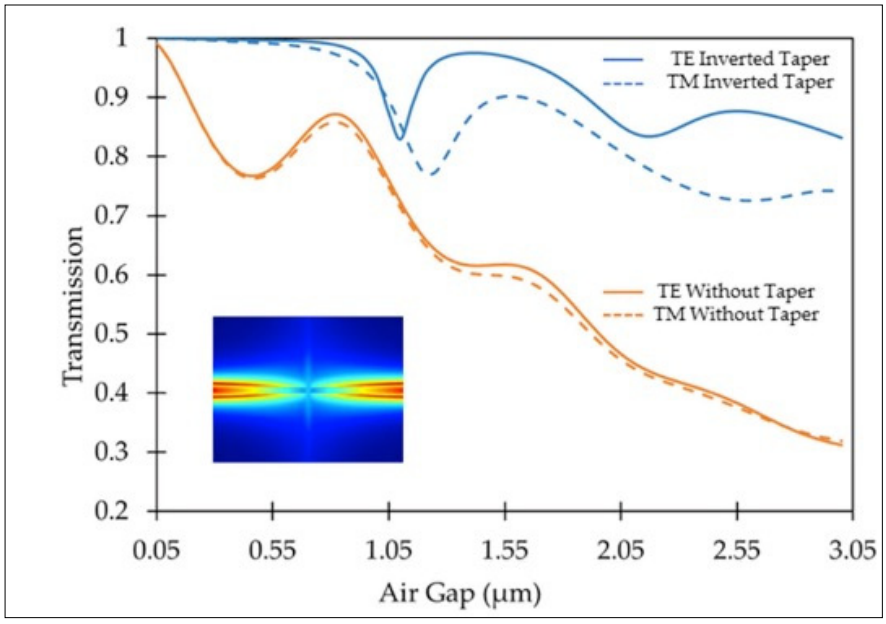

Figure 4.7 Design illustration with a cross-sectional view of the MEMS integrated with SiN waveguides over suspended and fixed Si structures as per the proprietary AEPONYX microfabrication process
Taken from Sharma et al. (2022)

4.6 Summary

In this chapter, advantages of SiN photonics over Si photonics were presented following which following which various existing SiN photonics switching solutions were discussed in section 4.1. State-of-art SiN photonics switches that use thermal tuning of optical components such as MZI were discussed along with the challenges associated with thermal tuning method for optical switching in section 4.2. Thermal tuning consumes large power and has limited broadband switching function. Existing MEMS integrated SiN photonics switches were discussed in section 4.3. We saw that most of the existing MEMS-based solutions provide energy efficient tuning of optical components such as ring resonators. Proprietary microfabrication technology by AEPONYX Inc. for integration of SiN waveguides with SOI-based MEMS structures was presented in section 4.4. Critical factors that can affect the performance of an optical switch fabricated using this technology was discussed in section 4.5. We can conclude through this literature review that there is a need for a MEMS-based SiN optical switch that consumes low power, has efficient optical switching and wide operational (i.e., broadband) wavelength range.

In chapter 5, a translational MEMS platform prototype device that can minimize the air gap between suspended and fixed Si layers is presented. This device was fabricated using commercially available PiezoMUMPs technology. In chapter 6, integration of this translational MEMS platform with SiN waveguides in a 1 x 3 optical switching configuration is discussed, along with impact of residual stress and fabrication variations upon device performance. The device tested was fabricated using MEMS and SiN waveguide integration process available through AEPONYX Inc. MEMS prototype device (fabricated using PiezoMUMPs technology) performance was enhanced through a new design approach that integrated electrostatic and piezoelectric actuators to achieve 3 degrees -of-freedom (DOF). This device is discussed in chapter 7. Finally, a 1 x 5 MEMS integrated SiN optical switch based upon the MEMS protype discussed in chapter 7, is presented in chapter 8, with analog and digital control over multiple channel waveguides.

CHAPTER 5

TRANSLATIONAL MEMS PLATFORM FOR PLANAR OPTICAL SWITCHING FABRICS

Suraj Sharma[1], Niharika Kohli[1], Jonathan Brière[2], Michaël Ménard[3], and Frederic Nabki[1]

[1]Department of Electrical Engineering, École de Technologie Supérieure, Montreal, Quebec H3C 1K3, Canada

[2]AEPONYX Inc., Montreal, Quebec H3C 4J9, Canada

[3]Department of Computer Science, Universite du Quebec a Montreal, 201 President-Kennedy Avenue, Montréal, Québec, Canada H2L 2C4

Paper published in *Micromachines*, June 2019

Preface

In this chapter, SOI-based translational MEMS platform that moves along two axes is presented. Critical MEMS and optical design considerations that are required to propose the use of this device as an integrated SiN optical switch are discussed in detail in this chapter. Actuator and silicon spring design challenges that are key to achieve uniform motion of the MEMS device devoid of any rotational behaviour are presented here. The SOI-based MEMS device proposed in this chapter can be potentially integrated with SiN waveguides where the unique bi-axial motion of the central platform in the MEMS structure can enable a 1 x 3 or 2 x 2 optical switch configurations. Characterization results for MEMS prototype device fabricated using Piezo MUMPs process are included in this chapter. The chapter concludes with proposed integration of the MEMS platform with SiN waveguides for optical switching which forms the basis for the following chapter.

S.S. designed, simulated, and characterized the MEMS devices. N.K. performed optical simulations required in this chapter. J.B. provided MEMS design expertise. M.M. and F.N. supervised the work presented in this chapter.

5.1 Abstract

While 3-D microelectromechanical systems (MEMS) allow switching between a large number of ports in optical telecommunication networks, the development of such systems often suffers from design, fabrication and packaging constraints due to the complex structures, the wafer bonding processes involved, and the tight alignment tolerances between different components. In this work, we present a 2-D translational MEMS platform capable of highly efficient planar optical switching through integration with silicon nitride (SiN) based optical waveguides. The discrete lateral displacement provided by simple parallel plate actuators on opposite sides of the central platform enables switching between different input and output waveguides. The proposed structure can displace the central platform by 3.37 μm in two directions at an actuation voltage of 65 V. Additionally, the parallel plate actuator designed for closing completely the 4.26 μm air gap between the fixed and moving waveguides operates at just 50 V. Eigenmode expansion analysis shows over 99% butt-coupling efficiency the between the SiN waveguides when the gap is closed. Also, 2.5 finite-difference time-domain analysis demonstrates zero cross talk between two parallel SiN waveguides across the length of the platform for a 3.5 μm separation between adjacent waveguides enabling multiple waveguide configuration onto the platform. Different MEMS designs were simulated using static structural analysis in ANSYS. These designs were fabricated with a custom process by AEPONYX Inc. (Montreal, QC, Canada) and through the PiezoMUMPs process of MEMSCAP (Durham, NC, USA).

Keywords: microelectromechanical systems (MEMS); electrostatic actuator; parallel plate actuation; optical switch; silicon-on-insulator (SOI); micro-platform; optical waveguide; silicon nitride photonics; integrated optics

5.2 Introduction

Over the years, micro devices with optical and microelectromechanical systems (MEMS) components known as micro-opto-electro-mechanical systems (MOEMS) have been developed for use in digital micro mirror display (Monk & Gale, 1995) and laser scanners (Holmström et al., 2014). Development of such optical MEMS devices subsided due to immaturity of the technology and market penetration challenges (Kaajakaari, 2009). However, with the world moving towards higher bandwidth optical fiber-based communication, MOEMS can help meet the ever-growing demand for power and transmission efficient integrated silicon photonics solutions. Conventional electronic data centers are often associated with high cost, and high energy and space consumption (Hammadi et al., 2014). These technological, environmental and monetary constraints have paved the way for MEMS integration towards the development of hybrid optical data center designs such as Helios (Farrington et al., 2010) and novel Scaled Out Optically Switched Network Architecture (Ménard et al., 2015). MEMS integration into data centers can reduce power consumption from 12.5 Watts per port for electronic switches to just 0.24 Watts per port for optical switches but with a re-configurability that is restricted to a few milliseconds (Hammadi & Mhamdi, 2014). Such data centers often rely upon 3-D MEMS with out-of-plane rotating micro-mirrors for beam steering inside an optical cross connect switch (Kim et al., 2003) using piezoelectric actuation (Truex et al., 2003) or electrostatic actuation (Fernandez, 2004; Aksyuk et al., 2003). Although 3-D MEMS allow the implementation of optical switches with a large number of ports, the development of such systems often suffers from fabrication and packaging constraints due to the complex structures and wafer bonding processes involved (Li et al., 2011; Liu et al., 2013). Thus, paving the way for simpler more affordable 2-D MEMS based integrated photonics solutions for switching applications.

Piezoelectric (Koh et al., 2010), electrothermal (Kwan A.M.H et al., 2012) and electrostatic (Member & Lohmann, 2003) actuators provide precise mechanical motion at the micron scale. Piezoelectric actuators, although fast and suitable for applications with resonators, involve the

use of complex piezoelectric materials such as AlN and PZT for actuation (Puder et al., 2015; Cassella et al., 2017). These materials can be integrated with silicon-on-insulator (SOI) technology to make optical switches (Kim et al., 2008) but the use of lead in PZT raises environmental concerns (Panda & Sahoo, 2015). Alternative piezo materials, such as AlN, are difficult to reproduce with the same piezo properties because of their dependency on the film texture and dipole orientation, and that they can have large residual stress with even a slight change in the deposition parameters (Tonisch et al., 2006; Iborra et al., 2004). Electrothermal actuators produce large displacements at low actuation voltages but are slow, consume high power and produce heat during actuation (Liu et al., 2012; Peters & Tichem, 2016). This makes them undesirable for the green optical data centers envisioned for the future. Thus, low voltage electrostatic actuators based upon widely used comb drives and parallel plate designs become the right choice for planar optical switching applications (Li et al., 2003; Sabry et al., 2015). These can also be fabricated with ease through commercial SOI microfabrication processes to validate MEMS designs before integration with optical waveguides (Brière et al., 2015; Cowen et al., 2014).

Electrostatic actuators connected to a central platform have been demonstrated in the past for 2-D and 3-D MEMS based solutions such as optical scanners and cold atom detectors (Chu & Hane, 2011; Srinivasan et al., 2010. These designs have largely relied upon out-of-plane rotational motion of the central platform due to torsional beams (Lee et al., 2004; Zhao et al., 2017; Hung et al., 2015). A few translational MEMS structures exist, but they are largely designed for out-of-plane optics applications (Zhang et al., 2018; Dziuban et al., 2010; Xue et al., 2015). The MEMS for planar switching applications reported in the literature rely upon bringing movable waveguides closer to fixed waveguides in ON/OFF state (Bulgan et al., 2008; Abe & Hane, 2013) or as a 1 × 3 optical switch (Munemasa & Hane, 2013). Through complex MEMS integration of soft polymer waveguides, a 2 × 2 optical switch has also been demonstrated (Liu & Chollet, 2009). Recent developments include planar switching done by adiabatic coupling between waveguides through vertical actuation at very low voltage (Han et

al., 2015; Seok et al., 2016), and butt coupling through in-plane rotational actuation (Brière et al., 2017).

Accordingly, in this work, we present a translational MEMS platform capable of motion along two axes using multiple electrostatic actuators. A detailed overview of a translational MEMS platform compatible with different planar optical switching configurations is presented in section 5.3 along with optical design considerations. Results of EigenMode Expansion (EME) and Finite Difference Time Domain (FDTD) simulations for the butt coupling of SiN waveguides and the cross-talk between parallel SiN waveguides are also presented in this section. Alignment tolerance simulations show the potential for efficient optical switching with the proposed MEMS platform. The evolution of the actuator and spring designs along with the critical design choices made for a simple switching approach are also discussed. Design of the translational MEMS platform and the critical design parameters and dimensions are presented in section 5.4. The fabrication process used, and the analysis of the fabricated devices are discussed in section 5.5. In this section, the test setup used for the actuation experiments and the results obtained are also reported. A discussion of these results is presented in section 5.6 and is followed by the envisioned future work and concluding remarks in section 5.7.

5.3 Design Considerations

5.3.1 Translational MEMS Platform for Optical Switching

Previous devices developed by our research group relied upon a rotational MEMS platform for planar optical switching using SiN waveguides surrounded by a SiO2 cladding (Brière et al., 2017). The device uses 5º of its total 9.5º of rotation on each side to form a crossbar switch requiring 113 V to actuate and having a 1.3 mm by 1 mm footprint. Also, the air gap closing actuator designed operates at 118 V with a minimal gap of 250 nm upon actuation.

In this work, a unique translational MEMS platform capable of bi-axial motion is proposed and demonstrated. The lateral motion of the platform is bi-directional and can provide optical switching in 1 × 3 or 2 × 2 crossbar switch configurations. The longitudinal motion of the central platform is unidirectional and designed to completely close the air gap between waveguides on the substrate and the platform to achieve highly efficient butt-coupling. The design operates at a reduced actuation voltage for both switching and gap closing motions compared to that reported in (Brière et al., 2017), and the device footprint is smaller. Figure 5.1 shows illustrations for the translational MEMS platform as a 1 × 3 optical switch Figure 5.1(a) and as a 2 × 2 crossbar optical switch Figure 5.1(b). These structures are meant to include integrated SiN waveguides which are not the focus on this work but that have been

demonstrated in (Brière et al., 2017; Ménard et al., 2017). A cross sectional representation of the entire optical MEMS stack envisioned is also shown in Figure 5.1(c).

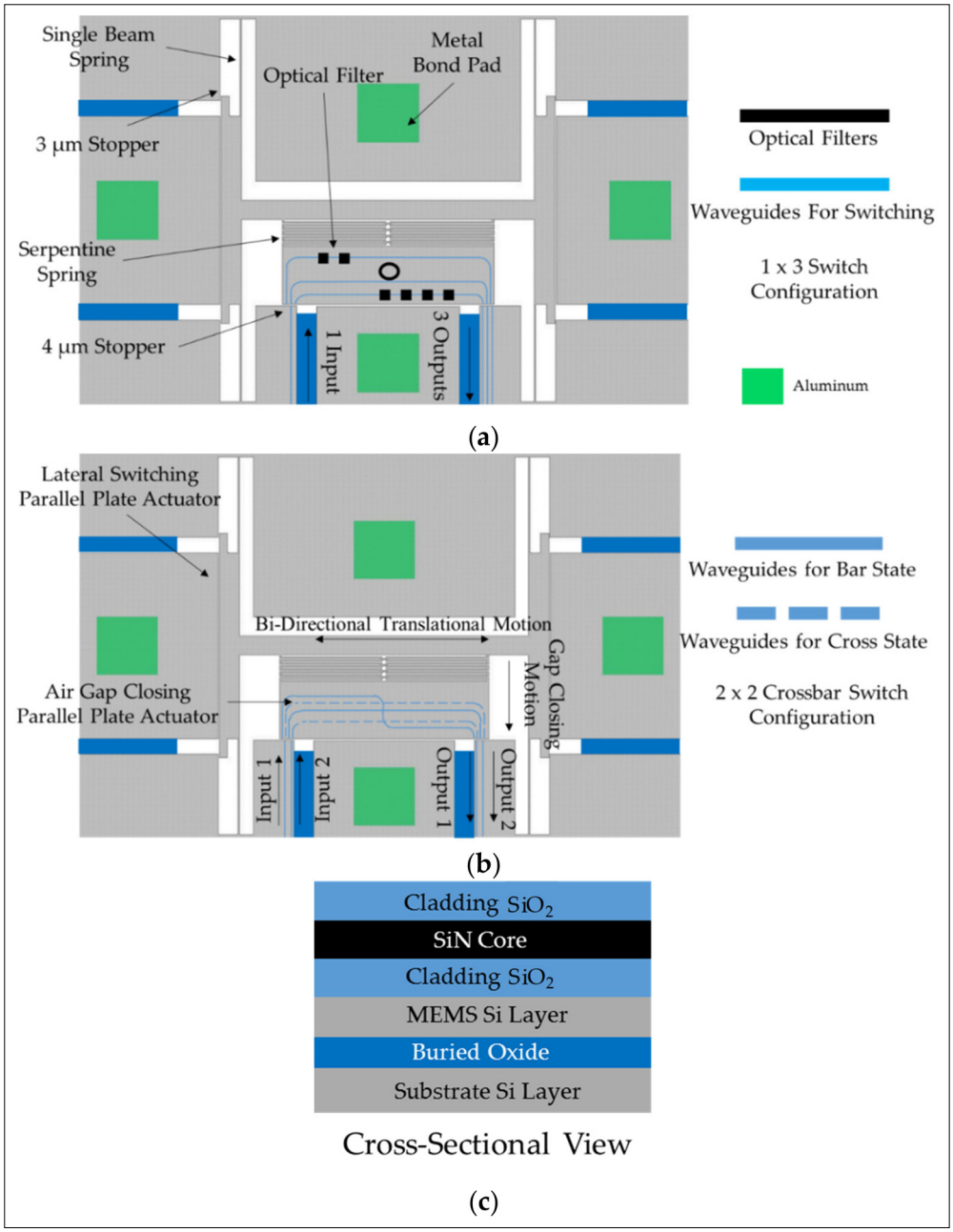

Figure 5.1 Illustrations of the proposed translational actuator: (a) 1 x 3 switch configuration with integrated optical filters, (b) 2 x 2 crossbar switch configuration, (c) cross sectional view of the optical MEMS stack proposed. The color scheme to represent the different materials is consistent throughout the figure

In the 1 × 3 optical switch configuration, the central platform accommodates three separate SiN waveguides. The input side on the left of the platform has one waveguide on the fixed substrate. The output side on the right of the platform is designed to have three separate waveguides. Four symmetrical single silicon beam springs support the entire MEMS structure. These beams provide the necessary spring action to allow lateral displacement through parallel plate actuators on the opposite side of the platform. The central platform is connected to the lateral actuators through a central beam and a serpentine spring structure. This design choice decouples the lateral and longitudinal motion of the platform. The serpentine spring enables longitudinal displacement through a parallel plate actuator at the bottom of the platform. Whereas the parallel plate actuators on the opposite sides of the platform are designed to provide discrete lateral displacement of 3 μm on each side, the bottom parallel plate actuator is designed to close the 4 μm air gap between the platform and the substrate. The discrete lateral displacement of 3 μm on either side along with the neutral position of zero lateral displacement provides 3 switching possibilities to form a 1 × 3 switch. The platform is large enough to integrate optical filters, such as Bragg gratings and ring resonators (Tabti et al., 2017; Gondarenko et al., 2009), and it can be used to select among a bank of filters to implement discretely tunable devices. Examples of optical filters are also illustrated in Figure 5.1(a).

Figure 5.1(b) shows the MEMS platform envisioned as a 2 × 2 crossbar switch. There are two input and output waveguides on the substrate. The actuation mechanism and operational parameters remain the same as the 1 × 3 switch configuration, but the platform accommodates four SiN waveguides. When the platform is actuated to the right, the waveguides on the platform shown as solid lines in Figure 5.1(b) are aligned with the input and output waveguides. In this position light travels from input 1 to output 1 and from input 2 to output 2, creating the ‘bar’ configuration. When the platform is actuated to the left, waveguides on the platform shown as dotted lines in Figure 5.1(b) are aligned to the input and output waveguides. The optical signal then propagates from input 1 to output 2 and from input 2 to output 1, creating the ‘cross’ configuration. In both configurations, the gap closing mechanism provides

highly efficient butt-coupling between the waveguides. The discrete motion of the platform also eliminates optical losses due to displacement / voltage fluctuations in the system, as the MEMS platform is designed to operate in the pull-in state for both the lateral and longitudinal actuators.

5.3.2 Optical Design Considerations

Our work involves the validation of the MEMS (Cowen et al., 2014) structures, prior to employing the commercial process enabling the addition of optical waveguides which has been developed by our group in collaboration with AEPONYX. The commercial process used to validate the MEMS requires a minimal gap of ~3 μm. This constraint leads to a significant air gap between the fixed and moving waveguides envisioned in a planar optical MEMS device. In the previous rotational MEMS developed by our group, the input and output waveguides were located on top of the gap closing actuator due to design constraints (Brière et al., 2017). This enables the air gap to be reduced to only 250 nm as the rotational platform that is grounded cannot come in contact with the gap closing actuator that is kept at a high DC voltage. If the two come in contact, shorting during actuation would damage the MEMS device. This phenomenon can be prevented by dimpled structures but leads to a residual air gap even after gap closing. However, on the translational MEMS platform shown in Figure 5.1, the input and output waveguides are separated from the gap closing actuator. The air gap between the platform and the fixed section of the switch (with input / output waveguides) is designed to be 4 μm whereas the gap for the bottom parallel plate actuator is designed to be 6 μm. As a result, the platform and the fixed section of the switch can both be grounded to eliminate shorting during gap closing actuation. This provides complete gap closing between waveguides eliminating any significant residual air gap.

EME analysis using MODE Solutions from Lumerical (Vancouver, Canada) study the effect of an air gap on optical signal transmission between two butt-coupled SiN channel waveguides with a core of 435 nm × 435 nm and with a top and bottom SiO2 cladding thickness of 3.4 μm

for both the TE and TM modes. All of the optical simulations shown in this section were performed at a wavelength of 1550 nm. EME results show a transmission efficiency of over 99% for direct butt-coupling between these waveguides with an air gap of 50 nm or less, which is reduced to 33% when the gap is 3 µm. To reduce the expansion of the light beams in the gap and increase the coupling between the two waveguides, we introduced inverted tapers where the core width narrows down to 250 nm at both waveguide edges. The optimal length of the tapers was found to be 20 µm. The transmission efficiency is almost 100% with a 50 nm air gap and even on increasing the gap to 3 µm, the coupling efficiency dropped to 83% for the transverse electric (TE) mode and 74% for transverse magnetic (TM) mode in waveguides with inverted tapers. This result is shown in Figure 5.2(a) and demonstrates that a high coupling efficiency can be obtained even if fabrication imperfections limit the minimum size of the gap. Furthermore, the ability to reduce the gap to dimensions significantly smaller than the wavelength of light (which is typically around 1.3 µm or 1.5 µm in telecommunication applications) remove the need for an antireflection coating at the interface of the waveguides. When the gap size is larger than approximately half a wavelength, multiple beam interference

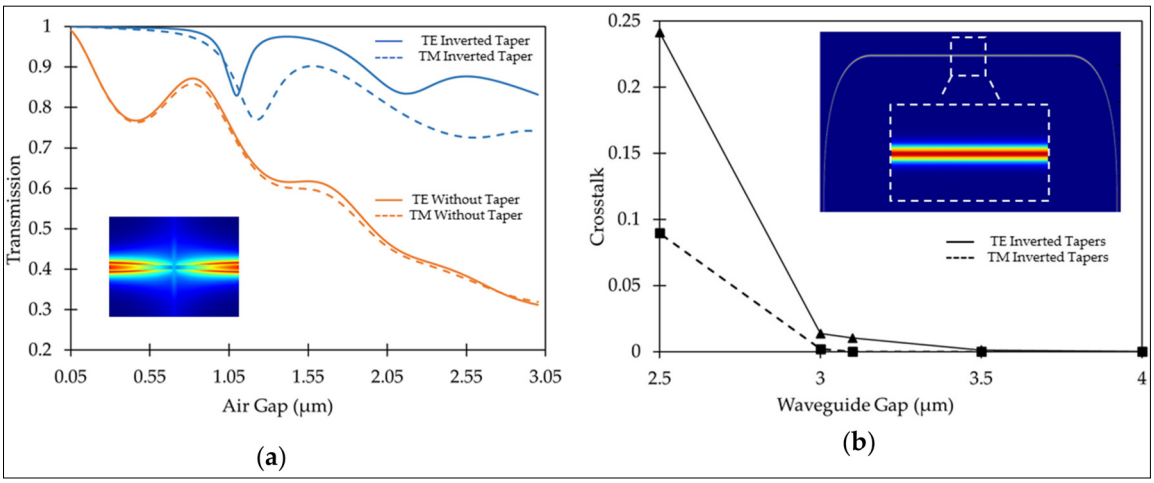

Figure 5.2 Optical simulation results for: (a) EME analysis showing transmission efficiency for TE and TM modes between two butt-coupled SiN waveguides as a function of air gap with and without inverted tapers. The inset shows the top-view of the magnitude of the electric field of TE mode for butt-coupling with inverted tapers at a gap of 500 nm, (b) 2.5D FDTD analysis showing cross-talk for TE and TM modes as a function of the gap between two SiN waveguides with 90º bends and 75 µm bending radius. Inset shows top-view of the magnitude of electric field of TE mode for the complete optical path with two parallel SiN waveguides at a gap of 3.1 µm. Image shows that the field remains completely confined in the input waveguide

phenomena can occur because of reflections at the waveguide interfaces, which explains the undulations that are visible in Figure 5.2(a).

The dimensions of the central platform in an optical MEMS device as shown in Figure 5.1 are highly critical. The platform must accommodate at least three waveguides to operate as a 1 × 3 switch and four waveguides to operate as a 2 × 2 crossbar switch. Another important design consideration is the width of the gap closing interface between the platform and the substrate. The platform must be able to accommodate the number of waveguides envisioned with minimal optical cross-talk and optimal bending radius for low propagation losses (Jones et al., 2013). Therefore, to have an estimate of the number of waveguides that can be implemented on the platform, we studied the cross-talk between two parallel SiN waveguides as function of the gap between them. 2.5D FDTD analysis were performed for 435 nm × 435 nm waveguides with a 3.4 μm thick top and bottom SiO2 cladding where the total length of the inner waveguide is 565.5 μm with a bending radius of 75 μm. It was found that for the TE mode the field remains confined in the input waveguide and does not couple to the adjacent outer waveguide when the gap between them is 3.5 μm or greater. The simulated propagation loss in the input waveguide of length 565.5 μm is only 0.01 dB for a 3.5 μm gap between adjacent waveguides. Results of the 2.5D FDTD cross-talk simulations are shown in Figure 5.2(b). It can also be observed that the cross-talk for the TM mode is smaller than the TE mode and becomes negligible at a gap of 3.0 μm.

The optical simulation results show that a rectangular platform of 150 μm by 520 μm is large enough to accommodate four separate SiN waveguides with a 75 μm bending radius. Also, the gap closing interface between the platform and the fixed section of the switch is 35 μm wide and can easily accommodate three separate 435 nm wide SiN waveguides with a 3.5 μm gap between them. These can be fabricated with inverted tapers having tip-width of 250 nm and 20 μm length in the coupling region at the edges for minimal optical loss. The transverse horizontal and vertical alignment tolerance between the butt-coupled waveguides with and without tapers were also analyzed as shown in Figure 5.3. The inverted tapered structures have a high alignment tolerance providing a transmission of more than 80% in case of the TE mode

and of more than 70% in case of the TM mode even when one waveguide is displaced by 700 nm relative to the other. These transmission coefficients were obtained with an air-gap of 250

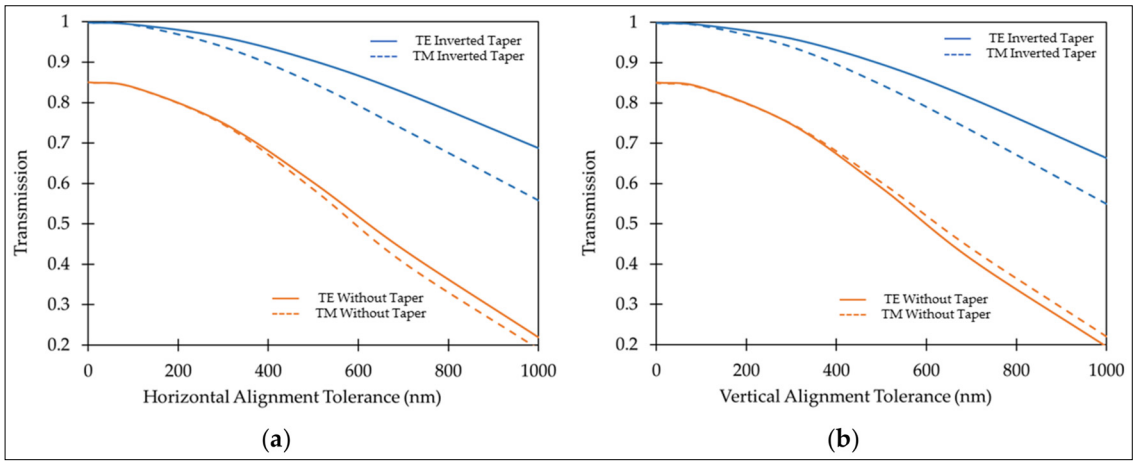

Figure 5.3 Optical simulation results for EME simulations showing the transmission efficiency of TE and TM modes between two butt-coupled SiN waveguides with and without inverted tapers as a function of: (a) horizontal, (b) vertical alignment tolerance

nm between the waveguides. Therefore, the proposed switch has high fabrication tolerances in comparison to typical silicon photonic devices implemented with SOI wafers that have a 220 nm thick device layer.

5.3.3 MEMS Design Considerations

The initial MEMS actuator choice for the translational platform was to use of a unidirectional comb drive for lateral switching whereas the gap closing actuator was the same parallel plate actuator discussed above. This first MEMS design incorporated serpentine spring structures for both lateral and longitudinal motions. Since comb drives enable large controlled displacements, the MEMS was designed in ANSYS using static structural analysis to provide up to 6 µm of displacement at ~220 V. This design was fabricated by AEPONYX with an in-house microfabrication process for MEMS based on SOI technology. However, the fabricated devices showed rotational effects in the comb drive after a displacement of 2.39 µm at 100 V

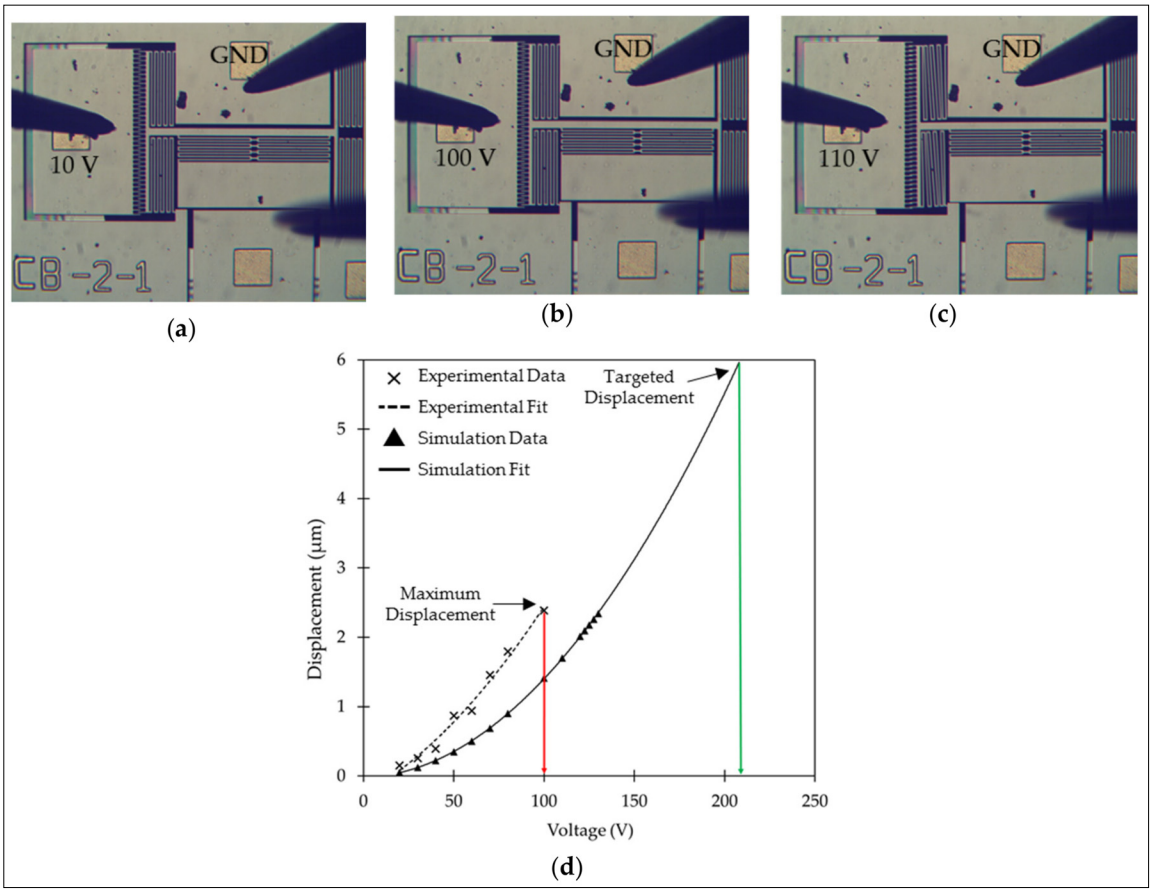

Figure 5.4 Microscopic micrographs of the translational MEMS platform with comb drive during actuation: (a) at 10 V; (b) maximum displacement at 100 V; (c) rotation at 110 V; (d) experimental and simulation based lateral switching displacement v/s actuation voltage curves for the translational MEMS design with comb drive

during testing. Figure 5.4 shows micrographs of a device during actuation tests along with the actuation curves for simulation and experimental results. The experimental measurements appear to follow a linear relationship in comparison to the simulation results because the displacements recorded during the experiment are limited to the beginning of the polynomial actuation curve where the slope is increasing slowly. Before we could observe the non-linear behaviour of the actuator, the comb drive-based actuator rotated inhibiting further actuation. SEM analysis of the MEMS device showed some fabrication discrepancies. Fabricated dimensions varied from 2.35 µm to 2.58 µm in the comb drive compared to the design

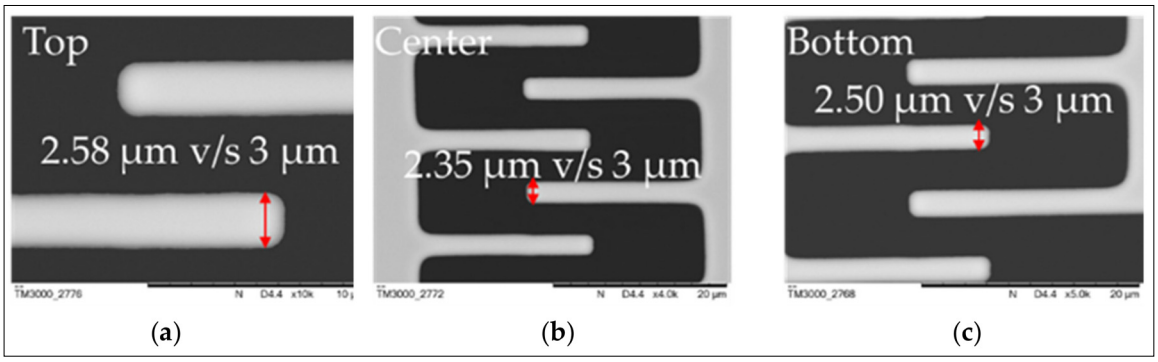

Figure 5.5 Fabricated v/s design dimensions through SEM micrograph analysis of the drive fingers for comb drive-based translational MEMS platform in various parts of the actuator: (a) top; (b) center; (c) bottom

dimensions of 3 µm. This varies the gap between the drive fingers in different regions of the comb. These observations are shown in Figure 5.5.

The vertical in-plane stiffness of the main horizontal beam was further analyzed following the actuation results obtained. A static structural analysis of the structure was performed using ANSYS. A load force of 10 µN was simulated on the top left corner of the device model to verify the vertical stiffness of the main horizontal beam. These simulation results are shown in Figure 5.6(a). The MEMS design has a low vertical stiffness as the 10 µN force applied led to a total maximum deformation of 322 nm. The fabrication discrepancies described earlier are assumed to make the electrostatic field generated by the fabricated comb drive slightly asymmetrical compared to the simulated model with an ideal comb drive. This is due to the varying gap between the fabricated fingers in different regions of the actuator. These fabrication geometry discrepancies combined with the low vertical stiffness of the system make the structure highly susceptible to the rotational effect observed. Designs for the lateral switching actuator and serpentine spring were modified to the final iteration shown in Figure 5.6(b). Parallel plate actuators were chosen for lateral switching to simplify fabrication. The vertical stiffness was increased through a single beam spring for lateral actuation that is anchored on two ends unlike the previous serpentine spring design. A static structural simulation for a 10 µN force on the top left corner of the new design yielded only 1.18 nm of

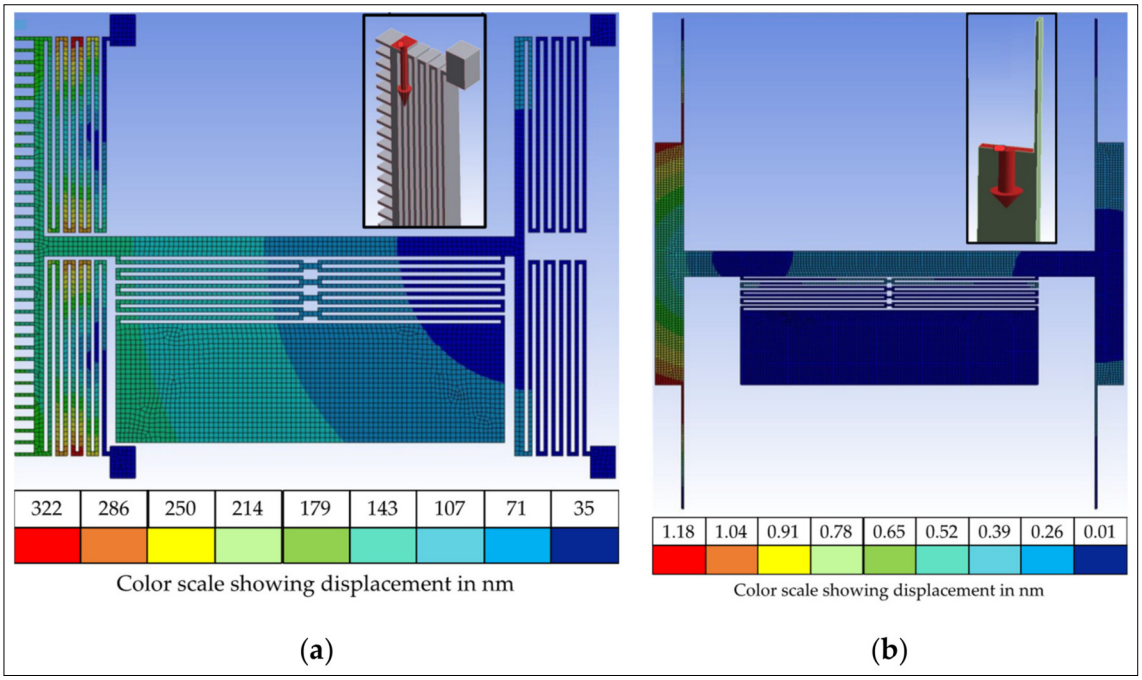

Figure 5.6 Total deformation heatmap when 10 μN of force is applied on the top left corner of the structure (force location shown in image insets): (a) comb drive and serpentine spring design, (b)parallel plate and single beam spring design

total maximum deformation, more than 300× reduction over the prior design shown in Figure 5.6(a).

The completely parallel plate actuation-based design with a single beam spring was successful in eliminating any rotation due to the fabrication discrepancies caused by the complex comb drive structure, and to increase the vertical in-plane spring constant. In order to achieve the same targeted 6 μm of displacement as the comb drive, two lateral parallel plate actuators were designed on opposite sides of the platform.

5.4 Final Translational MEMS Platform

The final iteration of the translational MEMS platform was designed on the basis of the optical design considerations and comb drive-based MEMS results discussed in the previous sections. Two parallel plate actuators were implemented on the opposite sides of the central rectangular

platform for lateral displacement. Another parallel plate actuator was created on the bottom of the actuator for air gap closing. All actuators were designed as parallel-plate and operated under the pull-in effect [3]. In case of a parallel plate actuator with initial gap (d) and total overlap area (A) between the plates, the actuation voltage (Vp) where the pull-in effect occurs is given by:

$$V_p = \sqrt{\frac{8kd^3}{27\varepsilon A}} = \sqrt{\frac{4V_c}{27}} \tag{5.1}$$

where k is the spring constant of the system in the direction of actuation and ε is permittivity of the dielectric medium. Also, the maximum controlled displacement (Xp) for these actuators before pull-in is given by:

$$X_p = \frac{d}{3} \tag{5.2}$$

These lateral actuators were designed with an initial gap (d) of 4 μm making the maximum displacement (Xp) before pull-in to be 1.3 μm. Similarly, for the longitudinal actuator with an initial gap (d) of 6 μm, the maximum displacement (Xp) before pull-in is 2 μm. Since the pull-in effect enables a quick and large displacement, the two parallel plates in the actuator tend to snap together. In order to prevent shorting during pull-in, 10 μm long stoppers at a 3 μm gap (less than the actuator initial gap of 4 μm) were added at the two ends of both the lateral actuators. These stoppers also provide the necessary 3 μm of maximum displacement to translate the waveguides on the platform and form a 2 × 2 crossbar optical switch as discussed earlier. Similar 35 μm wide stoppers forming a 4 μm gap (less than the actuator initial gap of 6 μm) were built for the longitudinal actuator. These stoppers are larger than the lateral stoppers in order to accommodate multiple SiN waveguides. Images of the fabricated MEMS device along with the critical stopper and actuator dimensions are shown in Figure 5.7.

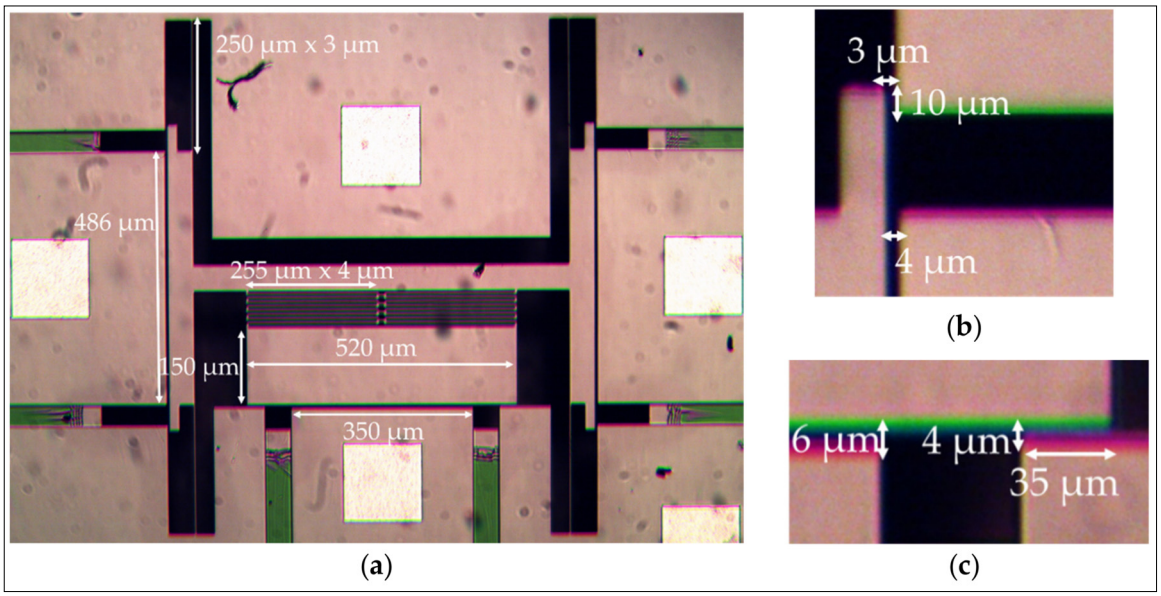

Figure 5.7 Micrographs of the final translational MEMS platform with critical design dimensions for: (a) platform, springs and actuators, (b)lateral switching actuator and stopper, (c) longitudinal gap closing actuator and stopper

A static structural analysis for the device model in ANSYS was performed to estimate the lateral and longitudinal spring constants of the MEMS. The spring constant of the lateral actuators' springs was found to be 15.37 N/m, whereas the spring constant of the platform's serpentine spring is 1.81 N/m. The lower stiffness of the serpentine spring reduces the downward electrostatic force needed to close the gap. This helps limit the impact of gap closing actuation upon the lateral actuators and prevent any rotation of the platform. Since the stiffness of the serpentine spring is considerably lower, the gap closing actuator dimensions are different from the lateral actuators. The initial gap and length of the gap closing actuator was kept at 6 µm and 350 µm, respectively, whereas the initial gap and length of the lateral actuator was kept at 4 µm and 486 µm, respectively. These choices were made to enable the operation of all the actuators within a small voltage range. Theoretical calculations using the spring constant simulation results presented in this section predict a pull-in voltage of ~82 V and ~61 V for lateral switching and longitudinal gap closing, respectively. Modal analysis was also performed with the device model in ANSYS to obtain the resonance frequencies of the structure. The resonance frequency of the gap closing actuator was found to be 4.6 kHz

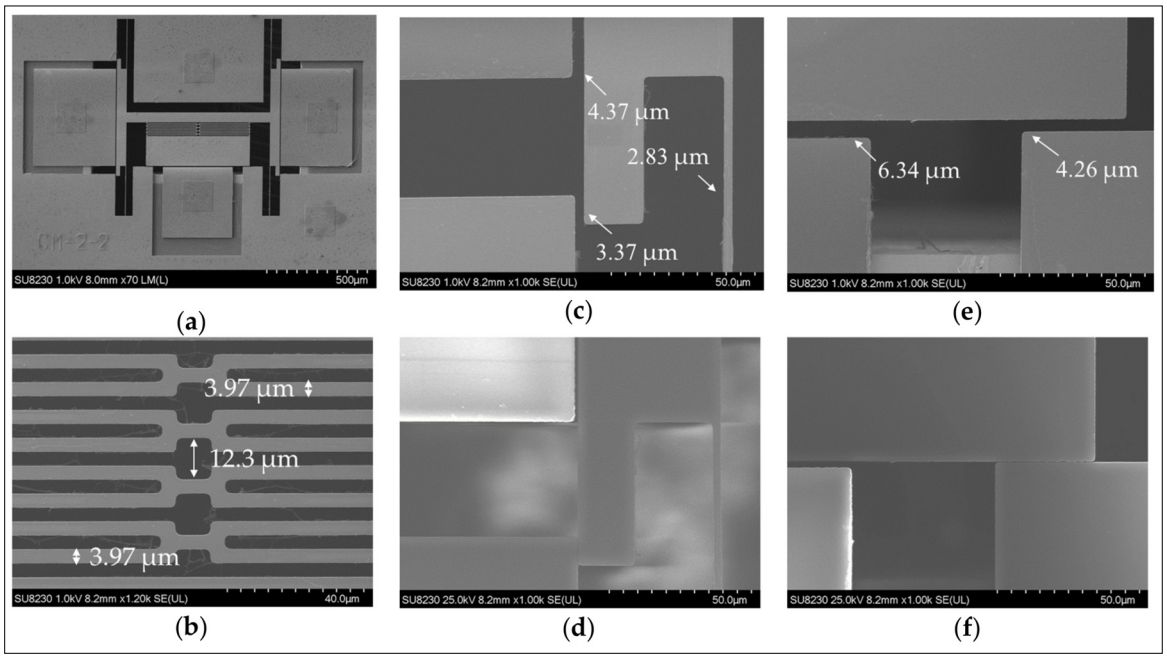

Figure 5.8 Detailed SEM micrographs with measurements of the fabricated translational MEMS platform: (a) final translational MEMS platform; (b) serpentine spring; (c) lateral actuator and spring's fabricated dimensions; (d) lateral actuation during high power imaging; (e) gap closing actuator's fabricated dimensions; (f) gap closing during high power imaging

whereas that of the switching actuator structure was 9.2 kHz. This limits the operational frequency for the switch at ~4.6 kHz. The MEMS cell as demonstrated can be used in both a 2 × 2 crossbar switch configuration as well as a 1 × 3 switch configuration.

5.5 Experimental Results

5.5.1 Microfabrication Results

The MEMS devices were fabricated with a commercial process (PiezoMUMPs by MEMSCAP) (Cowen et al., 2014). The process uses SOI technology with a 10 µm device layer. SEM micrographs of the fabricated structures with measured critical dimensions are presented in Figure 5.8.

An analysis of the SEM micrographs showed that the fabricated dimensions were slightly different from the design dimensions. The lateral actuator gap increased from 4 μm to 4.37 μm and the stopper gap from 3 μm to 3.37 μm. The gap closing actuator gap increased from 6 μm to 6.34 μm and the stopper gap increased from 4 μm to 4.26 μm. These slight variations should increase the actuation voltage due to increased gap between the actuator plates. However, the spring beam dimensions were also smaller by a margin of ~0.17 μm for the lateral spring beams and by a margin of ~0.03 μm for the serpentine spring beams. This lowers the spring stiffness thereby negating the effect of the increase of the actuator gaps to some extent. A video showing both lateral switching and gap closing actuators in motion during SEM imaging is provided in the Supplementary Materials section. Actuation tests were performed to study the impact of these fabrication variations upon the actuation voltage. The test setup used, and the results obtained are presented in section 5.5.2.

5.5.2 Actuation Test Results

Different fabricated devices were tested using a Wentworth probe station with a Bausch & Lomb microscopic system. Four DC probes were used during these tests. High voltage DC sources were used to provide the necessary voltage for actuation. A high resolution camera from Omax was used to image the devices during these tests. The actuator was grounded through a 100 kΩ resistor to prevent any device damage due to high current during actuation. Detailed image of the test setup used along with a schematic of the test circuit for the actuation experiments is given in Figure 5.9.

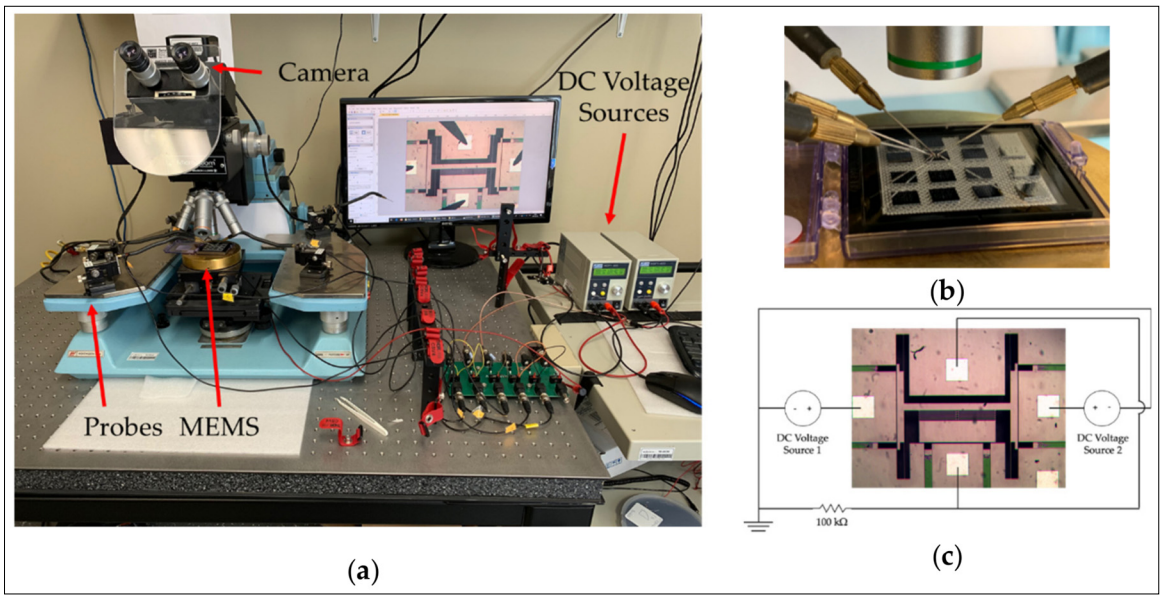

Figure 5.9 (a) Experimental actuation setup used; (b) zoomed in image of the probes on the MEMS device during tests; (c) schematic of the test circuit used for lateral actuation experiments

The lateral actuator on both the sides showed pull-in at an actuation voltage of 65 V. Since after pull-in the movable actuator plate snaps towards the fixed plate, the total displacement obtained should be equivalent to the gap between the actuator plates. However, 3 µm stoppers were included specifically in the design to prevent any shorting through contact between the two actuator plates. The fabricated dimensions for the devices discussed in section 5.5.1

showed that a 3.37 μm stopper gap was fabricated instead. Our lateral actuator shows 3.37 μm of displacement for the central platform at just 65 V of pull-in voltage. Similarly, the results for the longitudinal gap closing actuator show pull-in at 50 V. The fabricated dimensions for the gap closing stoppers was 4.26 μm instead of 4 μm as per the design. The gap closing actuator provides a 4.26 μm displacement to the central platform at a pull-in voltage of just 50 V. No stiction issues or damage to the fabricated stoppers were observed after repeated actuation. The measured displacement for different actuation voltages of the lateral switching actuator follows a linear trend over the range of voltages used in the experimental characterization in comparison to the non-linear behavior of the gap-closing actuator before electrostatic pull-in. This can be explained by the difference in spring stiffness between the lateral switching and gap-closing actuators. The spring constant values for the single beam spring design of the lateral switching actuator in the simulation model was found to be 15.37 N/m, whereas that for the multi beam serpentine spring design of the gap-closing actuator is only 1.18 N/m. Therefore, the non-linear response of the gap-closing can be observed by applying a much smaller force or equivalently, a smaller actuation voltage. Also, the spring for the lateral switching actuator is similar to a clamped-clamped beam system which follows linear displacement as per small beam deflection theory up to a quarter of the beam thickness following which non-linear displacement can be observed for larger displacements

(Legtenberg et al., 1996). Since the thickness of the SOI device layer used is 10 μm, the

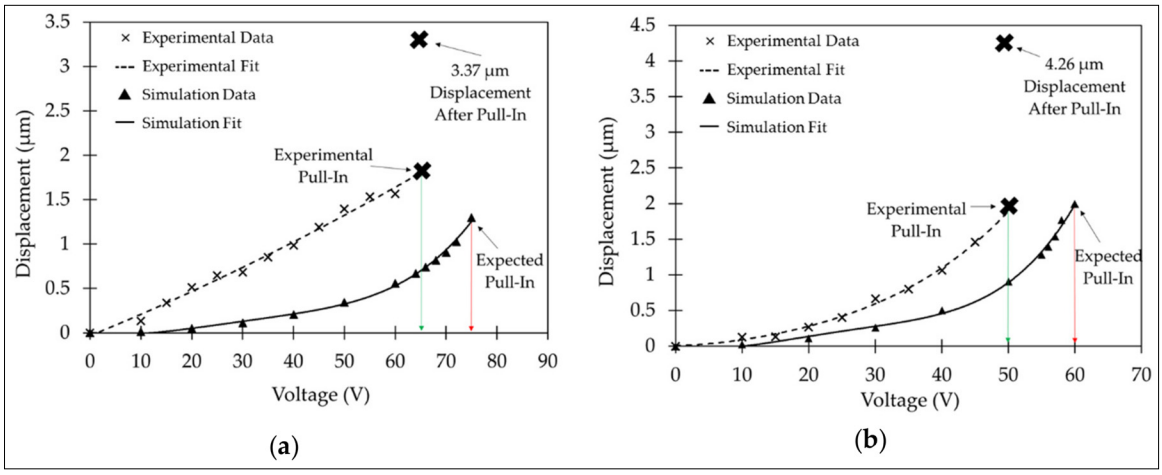

Figure 5.10 Experimental and simulation based displacement v/s actuation voltage results along with relevant pull-in voltages and maximum displacement obtained for (a) the lateral switching actuator; (b) the gap closing actuator

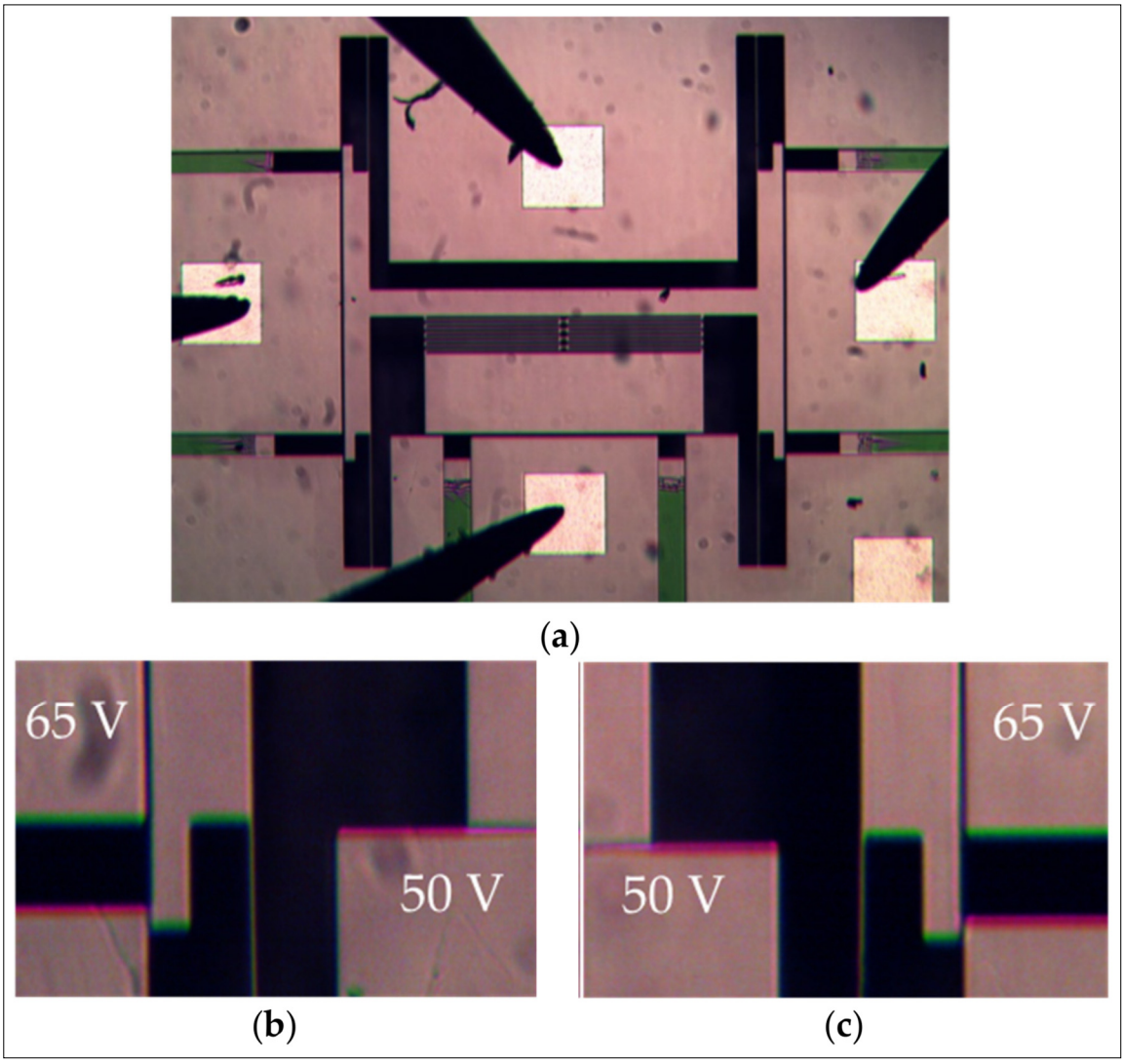

Figure 5.11 (a) Microscopic micrographs of the device at 0 V during actuation tests with probes on MEMS; (b) zoomed in image of the left switching actuator at 65 V and gap closing actuator at 50 V; (c) zoomed in image of the right switching actuator at 65 V and gap closing actuator at 50 V

maximum displacement observed before pull-in is much lower than a quarter of the silicon beam thickness (i.e., 2.5 μm resulting in the linear behavior of the fabricated actuator). The simulation model for the lateral switching actuator shows an initial linear behavior which becomes non-linear with a larger displacement than seen in the measurements, which could be due to the higher stiffness of the spring by the actuator in the simulation model, due to the

geometry variations resulting from the fabrication process, as seen in Figure 5.8. The experimental actuation voltage to reach pull-in was lower in comparison to the simulated model for both the lateral switching actuator and the gap-closing actuator. This can be explained by the difference in the fabricated and simulated silicon beam dimensions. As discussed earlier in section 5.5.1, the width of the fabricated silicon beams in the spring structure was slightly less than in the simulation model. This reduces the stiffness of the spring leading to lower experimental actuation voltages for the simulated displacements compared to simulated actuation voltages. The experimental displacement before pull-in was also observed to be larger in comparison to the simulated model. This is because the fabricated gap between the parallel plates of the actuator was larger, as discussed earlier in section 5.5.1.

Simulation v/s experimental results are presented in Figure 5.10 and they show the pull-in voltage for both lateral switching and longitudinal gap closing actuators. Micrographs of the bi-directional lateral switching action at 65 V combined with vertical gap closing at 50 V along with the neutral position of the actuator are shown in Figure 5.11.

5.6 Discussion

Different translational MEMS actuator designs were implemented and tested. The comb drive-based actuator design showed a maximum displacement of 2.38 μm before a rotational effect occurred at 110 V precluding further motion. This maximum displacement of 2.38 μm achieved for the central platform could not provide the displacement of at least 6 μm needed for successful operation as a 2 × 2 crossbar switch. The MEMS design was improved through the incorporation of single beam spring for lateral switching actuation. Silicon beams anchored at two ends provide the necessary higher vertical stiffness and eliminated any rotational effect due to the serpentine spring structure with low vertical stiffness. Incorporation of simple parallel plate actuator design for lateral switching actuators eliminates any rotational effect caused due to fabrication discrepancies in the comb drive geometry. Two parallel plate actuators on the opposite side of the central platform provide the necessary discrete

displacement of at least 6 μm (i.e., 3 μm on each side) after pull-in for lateral switching. Parallel plate actuator designed for air gap closing motion of the central platform provides zero gap between platform and the substrate upon actuation. Soft spring design for the central platform using serpentine spring system also ensures zero impact of the air gap closing motion upon the lateral switching motion of the platform.

The state-of-the-art planar optical switch developed in (Seok et al., 2016) demonstrates low loss switches which rely upon polarization sensitive vertical adiabatic coupling between polysilicon ridge waveguides. Although polarization insensitive switches based upon polysilicon waveguides have also been realized, these involve a complex 20 masks fabrication process with 3 waveguide layers (Han et al., 2018). State-of-the-art 2 × 2 MEMS switches with zero gap butt-coupling between suspended and fixed waveguides has also been demonstrated in the past through the incorporation of soft polymer waveguides over the MEMS actuator and had a low switching speed of < 0.5 ms. This approach involves a complex bonding process between the polymer waveguides and MEMS structures (Liu & Chollet, 2009). Also, the actuator springs need to be precompressed into latching position using probes under a microscope to provide the zero gap coupling between waveguides and optical fibers.

The translational platform presented in this work is designed to be integrated with polarization insensitive square SiN waveguides in a single optics layer with SiO2 cladding for less stringent packaging requirements. The actuator springs designed do not require any complex assembly procedure before switching operation for zero gap closing either. This is due to the independent spring design for lateral switching and air gap closing motions which provides bi-axial motion to the central platform necessary for its operation in 2 × 2 crossbar switch configuration. Recently, a rotational MEMS platform demonstrated crossbar switching capability at 118 V with the ability to reduce the air gap between fixed and movable waveguides down to 250 nm at an actuation voltage of 113 V (Brière et al., 2017). The translational platform presented in this work operates at a much lower voltage of 65 V for 2 × 2 crossbar switching and 50 V for

air gap closing. The rectangular platform design also provides the unique possibility to integrate SiN based optical filters on the platform itself in 1 × 3 switch configuration.

Although the design choice of parallel plate-based actuation for lateral switching makes the alignment of the optical waveguide mask with the MEMS mask during microfabrication critical, previously SiN waveguides have been successfully integrated with high precision (Brière et al., 2017). Also, optical simulations of the alignment tolerances showed more than 80% efficiency for 700 nm of misalignment and more than 96% efficiency for less than 300 nm of misalignment with a 250 nm gap between the waveguides. Stepper tools for lithography can be used to precisely align the MEMS layer with the waveguides during microfabrication process. Optical simulations show that the gap closing motion of the platform can provide over 99% transmission efficiency for butt-coupling waveguides. Waveguides with inverted tapers can provide more than 83% efficiency even when there is a separation of 3 μm between them. The design is capable of minimizing the optical losses due to the air gap. The effect of surface roughness of the fabricated devices upon the minimal gap achievable should not cause significant optical losses either.

5.7 Conclusion

In this work, a translational MEMS platform was presented for planar optical switching applications. The lateral switching actuator designed for this translational MEMS device operates at an actuation of voltage of 65 V while closing the air gap completely at just 50 V. The ability to integrate up to four SiN waveguides with minimal crosstalk on the large 150 μm by 520 μm platform provides 2 × 2 crossbar switching capability. A 2 × 2 crossbar switch can be realized with just one core switch cell in a smaller device footprint of 1 mm by 1 mm when compared to (Brière et al., 2017). This switch also operates at a much lower voltage when compared to the rotational MEMS platform designed for planar crossbar switching. It can also be used to demonstrate a wavelength channel selection system through integration with SiN based optical filters on the central platform for Reconfigurable Optical Add–Drop Multiplexer

(ROADM) applications (Nakamura et al., 2016; Strasser &Wagener, 2010). In the future, we aim to integrate SiN waveguides and optical filters with the fabrication process demonstrated previously (Brière et al., 2017). Spring stiffness and actuator dimensions will be further optimized so that both lateral and gap closing actuators operate at the same voltage. Actuator stopper dimensions will also be optimized for minimal stiction and high reliability.

CHAPTER 6

INTEGRATED 1 X 3 MEMS SILICON NITRIDE PHOTONICS SWITCH

Suraj Sharma[1], Niharika Kohli[1,2], Jonathan Brière[3], Frederic Nabki[1], and Michaël Ménard[1]

[1]Department of Electrical Engineering, École de Technologie Supérieure, Montreal, Quebec H3C 1K3, Canada

[2]CMC Microsystems, Montreal, Quebec H3C 6M8, Canada

[3]AEPONYX Inc., Montreal, Quebec H3C 2M7, Canada

Papers published in *Optics Express*, June 2022

Preface

In this chapter, a 1 x 3 optical switch that integrates SiN waveguides with SOI-based translational MEMS platform (like the actuator prototype presented in the previous chapter) that moves along two axes is presented. A brief introduction about MEMS actuator integration with Si and SiN waveguides for optical switching is followed by a detailed description of the design methodology followed to realise an integrated MEMS SiN photonics switch. Key design choices made to reduce mechanical stress due to fabrication of SiN waveguides over suspended Si along with the choice for spring system used for the prototype devices fabricated and tested are described here. Microfabrication process used, SEM micrograph analysis, MEMS and optical characterization results are included in this chapter. Key findings related to microfabrication impact upon device performance are presented in this chapter. The chapter concludes with future work recommendations to improve MEMS actuator design to maximize displacement to minimize optical loss in different switching channels. This recommendation forms the basis for the hybrid MEMS actuator discussed in the following chapter.

S.S. designed, simulated, and characterized the MEMS devices along with complete optical characterization. N.K. designed the optical components required in this chapter. J.B. provided MEMS design expertise. M.M. and F.N. supervised the work presented in this chapter.

6.1 Abstract

We present a 1 × 3 optical switch based on a translational microelectromechanical system (MEMS) platform with integrated silicon nitride (SiN) photonic waveguides. The fabricated devices demonstrate efficient optical signal transmission between fixed and suspended movable waveguides. We report a minimum average insertion loss of 4.64 dB and a maximum average insertion loss of 5.83 dB in different switching positions over a wavelength range of 1530 nm to 1580 nm. The unique gap closing mechanism reduces the average insertion loss across two air gaps by a maximum of 7.89 dB. The optical switch was fabricated using a custom microfabrication process developed by AEPONYX Inc. This microfabrication process integrates SiN waveguides with silicon-on-insulator based MEMS devices with minimal stress related deformation of the MEMS platform.

6.2 Introduction

Photonics switching technologies were developed using different kind of microelectromechanical actuators (Liu et al., 2019; Sattari et al., 2021; Qiao et al., 2020). These actuators use piezoelectric (Ramesh et al., 2012), electrothermal (Gerson et al., 2010), electromagnetic (Jia et al., 2021) and electrostatic (Plander & Stepanovsky, 2016) actuation-based methods in both planar 2-D (Bulgan et al., 2008; Abe & Hane, 2013) & out-of-plane 3-D (Sun et al., 2005; Pallay & Towfighian, 2018) configurations. Piezoelectric actuators provide fast switching but largely rely upon out-of-plane actuation for optical switching (Kim et al., 2008; Liao et al., 2013). Electrothermal actuators have also been designed for out-of-plane switching but are relatively slow and operate at high power (An et al., 2021; Peters & Tichem, 2016). Electrostatic actuators can provide both out-of-plane and planar switching solutions through comb drives or parallel plate-based actuation with low power consumption and fast

switching operation (Li et al., 2003; Takahashi et al., 2008; Kaykisiz & Bulgan, 2011; Seok et al., 2016). Optical switching technologies based upon electrostatic actuators have been widely designed for silicon (Si) based photonics (Akihama et al., 2011; Munemasa & Hane, 2013; Fuchs et al., 2004; Hane et al., 2016) whereas only a few optical switches exist that integrate optical switching with silicon-nitride (SiN) photonics (Nielson et al., 2005; Briere et al., 2017). Due to their lower refractive index contrast, SiN waveguides are less sensitive to width variations in comparison to Si waveguides (Baets et al., 2016). Also, SiN waveguides can have lower scattering losses from sidewall roughness in comparison to Si waveguides (Barwicz & Haus, 2005; Bauters et al., 2011).

In this work, we present a planar 1 × 3 optical switch based on a translational microelectromechanical system (MEMS) platform. The MEMS platform is designed in the device layer of a silicon-on-insulator (SOI) wafer and integrated with SiN channel waveguides that carry the optical signal across the MEMS platform. The MEMS platform presented here is a significant improvement upon our previous work (Sharma et al., 2019) where only the in-plane translational motion of the actuator was verified since no waveguides were fabricated on it. The PiezoMUMPs microfabrication process available through MEMSCAP (Cowen et al., 2018) was then used to demonstrate the actuator. The improved MEMS presented in this article is designed to manage the residual stress caused by the silicon dioxide (SiO) cladding of the SiN waveguides (Yang & Pham, 2018) upon integration with the 2 suspended MEMS layer. A schematic of the 1 × 3 optical switch along with its operating principle is presented in section 6.3. The trade-offs made to accommodate the residual thin film stress while minimizing the switching actuation voltage are also discussed in section 6.3. A brief overview of the microfabrication process flow and high-resolution scanning electron microscope (SEM) images of the fabricated devices are given in section 6.4. Mechanical and optical characterization results are reported in section 6.5. A discussion of the characterization results is presented in section 6.6, followed by concluding remarks and the envisioned future work in section 6.7.

6.3 Design Methodology

6.3.1 1 x 3 Optical Switch

The basic MEMS structure of our 1 × 3 optical switch is inspired from our previous work on electrostatic actuators (Sharma et al., 2019). Electrostatic actuation relies upon two isolated actuator plates fabricated in the same Si device layer. One of the actuator plates is fixed to the substrate and the movable plate is anchored through supporting spring system. The air gap between the actuator plates acts like the dielectric medium, and overall, the actuator is electrically equivalent to a capacitor. One of the actuator plates is grounded and the other plate is kept at a potential difference. This creates an electrostatic force of attraction due to charge accumulation of opposite polarity on the two actuator plates. As shown in Figure. 5.1, our device consists of a central waveguide platform connected through serpentine spring structures to a support beam. Left and right parallel plate switching actuators are located on opposite ends of the support beam. Each switching actuator takes advantage of the electrostatic pull-in phenomenon and is designed to provide a lateral displacement of 4 μm. This displacement is limited to 4 μm through mechanical stoppers located on the two opposite corners of each actuator. The gap closing actuator works following a similar principle as the switching actuators. Upon actuation, the waveguide platform is pulled closing the two air gaps between the suspended waveguides on the platform and the fixed waveguides on the substrate. This is required to reduce the optical coupling loss between suspended and fixed waveguides. The

interfaces between the suspended and fixed waveguides at the two air gaps act as mechanical stoppers and limit again the displacement to 4 µm. The serpentine spring structures are designed to provide low mechanical stiffness to minimize the required actuation voltage during both switching and gap closing actuation.

A top view of the SiN channel waveguides in a 1 × 3 switching configuration is shown in Figure 6.1. The single input waveguide is located over a non-movable substrate portion. It is aligned to the center switching waveguide on the suspended MEMS platform when no switching voltage is applied. The waveguide platform can be moved in the left and right directions using the left and right switching actuators, respectively. Once a switching voltage is applied, the left or right output waveguide is aligned to the input waveguide depending upon the actuator used. The gap closing actuator can be used in all three switching positions (center, left and right) to minimize optical losses over the two air gaps. The waveguide platform size is 162.5 µm x 520 µm to accommodate all three waveguides. SiN channel waveguides with 3.2 µm top and bottom SiO cladding, and a core of 435 nm x 435 nm are used to implement the optical paths. The side cladding of the input and output waveguides over the fixed sections

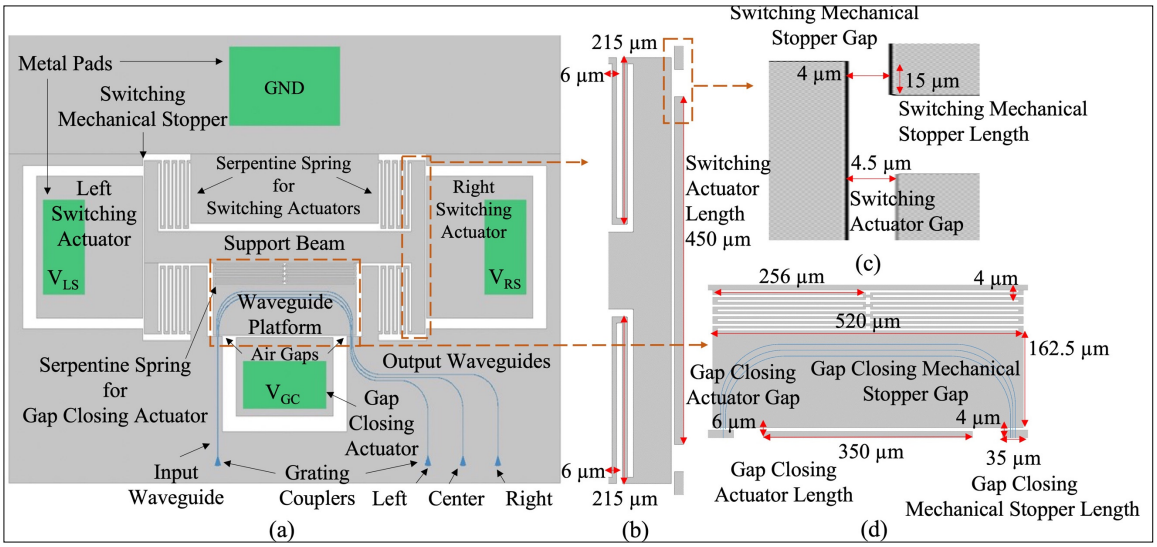

Figure 6.1 (a) Schematic of the 1×3 optical switch showing the MEMS platform with switching and gap closing actuators along with the waveguide layout. The insets show design dimensions for the (b) spring, (c) switching actuator and (d) gap closing actuator

of silicon is 12.25 μm wide on each side. The three output waveguides are spaced on a 127 μm pitch to match that of our test setup optical I/O fiber array. Each waveguide has four 90° bends. Two of these bends are on the suspended platform to minimize the size of the platform. The other two bends are over the fixed silicon to separate the three output waveguides as per the aforementioned 127 μm pitch. Each bend has a 100 μm radius to minimize optical losses due to bending of the waveguides. Our previous work (Sharma et al., 2019) presented 2.5 Finite Difference Time Domain (FDTD) simulations to estimate the crosstalk between adjacent waveguides for different separations, and Eigen Mode Expansion analysis for the edge-coupling between the waveguides on the fixed substrate and the movable platform with inverted tapers. Based on this work, inverted tapers with a tip-width of 400 nm and a length of 20 μm were included at the edge of the platform and fixed silicon to improve the coupling efficiency with minimum crosstalk. The tip-width was limited to 400 nm to comply with the minimum feature size of the optical lithography process used to fabricate the switch. The dimensions for the cladding and the space between waveguides are modified near the air gaps

and on the suspended MEMS platform. Detailed dimensions of the layout of the waveguides are shown in Figure 6.2.

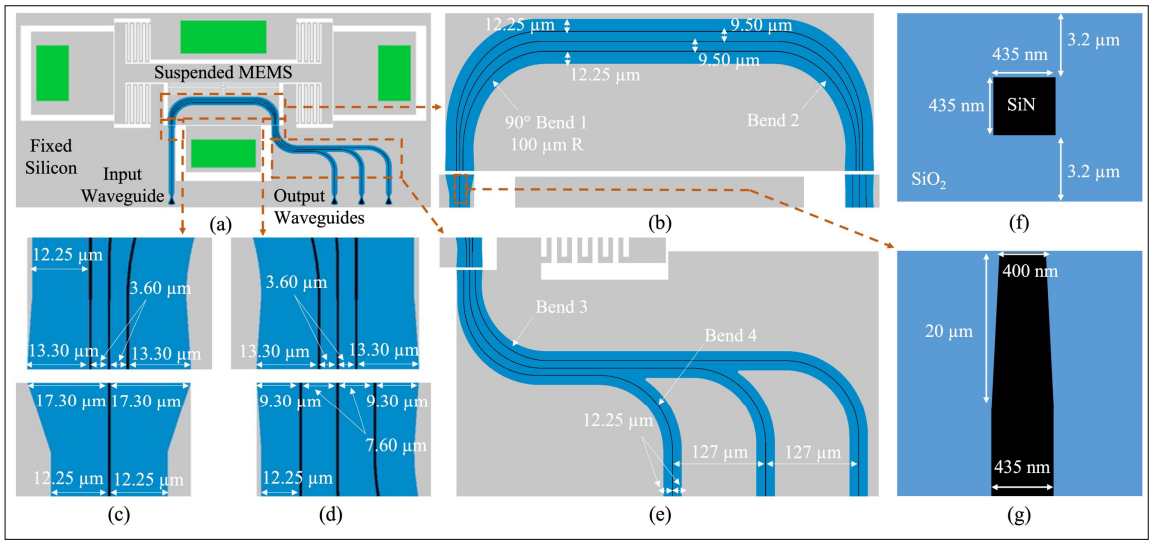

Figure 6.2 (a) Schematic of the 1 × 3 optical switch. The insets show the waveguide spacing and side cladding dimensions for (b) waveguides on the suspended platform, (c) the input waveguide interface, (d) the output waveguides interface, and (e) the output waveguides over fixed silicon. Cross-sectional view of (f) waveguide core and cladding dimensions. Top view of (g) inverted taper design near air gaps with dimensions

6.3.2 Optical Material Stack Residual Mechanical Stress

In our previous work, we designed a translational switching MEMS platform without optical waveguides using a 10 µm thick silicon device layer. However, previous research has shown that the thin films used to build the optical waveguides cause significant residual mechanical stress. This can lead to deformation of the silicon platform (Yang &Pham, 2018). In this work, we integrated 435 nm thick SiN waveguides with 3.2 µm thick top and bottom SiO_2 cladding layers with the MEMS for optical switching. Thus, before fabricating the optical switch, a finite element modelling (FEM) analysis was performed to assess the impact of mechanical stress from the integration of the optical material stack (i.e., cladding and waveguide). Stress related deformation of our MEMS platform was simulated using the COMSOL Multiphysics

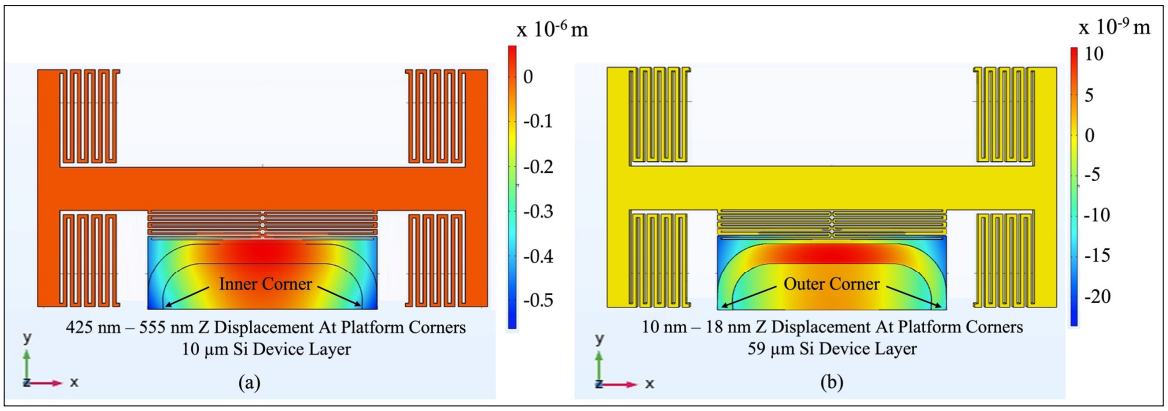

Figure 6.3 FEM simulation results of vertical (z-axis) displacement of the MEMS structure due to the mechanical stress caused by the optical waveguides with: (a) a 10 µm thick silicon device layer; and (b) a 59 µm thick silicon device layer used in this work

software (version 5.5, COMSOL, Inc., Burlington, MA, USA). FEM simulation results shown in Figure 6.3 demonstrate that using a thicker silicon device layer significantly reduce stress related deformation across the entire waveguide platform. Since our waveguide couplers are located at the corners of the platform, it is important to minimize the out-of-plane displacement of the platform near these regions. Therefore, in this work we used a thicker Si device layer of 59 µm. As seen in Figure 6.3, a device layer with a thickness of 59 µm shows only 10 nm to 18 nm of displacement along the vertical direction (i.e., the z-axis in Figure 5.3) at the corners of platform. In comparison, a device layer of 10 µm shows a vertical displacement of 425 nm to 555 nm at the corners of the platform. The inner corner of the optical stack shows higher displacement in comparison to the outer corner for both device layer models. Clearly, increasing the thickness of the silicon device layer helps minimizing vertical misalignment between the waveguides on the suspended platform and those on the fixed substrate. It should be noted that the minute deformation of 10 nm to 18 nm of the suspended waveguide platform will not have any impact on the gap closing actuator mechanism. This is because the electrostatic force generated by the gap closing actuator relies upon the 59 µm silicon device layer thickness, which is significantly larger than the deformation of the platform. Also, the left and right switching actuators were not affected by the residual stress in the simulation model shown in Figure 6.3(a). Thus, the switching actuation mechanics are not impacted by

the integration of the waveguides. Optical simulation results for vertical misalignment between the suspended and fixed waveguides performed in our previous work also show that a 10 nm to 18 nm misalignment has negligible effect on the optical performance of the switch (Sharma et al., 2019).

6.3.3 Serpentine Springs

As demonstrated in section 6.3.2, increasing the thickness of the device layer from 10 μm to 59 μm helps minimize the impact of the residual stress on the vertical optical alignment. However, increasing the thickness of the device layer creates other challenges. In our previous work (Sharma et al., 2019), translational MEMS actuators with a single beam spring required a switching voltage of 65 V. Also, the use of springs made of a single beam anchored at opposite ends provided enough planar vertical stiffness to avoid rotation of the platform during its displacement. The increase in the thickness of device layer dramatically increases the stiffness of the supporting spring structure. Static structural analysis of the actuator design based upon (Sharma et al., 2019) with a 59 μm device layer was performed using ANSYS (version 19.0, ANSYS Inc., Canonsburg, PA, USA). Devices with a single beam spring of 4 μm x 250 μm for the switching actuator showed electrostatic pull-in at a voltage of 165 V. This is significantly higher than the 65 V pull-in voltage for the switching actuator with a 10 μm device layer (Sharma et al., 2019).

Similar electrostatic simulations for the gap closing actuator were performed with ANSYS for both 59 μm and 10 μm device layer thicknesses. The gap closing actuator showed electrostatic pull-in at 62 V with a 59 μm device layer in comparison to 50 V for a 10 μm device layer (Sharma et al., 2019). The increase in pull-in voltage for the gap closing actuator is significantly less than the increase in pull-in voltage for the switching actuator with the increase in device layer thickness. The serpentine spring supporting the gap closing actuator has a lower stiffness of 127 N/m in comparison to 171 N/m for the single beam spring

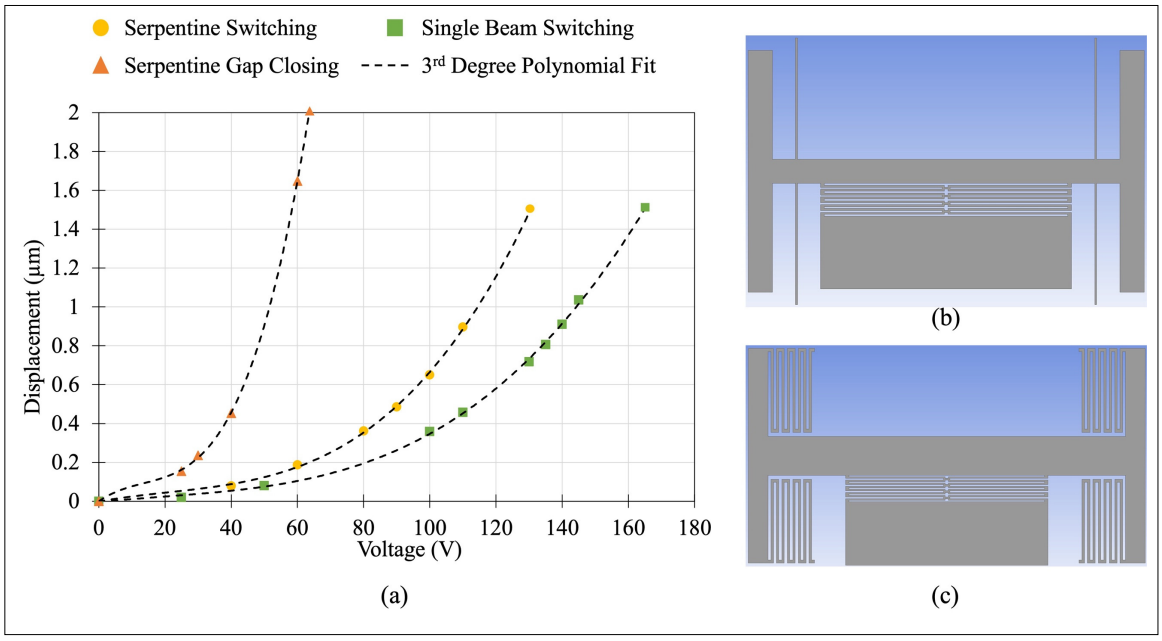

Figure 6.4 (a) Simulation based displacement vs actuation voltage results for switching and gap closing actuators of (b) single beam spring and (c) serpentine spring-based MEMS structures with 59 µm device layer thickness. The dotted lines are a polynomial fit to the simulated data with the electrostatic pull-in point represented at the end of each curve

supporting the switching actuator. Thus, static structural analyses were performed for MEMS devices with serpentine spring structures for both the switching and gap closing actuators.

The simulated structure was similar to the illustration presented earlier in Figure 6.1. Each silicon beam in the serpentine spring model of the switching actuator was designed to be 6 µm x 215 µm. The switching actuator gap was kept at 4.5 µm. The serpentine spring dimensions for the gap closing actuator were designed to be 4 µm x 256 µm for each silicon beam. The gap closing actuator gap was kept at 6 µm. It should be noted that electrostatic pull-in in a parallel plate actuator occurs when the movable actuator plate is displaced by 1/3rd of the initial gap between the fixed and movable actuator plates. Thus, electrostatic pull-in is expected after 1.5 µm and 2 µm of displacement for the switching and gap closing actuators, respectively. The simulation results shown in Figure 6.4 present the clear advantage of the serpentine springs since they require a switching pull-in voltage of 130 V in comparison to

165 V for the single beam springs. The simulated gap closing actuation voltage for electrostatic pull-in is 62 V. The electrostatic pull-in points are present at the end of each curve presented in Figure 6.4(a).

6.4 Microfabrication

A proprietary fabrication process developed by AEPONYX inc. in a commercial foundry was used to integrate SiN waveguides with Si MEMS on SOI wafers with predefined cavities underneath the device layer. These cavities simplify the release of the MEMS structure. Initially, a 3.2 μm thick SiO2 bottom cladding layer was deposited through Tetra EthOxy Silane (TEOS) low pressure chemical vapor deposition (LPCVD) over a SOI wafer with a 59 μm Si device layer. A 435 nm thick SiN waveguide core layer was then deposited through LPCVD on top of the bottom cladding layer. Photolithography with a stepper tool and dry etching was used to pattern the SiN waveguides. A 3.2 μm thick SiO2 top cladding layer was then deposited through TEOS plasma enhanced chemical vapor deposition over the SiN waveguides. Openings were patterned and etched into the optical stack to expose the silicon layer underneath. A 250 nm thick film of aluminum copper (AlCu) alloy was then sputtered and patterned in the exposed Si regions to form the bonding pads required to actuate the MEMS electrostatically. The optical stack next to waveguides and over the MEMS region was removed through dry etching to minimize residual stress in the final device. The MEMS actuator structures were patterned in a hard mask before being transferred into the Si through deep reactive ion etching. This also released the MEMS since they are fabricated over empty cavities. A cross sectional view of the optical switch is shown in Figure 6.5.

Following microfabrication, high resolution SEM imaging was performed. An analysis of the SEM micrographs obtained showed variations in the fabricated dimensions of the actuator and stopper gaps. The images shown in Figure 6.6 are from one of the three samples tested. The mechanical stopper gap for switching was designed to be 4 µm and the switching actuator gap was designed to be 4.5 µm. As shown in Figure 6.6(b) and 6.6(c), these dimensions changed to 4.74 µm and 5.86 µm, respectively. As shown in Figure 6.6(d), the air gap closing actuator dimension also changed to 7.19 µm after fabrication (compared to 6 µm in the design). The mechanical stopper / air gap closing interface between waveguides is shown in Figure 6.6(e) and 6.6(f) with dimensions and the slope etch angle. The etch profile of the SiO_2 cladding and SiN waveguide clearly shows that the slope of the etch is not vertical. This slope creates a variation in the air gap across the height of the optical stack. The top layer of SiO_2 shows an air gap of 5.04 µm at the waveguide interface region. However, when measured at the level of the silicon layer underneath the optical stack the gap is 3.68 µm. These variations in the

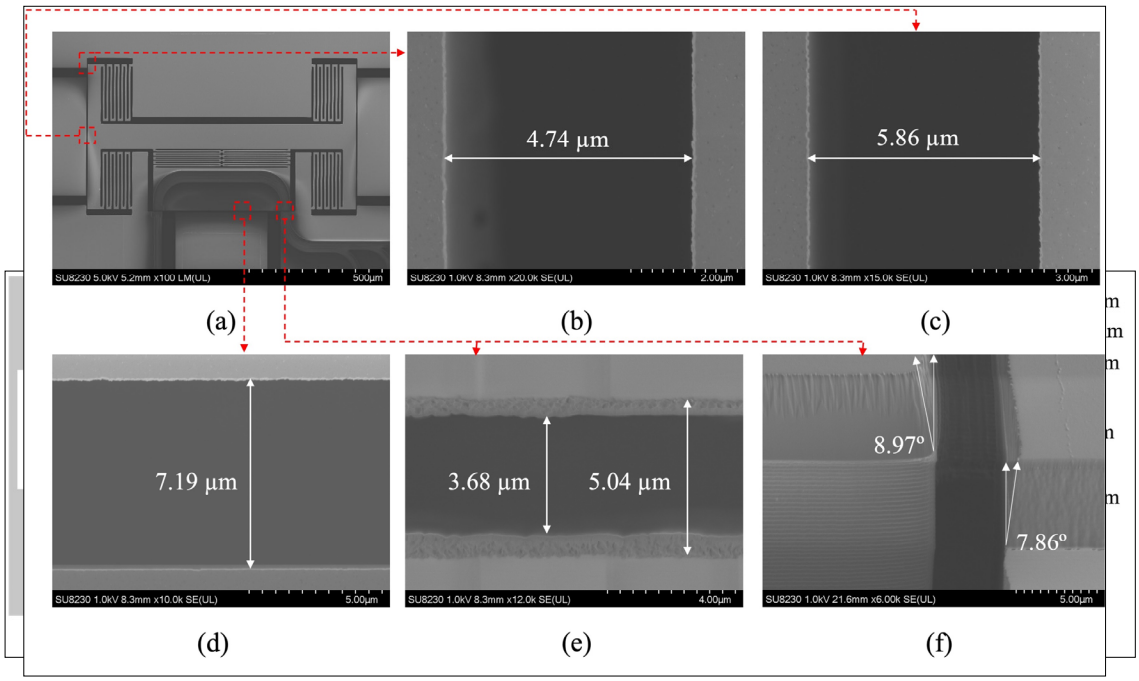

Figure 6.5 1 × 3 optical switch (a) top view and (b) cross-sectional view

Figure 6.6 High resolution SEM micrographs with measurements of the fabricated 1 × 3 optical switch sample 1: (a) fabricated device; (b) mechanical stopper gap; (c) switching actuator gap; (d) air gap of the gap closing actuator; (e) air gap closing interface; and (f) etch profile of the optical stack

geometry of the fabricated devices were expected since AEPONYX's process is optimized for specific etch loading and aspect ratios that differ from our experimental devices. The impact of these variations on the actuation voltage and the optical performance of the devices are presented in the next section.

Similar variations were observed during SEM imaging for the other two samples. The mechanical stopper gap for switching varies between 4.58 μm – 4.87 μm across samples. The switching actuator gap varies between 5.55 μm – 6.01 μm. The mechanical stopper gap and actuator gap for the gap closing actuator also vary between 3.62 μm – 3.85 μm and 6.69 μm – 7.41 μm, respectively. Variations in the width of the gap around the mechanical stoppers of the gap closing actuators will not impact the optical performance as the device relies upon the pull-in phenomena for closing the air gap between suspended and fixed waveguides. However, variation in the mechanical stopper gaps for the switching actuator can lead to misalignment between waveguides during switching. Experimental optical measurement results showing the impact of device fabrication variations upon transmission during switching are presented in section 6.5.2. The critical dimensions of the three samples tested are shown in Table 6.1.

Table 6.1 Fabrication variations across samples

Critical Parameter		**Dimension (μm)**			
		Design	**Sample 1**	**Sample 2**	**Sample 3**
Stopper gap	Left switching	4	4.74	4.82	4.58
	Right switching	4	4.75	4.87	4.67
	Gap closing	4	3.68	3.85	3.62
Actuator gap	Left switching	4.5	5.86	5.99	5.59
	Right switching	4.5	6.01	6.01	5.55
	Gap Closing	6	7.19	7.41	6.69

6.5 Results

6.5.1 MEMS Characterization

MEMS characterization was done using a Wentworth microprobes station. Two high voltage DC sources were connected to the switching and gap closing actuators through microprobes, as shown in the test circuit in Figure 6.7. While one of the high voltage sources was connected to a switching actuator, the second voltage source was connected to the gap closing actuator for bi-axial motion of the central waveguide platform. Both actuators were grounded through a 100 kΩ resistor to prevent device damage in case the grounded moveable actuator plate comes in contact with the high voltage static actuator plate.

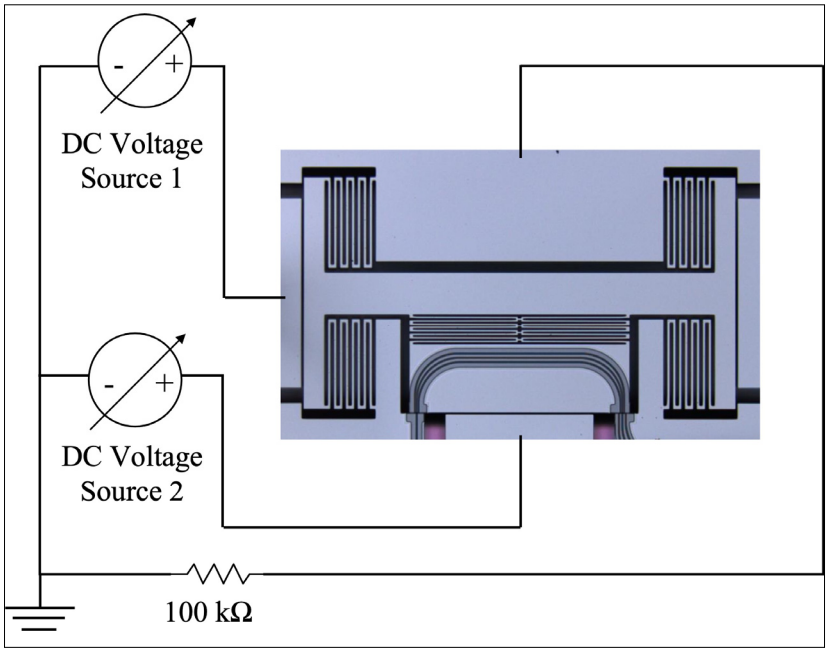

Figure 6.7 Schematic of the test circuit used for left channel switching and gap closing actuation

A high magnification lens system was used along with a high-resolution camera to image the devices during actuation. Microscope images of the device under actuation in different

switching positions are shown in Figure 6.8. Images of the actuator in different switching positions at different voltages for one of the samples were analyzed using the ImageJ (version 1.53a) software to extract the displacement vs voltage curves and pull-in voltage. Experimental results for both the left and right switching actuators showed electrostatic pull-in at 170 V. This was higher than the 130 V expected from the simulation results presented in section 5.3.3 Similarly, the experimental pull-in voltage for the gap closing actuator was 80 V. This was also higher than the 62 V pull-in voltage predicted by simulation. This increase in pull-in

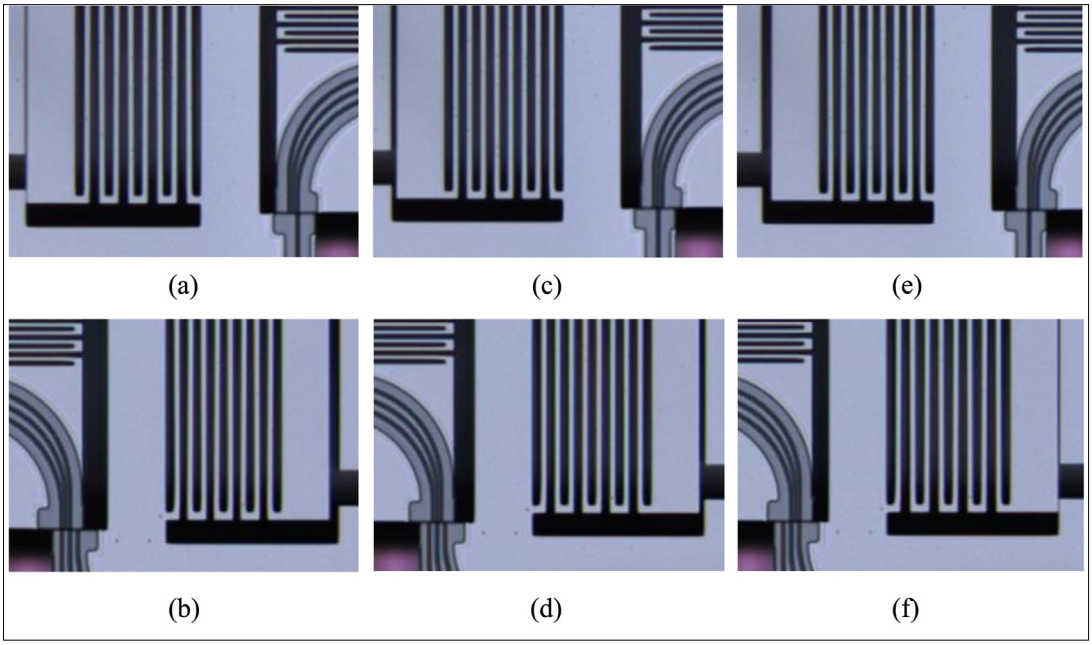

Figure 6.8 Zoomed in microscope images of the fabricated 1 × 3 optical switch device at the input and output waveguide interface during actuation in: (a, b) left switching position; (c, d) center switching positions; (e, f) right switching position

voltage can be explained by the larger gap dimensions in the fabricated devices in comparison to the designed dimensions presented in section 6.4.

Simulations based on the fabricated dimensions are compared with the experimental results for one of the samples in Figure 6.9. We can see that the simulation results with modified dimensions are closer to the experimental results, although the simulated pull-in voltages are slightly higher than the experimental values. The difference between simulation and

experimental results could be due to variations in the spring beam width along the length of silicon beams and potential device layer sidewall topography. It should be noted that no cross sensitivity was observed between the switching and gap closing actuators in the three switching positions. This is due to the high electrostatic force generated during pull-in in left and right switching positions that maintain the desired platform position while the gap closing actuator

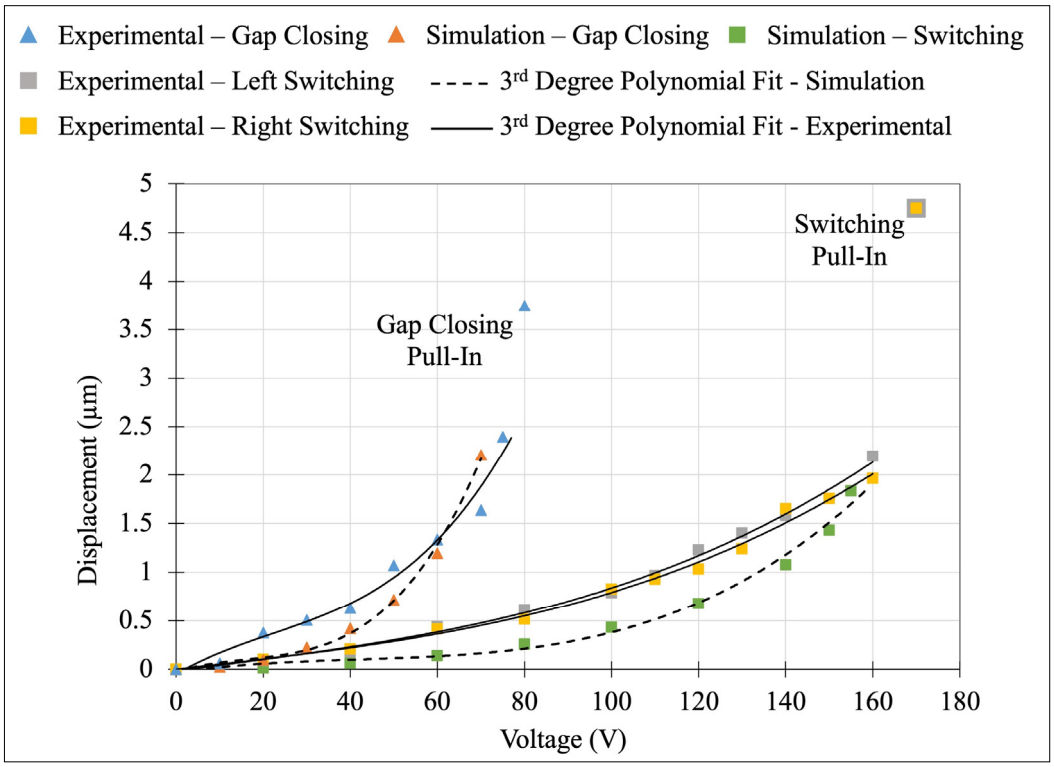

Figure 6.9 Experimental and simulation actuation results for the gap closing and switching actuators with the pull-in points. The dotted lines are a polynomial fit to the simulated data based on the fabricated dimensions and the solid lines are a polynomial fit to the experimental measurements

is enabled. The center switching position demonstrated no cross sensitivity as only the gap closing actuator is required for efficient transmission in this position. The symmetry in the design of the device mitigates cross sensitivity in this switching position.

6.5.2 Optical Characterization

The transmission of optical signals was successfully characterized for all switching positions for three samples. Each sample was wire bonded to a custom printed circuit board (PCB) designed to control the actuation of the MEMS. A tunable laser (T100S-HP) and optical component tester (CT440) from EXFO were used for these measurements. The output of the tunable laser was connected to the input optical fiber array with a 30° polish angle through the optical component tester. The fiber array could be optimally aligned with the surface grating couplers (SGCs) at the input and output ports of the chip on each sample at a vertical distance of approximately 50 μm. Three detector ports on the optical component tester were connected to the output optical fibers from the fiber array. Polarization maintaining fibers were used for the optical connections between the tunable laser, optical component tester and the fiber array to maintain the transverse electric (TE) mode during these tests since the alignment between the fiber array and SGCs used to demonstrate these prototypes were optimized for this polarization. The pitch between the SGCs was designed to match the pitch of the optical fiber array, which was fixed at 127 μm. A microposition controller was used to align the sample and the optical fiber array with 1 μm precision. The sample could be moved in-plane (X & Y

direction) and the fiber array could be moved vertically (Z direction) for this purpose. A detailed image of the test setup used for optical characterization is shown in Figure 6.10.

We fabricated reference waveguide structures on all our samples. The length of the reference waveguide was the same as the total length of the center channel in our device. The number and position of bends was kept the same for both the reference waveguide and the center channel waveguide. Our reference waveguide structure also consisted of adjacent output waveguides similar in position and length to the left and right channels. This would help us replicate crosstalk, if any, between the waveguides present on our optical switch. It should be noted that only the center channel had the input port in the reference waveguide structure for optical measurements. The transmission data obtained for the reference waveguide was used to normalize experimental results for the 1 × 3 optical switch in all switching positions. This was done by subtracting the transmission data of the reference waveguide from transmission

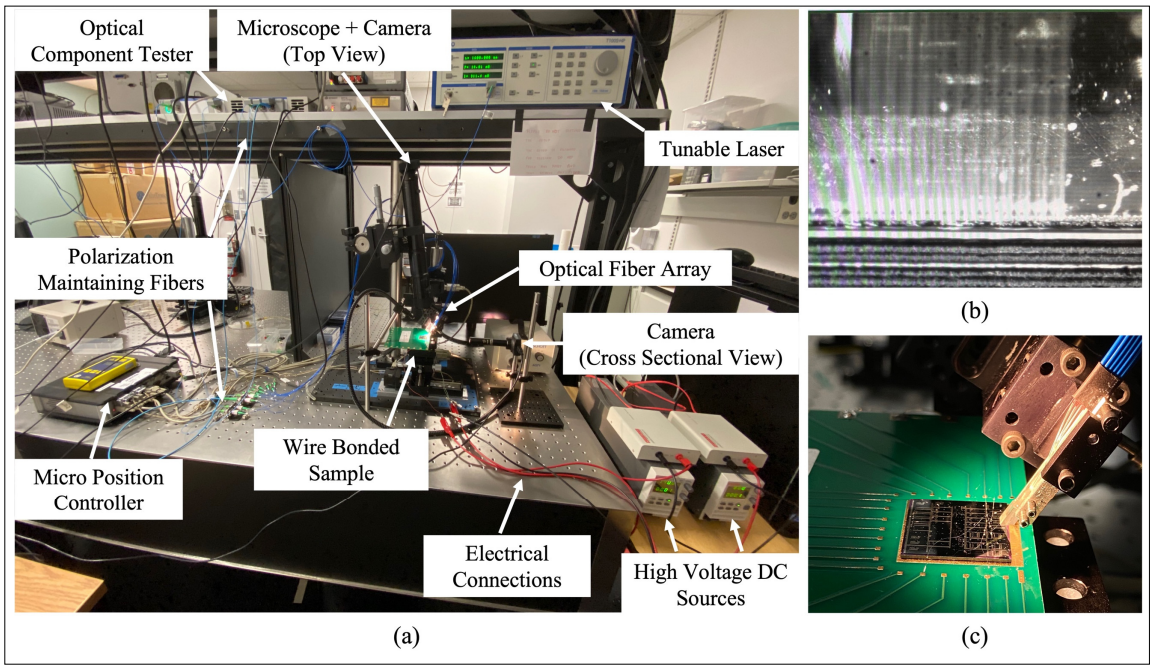

Figure 6.10 a) Test setup for optical characterization of the 1 × 3 optical switch; (b) cross- sectional camera view of the optical fiber array aligned to the sample; (c) a zoomed in image of the sample wire bonded to the PCB during measurements

data of each switching position at each wavelength. The wavelength scan resolution used was 10 pm. The propagation loss for the TE mode in the C-band and L-band is 3.3 dB/cm in the fabrication process used. Therefore, for the center switching waveguide, which as a length of 7.618 mm, the total propagation loss was 2.48 dB. Each switching position (left, center and right) was tested with and without activating the gap closing actuator for all three samples. The average insertion loss obtained for the three samples in all switching positions at wavelengths between 1530 nm to 1580 nm is shown in Figure 6.11. The measured transmission spectra for the three switching positions of the three samples are presented in the Appendix I. The experimental results presented focus mainly on the C-band and the beginning of the L-band of the telecommunication spectrum because the SGCs were optimized for this wavelength range. The transmission data of the optical switch in Figure 6.11 showed small undulations for the entire wavelength scan. These undulations increased outside the wavelength range presented for all three samples. Since we observe the same undulations in our reference waveguide structures, it is safe to assume that the switch does not cause these undulations. They are probably caused by unwanted reflections between the SGCs and the fiber array.

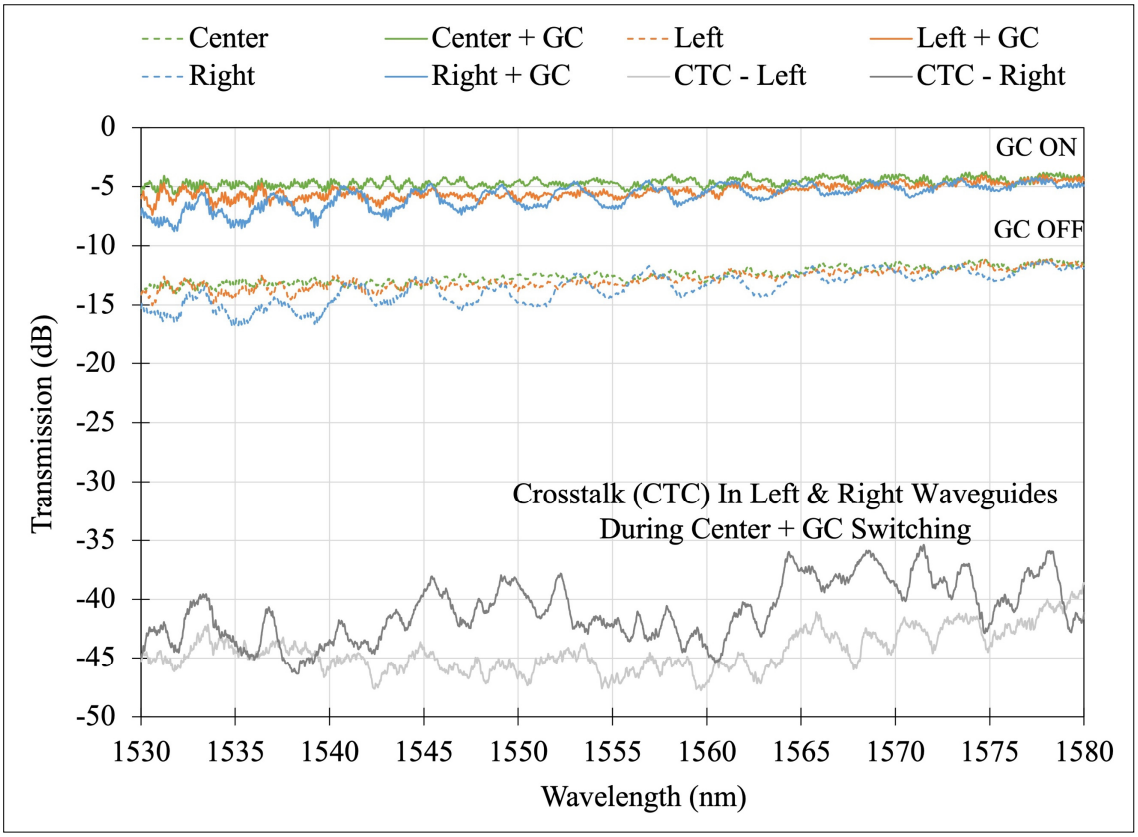

Figure 6.11 Average transmission of three 1 × 3 optical switch samples in all three switching positions with/without gap closer (GC) actuator across the 1530 nm – 1580 nm wavelength. Crosstalk center (CTC) represents the optical signal transmission in the left and right channels when the center switching position and GC actuator are ON

The average insertion loss over the entire wavelength scan for the three samples was 4.64 dB when the gap closing actuator is ON and the switch is aligned to the center position (solid green curve in Figure 6.11). This is less than the average insertion loss observed for the left and right switching positions with the gap closer actuator ON, which were 5.38 dB (solid orange curve in Figure 6.11) and 5.83 dB (solid blue curve in Figure 6.11), respectively. This can be explained by the fabrication variations in the mechanical stopper gaps of the switching actuators observed during SEM imaging. While the mechanical stopper gap for switching actuator was designed to be 4 μm, the fabricated gap varied between 4.67 μm and 4.87 μm, as

discussed in section 6.3. Since the switch is digital and relies upon the ON and OFF state of the switching actuators, this 670 nm to 870 nm gap variation creates a misalignment between waveguides when switching to the left and right positions. Similar average insertion loss variations at the different switching positions were observed in all three samples. The average

Table 6.2 Average insertion loss comparison between samples

Switching Position	**Average insertion loss (dB)**			
	Sample 1	**Sample 2**	**Sample 3**	**Average**
Center	12.71	12	12.88	12.53
Center + gap closer	4.97	4.45	4.50	4.64
Left	12.80	13.31	12.41	12.84
Left + gap closer	5.35	6.91	3.88	5.38
Right	13.52	13.77	13.46	13.58
Right + gap closer	6.49	5.85	5.16	5.83

insertion loss for each sample is shown in Table 6.2. Once the gap is closed, the crosstalk between adjacent waveguides is less than -30 dB.

The etch profile shown in section 6.4 (see Figure 6.6) creates up to a 1 μm gap between the waveguides on the fixed substrate and the ones on the suspended platform (see Figure 6.12(b)). Optical losses due to this residual air gap cannot be compensated with the gap closing actuator. The simulated and experimental average insertion losses for all samples over the wavelength range of 1530 nm to 1580 nm are compared in Figure 6.12. The simulation results were obtained through FDTD simulations using Lumerical (version 2020 R2) software for edge coupling between waveguides with slanted sidewalls (see Figure 6.12(b)). The simulation also includes the scenario for perfectly aligned waveguides and waveguides misaligned laterally by 740 nm, which corresponds to the shift observed in sample 1. Both cases include a 1 μm residual air gap at the center of the waveguide core due to etch profile of the optical stack. The waveguide dimensions were kept at 435 nm by 435 nm except for 20 μm long inverted tapers with a 400 nm tip width near the air gap interface. Simulation results compare well with the experimental one. However, as explained earlier the SGCs cause undulations in the

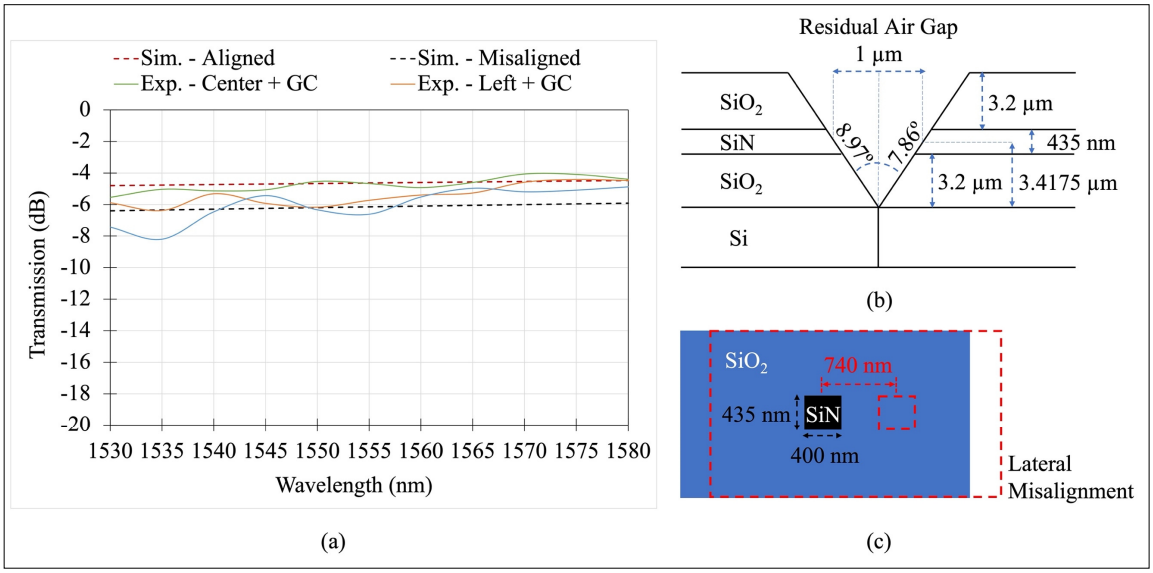

Figure 6.12 (a) Simulated and experimental average insertion losses comparison for all samples in three switching positions with the gap closing actuator ON, (b) measured etch profile and residual air gap between center of the SiN waveguides, and (c) dotted lines showing 740 nm lateral misalignment scenario used for FDTD simulations of edge coupling waveguides

experimental results in Figure 6.12(a). Our simulation model did not include the SGCs due to computational limitations. The simulation and experimental results in Figure 6.12(a) also show reduced optical losses with increase in wavelength. This is expected due to lower confinement and hence, higher coupling efficiency at the air gaps for higher wavelengths.

The effect of increasing incrementally the voltage across the gap closing actuator on the insertion loss of the device was also characterized. The voltage applied to the gap closer was increased in 10 V increments up to 70 V and in 5 V increments afterwards until the optical losses in the center switching waveguide were minimized. The voltage for the lowest optical losses was found to be 80 V for all three samples. This corresponds to the electrostatic pull-in voltage for the gap closing actuator presented earlier in section 6.5.1. The gap closing actuator provides a large reduction in the insertion loss as shown by the loss vs applied voltage curves in Figure 6.13(a). Results from the three samples are shown demonstrating the repeatability of the performance of the GC actuator.

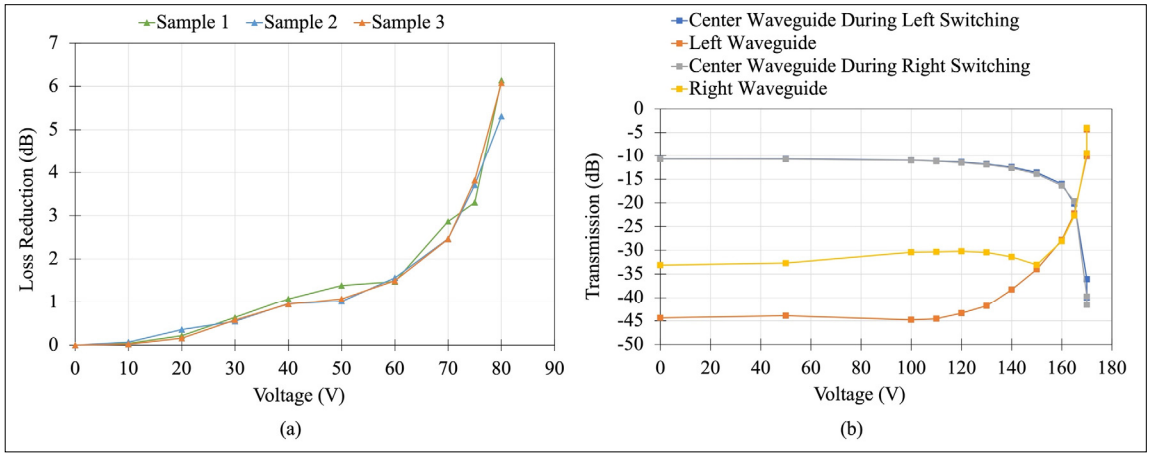

Figure 6.13 Optical characterization results at a wavelength of 1600 nm showing (a) a reduction in the optical loss across the center switching position as the gap closer actuation voltage increases for three samples from different wafers and (b) the impact of left and right switching actuation voltage upon optical signal transmission in the center and switching waveguides for sample 1. The ends of curves show the experimental data points for loss reduction and transmission after electrostatic pull-in of the gap closing actuator

The optical switch is designed such that the center waveguide is aligned to the input when no voltage is applied. When a voltage is applied to a switching actuator (left or right), the optical signal is transmitted through the corresponding waveguide. This switching effect was characterized for the left and right switching channels and the effect of switching upon the center waveguide was measured simultaneously. A voltage was applied to the two switching actuators in 50 V increments up to 100 V and in 10 V increments afterwards up to 170 V. The results for sample 1 can be seen in Figure 6.13(b). After applying the switching voltage of 170 V, the gap closing actuator was also used to further reduce the optical losses. This explains why the signals transmitted through the left and right waveguide have lower losses than the initial value in the center waveguide. The optical signal transmission through the center waveguide was monitored to clearly show the digital switching behavior of the MEMS. These measurements were performed at a wavelength of 1600 nm with 10 dBm of input power during

our initial alignment tests. Similar results can be expected for the wavelength range presented in Figure 6.10 with minor offset in transmission due to the response of the SGCs.

6.6 Discussion

The translational MEMS platform for planar optical switching (Sharma et al., 2019) was modified to accommodate SiN channel waveguides in a 1 × 3 optical switch configuration. The thickness of the silicon device layer was increased to sustain the residual mechanical stress caused by the optical material stack used to create waveguides on the suspended MEMS structure. The spring mechanism for the switching actuator was improved to minimize the actuation voltage. Multiple devices were fabricated and tested. The maximum displacement of the switching actuator was 4.87 μm after electrostatic pull-in at 170 V. Similarly, the gap closing actuator closed the two air gaps between the suspended and fixed waveguides by moving the platform by up to 3.85 μm after electrostatic pull-in at 80 V.

The optical characterization of the 1 × 3 switch presented in this work showed the lowest average insertion loss of 4.64 dB for the center switching channel for wavelengths between 1530 nm and 1580 nm. The left and right channels showed a minimum average insertion loss of 5.38 dB and 5.83 dB, respectively, across the same wavelength range. The difference in insertion loss is due to the misalignment variation between waveguides in the left and right switching channels across samples. The residual stress simulations presented in section 6.3.2 showed a slight variation of the height of the suspended platform across the width of the waveguides. The inner corners of the waveguide array showed lower vertical displacement in comparison to the outer corners along the edge of the platform. The left switching channel was fabricated closer to the inner corner of the array and the right switching channel near the outer corner. The placement of waveguides on the platform therefore creates a variation in the vertical misalignment of left and right switching channels. In addition to this variation, the slight difference in total optical path length of the switching waveguides can contribute towards variation in optical losses measured as well. The center switching channel has an optical path

length of 7.618 mm. The left switching channel has the shortest optical path length of 7.471 mm while the right switching channel has the longest optical path length of 7.765 mm. This length difference along with the variation in the height of the suspended waveguides can explain the small 0.45 dB variation in insertion loss between the left and right channels. Also, fabrication variations in the left and right switching stopper gaps across samples (see Table 6.1) cause optical loss variations across samples during switching (see Table 6.2).

The optical switch presented in this work could in theory completely close the air gap between the suspended and fixed waveguides. However, in practice the slope at the edge of the waveguides (see Figure 6.12(b)) creates a residual air gap of up to 1 μm when measured between the center of the core of the waveguides. Nevertheless, this is an improvement over our previous MEMS silicon nitride waveguide based optical switch (Briere et al., 2017), which only closes the air gap to a minimum of 500 nm by design in addition to any residual air gap due to etch profiles, across each coupling region. The reduction in the air gap presented in this work helps lowering the average insertion loss by 7.89 dB, 7.46 dB and 7.75 dB for center, left and right switching channels, respectively.

The fabrication variation in the switching stopper gap dimension of sample 1 leads to a misalignment of 740 nm and 750 nm between the suspended and fixed waveguides during left and right channel switching, respectively (see Table 6.1). This variation increases the optical insertion losses for these channels (see Table 6.2). The 740 nm change in stopper gap increases the average optical loss by 0.74 dB for the left switching channel. The 750 nm variation for the right switching channel increases the optical loss by 1.19 dB. The slight difference in the fabricated stopper gaps along with the difference in length of switching waveguides discussed earlier in this section can contribute towards this observed variation in optical losses. FDTD simulation results showed a 1.51 dB variation in insertion loss due to a 740 nm misalignment between suspended and fixed waveguides with a 1 μm residual air gap. These optical switching losses can be successfully minimized in a future implementation by introducing a fabrication bias in the photolithography mask. The mask can be designed for a smaller stopper gap

dimension to compensate for the over etching observed during fabrication. This can help minimize optical losses by reducing the misalignment between waveguides during switching. However, even with this misalignment the device successfully manages to switch the optical signal between different SiN channel waveguides with a crosstalk level below -30 dB. The grating coupler could also be optimized further to reduce reflections across the wavelength range.

During our experiments we also found that some of the devices shorted during switching unlike our previous work, which involved testing only the MEMS actuators for translational motion (Sharma et al., 2019). This was due to the critically low difference between the stopper gap and the actuator gap dimensions. The minimum gap in the Si device layer allowed by our fabrication process is 4 μm to release the MEMS structure. The switching mechanical stopper gap was thus kept at 4 μm while the switching actuator gap was kept at 4.5 μm, creating a difference of 500 nm in the stopper and actuator gap designs sent for fabrication (see Figure 6. 1(c)). This 500 nm gap variation was detrimental towards successful testing of the switching actuator as some of the devices would short during electrostatic pull-in. The switching actuator gap was not increased beyond 4.5 μm to minimize the actuation voltage for switching. It should be noted that the gap closing actuator had a 2 μm difference between the actuator gap and the mechanical stopper gap (see Figure 6.1(d)). No shorting was observed while closing the gap in any of the devices. Thus, a larger difference in the actuator and mechanical stopper gap can easily mitigate this issue in future implementation and increase device reliability.

Most of the SiN based optical switching solutions reported in the literature rely upon thermal tuning of optical components, such as Mach-Zehnder interferometers (MZIs), to switch light between waveguides. Although a large number of ports can be achieved through this method, such structures consume a lot of power due to the DC current required to heat the MZI arm for optical switching (Joo et al., 2018; Sun et al., 2019). Alternatively, a few MEMS based phase shifting / switching solutions exist that work with SiN based optical filters. A low power electrostatic actuation-based solution that can filter only 3 wavelengths in the C-band through

digital control of a suspended aluminum-based MEMS bridge over a silicon nitride ring resonator was demonstrated in (Nielson et al., 2005). Another low power piezoelectric actuation-based solution that can filter multiple wavelengths by straining a silicon nitride (Si3N4) ring resonator using an integrated Lead Zirconate Titanate (PZT) actuator arm was reported in (Jin et al., 2018). However, this switch can operate over a wavelength range of only 10 nm and has high losses due to the PZT fabrication and release processes. Also, PZT based piezoelectric actuation comes with environmental concerns due to the lead contained in the material. Similarly, aluminum nitride (AlN) based piezoelectric actuation has been recently used to tune Si3N4 based ring resonators (Dong et al., 2018). However, the tuning range is limited to only 20 pm. A rotational SOI based MEMS actuator has been integrated with SiN waveguides in a crossbar switching configuration in recent years (Briere et al., 2017). This rotational switch design had 12.2 dB– 14.8 dB total insertion loss at an operational wavelength of 1550 nm. The air gaps between the suspended and fixed SiN waveguides could not be completely closed in this approach due to design limitations. In this work, the air gaps can be closed to reduce optical losses, and simple parallel plate actuators allow for simple digital control of the switch. Also, the optical switch in this work provides broadband operation with an insertion loss of 4.45 dB – 6.64 dB over a 50 nm wavelength range across multiple samples. We obtained the switching time for the switching and gap closing actuators by performing time domain simulations with COMSOL Multiphysics. The switching actuator requires 50 μs to close completely whereas the gap closing actuator needs 100 μs as per our simulation results. Since the center switching channel relies only upon gap closing actuation for efficient coupling, the switching time for this channel will be 100 μs. The left and right switching channels can operate at 50 μs without the gap closing actuator. Combining gap closing actuation with either the left or right switching actuators will result in efficient optical coupling after 150 μs. Also, simulations including the effects of gravity were performed on our device model in COMSOL Multiphysics. This showed no impact of gravity upon the device structure. The high stiffness of our device due to the 59 μm Si thick device layer mitigates any impact of gravity upon our device. In addition to this, the electrostatic force generated during pull-in makes the structure very stable to g-forces and vibrations. The direct contact of the movable

structure and continuous use of the pull-in voltage to keep the switch in the required switching state anchor the structure as opposed to a free-standing structure that can be sensitive to vibrations. However, the optical performance of a switch can be sensitive to vibrations as they can impact the alignment between the fiber array and the grating couplers. We measured less thana 0.15 dB optical loss variation across 10 measurements in all switching positions for Sample 1. Furthermore, the 15 μm and 35 μm mechanical stoppers (see Figure 6.1(c) and 6.1(d)) ensure minimal device contact during actuation. We did not notice any stiction issues

during our testing for any of the samples. A comparison with the state-of-the-art SiN based optical switching solutions is presented in Table 6.3.

Table 6.3 Comparison of SiN based optical switches

Refer-ence	Switch type	Operation and Voltage (V)	Experi-mental wavelength range (nm)	Power required (mW)	Switch-ing time (µs)	Insert-ion loss (dB)
Briere et al. 2017	MEMS based crossbar switch	SOI based electrostatic actuation 180	1550	No DC power due to electrostatic actuation	300	12.2-14.8
Nielson et al. 2005	MEMS based wavelength selective switch using ring resonator	Aluminum based electrostatic actuation 30	1545-1585	0.0001	60	11-15
Jin et al. 2018	MEMS based switch using tunable ring resonator	PZT based piezoelectric actuation 16	1549.50-1551.50 Tuning range 10 nm	Less than $5e^{-5}$ and below 5V operation	1-10	NA
Dong et al. 2018	MEMS based optical resonance tuner	AlN based Piezoelectric actuation 60	1547.95-1550.35 Tuning range 20 pm	$3e^{-5}$	1	NA
Joo et al. 2018	2 x 2 Optical switch using tunable MZI	Thermal tuning -	1325.8 and 1550.8	55.6-64.4	17.25-17.48	0.23-0.48
Sun et al. 2019	4 x 4 Optical switch using tunable MZI	Thermal tuning -	1560-1600	19.98-125.29	24.5-30.5	5.7-7.2
This work	MEMS based 1 x 3 optical switch	SOI based electrostatic actuation 80-170	1530-1580	No DC power due to electrostatic actuation	50-150	4.45-6.64

6.7 Conclusion

A novel 1 × 3 planar MEMS optical switch with integrated SiN channel waveguides was presented. The challenges of integrating SiN waveguides with residual mechanical stress onto a MEMS switching platform were mitigated by using a thick silicon device layer. The design of serpentine springs for both the switching and gap closing actuators to minimize actuation voltages was also presented. The 1 × 3 optical switch was fabricated successfully and required a switching voltage of 170 V and a gap closing voltage of 80 V. No actuation is required to couple light into the center switching waveguide and it demonstrates an average optical loss of 4.64 dB across the 1530 nm to 1580 nm wavelength range with only the gap closing actuator activated. The left and right channels required actuation of the relevant switching actuator and the gap closing actuator and achieve an average optical loss of 5.38 dB and 5.83 dB across the same wavelength range.

The wide bandwidth of the proposed optical switch makes it a versatile device to enable reconfigurable SiN photonic circuits. For example, it can be integrated with high performance passive SiN optical filters (e.g., ring resonators, Bragg gratings and/or micro-disk resonators) to select wavelength channels or even an entire wavelength band inside an optical telecommunication network. The key advantage over existing SiN based wavelength channel selection systems will be low power operation, no thermal tuning, and a simple fabrication process that allows us to control dimensions for each output waveguide and optical filter. Furthermore, since the switch and filters can be manufactured at low cost at high volumes, these systems can make possible the deployment of wavelength selective devices, such as receivers, at large scale in access networks to increase their capacity. For instance, access networks based on the NG-PON2 standard require receivers able to select among a few channels (4 to 8) that could be implemented with this technology (Pinho et al., 2020). The experimental results presented in this work focused on the C-band of the telecommunication spectrum. This was because of the bandwidth limitation our SGCs. However, the switch is broadband and can work across the whole wavelength range for which the waveguides are

single mode and transparent. For the waveguide configuration used in the prototypes, this goes from 1100 nm up to 2200 nm. The demonstrated wavelength range of the switch in this work can be useful towards realization of a MEMS based tunable transceiver operational in the C-band of the telecommunication spectrum. Such a system can provide viable solutions towards building cost effective and energy efficient passive optical networks (Walker, 2000).

In the future, we aim to minimize fabrication variations and improve the device reliability through optimization of the MEMS design prior to fabrication. We also look towards improving the MEMS design further to provide larger displacement for the switching motion at a lower actuation voltage. Larger displacement of the switching actuator will allow to integrate more waveguides on the central platform, and hence, increase the number of channels. It can also enable greater degree of control and minimize optical losses due to misalignment between waveguides during digital switching.

CHAPTER 7

HYBRID MEMS ACTUATOR WITH 3 DEGREES-OF-FREEDOM FOR EFFICIENT PLANAR OPTICAL SWITCHING

Suraj Sharma[1], Seyedfakhreddin Nabavi[1], Almur Abdelkreem Saeed Rabih[1], Michaël Ménard[1], and Frederic Nabki[1]

[1]Department of Electrical Engineering, École de Technologie Supérieure, Montreal, Quebec H3C 1K3, Canada

Paper published in *Journal of Microelectromechanical Systems*, October 2023

Preface

In this chapter, a hybrid MEMS actuator with 3 degrees-of-freedom that integrates piezoelectric and electrostatic actuators for motion along three axes, is presented. A brief introduction about challenges in MEMS integration with SiN waveguides for optical switching is followed by a detailed description of the design methodology followed to realise the hybrid MEMS actuator described in this chapter. Details about key design choices made for the spring mechanism, in-plane electrostatic actuators, and out-of-plane piezoelectric actuators are presented as well. Details about the nuances of the microfabrication process used to implement this hybrid actuator are discussed with its current limitations. SEM micrograph analysis, and static and dynamic MEMS characterization results are included in this chapter. Key findings related to the use of electrostatic and piezoelectric actuators to compensate deformation in the MEMS platform due to residual stress caused by piezoelectric material deposition over suspended structure are describe here. The chapter concludes with future work recommendation to improve the device fabrication yield. The MEMS actuator prototype developed in this chapter is used for realizing a 1 x 5 SiN optical switch in the following chapter.

S.S. designed, simulated, and characterized the MEMS devices. S.N. and A.A.S.R. helped in device testing. M.M. and F.N. supervised the work presented in this chapter.

7.1 Abstract

This work demonstrates a hybrid MEMS actuator platform that combines electrostatic and piezoelectric actuators to displace a suspended MEMS platform along 3 degrees-of- freedom (DOF). The prototype MEMS actuator tested produces maximum displacements of 8.8 μm along the positive X-axis, and 8.5 μm along the negative X-axis, with digital control. Analog control produces maximum displacements of 5.9 μm along the positive X-axis, and 5.8 μm along the negative X-axis. It can also provide 2.2 μm of in-plane displacement along the negative Y-axis with analog control. The electrostatic actuator used for displacement along the negative Y-axis also compensates for any out-of-plane misalignment between the suspended MEMS platform and fixed silicon due to the significant residual stress caused by deposited piezoelectric material layers. In addition, up to 550 nm of misalignment compensation using the electro- static actuator before electrostatic pull-in is demonstrated. The piezoelectric actuator provides fine alignment capability with a maximum out-of-plane displacement of 200 nm and 100 nm with analog control along the positive and negative Z-axis, respectively. This hybrid MEMS actuator can be integrated with channel waveguides for efficient planar optical switching applications.

Keywords: 3-D MEMS, electrostatic devices, piezoelectric devices, hybrid actuators, microelectromechanical devices, micro actuators, PiezoMUMPs, photonic switching systems, silicon-on- insulator technology

7.2 Introduction

Micromachined actuators find extensive applications in the field of silicon (Si) photonics. Integration of microelectromechanical system (MEMS) devices with photonics components reduces power consumption and provides broadband operation (Seok et al., 2016; Akihama et

al., 2011). Over the years, numerous 3 degrees-of-freedom (DOF) MEMS actuators have been developed for optical switching applications. These devices were designed for beam steering using a reflective surface coating on MEMS structures to create 3D optical switching solutions that are based on free space optics (Kim et al., 2003; Afsharipour et al., 2018; Li et al., 2019). These MEMS optical switching devices are large and require complex packaging (An et al., 2021; Gu-Stoppel et al., 2020). Optical waveguides can be used for light confinement and to manage optical losses (Seok et al., 2016). Most planar optical switches using waveguides were developed based on optical filters, such as ring resonators (Kondo et al., 2020) and Mach-Zehnder interferometers (Qiu et al., 2021). These optical filters often require thermal tuning for switching, which consumes a significant amount of power to generate heat. Optical tuning of such filters through MEMS integration is possible, although limited by narrow operational bandwidth (Tian at al., 2018; Sattari et al., 2019). The integration of channel waveguides with MEMS structures allows for planar optical switching with low power consumption and wider operational bandwidth, which is useful for telecommunication applications (Seok et al., 2016; Sharma et al., 2022).

Most integrated optical switches are based on Si waveguides constructed with the device layer of silicon-on-insulator (SOI) wafers. It is worth mentioning that Si waveguides are more sensitive to width variations in comparison to silicon nitride (SiN) waveguides (Barwicz & Haus, 2005). Moreover, SiN can provide wide operating bandwidths with better optical performance around 1550 nm for telecommunication applications in comparison to Si (Blumenthal et al., 2018). However, the integration of SiN waveguides on SOI-based MEMS is challenging due to residual mechanical residual stress in the layers forming the waveguides. The suspended portion of the device can deform under stress, which can cause misalignments between the suspended and fixed optical components (Sharma et al., 2022). Such misalignments can lead to important optical losses. In this context, there is a need for planar MEMS switching solutions with multiple DOF for efficient planar optical switching. In the last decades, electrostatic and electrothermal actuators have been developed for planar optical switching solutions (Peters & Tichem, 2016; Du et al., 2016). Electrostatic actuators consume

less power than electrothermal ones and do not generate heat. Most electrostatic actuators described in the literature were developed based on SOI, and can only provide in-plane motion (Sharma et al., 2022; Takabayashi et al., 2021; Briere et al., 2017). In contrast, piezoelectric actuation can offer out-of-plane motion with low power consumption when piezoelectric thin films are added to SOI devices (Koh et al., 2010).

This work demonstrates a hybrid MEMS actuator capable of motion in the 3 DOF required for efficient planar optical switching. The MEMS actuator controls the position of a moveable platform made in the device layer of a SOI wafer, which could support SiN waveguides. In this regard, two sets of parallel plate electrostatic actuators provide in-plane motion to move the MEMS platform along the positive and negative X-axis, and the negative Y-axis. Aluminum nitride (AlN) based piezoelectric actuators provide out-of-plane displacement along the positive and negative Z-axis. The device was fabricated using the commercial PiezoMUMPs process avail- able through MEMSCAP (Cowen et al., 2014). The MEMS device presented in this work is an improvement over our previous translational MEMS platform by enabling enhanced displacement along the X-axis and an additional out-of-plane motion capability (Sharma et al., 2019). Moreover, it can be applied in the future to our previously reported integrated optical switches to increase the number of outputs and reduce the alignment-induced losses (Sharma et al., 2022; Sharma et al., 2022).

A detailed overview of the design methodology followed during the development of the hybrid MEMS actuator is presented in section 7.3. Section 7.4 presents the microfabrication process and imaging results of the fabricated device. The experimental results are presented and discussed in section 7.5 followed by a conclusion in section 7.6.

7.3 Design

The target application for the actuation system described below is the implementation of a 1 × 5 optical switch, where an input optical waveguide can be aligned with any of 5 output waveguides. The optical components of the switch can be formed using SiN waveguides

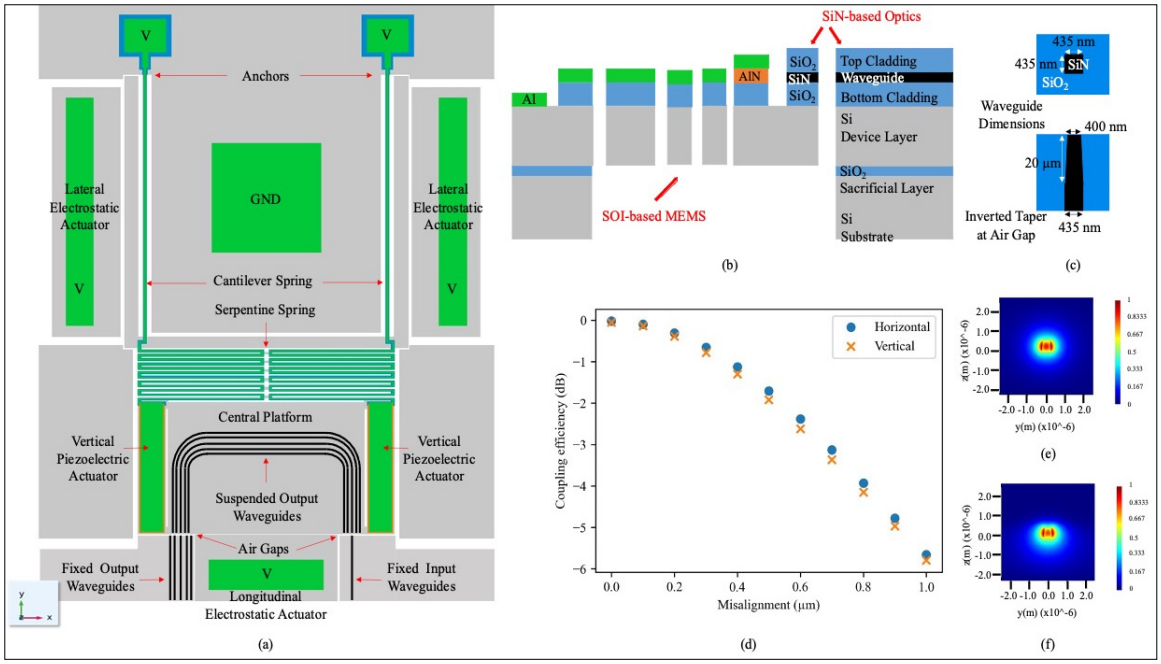

Figure 7.1 (a) Schematic of the proposed hybrid MEMS device with electrostatic and piezoelectric actuators in a 1x 5 optical switch configuration. (b) Cross sectional view of the proposed integration of the SOI-based hybrid actuator with SiN waveguides. (c) Waveguide dimensions, including the inverted taper, used in optical simulations to evaluate transmission. (d) 3D FDTD simulation results at a wavelength of 1550nm showing the impact of horizontal and vertical misalignments on the transmission efficiency between two perfectly butt-coupled SiN waveguides. Intensity profile of the guided transverse electric mode. (e) inside the 435nm wide SiN waveguide and (f) at the end of the 400nm wide inverted taper

whereas the SOI-based MEMS can provide the switching mechanism to connect to the different outputs (Sharma et al., 2022). Thus, in this work the actuator prototype is developed to address the challenges associated with the integration of SiN waveguides on SOI-based MEMS.

A schematic of the proposed actuator in a 1 × 5 optical switch configuration is shown in Figure 7.1(a). As per Figure 7.1(a), the motion of the suspended MEMS platform along the X-axis provided by a lateral electrostatic actuator can be used for switching optical signals from a single input waveguide to different output waveguides on the suspended platform. The

cantilever spring system enables this X-axis motion of the central platform. The displacement of the platform along the negative Y-axis enabled by a longitudinal electrostatic actuator can close the two air gaps between the suspended and fixed waveguides to minimize the optical losses. The serpentine spring system enables this Y-axis motion of the central platform. This optical switching concept has been reported in our recent work where a MEMS-based 1 × 5 optical switch has been demonstrated with an optical loss between 2.2 dB and 5.39 dB (Sharma et al., 2022). However, intrinsic residual stress caused by the deposition of the optical material layers over the suspended Si layer causes misalignment between the suspended and fixed waveguides. Therefore, the addition of piezoelectric actuation, as demonstrated in this paper, provides additional capability to finely align in the Z-axis the suspended waveguides with the fixed ones. Such reduction in misalignment can significantly increase the optical signal transmission efficiency.

The SOI-based MEMS can be integrated with AlN piezoelectric actuators and SiN-based optics as per the cross-sectional view of the material stack shown in Figure 7.1(b). The dimensions of the waveguides with inverted tapers used to lower optical loss in the coupling region between suspended and fixed waveguides are shown in Figure 7.1(c). A similar integration strategy with output SiN waveguides separated by 3.6 μm was used for a 1 × 3 SiN optical switch (Sharma et al., 2022). Thus, an approximate displacement of ±7.2 μm should enable a 1 × 5 optical switching configuration. Horizontal and vertical misalignments between two butt-coupled waveguides can lead to optical losses. Three-dimensional finite-difference time- domain (FDTD) simulation results at a wavelength of 1550 nm for misalignment up to 1 μm is shown in Figure 7.1(d) along with the intensity profile of the guided transverse electric (TE) mode in the SiN waveguide (Figure 7.1(e)) and at the end of the inverted taper (Figure 7.1(f)). The optical simulations were performed with Ansys Lumerical. Only the MEMS actuators of the device proposed in Figure 7.1(a) were fabricated and tested in this work. The integration within a switch is targeted as future work.

A structural illustration of the hybrid mems actuator fabricated is shown in Figure 7.2. With reference to Figure 7.2, the central platform is connected through a serpentine spring structure to the support beam. This support beam consists of two lateral electrostatic actuators on the opposite sides of the platform. These two actuators are capable of providing bi-directional lateral motion of the central platform along the x-axis. Mechanical stoppers are also designed with gap smaller than that of the electrostatic actuator gap to prevent any device shorting during pull-in. The entire MEMS device is anchored through two cantilever spring beams connected to the support beam. Aluminum (Al) and insulating silicon oxide (SiO2) layers for the piezoelectric actuators were designed over the cantilever beams and the serpentine spring. These layers are necessary to actuate the vertical piezoelectric actuators on the opposite edges of the central platform. These two actuators can be biased simultaneously to provide vertical out-of-plane displacement of the central platform along the z-axis. The lower edge of the platform also acts as a parallel plate actuator for the longitudinal electrostatic actuator. This actuator is responsible for longitudinal in-plane motion of the platform along the negative y-axis. All three actuators described provide motion along 3-DOF to the central platform which

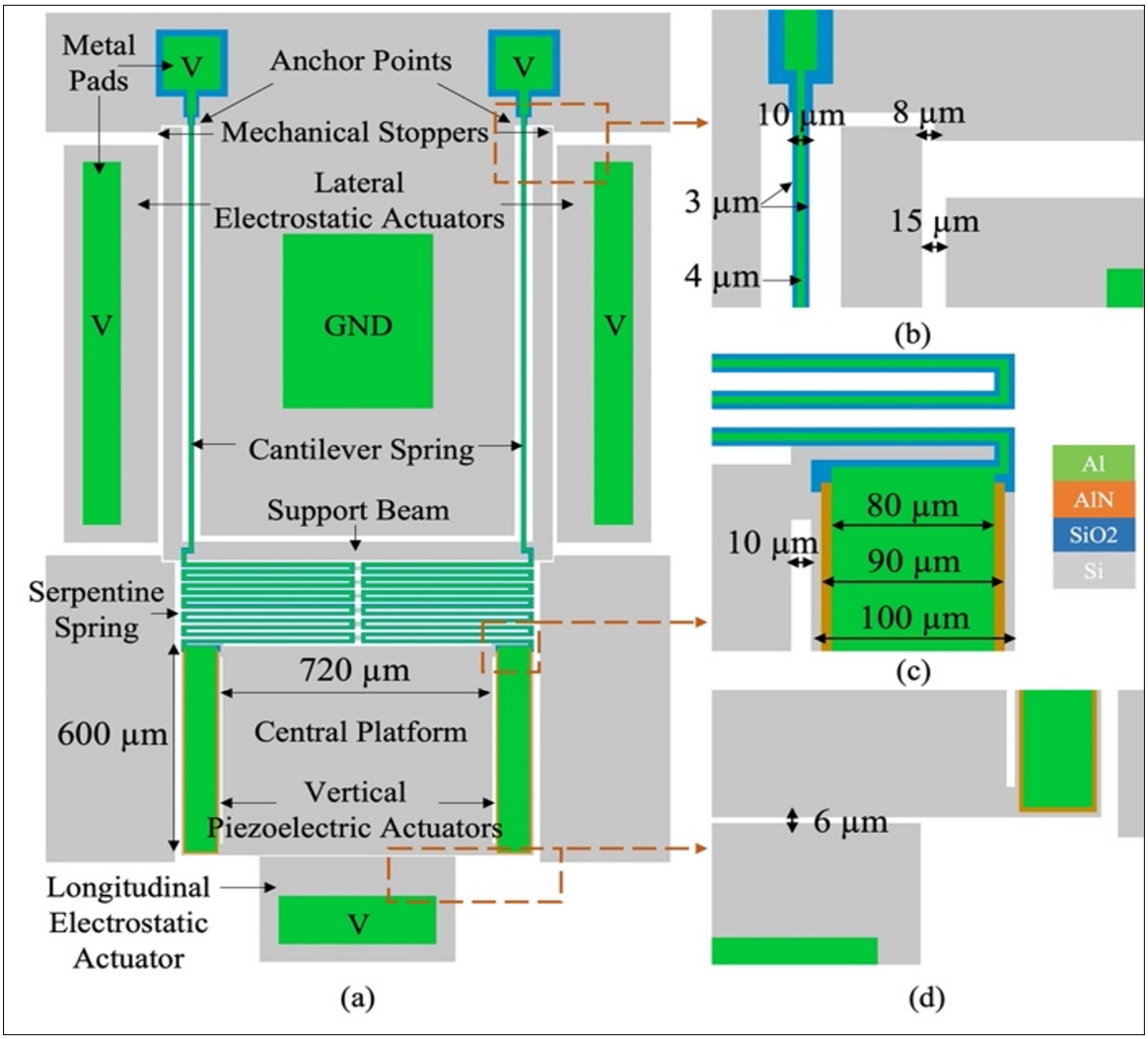

Figure 7.2 (a) Structural illustration of the hybrid MEMS actuator with detailed dimensions for the (b) lateral electrostatic actuator, (c) vertical piezoelectric actuator, and (d) longitudinal electrostatic actuator

is 720 µm wide and 600 µm long. As suggested in Figure 7.1, in the proposed configuration, it can accommodate five SiN channel waveguides with at least a 3.5 µm spacing between them and a 100 µm bending radii (Sharma et al., 2022). The critical dimensions of all the actuators and spring systems are shown in Figure 7.2. The spring and actuator configurations are two important aspects of any mems. In this section, the spring design and overall configuration of the actuator used to provide motion along 3 axes, namely the X-, Y- and Z-axis, are discussed.

The actuator performance was investigated with finite element modelling (FEM) simulations with the COMSOL Multiphysics software.

7.3.1 Springs

Cantilever springs, where the suspended silicon beams are anchored at one end, have been used mostly for creating out- of-plane MEMS actuators (Saba et al., 2015; Mousavi et al., 2022). Doubly clamped spring structures with anchor points on opposite ends of suspended silicon beams have been used in translational MEMS actuator devices to achieve uniform displacement. A symmetric spring design provides stable translational motion; however, it requires thin and long silicon beams with low stiffness to minimize the actuation voltage (Sharma et al., 2019). This can increase the overall size of the device. In this work, we developed a unique MEMS structure capable of large uniform in-plane translational motion using a cantilever spring (Rivlin et al., 2015).

The doubly clamped and cantilever springs were modelled for lateral stiffness analysis in COMSOL, and the overall device footprint of the simulated model was kept fixed at 2.10 mm in width and 1.04 mm in length. A schematic of the cantilever spring structure is shown in Figure 7.3(a). Each spring beam is 10 μm wide and 1200 μm long. The doubly clamped spring structure is shown in Figure 7.3(b). Each spring beam is 10 μm wide and 1025 μm long. A mechanical force (Fs) of 10 μN was applied on the suspended Si arm connected to the spring structure in the lateral negative X-axis direction as shown in Figure 7.3(a) and Figure 7.3(b). The suspended MEMS were anchored at the locations shown in Figure 7.2. The simulated displacement (x) obtained was used to predict displacement uniformity and estimate the spring constant (k) of the structure using the force-displacement equation (Kaajakari, 2009):

$$k = \frac{F_s}{x} \tag{7.1}$$

Both spring types show uniform lateral displacement of the central platform. The cantilever spring provided 6.66 µm of lateral displacement whereas the doubly clamped spring reached only 2.02 µm, as shown in Figure 7.3(a) and Figure 7.3(b), respectively. The calculated spring constant for the cantilever and doubly clamped spring are 1.50 N/m and 4.95 N/m respectively. Since the cantilever spring has a lower stiffness while still allowing for uniform lateral displacement, it will help reduce the actuation voltage.

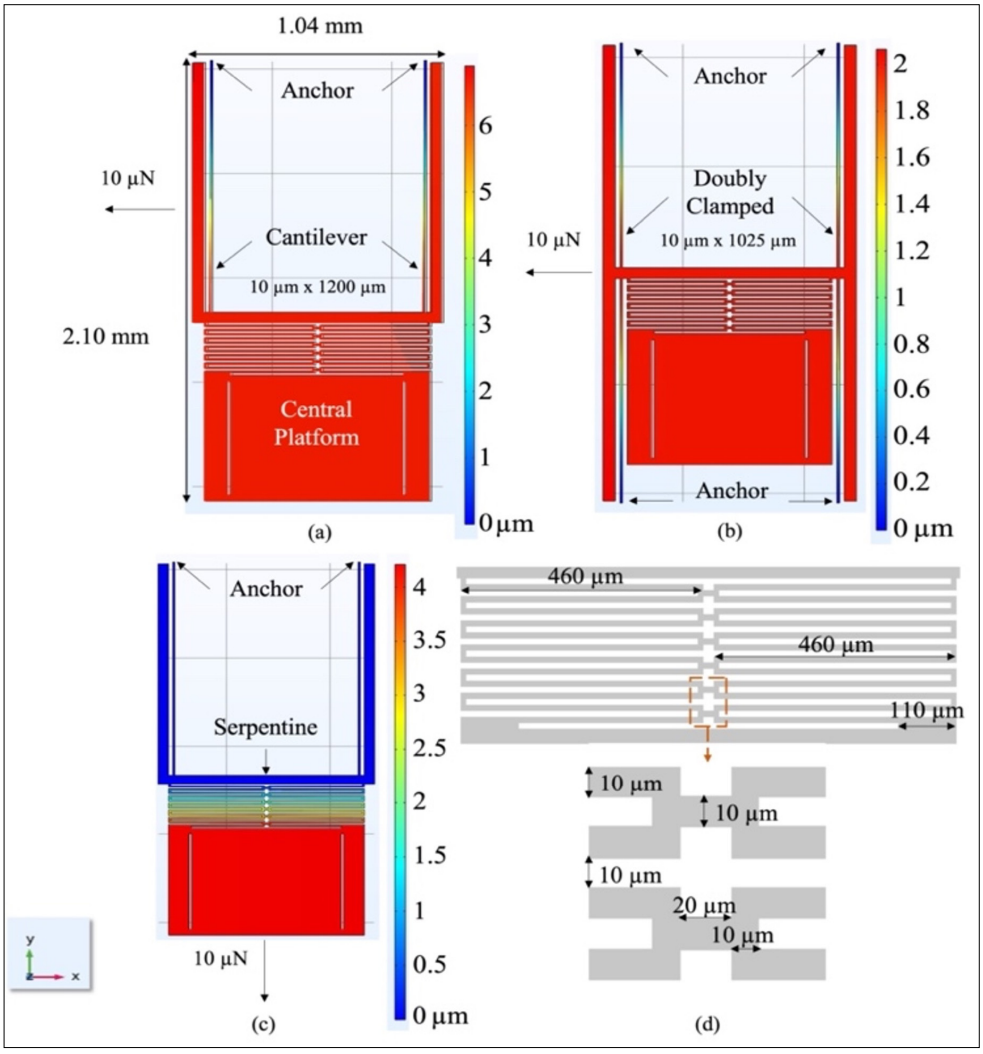

Figure 7.3 FEM simulation results to estimate spring stiffness and displacement uniformity for (a) cantilever spring, (b) doubly clamped spring, and (c) serpentine spring with (d) detailed serpentine spring dimensions

The serpentine spring connecting the central platform to the lateral switching actuators is shown in Figure 7.3(c) along with its dimensions in Figure 7.3(d). It is based on our previous work to obtain bi-axial motion of the suspended platform for efficient planar optical switching (Sharma et al., 2019). The serpentine spring system in which each spring beam is 10 μm wide by 460 μm long was modelled in COMSOL to estimate the spring constant and verify the capability of the structure to provide a uniform displacement. The structure showed 4.19 μm of displacement when a 10 μN of force was applied in the negative Y-axis direction. The spring constant obtained from mechanical simulations is thus 2.38 N/m. Uniform displacement of the platform was also observed with no effect on the cantilever spring system, as shown in Figure 7.3(c). Our simulation results showed that the cantilever and serpentine spring systems can be combined for bi-axial motion of the central platform providing 2 DOF.

7.3.2 In-Plane Electrostatic Actuators

In our previous work, we found that comb drive-based actuators fabricated using the PiezoMUMPs technology were susceptible to rotation upon actuation. This was due to variations in the fabricated dimensions of the comb drive (Cowen et al., 2014; Sharma et al., 2019). Therefore, a parallel plate-based actuation approach was used for the rotation-free lateral motion of the central platform along the X and Y axes. In this work, we also use parallel plate actuation for the in-plane bi-axial motion of the central platform. However, the displacement generated is increased through a larger length and gap of the lateral actuator from 486 μm to 1140 μm, and from 4 μm to 15 μm, respectively, in comparison with (Sharma et al., 2019). These modified actuator parameters enable a large displacement range with analog control over the lateral motion of the platform along the X-axis before electrostatic pull-in occurs. Such a configuration allows us to have analog control over the alignment of SiN waveguides when they are integrated with the platform (Sharma et al., 2022). Mechanical stoppers with a gap of 8 μm, which is smaller than the initial actuator gap, prevent device shorting during electrostatic pull- in. They also allow large digital displacement of the platform during lateral actuation, which is required to increase the number of waveguide channels (Sharma et al., 2022). The

longitudinal actuator allows a motion along the negative Y-axis. Simulation results for the lateral and longitudinal actuators at 50 V are presented in Figure 7.4(a) and 7.4(b), respectively. The simulated models showed uniform central platform displacements of 0.39 µm and 0.85 µm for the lateral and longitudinal electrostatic actuator, respectively.

The pull-in voltage (Vp) and maximum displacement (d_p) before the pull-in of the parallel plate

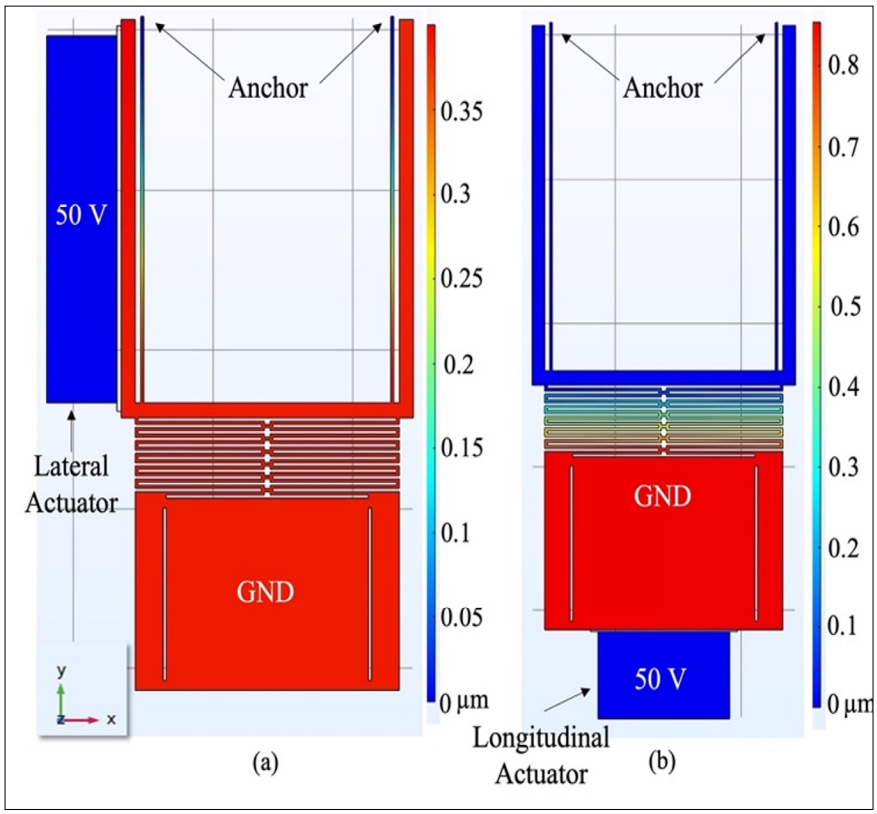

Figure 7.4 FEM simulation results for (a) the lateral and (b) longitudinal electrostatic actuators at 50 V

electrostatic actuators can be estimated as follows (Kaajakari, 2009):

$$V_p = \sqrt{\frac{8kg^3}{27\varepsilon_o A}} \tag{7.2}$$

$$d_p = \frac{g}{3} \tag{7.3}$$

where k is the spring constant, g is the initial transducer gap between the actuator plates, A is the overlap area between actuator plates and εo denotes the permittivity of air. The actuator dimensions and the main analytical results using the equations described above are presented in Table 7.1. The pull-in voltage for the longitudinal actuator is larger due to the increased stiffness of the serpentine spring. The width of each Si beam had to be set to 10 μm to accommodate the aluminum (Al) metal layer required for the out-of-plane piezoelectric actuation that will be discussed later. These limitations are set by the PiezoMUMPs fabrication technology (Cowen et al., 2014).

Table 7.1 Electrostatic actuator and spring parameters

Critical Parameter	**Actuator Type**	
	Lateral	**Longitudinal**
Length (μm)	1140	520
Gap (μm)	15	6
Thickness (μm)	10	10
Spring constant (N/m)	1.50	2.38
Maximum analog displacement (μm)	5	2
Pull-in voltage (V)	150	80

7.3.3 Out-of-Plane Piezoelectric Actuator

The PiezoMUMPs fabrication technology enables the integration of a piezoelectric layer of AlN onto SOI-based MEMS. This fabrication process enables the creation of piezoelectric actuators where an electric field generated across the piezoelectric layer can produce a transverse force, as shown in Figure 7.5(a). The Al metal layer fabricated on top of the AlN piezoelectric layer and the Si device layer below it represents the electrodes necessary to

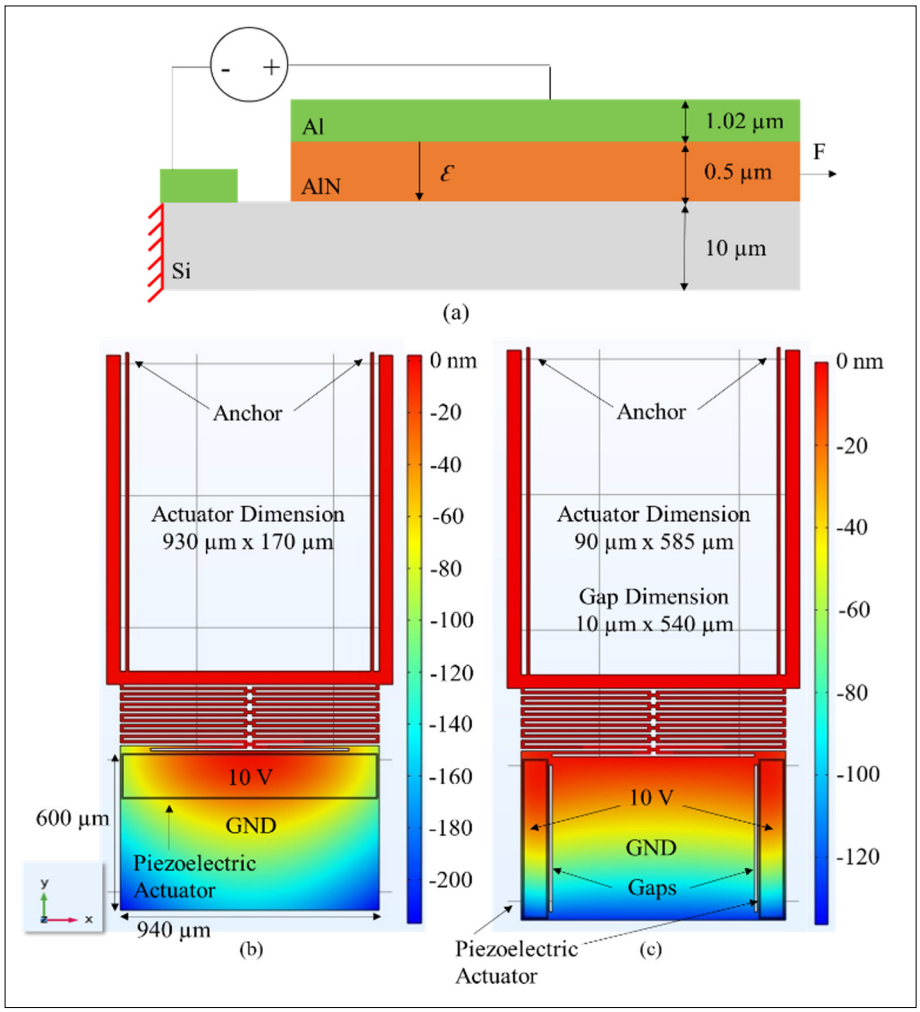

Figure 7.5 (a) Piezoelectric actuator layers with the thicknesses as per the PiezoMUMPs technology, and FEM simulation results for piezoelectric actuators with actuator dimensions in (b) parallel and (c) perpendicular configuration at 10 V

generate the electric field. We leverage the generated transverse piezoelectric force to displace the central platform in the vertical out-of-plane direction along the Z-axis.

The force (Fp) generated by the piezoelectric actuator can be calculated using the following (Kaajakari, 2009):

$$F_p = \frac{d_{31} A V_{in}}{h} \tag{7.4}$$

where A is the area of the actuator, Vin is the input voltage, d31 is the piezoelectric coefficient, and h is the thickness of the piezoelectric layer. The actuator can be configured on the platform in parallel or in perpendicular to the serpentine spring as outlined by the rectangular regions in Figure 7.5(b) and 7.5(c), respectively.

The center region of the platform provides space for the integration of optical waveguides for switching applications, as discussed further in (Sharma et al., 2022). FEM simulation results showed that the parallel configuration produces higher displacement along the platform edge in comparison to the perpendicular configuration. Displacement color maps obtained from the FEM simulations for both configurations are shown in Figure 7.5 along with the actuator and platform dimensions. However, a non-uniform displacement was produced by the actuator in the parallel configuration, which is undesirable for optical switching applications. The corners of the edge of the platform (i.e., bottom of Figure 7.5) moved vertically out-of-plane by 217 nm in the negative Z-axis direction whereas the center of the same edge moved by only 158 nm, at 10 V. This variation across the edge of the platform could be because the serpentine spring is connected to the outer edges of the platform. The two identical perpendicular actuators produced a uniform 128 nm displacement of the lower edge of the platform along the negative Z-axis at 10 V. It should be noted that we created gaps in the Si device layer next to piezoelectric actuators in the perpendicular configuration. This was done to increase the vertical displacement by approximately 20 nm at 10 V in comparison to a piezoelectric actuator design without these gaps. The dimensions of these gaps are also presented in Figure 7.5(c).

7.4 Microfabrication

The device under test (DUT) was fabricated using the PiezoMUMPs technology (Cowen et al., 2014). A simplified version of the process flow is shown in Figure 6.6. A SOI wafer with a 10 μm Si device layer, a 1 μm buried oxide (BOX) layer, and a 400 μm handle layer is used for

this fabrication process. A bottom oxide layer is already present on the starting wafer as shown in Figure 7.6(a). A 200 nm thermal oxide layer is grown on top of the Si device layer. The layer is then patterned and etched using reactive ion etching (RIE) as shown in Figure 7.6(b). This SiO2 layer acts like an insulating layer for the subsequent 0.5 μm thick AlN piezo layer deposited and patterned through wet etching as shown in Figure 7.6(c). A 1 μm Al metal layer is deposited and patterned through a lift off process to form metal bonding pads for actuators as shown in Figure 7.6(d). During this step, Al metal pads can be patterned over the insulating thermal oxide layer, AlN piezo layer and Si device layer. The Si device layer is then patterned and etched using photolithography and precise deep reactive ion etching (DRIE), respectively. The front side of the wafer is then protected with a polyimide layer during the subsequent RIE

of the bottom oxide and DRIE of the Si substrate. A cross section view of fabricated device after protective layer removal is shown in Figure 7.6(e).

The PiezoMUMPs process has limitations that impacted our design. Although the fabrication technology allows at least 2 μm wide suspended Si structures, such Si beams can only be up to 100 μm long when the structure is anchored at only one end. For the fabrication of longer suspended structures anchored at one end, Si beams with a width of more than 6 μm are required. In the hybrid actuator, we need to have the Al layer over the suspended Si spring beams to actuate the AlN piezoelectric actuators on the central platform. As per the design

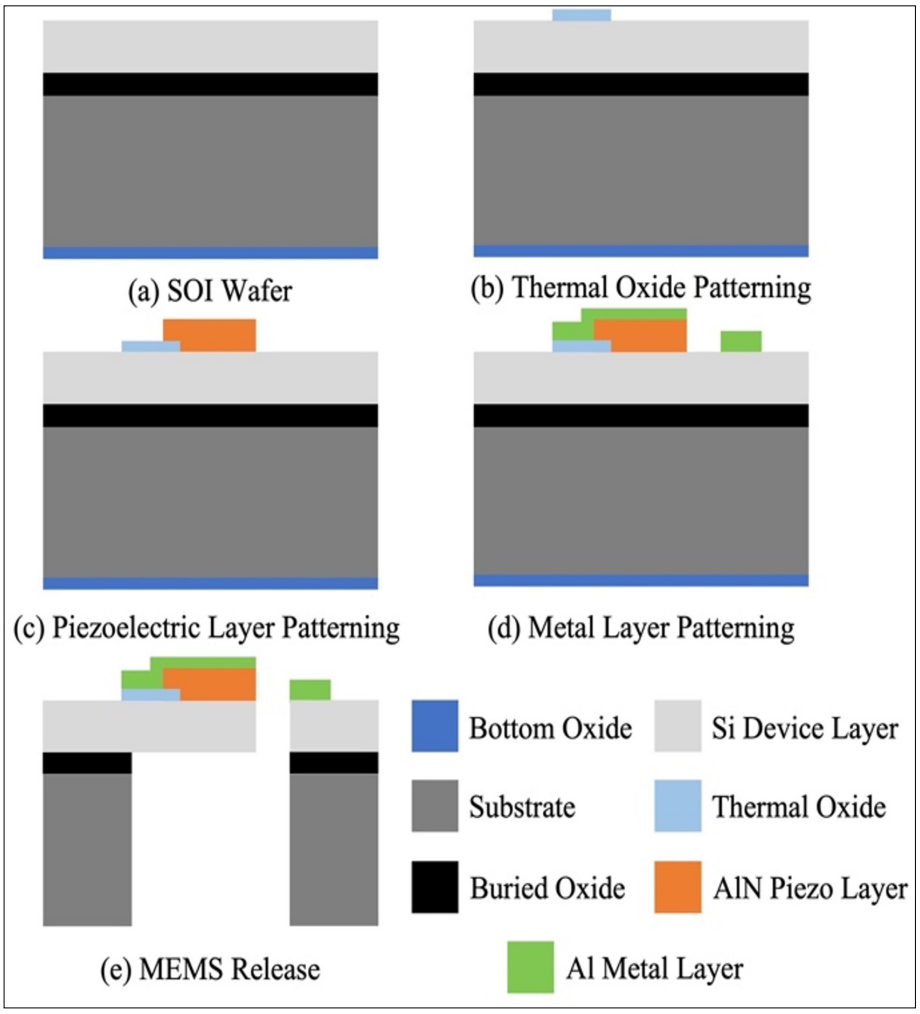

Figure 7.6 Simplified version of the PiezoMUMPs process flow

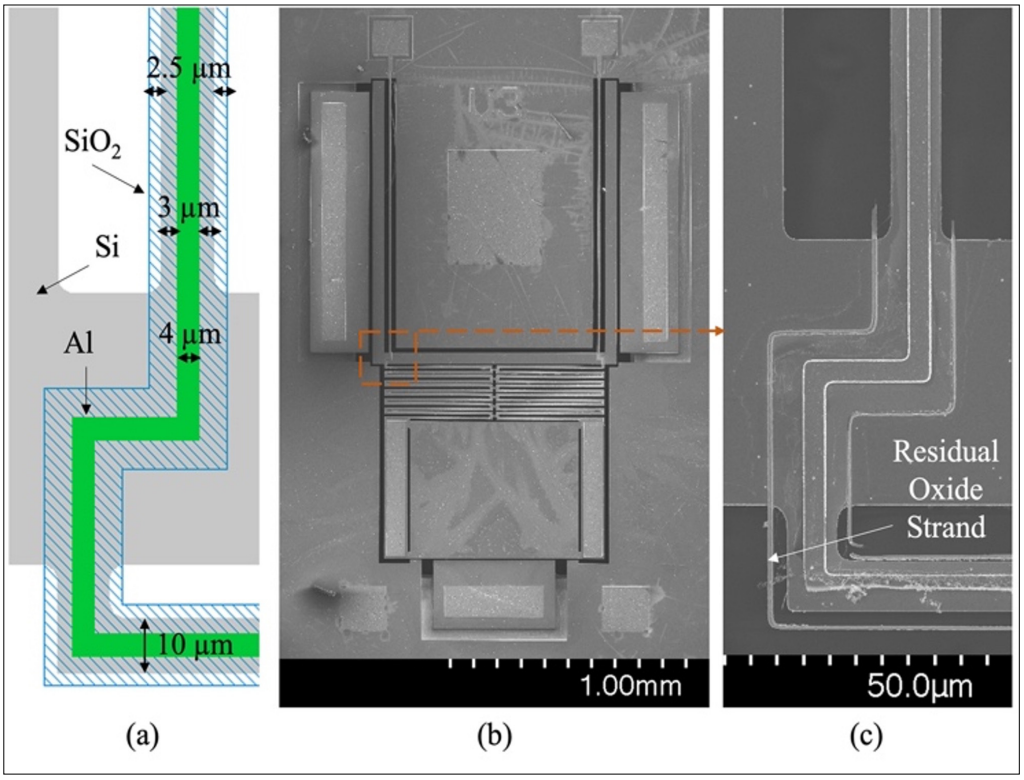

Figure 7.7 (a) Detailed layout with the dimensions used for the spring with an aluminum interconnect, (b) SEM image of the fabricated MEMS device, and (c) residual oxide strands along the Si spring beams

rules, this requires Si borders of at least 3 µm on each side of the Al layer. The Al layer over the spring structure also needs to be electrically insulated with a SiO2 layer underneath it to prevent device shorting during piezoelectric actuation. This requires a 15 µm wide SiO2 layer with 2.5 µm overhangs outside of the Si device layer. The details of this structure are shown in Figure 7.7(a). It should be noted that since the thickness of the SiO2 layer is only 200 nm, it should be etched away during the DRIE step of the underlying Si device layer. A SEM image of the fabricated device is shown in Figure 7.7(b). While most the SiO2 next to the suspended

Si beams was etched away during the fabrication process, some remaining SiO2 strands were observed close to the suspended Si beams in the fabricated device, as shown in Figure 7.7(c).

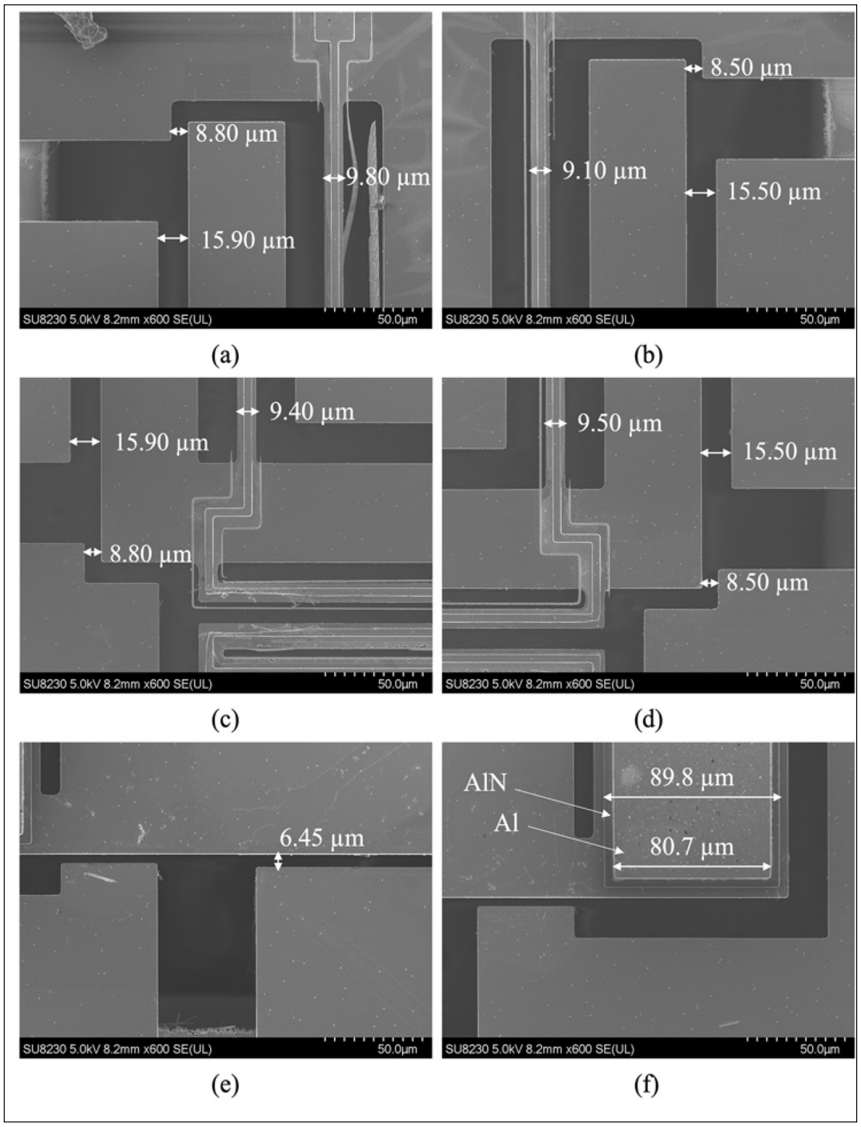

Figure 7.8 Dimensions obtained from SEM images for (a) the top left lateral actuator and stopper, (b) the top right lateral actuator and stopper, (c) the bottom left lateral actuator and stopper, (d) the bottom left lateral actuator and stopper, (e) the longitudinal actuator, and (f) the piezoelectric actuator

Slight over etch of the Si layer resulted in variations of the actuator and stopper gap dimensions. It also affected the Si spring beam width. Variations were also observed in the deposition of the Al layer over the spring structure. It can be assumed that increasing the width of the Si beam to accommodate the SiO2 overhangs would improve the fabrication quality of the Al layer over the suspended beams but would increase the actuation voltages required. Measured dimensions of the device as fabricated are shown in Figure 7.8. Variations measured in the fabricated device for key design parameters are summarized in Table 7.2. The effect of

Table 7.2 Design vs fabricated key dimensions

Design Parameter	**Dimension (µm)**		
	Design	**Fab**	**Variation**
Lateral actuator gap	15	15.5 to 15.9	0.5 to 0.9
Lateral stopper gap	8	8.5 to 8.8	0.5 to 0.8
Longitudinal actuator gap	6	6.45	0.45
Piezoelectric actuator width	90	89.8	-0.2
Spring beam width	10	9.1 to 9.8	-0.1 to -0.8

these variations over the operational voltages for electrostatic pull-in and piezoelectric actuation are comprehensively discussed in the next section.

7.5 Measurement Results

7.5.1 Static Response

The DUT was wire bonded to a custom printed circuit board (PCB) for actuation characterization. The test setup included three DC voltage supplies and a laser confocal 3-D microscope (LEXT4100 by Olympus) as shown in Figure 7.9(a). The DUT was connected to the voltage sources according to the circuit diagram shown in Figure 7.9(b). Figure 7.9(c) shows the wirebonded device. In this regard, DC voltage source 1 was connected simultaneously to the two metal pads of the vertical piezoelectric actuators. DC voltage source

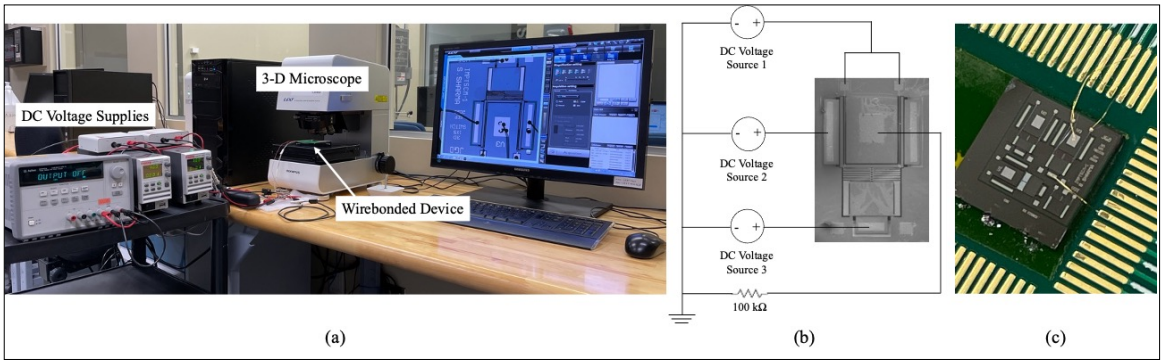

Figure 7.9 (a) Test setup for actuation characterization, (b) schematic of the test circuit used for actuation, and (c) wirebonded device

2 was connected to the lateral electrostatic actuator under test. DC voltage source 3 was connected to the longitudinal electrostatic actuator. The lateral, longitudinal, and vertical actuators were actuated separately three times. High-resolution images were taken for each actuation voltage applied using the 3-D microscope. The microscope software was used to analyze the images taken and the displacement obtained was measured at each actuation voltage applied.

7.5.1.1 Static Response of the Electrostatic Actuators

The lateral electrostatic actuator could displace the central platform in-plane along both the positive and negative X-axis. The actuation voltage was applied at 10 V intervals up to 90 V after which the interval was reduced to 1 V as the voltage was increased until electrostatic pull-in occurred. The average displacement obtained from three measurements are shown in Figure 7.10.

In continuous (i.e., analog) bias mode, the actuators produced in-plane displacement up to 11.7 μm at 90 V along the X-axis in both directions. Increasing the voltage further resulted in electrostatic pull-in with 17.5 um in-plane displacement, as limited by the mechanical stoppers in the non-continuous (i.e., digital) mode. Pull-in of the lateral actuator was observed at 102 V

along the negative X-axis and at 101 V along the positive X-axis. This asymmetric result can be explained by the fabricated dimensions of the device presented in section 7.4 (see Table 7.2). The right lateral actuator had an actuator gap of 15.9 μm and a mechanical stopper gap of 8.80 μm (see Figure 7.8(a)). The left lateral actuator had an actuator gap of 15.5 μm and mechanical stopper gap of 8.50 μm (see Figure 7.8(b)). This 300 nm variation causes a 1 V difference in the pull-in voltages between actuators. Also, the 300 nm variation in the mechanical stopper gap changes the maximum displacement obtained after electrostatic pull-in. The experimental pull-in voltage shown in Figure 7.10 was significantly less than the one predicted by the simulation curve for the device model simulated in COMSOL Multi- physics according to the final dimensions of the fabricated actuator. This variation could be due to fabrication variations in the suspended Si beams shown in section 7.4 (see Figure 7.8). Such variations could lead to early onset of the nonlinear behavior of the cantilever-shaped spring system that could not be replicated with the symmetrical dimensions used in the numerical

simulation. It is worth pointing out that in the simulation model, an average of the observed variations in the dimensions of the manufactured Si beams is considered.

The longitudinal electrostatic actuator could move the central platform in-plane along the negative Y-axis. The actuation voltage was applied at 10 V intervals up to 70 V. Two more data points were measured at 75 V and 78 V before electrostatic pull-in occurred. A maximum displacement of 2.2 µm was observed at an actuation voltage of 78 V. The average displacement obtained from three measurements are shown in Figure 7.11. The simulation

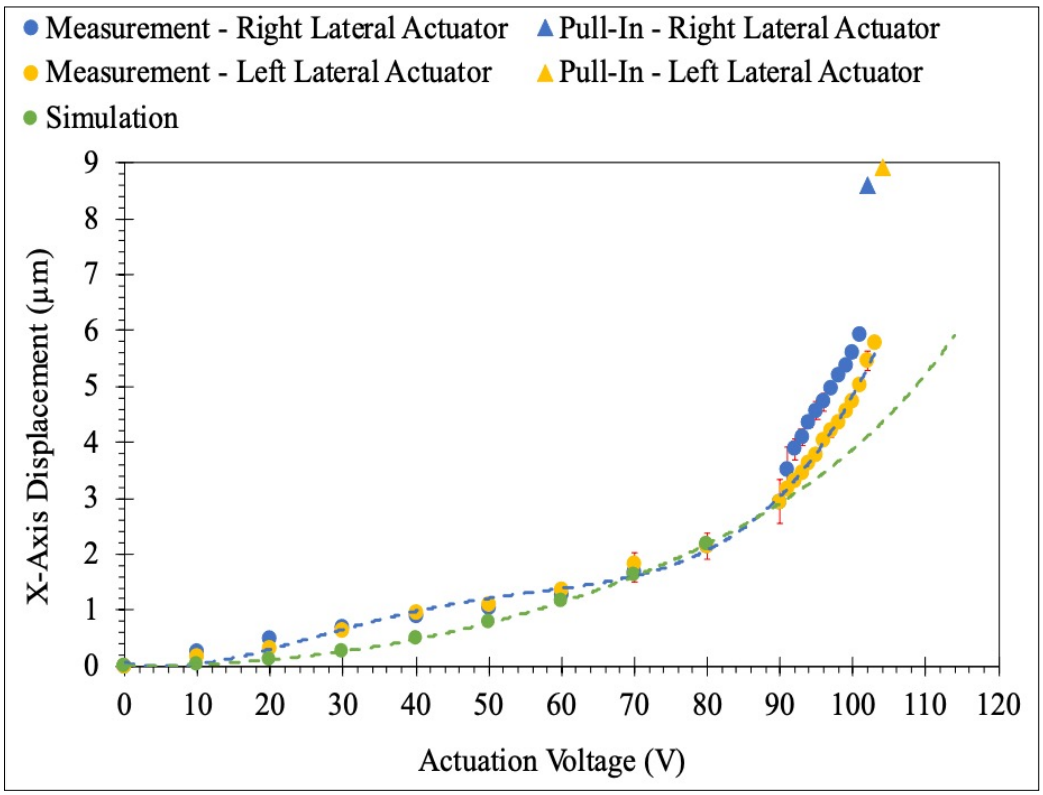

Figure 7.10 Experimental and simulated actuation curves for the lateral electrostatic actuators. The dotted lines are a polynomial fit to the experimental and simulation data points

model with the fabricated device dimensions shows an actuation behavior that compares well with the experimental measurements.

It should be pointed out that the discrepancy observed between the FEM simulation results and the measurement results could be due to the Si sidewall etch profile which leads to a narrower

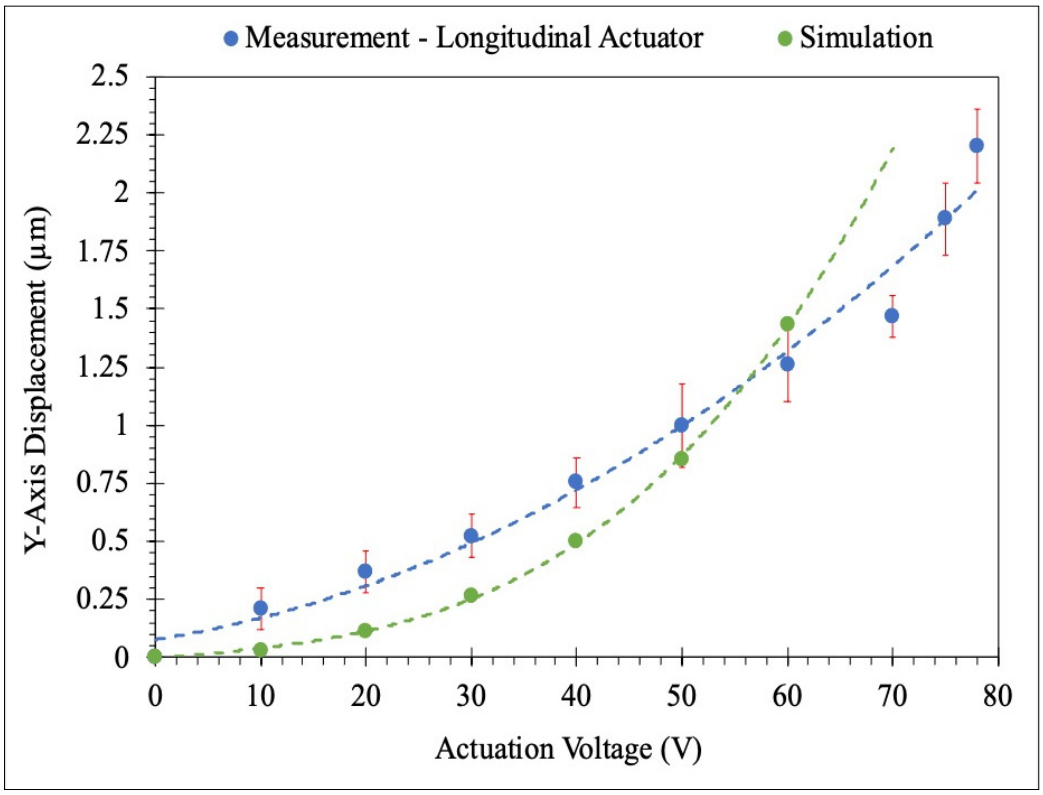

Figure 7.11 Experimental and simulated actuation curves for the longitudinal electrostatic actuator. The dotted lines are a polynomial fit to the data points

beam width at the bottom in comparison to the top view presented in the SEM imaging results earlier. Such variations would impact the Si beam stiffness and affect the measurement results in comparison to the FEM simulations. Variations in width along the length of the fabricated Si beam can also be a factor (see Figure 7.8). Since the etch profile of Si could not be measured, this variation was not considered in the FEM model. The nonlinear behavior in the initial measurement values of the lateral actuator at up to 80 V could be due to a nonlinear spring response from the cantilever-shaped spring system used for the lateral actuator. Above 80 V,

the nonlinear spring counteracts the nonlinear electrostatic force to produce large linear displacement before pull- in (Rivlin et al., 2015). Since the longitudinal actuator uses a serpentine spring system, it does not exhibit this behavior and is impacted solely by the nonlinear electrostatic actuation force.

The fabrication of the metal, oxide and piezoelectric layers over the suspended Si layer also

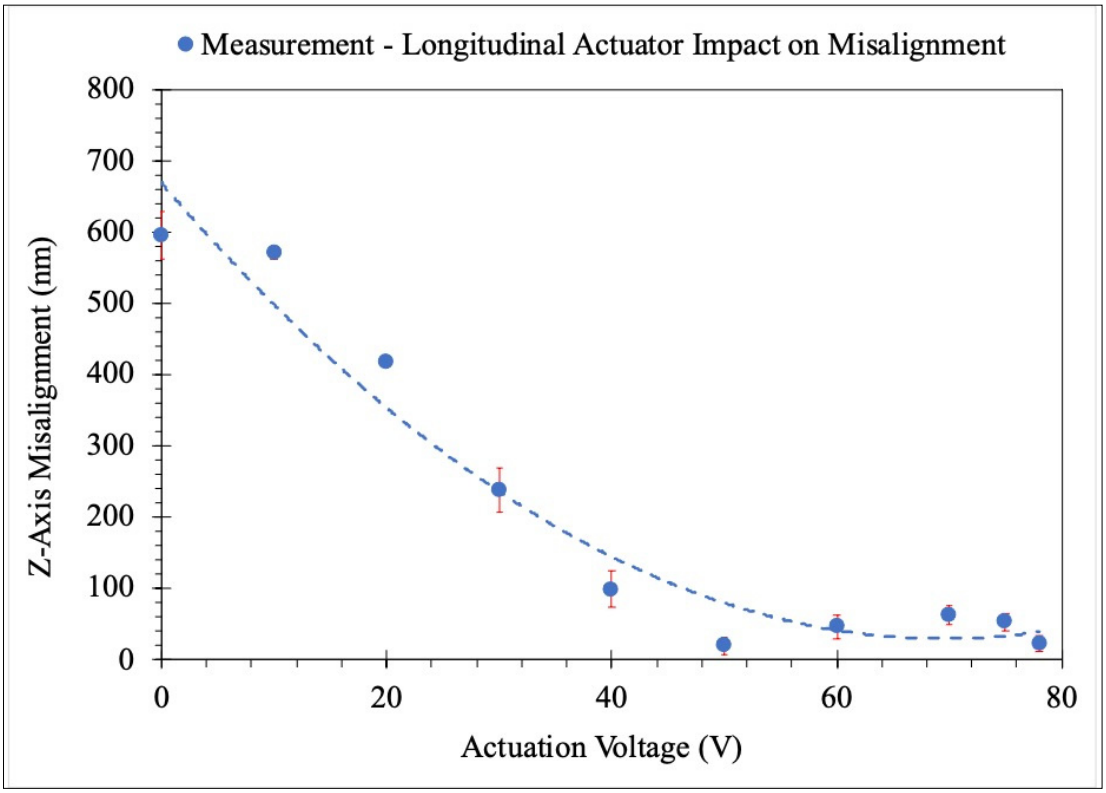

Figure 7.12 Experimental measurements of the vertical misalignment between the fixed Si device layer and the suspended platform edge as a function of the longitudinal electrostatic actuator voltage. The dotted line is a polynomial fit to the experimental data points

resulted in residual stress in the central platform (Dutta & Pandey, 2021). This residual stress caused a positive 600 nm out-of-plane displacement of the edge of the central platform next to the longitudinal actuator. This residual stress deformation along the positive Z-axis was measured using the 3-D microscope shown in the test setup in Figure 7.9. The longitudinal

electrostatic actuator also helps in eliminating this deformation along the platform edge upon actuation. In this regard, the electrostatic force generated by the longitudinal actuator pulls down the platform edge during motion along the negative Y-axis. The misalignment measured between the fixed edge and suspended MEMS platform is reduced to 50 nm or less beyond a 50 V actuation voltage for the longitudinal actuator. The vertical misalignment reduction obtained by exciting the longitudinal actuator is shown in Figure 7.12.

7.5.1.2 Static Response of the Piezoelectric Actuator

The piezoelectric actuator was tested to determine its ability to produce out-of-plane displacement along the Z-axis of the central platform. The actuation voltage was increased in 2 V increments from 0 V to 10 V. A similar characterization was performed with reversed polarity from 0 V to – 10 V with −2 V increments. The out-of-plane displacement of the edge of the central platform next to the longitudinal actuator was measured using the 3-D microscope at each actuation voltage. These results are shown in Figure 7.13.

The platform edge can be displaced out-of-plane by 200 nm along the positive Z-axis with – 10 V and by 100 nm along the negative Z-Axis with 10 V. Thus, this actuator can provide a total of 300 nm of out-of-plane displacement using only piezoelectric actuation, at a relatively low input voltage, i.e., 10 V. The variation in the positive and negative displacement is due to the initial residual stress that causes an intrinsic out-of-plane deformation along the positive Z-axis. Importantly, this actuation range is sufficient to mitigate the residual misalignment of 50 nm in the Z-axis in order to ensure optimal optical alignment after residual stress compensation by the longitudinal actuator, as previously discussed.

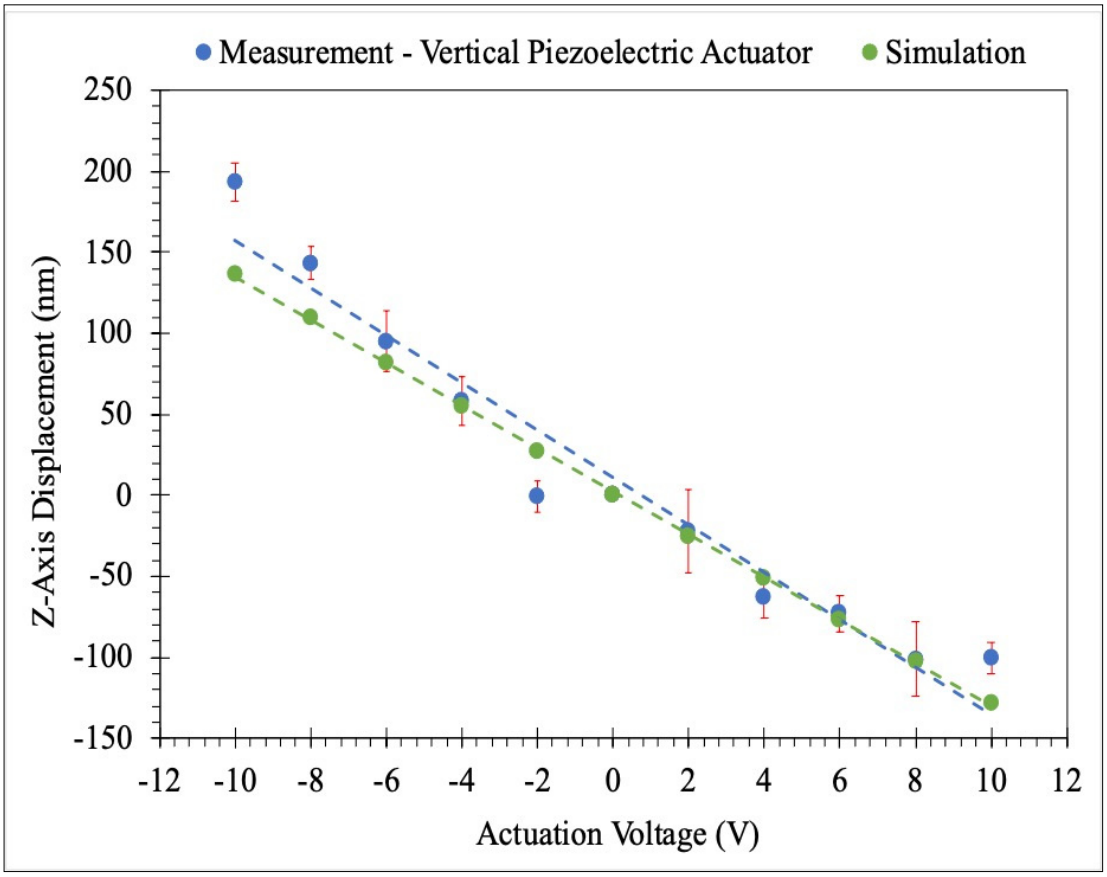

Figure 7.13 Experimental and simulated vertical displacement generated by the piezoelectric actuator for different actuation voltages. The dotted lines are a linear fit to the data points

7.5.2 Dynamic Response

In order to survey the dynamic behavior of the actuator, a laser doppler vibrometer (Polytec OFV-534) was used. This was only possible for the out-of-plane actuator due to the capabilities of the vibrometer. In this regard, the piezoelectric actuator was excited with an AC signal at an amplitude of 10 V and a variable frequency ranging from 100 Hz to 10 kHz supplied by a function generator (Agilent 33220a). The laser from the vibrometer was focused on the center of the central platform. Figure 7.14(a) shows the measured frequency response of the actuator. With reference to Figure 7.14(a), the first two resonant frequencies of the device are observed

at 1.8 kHz and 7.5 kHz. COMSOL Multiphysics was used to graphically represent the mode shapes of the actuator at these frequencies. The first and second resonant modes of the actuator are shown in Figure 7.14(b) and 7.14(c), respectively. It can be clearly seen that the actuator can produce a larger out-of-plane deflection when excited at a frequency close to its second

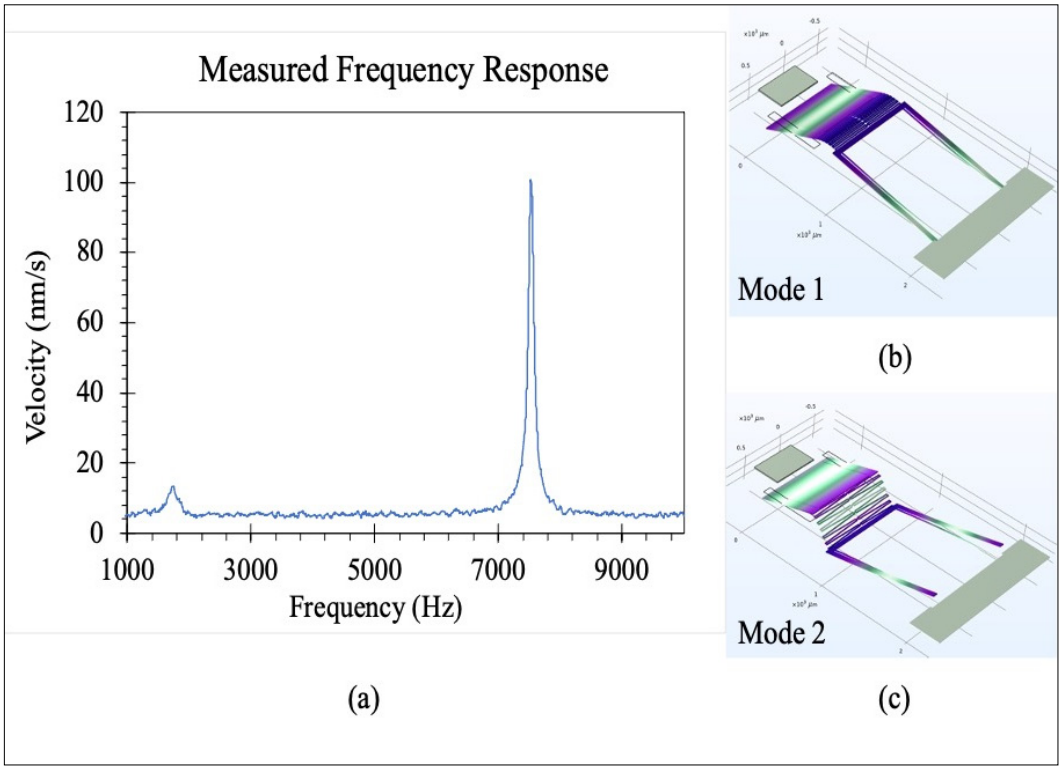

Figure 7.14 (a) Measured frequency response of the device, and simulated (b) first and (c) second resonant modes of the actuator

resonant mode, i.e., 7.5 kHz. This is mainly due to the expansion of the serpentine spring at this frequency.

7.5.3 Discussion

In this work, we were able to successfully integrate electrostatic and piezoelectric actuators to create a 3 DOF MEMS actuator that is suited to implement an integrated optical switch design with moveable waveguides. The electrostatic actuators were successfully tested to produce in-

plane motion of the suspended MEMS platform. The lateral electrostatic actuators produce a total of 11.7 μm of displacement with analog control. This analog control over the lateral actuator allows accurate positioning of the waveguides in the envisioned integrated optical switch. It will allow for fine alignment between suspended and fixed waveguides in the optical switch and hence minimize optical losses due to misalignment between two butt-coupled waveguides (Sharma et al., 2022). As shown in the alignment tolerance simulations in section 7.3 (see Figure 7.1(d)), a 1 μm horizontal or vertical misalignment can lead to a reduction of approximately 6 dB in coupling efficiency between two butt-coupled SiN waveguides. Just before pull-in, the displacement of the lateral actuator is 59 nm/V along the positive X-axis and 57 nm/V along the negative X-axis. Therefore, a controller that can provide a voltage with a precision of less than 1 V can ensure that losses due to lateral misalignment remain below 10% for the channels with analog control. The mechanical stoppers enable 17.5 μm of total displacement with digital control. This digital displacement will allow the addition of two switching channels, as shown in our previous work, to increase the channel count in the optical switch (Sharma et al., 2022). However, the precision of the alignment for these additional channels will depend upon the fabrication accuracy of the mechanical stopper gap. The fabricated mechanical stopper gap should match the fabricated lateral gap between the outermost output waveguide and the center waveguide in the rest state. This will ensure that after pull-in the input waveguide aligns perfectly with the outermost waveguide.

In our previous work, a fabrication variation of 430 nm in the mechanical stopper gap led to an additional 2.01 dB of loss in comparison to the channel with analog control (Sharma et al., 2022). The longitudinal electrostatic actuator produces 2.2 μm of total displacement of the central platform with analog control. This moveable platform can be integrated with SiN waveguides to create an optical switch and the transmission efficiency of the switch can be maximized by closing the air gap between suspended and fixed waveguides. The integration of SiN waveguides over suspended Si MEMS layers can lead to residual stress-induced deformations, which result in vertical misalignment causing optical losses (Sharma et al., 2022; Sharma et al., 2022). However, the longitudinal electrostatic actuator can compensate part of

this misalignment. It was shown that the intrinsic 600 nm out-of- plane misalignment can be reduced to 50 nm by activating the electrostatic longitudinal actuator. It should be noted that the initial misalignment due to residual stress limits the actuation performance of the longitudinal actuator. Absence of any initial misalignment would lead to better actuator performance with the required longitudinal displacement achieved at a lower actuation voltage. The vertical piezoelectric actuator provides an additional approach that can be used to finely align the movable waveguides to the fixed ones vertically with a total possible displacement of 300 nm measured at the edge of the platform. Such capability can significantly improve the performance of SiN waveguide-based MEMS optical switching system since a 500 nm misalignment between suspended and fixed waveguides can lead to a 10 % reduction in transmission efficiency (Sharma et al., 2019). It should be noted that the introduction of the AlN piezoelectric layer along with the required SiO2 insulating and Al metal layers over the suspended Si MEMS layer leads to vertical misalignment after the release of the device.

Nevertheless, the integration of SiN waveguides over suspended Si MEMS structures also causes significant vertical misalignments and as such requires a means of compensation.

The results of this work are now compared with state-of- the-art MEMS actuators with multi degrees of freedom in Table 7.3. The displacement values achieved are listed for analog control of the actuators and for digital control in parenthesis. While piezoelectric (Chen & Tian, 2021) and electrostatic (Ba-Tis & Ben-Mrad, 2015) actuators have been used in the past to achieve 2 degrees of freedom, their sizes are relatively large, and the second degree of freedom comes from rotational motion of the suspended platform. More recent work has been done to reduce device size significantly (Kim & Gorman, 2022; Barrett et al., 2019). A miniaturized MEMS based nano-positioner that utilizes low power electrostatic actuators can provide very small

Table 7.3 State of the art comparison

Reference	Actuation Method	Size (mm^2)	Voltage (V)	Displacement (µm)
Chen et al. 2021	Piezoelectric	309.76	90 90 90	47.2 in +Z 0.56º in θ 0.58º in Φ
Ba-Tis et al. 2015	Electrostatic	16	80 78 78	28 in +Z 0.78 in θ 0.78 in Φ
Kim et al. 2022	Electrostatic	1.5	100 100 100	0.2 in +X 0.4 in +Y 6 in +Z
Barrett et al. 2019	Electrostatic Electrothermal	6.25	130 130 130 130 50	7.1 in +X 7.1 in -X 7.1 in +Y 7.1 in -Y 39.5 in +Z
This Work	Electrostatic Piezoelectric	4.32	100 (101) 101 (102) 78 -10 10	5.9 (8.6) in +X 5.8 (8.9) in -X 2.2 in -Y 0.2 in +Z 0.1 in -Z

displacements between 0.2 µm and 0.4 µm along the lateral directions (Kim & Gorman, 2022). A hybrid actuator with a relatively compact size that uses electrostatic and electrothermal

actuation mechanisms to produce a large displacement of ±7.1 μm in-plane was reported in (Barrett et al., 2019). It can also generate 39.5 μm of motion along the Z-axis. However, electrothermal actuation consumes a lot of power, which makes the device inefficient compared to the structures reported here. In our work, we use electrostatic and piezoelectric actuation techniques with relatively low power consumption for all 3 axes of motion with a relatively compact device size of 4.32 mm2.

7.6 Conclusion

We demonstrated a 3 DOF hybrid MEMS actuator which includes electrostatic and piezoelectric actuators. The device was fabricated using a commercially available pro- cess (PiezoMUMPs). The actuators can move the suspended platform up to 17.3 μm laterally, 2.2 μm longitudinally, and 293 nm vertically. The lateral motion can be used for optical switching between channel waveguides in an integrated micro- opto-electro-mechanical system (MOEMS) switch design. The longitudinal actuator is designed to provide the motion required to minimize optical losses by reducing the air gaps between suspended and fixed waveguides. The longitudinal and vertical actuators can also minimize the misalignment between the suspended platform and the fixed Si device layer, thereby eliminating the impact of the residual stress above the platform from films deposited onto it. To the authors best knowledge, this is the first demonstration of a hybrid MEMS actuator with integrated electrostatic and piezoelectric actuators with such motional capabilities.

In the future, we intend to fabricate devices with wider Si beams in the spring structure to resolve the SiO2 over- hang issue and enhance yield. The MEMS actuator will also be integrated with SiN waveguides for efficient optical switching solutions with high potential in telecommunication applications.

CHAPTER 8

AN INTEGRATED 1 X 5 MEMS SILICON NITRIDE PHOTONICS SWITCH

Suraj Sharma[1], Niharika Kohli[1,2], Michaël Ménard[1], and Frederic Nabki[1]

[1]Department of Electrical Engineering, École de Technologie Supérieure, Montreal, Quebec H3C 1K3, Canada

[2]CMC Microsystems, Montreal, Quebec H3C 6M8, Canada

Paper accepted for publication in *Journal of Lightwave Technology*, March 2024

Preface

In this chapter, a 1 x 5 optical switch that integrates SiN waveguides with SOI-based translational MEMS platform (like the electrostatic actuator prototype presented in the previous chapter) is presented. A brief introduction about recent development in MEMS integration with SiN optics is followed by the operating principle description for the optical switch demonstrated in this chapter. Key design choices made to enhance the actuator displacement required for analog control over multiple waveguide channels in comparison to our previous 1 x 3 SiN photonics switch are described here. The microfabrication process used, SEM micrograph analysis, and MEMS and optical characterization results for multiple samples are included in this chapter. Key findings related to microfabrication impact upon device performance are also discussed in detail in this chapter. The chapter concludes with future work recommendations to improve MEMS actuator design to for analog control over multiple switching channels, and with potential piezoelectric actuation integration for vertical misalignment compensation.

S.S. designed, simulated, and characterized the MEMS devices along with complete optical characterization. N.K. designed the optical components required in this chapter. M.M. and F.N. supervised the work presented in this chapter.

8.1 Abstract

We demonstrate a microelectromechanical system (MEMS) based 1 x 5 optical switch with integrated silicon nitride channel waveguides. Our MEMS actuator allows analog control for fine alignment in three switching positions. The other two switching positions rely upon electrostatic pull-in phenomena for digital switching. The samples tested demonstrate the broadband capability of the optical switch over the wavelength range of 1540 nm to 1625 nm. A minimum average insertion loss of 2.2 dB and a maximum average insertion loss of 7.5 dB was recorded for these devices in different switching positions. A custom microfabrication process developed by AEPONYX Inc was used to fabricate the devices.

Keywords: MEMS, optics, photonics, silicon nitride, optical switch

8.2 Introduction

Lower scattering losses due to sidewall roughness (Shaw et al., 2005), less sensitivity to width variations and temperature (Blumenthal et al., 2018), and broadband operation (Micó et al., 2018) has increased interest in silicon nitride (SiN) photonics for telecommunication applications. SiN photonics systems have been proposed for optical switching in next generation passive optical networks 2 (NG-PON2) with 4 to 8 switching channels (Iovanna et al., 2020; Beyranvand et al., 2019). Conventional SiN photonics switching involves thermal tuning of optical components such as Mach-Zehnder interferometers (MZI) (Lin et al., 2022) and ring resonators (Liu et al., 2017). This switching mechanism consumes power and limits bandwidth. A few low-power electrostatically actuated MEMS integrated with SiN waveguides have been demonstrated recently. A MEMS cantilever-based direction coupler was integrated with SiN waveguides for single-photon detection (Gyger et al., 2021). MEMS integration with SiN to form suspended slot waveguides that can be moved to generate an optical phase tuning range of 13π has been demonstrated recently (Grottke et al., 2021). Similarly, a MEMS microbridge that can weakly interact with the evanescent field of a SiN

waveguide has been used to tune the effective index and act as a phase shifter in an MZI (Pruessner et al., 2016). A wavelength selective optical switch operating over a broadband wavelength range has been demonstrated by integrating a suspended MEMS bridge with an SiN-based ring resonator (Nielson et al., 2005). However, only a few truly broadband optical switching solutions that integrated MEMS with SiN photonics have been developed (Brière et al., 2017; Barazani et al., 2023; Swain et al., 2023). MEMS based optical switching has been extensively used in silicon (Si) photonics (Han et al., 2018; Sattari et al., 2021; Dobbelaere et al., 2002; Takahashi et al., 2008). The integration of Si-based waveguides with SOI-based MEMS requires trade-offs between the optical and MEMS components of the integrated device. This is because the thickness of the device layer of the silicon-on-insulator (SOI) will impact the specifications of the MEMS and optical components since this layer is used to implement both. Integration of SiN-based waveguides with SOI-based MEMS provides independent control over the dimensions of the optical and mechanical components. This capability helps to optimize performance, adding to the inherent advantages of SiN photonics technology.

In this work, we improve upon our previous work on MEMS based planar optical switching with integrated SiN waveguides (Sharma et al., 2022). In our previous work, we demonstrated digitally controlled switching in a 1 x 3 configuration. The transmission efficiency in this system was strongly affected by fabrication variations. In this work, we report on a new approach for a 1 x 5 switch (Sharma et al., 2022) using the same fabrication technology as our previous work that uses cavity silicon-on-insulator (C-SOI) wafers with a predefined cavity size of 1400 µm by 625 µm. Our new optical switch demonstrates analog control over three switching positions for efficient transmission between input and output waveguides. This control allows lower optical losses in comparison to our previous work. The two additional switching positions, which are at the extremes of the displacement range provided by the symmetric switching actuators use digital switching, completing the 1 x 5 switching configuration. Our switch has an operational bandwidth of 85 nm between 1540 nm and 1625

nm. This is also an improvement over our previous 1 x 3 SiN optical switch that had an operational wavelength range of 50 nm between 1530 nm and 1580 nm (Sharma et al., 2022).

The operating principle of the 1 x 5 optical switch is explained in section 8.3. The microfabrication process used is briefly discussed in section 8.4 along with scanning electron microscope (SEM) image characterization results. Mechanical and optical characterization results are presented in section 8.5 followed by discussion and a comparison with the state-of-the-art in section 8.6. The conclusion summarizes the contributions from this work and proposes future improvements.

8.3 Operating Principle

Our 1 x 5 optical switch uses low power electrostatic actuation for switching between output SiN channel waveguides. The device consists of a suspended Si platform of 600 μm by 200 μm. SiN channel waveguides with a core of 435 nm by 435 nm and SiO2 cladding are fabricated on top of the suspended platform and fixed Si, as shown in Figure 8.1. The waveguide platform is connected through a serpentine spring structure and a support beam to two switching (SW) actuators that are on opposite sides of the platform. The left switching actuator (LSW) can move the platform to the left upon actuation as per the top view of the optical switch design shown in Figure 8.1(a). The right switching actuator (RSW) can displace the platform to the right upon actuation. The two-single beam springs used for the switching motion allow large displacements in comparison to our previous work, which included four serpentine spring structures for a similar switching motion (Sharma et al., 2022). This large displacement allows us to include five output waveguides with a separation of 4 μm between the centers of the waveguide cores to realize a 1 x 5 optical switch. The fabrication of the MEMS requires releasing the suspended structure during fabrication to enable it to move. This design limitation leads to two air gaps between suspended and fixed waveguides. A third electrostatic actuator uses the lower edge of the platform as an actuator plate to generate an electrostatic force to displace the platform in the downward direction as per the top view shown

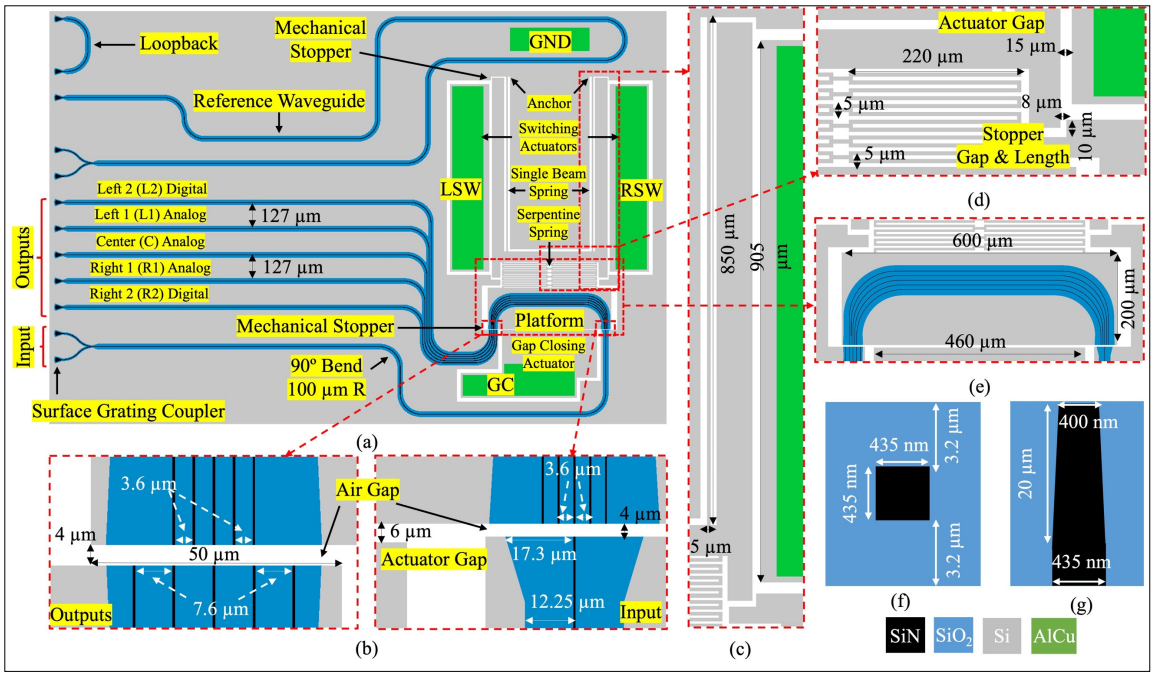

Figure 8.1 (a) Schematic of the integrated 1 x 5 MEMS silicon nitride photonics switch with reference waveguide and loopback structures. (b) Critical spacing dimensions for the interface between the suspended and fixed waveguides on the input and output side of the platform. The insets also show dimensions for the air gap between the suspended and fixed waveguides, between the platform and gap closing actuator, and the mechanical stopper length for the gap closing actuator. (c) Single beam spring and switching actuator dimensions. (d) Serpentine spring, switching actuator gap, and mechanical stopper dimensions. (e) Suspended waveguide platform dimensions along with the length of the gap closing actuator. (f) Waveguide core and cladding thickness. (g) Inverted taper dimensions for the waveguide used at the interface between the suspended and fixed waveguides

in Figure 8.1. This movement of the platform allows to close the two air gaps between the suspended and fixed waveguides as demonstrated in (Sharma et al., 2022). A detailed schematic of the optical switch and its critical dimensions are shown in Figure 8.1.

Surface grating couplers (SGC) are designed to couple light from a fiber array into the input waveguide. The input waveguide is aligned to the center waveguide on the suspended platform by default. When all actuators are at 0 V, the input optical signal is transmitted through the center (C) switching waveguide and coupled into the fiber array through the SGC at the end of

the C output waveguide. Similar SGCs are used for each output waveguide. The switching (SW) actuators have an initial actuator gap of 15 µm. This actuator gap should allow a maximum displacement of 5 µm before electrostatic pull-in since the maximum displacement by parallel plate electrostatic actuators is 1/3rd of the initial actuator gap (Kaajakari, 2009). Since the gap between adjacent waveguide cores is 4 µm, the switching actuators can provide the displacement necessary for fine alignment to the left 1 (L1) and right 1 (R1) switching positions. These actuators can also be used for alignment to the C switching position, enabling fine alignment capability to three switching positions. As shown in Figure 8.1(d), mechanical stoppers are designed with an 8 µm spacing to prevent any device shorting during the pull-in state. These mechanical stoppers allow placement of two more switching positions, left 2 (L2) and right 2 (R2). As the device stops when reaching the mechanical stopper, the input waveguide is aligned to the L2 or R2 output waveguides depending upon the actuator used for switching. This completes the 1 x 5 switching configuration.

The gap closing (GC) actuator can be actuated in any of the five switching positions to close the two air gaps between the suspended and fixed waveguides to improve the transmission of the optical signal. The GC actuator has an initial gap of 6 µm by design. This allows 2 µm of analog displacement before electrostatic pull-in. The initial air gap between the suspended and fixed waveguides is 4 µm, as per the requirements of the fabrication technology of AEPONYX Inc. Therefore, the GC actuator also relies upon the pull-in effect for closing the two air gaps where the interface between suspended and fixed waveguides acts as a mechanical stopper to prevent any device shorting. The LSW and RSW actuators are designed to provide up to 5 µm of displacement at 90 V before electrostatic pull-in, while the mechanical stoppers provide a

Table 8.1 Critical Actuator Design Parameters

Actuator Type	**Dimensions (µm)**	**Pull-In Voltage (V)**	**Maximum Analog Displacement (µm)**	**Maximum Digital Displacement (µm)**
Switching (SW)	Length: 905 Initial gap: 15	90	5	8
Gap closing (GC)	Length: 460 Initial gap: 6	72	2	4

maximum switching displacement of 8 µm on each side after pull-in. The GC actuator is designed to work at 72 V with electrostatic pull-in. These actuation voltages and displacements were obtained through static structural simulations of the device models in COMSOL Multiphysics v5.6. Critical actuator parameters and results obtained from simulations are summarized in Table 8.1.

SiN channel waveguides with a core of 435 nm x 435 nm and 3.2 µm-thick top and bottom SiO2 claddings are used for SiN-based optics, as shown in the cross-sectional view of the waveguide in Figure 8.1(f). Figure 8.1(g) also shows the inverted taper dimensions used to minimize optical losses between suspended and fixed waveguides. The gaps between adjacent waveguides in different parts of the device are shown in Figure 8.1(a) and 8.1(b). The bending

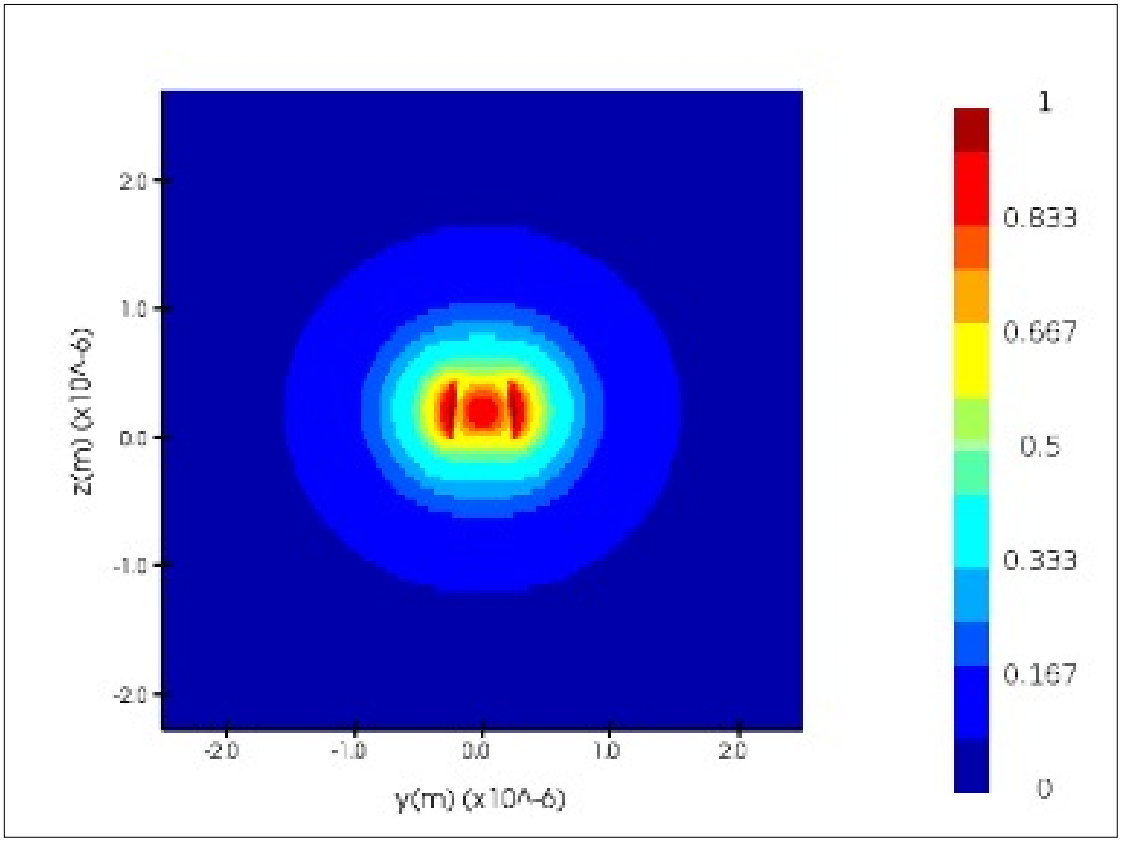

Figure 8.2 The mode profile (i.e., magnitude of the electric field) for the fundamental TE mode is shown in the figure. For the waveguide with width 435 nm, thickness 435 nm and sidewall angle 86°, the waveguide is single-mode with one TE (neff,TE = 1.508) and TM (neff,TM = 1.509) mode at a wavelength of 1.581µm

radius used for the waveguides was 100 µm. The spacing between adjacent SGCs at the edge of the die is 127 µm to match the fiber array used in testing. The critical waveguide dimensions in this work are the same as in (Sharma et al., 2022), which were optimized to minimize crosstalk between adjacent waveguides. In our previous work, we discussed the choices made in the design of the SiN optical waveguides along with alignment tolerances (Sharma et al., 2019). The profile of the fundamental TE mode of the single-mode SiN waveguides used in this work is shown in Figure 8.2. The total optical path length ranges between 6,185 µm for the R2 switching channel to 6,683 µm for the L2 switching channel.

8.4 Microfabrication

SOI wafers with predefined cavities were used for fabricating the optical switch. The 59 µm thick Si device layer of the SOI wafer was used to implement the MEMS actuators. The SiN

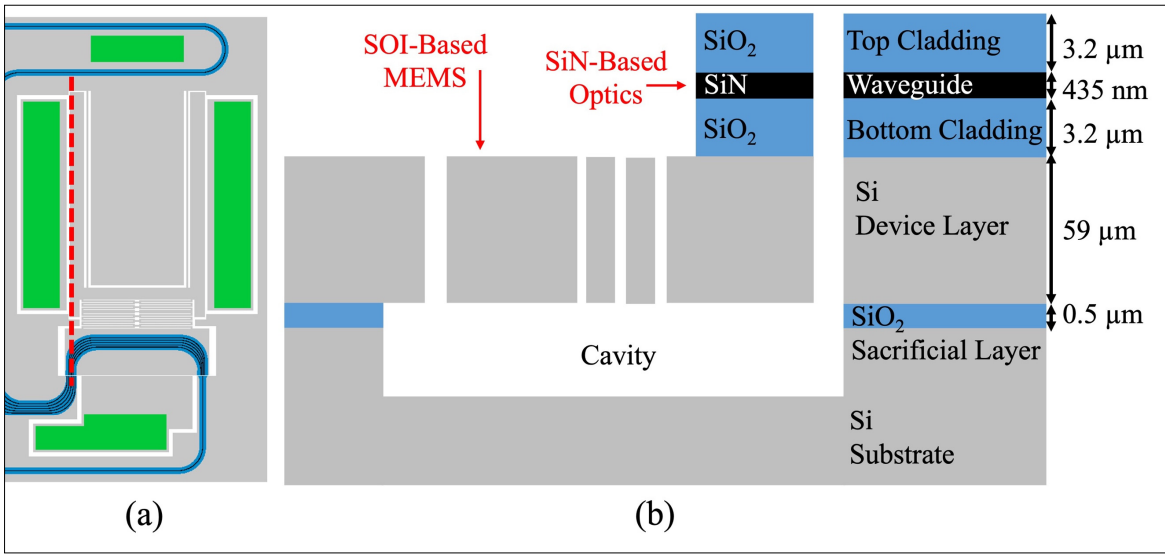

Figure 8.3 1 x 5 MEMS silicon nitride photonics switch layout with (a) top view and (b) cross-sectional view of the design, with material layers and their thicknesses

channel waveguides with SiO2 cladding layers were deposited over the Si device layer. Photolithography with a stepper tool was used to pattern the MEMS, waveguide, cladding and

metal layers. More details about the microfabrication process flow are presented in (Sharma et al., 2022). A top view and a cross-sectional view of the optical switch with all of the material layers and their corresponding thickness are shown in Figure 8.3.

High resolution SEM images were used to analyze the critical dimensions in the fabricated samples. Images from sample 1 are shown in Figure 8.4 along with the measured dimensions. While the LSW and RSW actuator gap was designed to be 15 µm, the fabricated dimensions varied between 16.2 µm and 16.4 µm in sample 1. Similarly, the mechanical stopper gap varied from the 8 µm design value to 8.43 µm – 8.56 µm and 8.5 µm – 8.81 µm for the left and right mechanical stoppers, respectively, in the fabricated device. The GC actuator gap also varied from 6 µm in the design to 7.67 µm in the device. The air gap between suspended Si platform

and fixed Si at the waveguide interface increased from 4 µm in the design to 5.05 µm – 5.32 µm in the prototype, when measured at the top edge of the waveguide near the air gaps.

Similar fabrication variations were observed in sample 2, and a summary of the critical dimensions of the samples tested is presented in Table 8.2. The impact of these fabrication variations on the MEMS and optical characterization results are discussed in section 8.6.

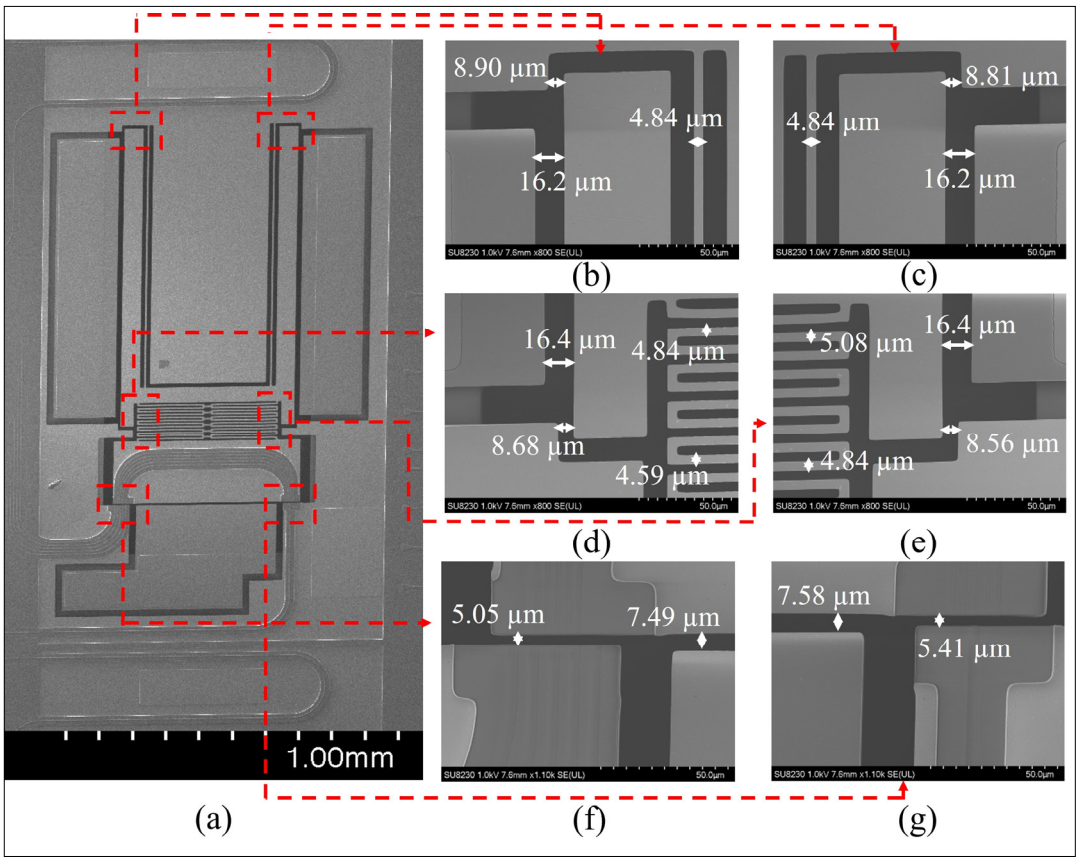

Figure 8.4 (a) High resolution SEM micrograph of the fabricated 1 x 5 MEMS silicon nitride photonics switch sample 1 with dimensions for (b) LSW actuator gap, top left mechanical stopper gap, and left single beam spring; (c) RSW actuator gap, top right mechanical stopper gap, and right single beam spring; (d) LSW actuator gap, bottom left mechanical stopper gap, and serpentine spring beam width; (e) RSW actuator gap, bottom right mechanical stopper gap, and serpentine spring beam width; (f) air gap between platform and fixed silicon on the output side, and the gap closing actuator gap; and (g) air gap between platform and fixed silicon on the input

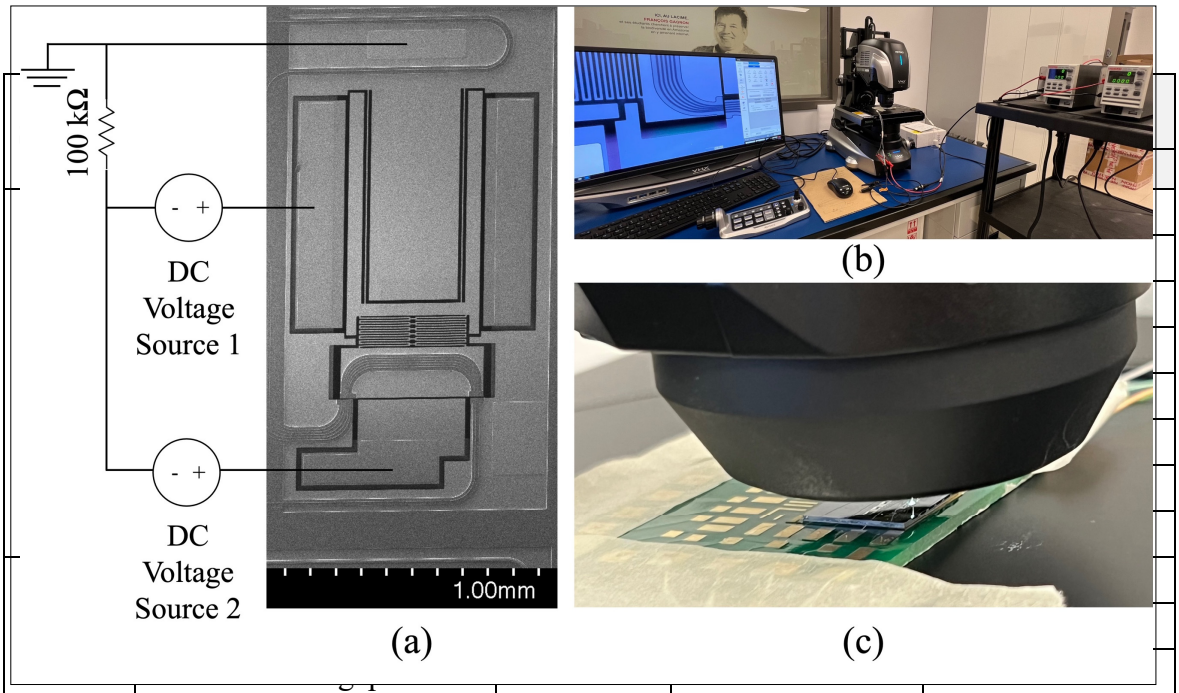

Figure 8.5 (a) Test circuit schematic for MEMS characterization with left switching and gap closing actuator. (b) Test setup with microscope and voltage sources used. (c) Zoomed in image of the wirebonded device during testing under microscope lens

RSW stopper gap	8	8.56-8.81	8.69
GC actuator gap	6	7.49-7.58	7.54
GC stopper gap	4	5.05-5.41	5.23
Single beam spring	5	4.84	4.84
Serpentine spring	5	4.59-5.08	4.84

8.5 Results

8.5.1 MEMS Characterization

Wire bonded devices were actuated under a Keyence VHX-7000 digital microscope for characterization. Two high voltage DC sources were used to actuate the switching and gap closing actuators while high resolution images were captured through the microscope. The images captured were analyzed using the software provided by Keyence to measure the displacement of the central MEMS platform during switching and gap closing actuation at different voltages. 100 kΩ resistors were used to prevent device damage in case an electrical

short was created between the static and movable surfaces during actuation. The suspended MEMS structure and the mechanical stoppers were grounded to prevent any short during contact upon electrostatic pull-in. The test setup and a schematic of the test circuit are shown in Figure 8.5. High resolution microscope images of the interface between the suspended and fixed waveguides in different switching positions with the GC actuator enabled at 120 V are shown in Figure 8.6.

The measured actuation curves for the two samples tested showing the displacement as a function of voltage for the left and right switching actuators and the gap closing actuators are shown in Figure 8.7. Simulation results for the MEMS model with the fabricated dimensions are also shown in the same figure. COMSOL Multiphysics v5.6 was used to obtain the simulation results. Sample 1 showed up to 5.45 μm of displacement at 89 V with analog control for the LSW actuator. The electrostatic pull-in for the same actuator occurred at 90 V and provided 8.49 μm of displacement with digital control. The RSW actuator provided up to 4.73 μm of displacement at 88 V with analog control. The electrostatic pull-in for the same actuator occurred at 89 V with 8.66 μm of displacement with digital control. The GC actuator for

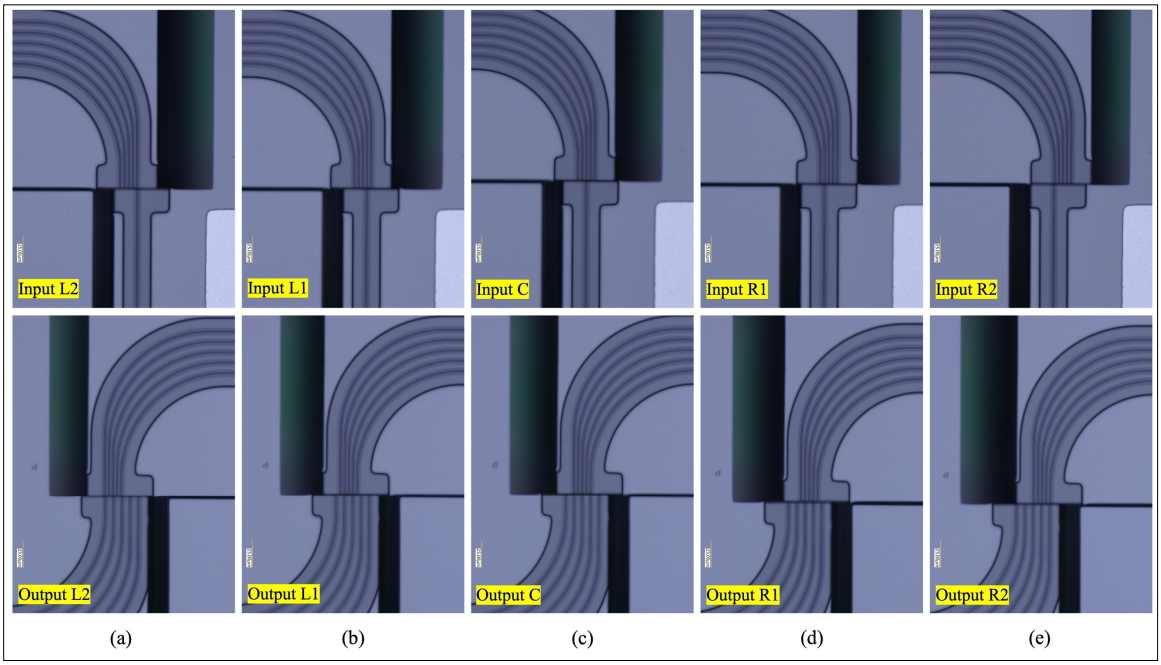

Figure 8.6 High resolution microscope images of the 1 x 5 MEMS silicon nitride photonics switch sample 1 at the input and output waveguide interface in (a) L2 switching position; (b) L1 switching position; (c) C switching position; (d) R1 switching position; and (e) R2 switching position

sample 1 operated at 118 V with a displacement of 5.19 µm after electrostatic pull-in. Sample 2 showed up to 5.25 µm of displacement at 88 V with analog control for the LSW actuator. The electrostatic pull-in for the same actuator occurred at 89 V and provided 8.79 µm of displacement with digital control. The RSW actuator provided up to 4.81 µm of displacement at 87 V with analog control. The electrostatic pull-in for the same actuator occurred at 88 V with 8.69 µm of displacement with digital control. The GC actuator for sample 2 operated at 118 V with a displacement of 5.23 µm after electrostatic pull-in.

The variation in simulation and experimental results is larger in case of the GC actuator in comparison to the SW actuators. This could be due to the initial misalignment between the suspended platform and the fixed electrode of the GC actuator in the samples tested. Such misalignment could result from mechanical stress caused by the material stack of SiN waveguides and SiO2 cladding fabricated over the MEMS platform. A LEXT4100 laser

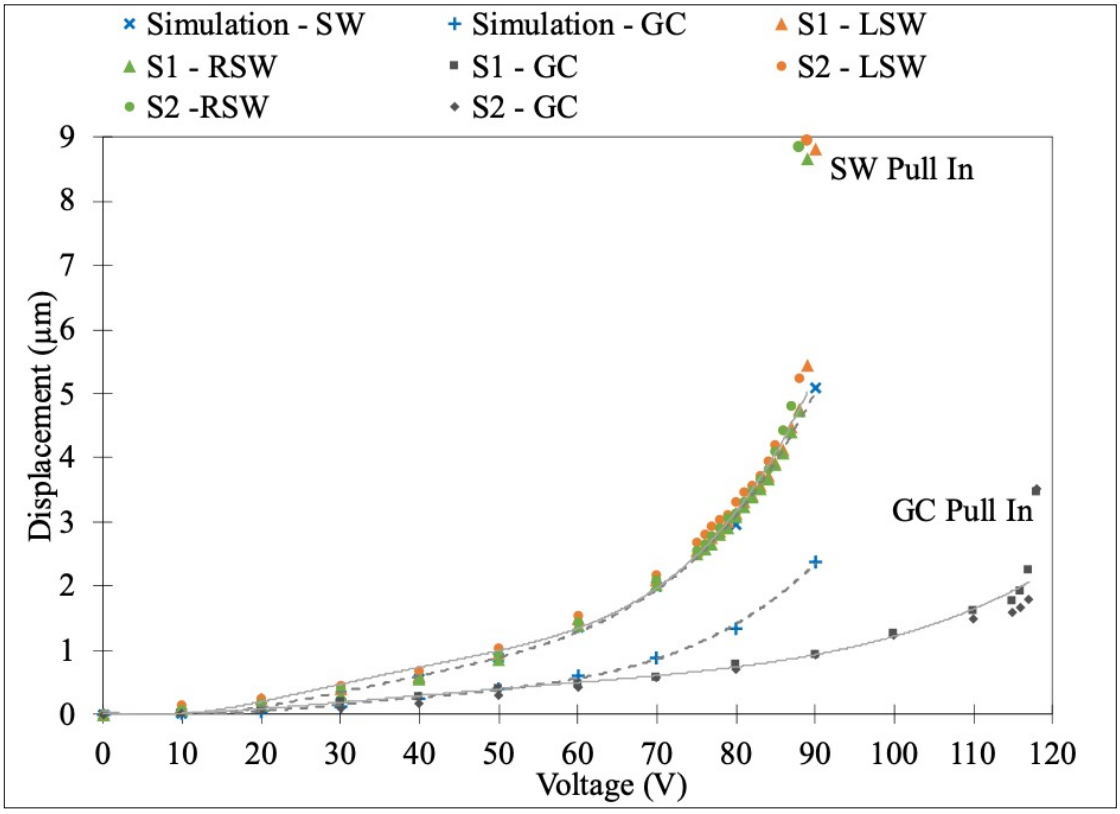

Figure 8.7 Simulation vs measured actuation results of switching (SW) and gap closing (GC) actuators for sample 1 (S1) and sample 2 (S2). The dotted and solid lines are a polynomial fit to the simulated and experimental data, respectively. The displacement after electrostatic pull-in, which depends on the mechanical stopper gap, is shown for the experimental results

confocal 3-D microscope by Olympus was used to observe this phenomenon. The maximum 100x magnification lens was used to understand the slight variations on a nm scale between the suspended and fixed device parts when no actuator was used. This allowed us to measure the effect of residual stress upon different parts of our optical switch. Results from these measurements are shown in Figure 8.8. Notably, the part of the MEMS device that forms the SW actuators does not have any optical material deposited over their suspended beams, leading to less residual stress on the suspended part of the SW actuator in comparison to the suspended part of the GC actuator.

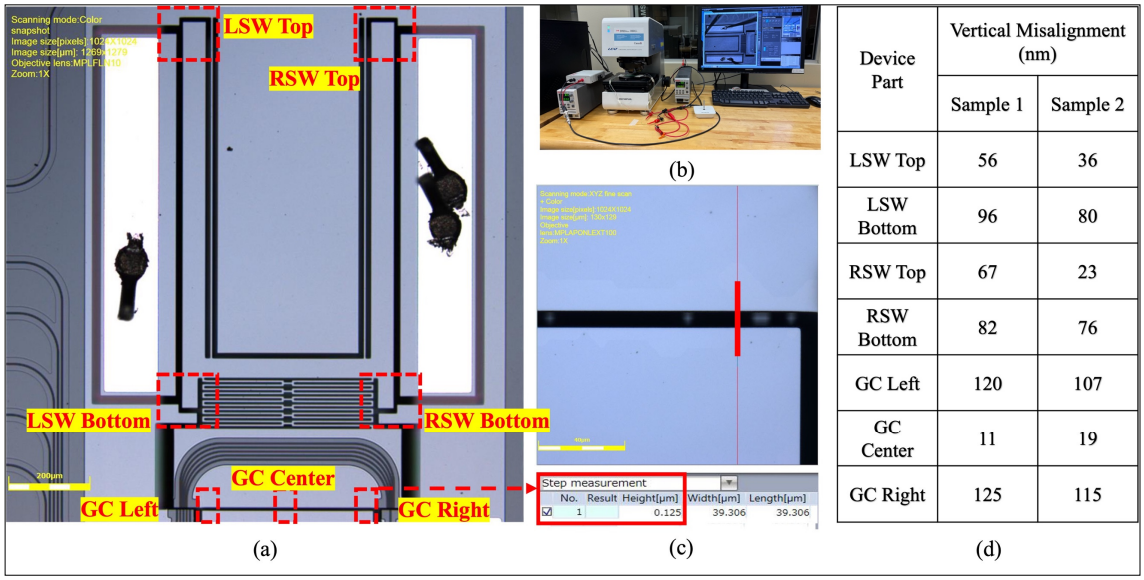

Device Part	Vertical Misalignment (nm)	
	Sample 1	Sample 2
LSW Top	56	36
LSW Bottom	96	80
RSW Top	67	23
RSW Bottom	82	76
GC Left	120	107
GC Center	11	19
GC Right	125	115

Figure 8.8 (a) 1 x 5 MEMS silicon nitride photonics switch image using the 10x lens of a laser confocal 3-D microscope showing the specific parts of the switch that were characterized using the 100x lens. (b) Test setup used for 3-D analysis of the samples. (c) Image and step measurement from the GC right part of sample 1. (d) Vertical misalignment measured in different parts of the device for samples 1 and 2

It should be noted that some cross sensitivity was observed between the switching and gap closing actuators in the three analog switching positions when the two actuators were used together. However, the impact of this cross-sensitivity could be negated through voltage variation in the switching actuator during gap closing in the analog switching positions L1, C, and R1. Different switching voltage were tested in these analog positions to get the best alignment between the suspended and fixed waveguides for minimal optical loss. These results and their impact on the optical performance of the device are presented in section 8.5.2.

8.5.2 Optical Characterization

Optical signal transmission results for the two samples were obtained for all five switching positions. A custom printed circuit board (PCB) with wire bonded samples was placed on a bi-axial stage controlled by micropositioners with a 1 µm precision. A micropositioner also

controlled the vertical motion of the fiber array required for fine alignment with the SGCs on each sample. A tunable laser (EXFO T100S-HP) was used to generate an optical signal that was measured with an optical component tester (EXFO CT440) at the output. The optical fiber array had a 30º polish angle. The optimal vertical gap between the fiber array and the sample was 10 µm. The optical measurements were done with the transverse electric (TE) mode since the SGCs were optimized for this polarization. Polarization maintaining fibers were used to make connections between the tunable laser, optical component tester, and the fiber array. A detailed schematic of the test setup is shown in Figure 8.9.

Reference waveguide structures were fabricated on each sample as shown in section 8.3 (see Figure 8.1). The optical path length of the reference waveguide was the same as the center channel waveguide. A loopback structure, also shown in section 8.3 (see Figure 8.1), was used to characterize the coupling loss. The measured propagation loss for SiN waveguides fabricated by AEPONYX was 1.5 dB/cm for TE mode in the L-band. The output transmission power obtained while coupling the input fiber to the reference waveguide structure was used to normalize the optical transmission results for each switching channel. The measured transmission spectra for the five switching positions of the two samples are presented in the

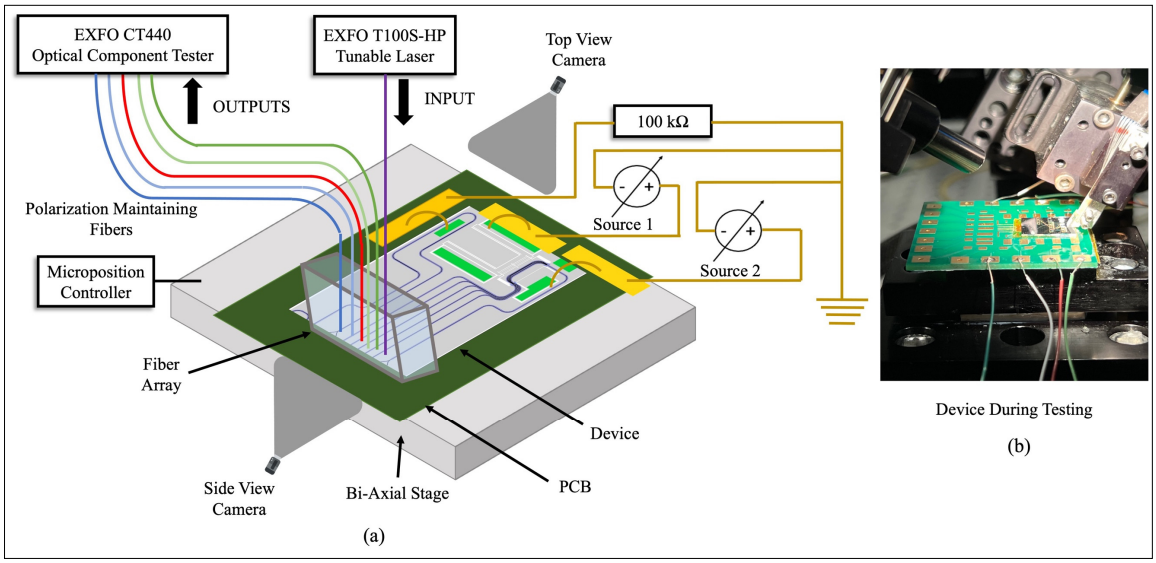

Figure 8.9 (a) Schematic of the test setup used for optical characterization of wirebonded samples. (b) Test setup image of the fiber array aligned over the device under test

Appendix II. To normalize the transmission spectra, the output power detected for a given switching position was subtracted from the output power measured from the reference waveguide structure on the same sample at each wavelength. This removes the propagation loss of the waveguides from the normalized transmission spectrum providing only the transmission response of the butt coupled waveguides in the switch (including the air gap between the waveguides). The normalized transmission results are shown in Figure 8.10. The undulations in the transmission curves were due to the SGCs used for coupling input and output optical signal. The crosstalk in the L1 and R1 channels are also shown in Figure 8.10. This was measured while the input is in the C switching position with the GC actuator ON for both samples. To calculate the average insertion loss, the normalized data obtained for each switching position was averaged over the wavelength range from 1540 nm to 1625 nm. The average insertion loss and crosstalk in the adjacent channels over the wavelength range of 1540 nm to 1625 nm are shown in Table 7.3. Our optical switch design provides analog control over

Table 8.3 Average insertion loss, switching voltage & average crosstalk

Sample	**Average Insertion Loss* (dB) Switching Actuator** Voltage (V) Average Crosstalk in Adjacent Channels (dB)**				
	L2 (Digital)	**L1 (Analog)**	**C (Analog)**	**R1 (Analog)**	**R2 (Digital)**
1	5.4	3.4	4.1	2.2	4.1
	LSW 90	LSW 83	LSW 50	RSW 78	RSW 89
	41.7	39.1	39.2	38.15	36.2
2	7.5	3.7	4.7	2.3	5.9
	LSW 89	LSW 82	LSW 40	RSW 79	RSW 88
	41.6	39.3	39.8	39.1	35.7

* Average insertion loss calculated over the wavelength range of 1540 nm – 1625 nm.

** Switching actuation in these results also included using the gap closing actuator in all switching positions at 120 V for minimal optical loss.

*** Average crosstalk calculated over the wavelength range of 1540 nm – 1625 nm. In case of L2 and R2 channels, the cross talk was measured only for the one adjacent channel, L1 and R1 respectively. In case of L1, C, and R1 channel, the crosstalk results shown are an average of the two adjacent channels, L2 and C, L1 and R1, and C and R2, respectively.

three switching channels, C, L1, and R1 whereas channels L2 and R2 operate in a digital manner since they rely upon the pull-in phenomenon.

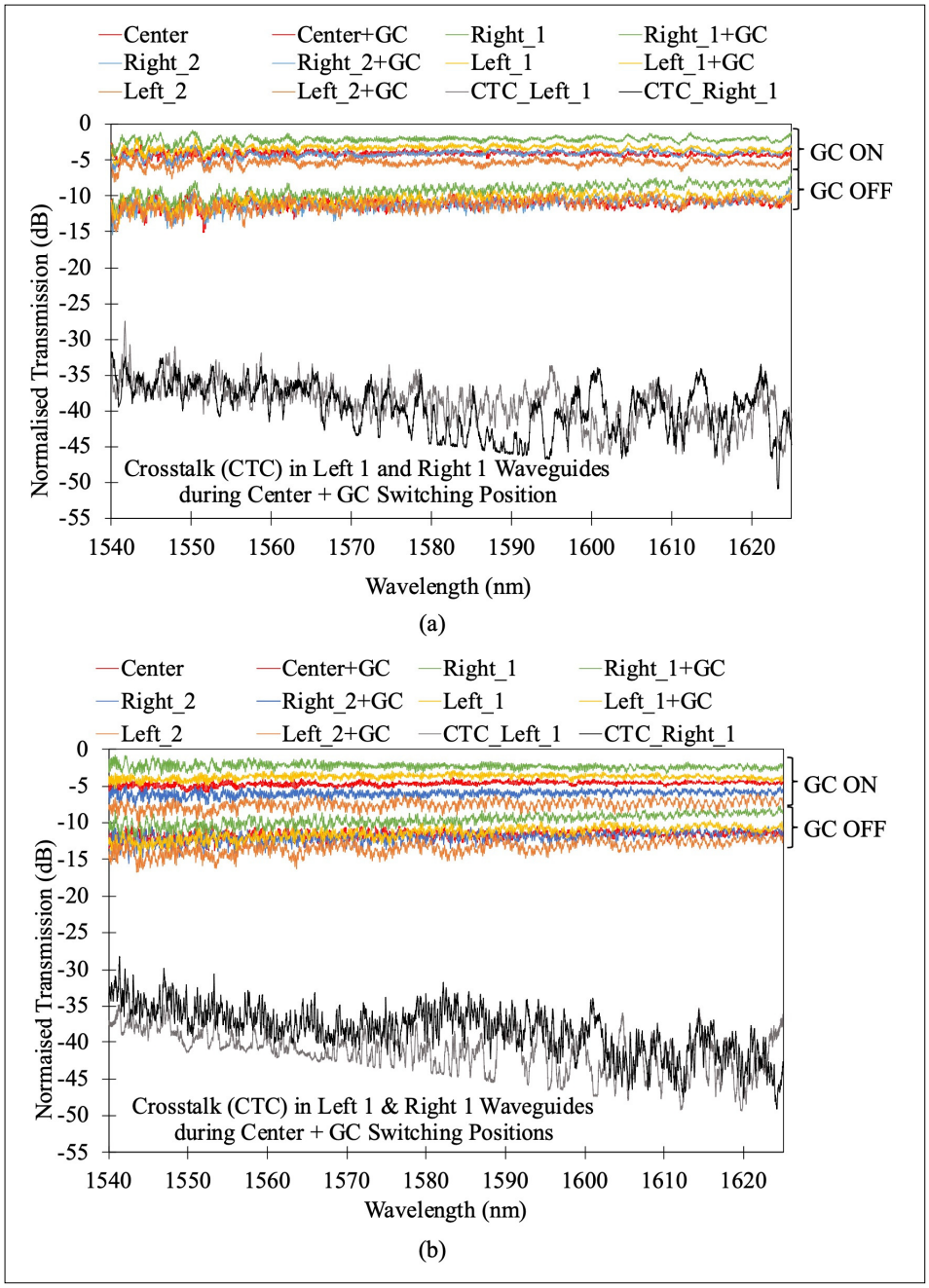

Figure 8.10 Normalized transmission results over the wavelength range of 1540 nm to 1625 nm in all switching positions with crosstalk in adjacent channels during center waveguide switching for (a) sample 1, and (b) sample 2

The control provided by the switching actuators over the average insertion loss in the three analog switching channels, L1, C and R1 is shown in Table 8.4. Voltage variations of 1 V in the LSW actuator, from 82 V to 84 V, when combined with the GC actuator at 120 V, result in variations in average insertion loss from 4.0 dB to 3.5 dB respectively, for the L1 channel in sample 1. Similarly, voltage variations of 1 V in the RSW actuator, from 76 V to 78 V, when combined with GC actuator at 120 V, result in variations in average insertion loss from 2.6 dB to 2.2 dB respectively, for the R1 channel in sample 1. In the C switching position, applying 40 V on the LSW actuator in sample 1 maximize the transmission efficiency with an optical loss of 4.1 dB. This shows that the switching actuators can be used for fine alignment between input and output waveguides in three switching positions. Similar results were observed for variations in optical loss with variation in switching voltage for the analog switching channels

Table 8.4 Control over loss in different switching positions

Sample		**Position**	**L2 (Digital)**	**L1 (Analog)**			**C (Analog)**		**R1 (Analog)**			**R2 (Digital)**
		Actuator	**LSW**	**LSW**			**LSW**	**-**	**RSW**			**RSW**
1	GC OFF	Voltage (V)	90	85	86	87	40	0	85	86	87	89
		Loss* (dB)	11.2	10.6	10.5	10.8	12	11.3	9.3	9.2	9.4	11.1
	GC ON	Voltage (V)	90	82	83	84	40	0	76	77	78	89
		Loss* (dB)	5.4	4.0	3.4	3.5	4.1	5.3	2.6	2.4	2.2	4.1
2	GC OFF	Voltage (V)	89	84	85	86	40	0	84	85	86	88
		Loss* (dB)	13.3	11.6	11.4	11.5	12.5	11.8	9.7	9.6	9.7	11.9
	GC ON	Voltage (V)	89	81	82	83	40	0	77	78	79	88
		Loss* (dB)	7.5	4.7	3.7	4.1	4.7	5.2	2.5	2.4	2.3	5.9

Loss presented in this table is the average insertion loss calculated over the wavelength range of 1540 nm – 1625 nm. The lowest optimized loss measured in each switching position is highlighted in grey.

* Switching actuation in these results do not include the gap closing actuator.

** Switching actuation in these results included using the gap closing actuator at 120 V for minimal optical loss.

without the use of the GC actuator for both the samples. Without the use of the GC actuator, the switching voltages are slightly higher for analog switching positions L1 and R1, in comparison to the switching voltages required with the GC actuator ON at 120 V. This outlines some cross-sensitivity between the SW and GC actuators when used together for analog switching. However, the results presented in Table 8.4 for both samples also demonstrate that such cross-sensitivity has no impact on the ability of the optical switch to achieve efficient transmission of the optical signal in the three analog switching positions. It should be noted that the variation in average insertion loss results for analog switching positions L1, C, and R1 is likely due the combination of variations the in optical path length, and misalignment between the suspended and fixed waveguides due to residual stress (discussed further in section 8.6). The L2 and R2 switching positions show higher losses due to the digital switching because of the variations in the fabricated dimensions of the mechanical stopper gap that were discussed in section 8.4. These results are further discussed in detail in section 8.6.

During the GC actuation, the suspended waveguide platform moves towards the fixed waveguides. This motion reduces the air gap between the suspended and fixed waveguides, which lowers optical losses. The average insertion loss and air gap was measured at 10 V intervals over the wavelength range of 1540 nm to 1625 nm. The positive impact of the GC actuator upon the insertion loss in the center switching position can be clearly seen in the results presented in Figure 8.11. Although the GC actuator completely closed the air gap at the level of the Si device layer, a residual air gap remains between the suspended and fixed waveguides due to the etch profile of the end facets, which leads to the insertion loss recorded for the two devices with GC ON (Sharma et al., 2022). This is discussed in detail in section 8.6.

The impact of the switching actuators on transmission in the different channel waveguides was also characterized. During LSW actuation, the voltage was increased incrementally at intervals of 10 V up to 80 V. Above 80 V, the voltage was increased in 1 V increments until electrostatic pull-in was reached for both samples. The average insertion loss for each switching channel was measured at each actuation voltage. During LSW actuation, the transmission in the C, L1,

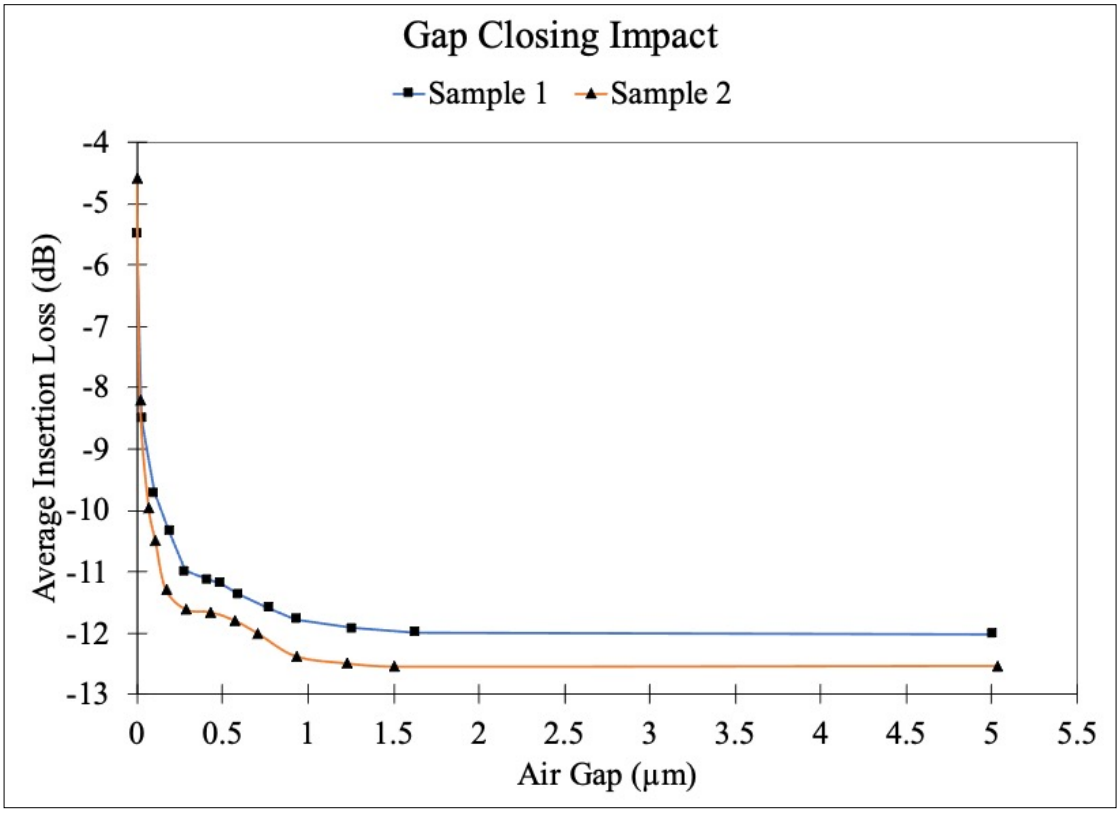

Figure 8.11 Impact of gap the closing actuator on the average insertion loss measured in the center switching channel (C) over the 1540 nm to 1626 nm wavelength range for both samples

and L2 waveguides was measured. During RSW actuation, the voltage was also increased in steps of 10 V but only up to 70 V. Above 75 V, the voltage was increased in 1 V increments until electrostatic pull-in was reached for both samples. This time, the transmission was measured for waveguides C, R1, and R2. These insertion loss results showing the impact of the position of the switching actuators are shown in Figure 8.10 for both samples. It can be clearly seen that with the switching actuator, the transmission in the C switching channel started reducing until the optical signal couples to the L1 or R1 switching channel. Further increase of the actuation voltage results in an abrupt switch from L1 to L2 of the left side and from R1 to R2 on the right side due to electrostatic pull-in. Note that the results shown in Figure 8.12 were obtained with the GC actuator OFF.

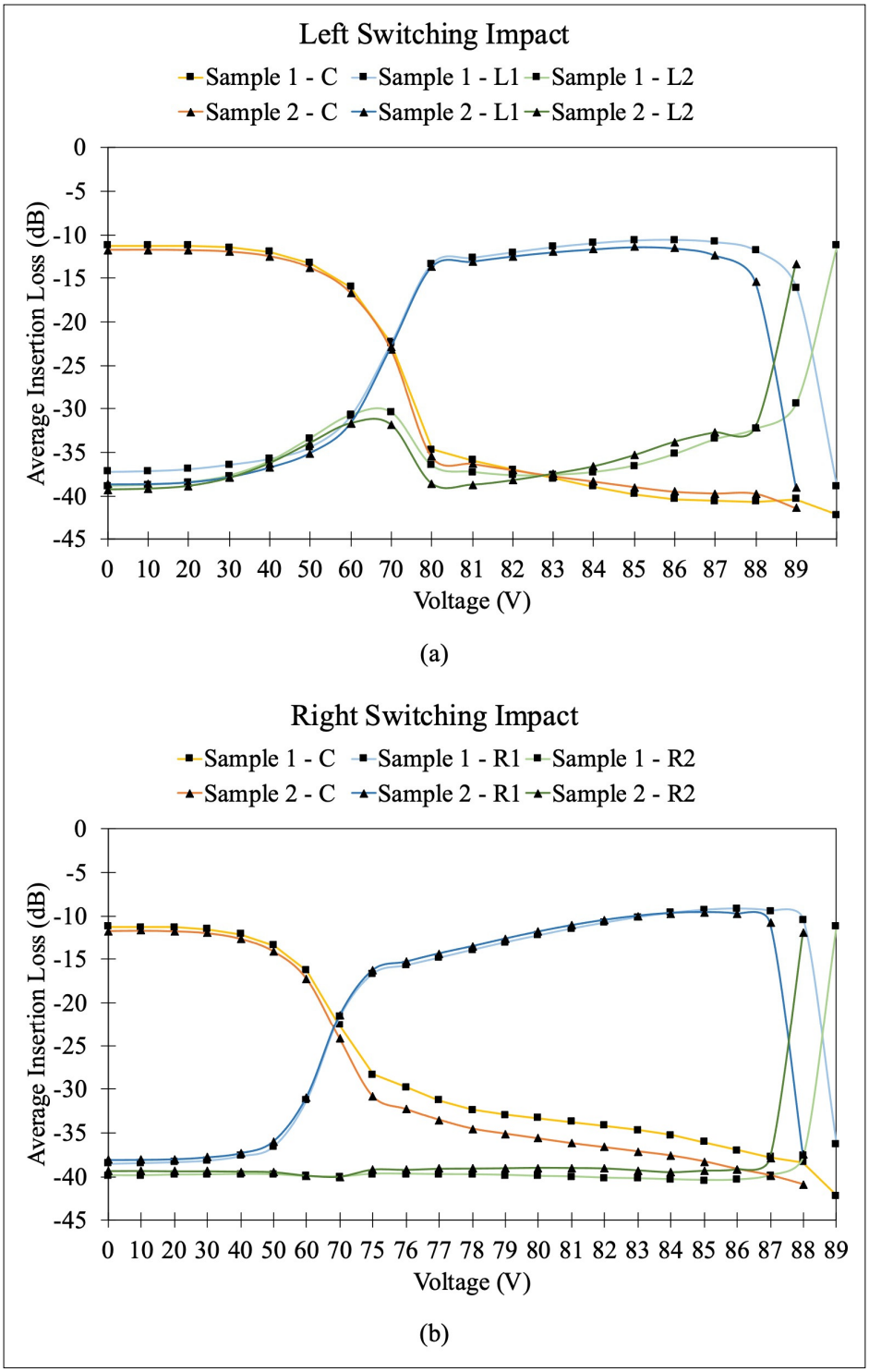

Figure 8.12 Impact of the (a) left and (b) right switching actuators on the average insertion loss of both samples over the wavelength range of 1540 nm to 1625 nm in all channels during actuation. Note that the GC was turned OFF for these measurements

8.6 Discussion

In this work, we were able to successfully integrate SiN waveguides with Si based MEMS to implement a planar optical switch. The LSW and RSW actuators enable sufficient lateral motion of the suspended platform to create a 1 x 5 switch. The addition of a GC actuator allows to close the two air gaps between the suspended and fixed waveguides to minimize losses. The switching actuators have a pull-in voltage between 88 V and 90 V. This is very close to the simulated pull-in voltage of 90 V (see Table 8.1). Although the fabricated actuator gap varied from 16.2 μm to 16.4 μm in comparison to the design dimension of 15 μm, the experimental results are close to the design simulations. This is because the reduction in width of the fabricated single beam spring compensates for the increase of the gap by reducing the spring stiffness. The fabricated width was as small as 4.46 μm vs 5 μm in the original design (see Table 8.2). Moreover, this effect is confirmed by the simulation results with the fabricated MEMS dimensions (see Figure 8.6). The GC actuator shows a higher pull-in voltage of 118 V in both samples in comparison to the design value of 72 V. This is because of the residual stress in the fabricated devices caused by the thick SiO_2 cladding layers required for the confinement of optical signals in the SiN waveguide layer (Ghaderi et al., 2016). Such residual stress creates an out-of-plane misalignment between the suspended Si platform and the fixed Si as discussed in the previous section (see Figure 8.8). Vertical misalignment between the suspended platform and the fixed Si along the GC actuator was measured at 120 nm and 107 nm close to the left corner of the platform (i.e., next to the waveguides) for sample 1 and sample 2, respectively. Similarly, along the right corner of the platform (i.e., next to the waveguides) the misalignment was measured at 125 nm and 115 nm for sample 1 and sample 2, respectively. The large variation also comes from the significant increase of the actuator gap, which is between 7.49 and 7.67 μm whereas the design value is 6 μm.

Additionally, variations in the fabricated serpentine spring beam dimensions, which were reduced to as low as 4.46 μm in comparison to 5 μm in the original design, would lead to reduced stiffness of the serpentine spring system leading to large variations between simulation

and experimental pull-in. It should be noted that all actuators are electrostatic, which consumes no DC power. Conventional SiN waveguide based optical switching typically relies on thermal tuning, which dissipates large amount of DC power (Lin et al., 2022; Liu et al., 2017).

The average insertion loss over the wavelength range of 1540 nm to 1625 nm in the five switching positions showed variations between 2.2 dB to 5.4 dB for sample 1, and 2.3 dB to 7.5 dB for sample 2 (see Table 8.3). These variations are due to three factors. The first is the etch profile of the cladding and waveguide layers. SEM images used to measure the etch profile are shown in Figure 8.13(a) along with the residual air gap calculation in Figure 8.13(b). This factor affects all five switching positions in the same sample. The etch angles of the optical stack consisting of the SiN core and the SiO2 cladding layers for sample 1 were measured to be 4.54° and 8.72° on the fixed Si and suspended Si, respectively. These etch profile angles lead to a 795 nm air gap between center of the waveguide cores even when the gap is completely closed between the Si layer underneath the optical stack. Sample 2 has etch profile angles of 5.65° and 8.99° on the fixed Si and suspended Si side, respectively. This leads to an 879 nm air gap between center of the waveguide cores upon GC actuation.

The second factor is the variation in the fabricated stopper gap in the two samples. This variation resulted in different optical loss at the L2 and R2 switching positions which rely upon digital switching. Sample 1 had a minimum stopper gap of 8.56 μm and 8.50 μm for the left and right stopper, respectively. This creates a 560 nm and 500 nm misalignment in the L2 and R2 switching position, respectively, for sample 1. Similarly, sample 2 had a minimum stopper gap of 8.63 μm and 8.56 μm for the left and right stopper, respectively. This leads to a 630 nm and 560 nm misalignment in the L2 and R2 switching positions, respectively, for sample 2. The larger misalignments in sample 2 result in higher losses in the L2 and R2 positions in comparison to sample 1 (see Table 8.3). Figure 8.13(c) shows the stopper gap variations in the two samples measured through high resolution SEM imaging. Lateral misalignment due to this fabrication variation in the outermost switching channel is shown through a schematic representation in Figure 8.13(d).

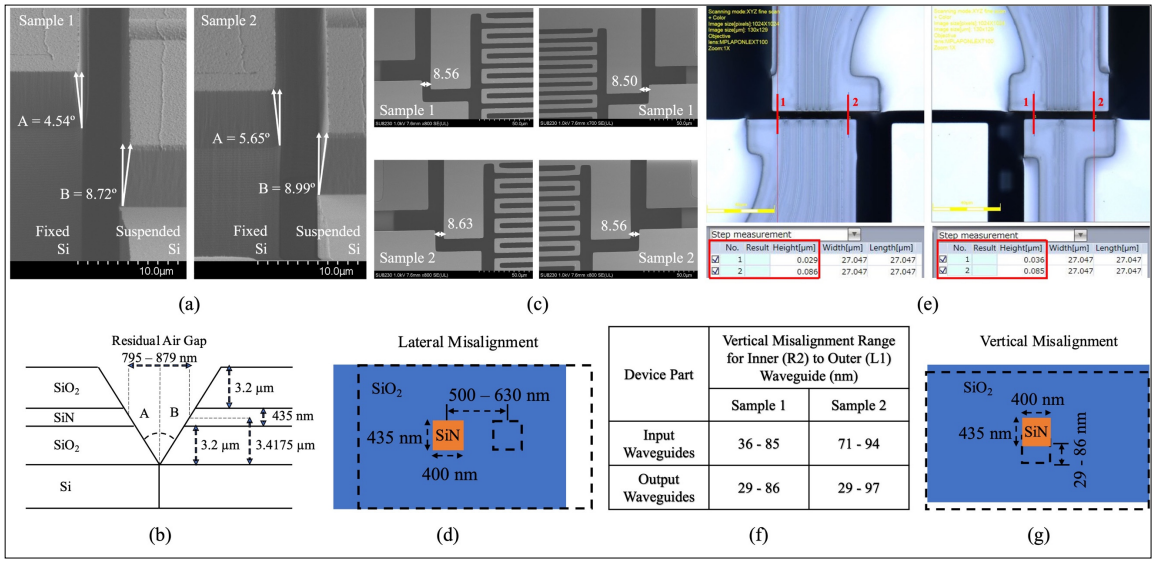

Figure 8.13 (a) Etch profile of the waveguide interface near the air gaps leading to (b) a residual air gap between the suspended and fixed waveguides. (c) Stopper gap fabrication variation leading to (d) a lateral misalignment between the suspended and fixed waveguides during the digital switching in the L2 and R2 channels. (e) 3-D measurements for sample 1 using a LEXT4100 laser confocal microscope with a 100x lens along with (f) the measurement results for sample 1 and sample 2 to estimate (g) the minimum and maximum vertical misalignment between the suspended and fixed waveguides

The third factor is the variation in residual stress across the platform caused by the optical stack above it. 3-D characterization of the samples using a laser confocal microscope showed that the residual stress impacts the innermost waveguides on the suspended platform (R1 and R2) the least, whereas waveguides L1 and L2 were impacted the most by the residual stress. This impact can be seen in the lower optical loss of R1 in comparison to L1 for both samples. A similar trend is visible in the average insertion loss results for the R2 and L2 positions in both samples (see Table 8.3). Results from misalignment measurements between the suspended and fixed waveguides are shown in Figure 8.13(f), along with an illustration of the vertical misalignment created by the residual stress in Figure 8.13(g). The average insertion loss for

Table 8.5 Average insertion loss & loss variation factors

Sample	Switching Channel	L2 (Digital)	L1 (Analog)	C (Analog)	R1 (Analog)	R2 (Digital)
1	Average Insertion Loss* (dB)	5.4	3.4	4.1	2.2	4.1
	Residual Gap due to Etch Profile Angle (nm)	795				
	Average Insertion Loss due to Etch Profile** (dB)	1.61				
	Lateral Misalignment due to Stopper Gap Variation (nm)	560	-	-	-	500
	Average Insertion Loss due to Stopper Gap** (dB)	2.92	-	-	-	2.67
	Vertical Misalignment due to Residual Stress*** (nm)	86				29
	Average Insertion Loss due to Residual Stress** (dB)	1.76				1.62
2	Average Insertion Loss* (dB)	7.5	3.7	4.7	2.3	5.9
	Residual Gap due to Etch Profile Angle (nm)	879				
	Average Insertion Loss due to Etch Profile** (dB)	1.74				
	Lateral Misalignment due to Stopper Gap Variation (nm)	630	-	-	-	560
	Average Insertion Loss due to Stopper Gap** (dB)	3.3	-	-	-	2.98
	Vertical Misalignment due to Residual Stress*** (nm)	97				29
	Average Insertion Loss due to Residual Stress** (dB)	1.95				1.76

* Experimentally measured average insertion loss calculated over the wavelength range of 1540 nm – 1625 nm.

** Simulated average insertion loss calculated over the wavelength range of 1540 nm – 1625 nm.

*** Values estimated upon 3-D characterization of samples using laser confocal microscope LEXT4100.

the five switching positions with the GC actuator ON along with a quantification of the three contributing factors described above is presented in Table 8.5.

Our 3-D characterization of the samples also shows that although the main impact of the residual stress is on the platform with suspended waveguides, the rest of the structure is also

affected by the residual stress (see Figure 8.8). The LSW, RSW and GC actuators would compensate for such vertical misalignment as the electrostatic force produced by both actuators would help in aligning the misaligned structure (Chiou et al., 2005). Since the SW actuation voltage used in analog switching position L1 and R1 is higher than the SW actuation voltage used for analog position C (see Table 8.4 in section 8.5.2), it is likely that the vertical misalignment compensation due to the electrostatic actuation would have more impact in the L1 and R1 positions that require a higher SW actuator bias voltage. This would result in higher optical average insertion loss in the C switching position. Our current test setup for 3-D characterization allowed use of 10x lens with wirebonded samples. Higher magnification lenses could not be used with wirebonded devices as the working distance of the lens was too

small, leading to interference of the lens with the wirebonds needed for actuation. 3-D characterization of Sample 2 with a 10x lens showed a reduction of the vertical misalignment between the suspended platform and the fixed Si substrate. A 34% vertical misalignment reduction was measured for the LSW actuator during pull-in, and a 41% reduction was measured for the RSW actuator, also at pull-in. The GC actuator for Sample 2 provided an 87% reduction in vertical misalignment, similar to our previous work, where the electrostatic actuator helped compensate the misalignment between the suspended and fixed parts of a

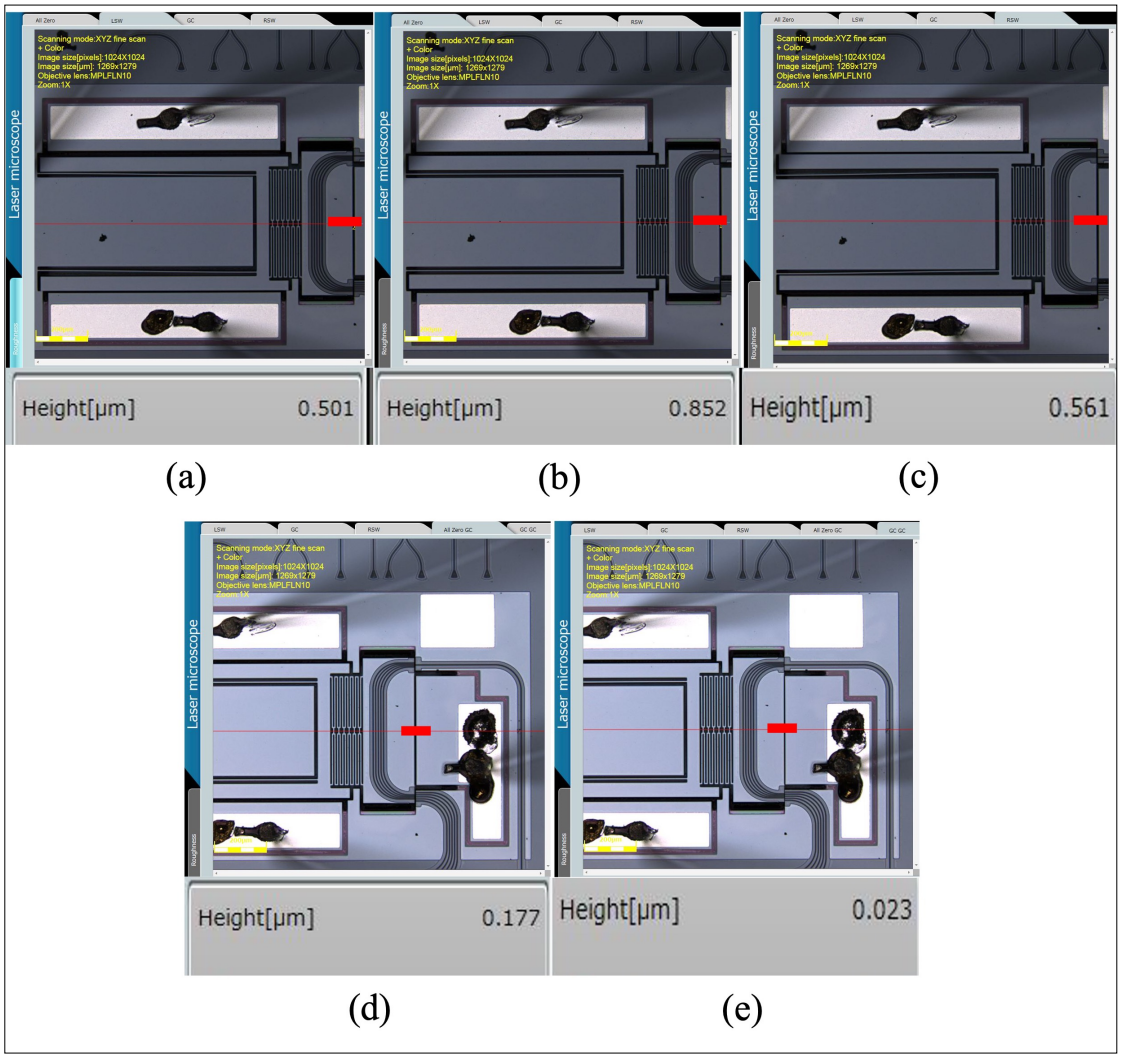

Figure 8.14 3-D image analysis of the vertical misalignment in Sample 2 using a 10x lens on a LEXT4100 Microscope across various states: (a) LSW actuator pull-in, (b) all zero state (SW actuators in focus), (c) RSW actuator pull-in, (d) all zero state (GC actuator in focus), and (e) GC actuator pull-in

hybrid MEMS structure by 91% (Sharma et al., 2023). These results are presented in Figure 8.14.

A comparison with the state-of-the-art MEMS based SiN based optical switching solutions is presented in Table 8.6. Only a few devices that integrate MEMS with SiN based optics exist in literature (Han et al., 2018; Sattari et al., 2021; Barazani et al., 2023) , (Sharma et al., 2022; Chiou & Lin, 2005). A MEMS based ON-OFF switching solution that uses a single SiN ring resonator for wavelength filtering has been demonstrated to work in the wavelength range of 1545 nm – 1585 nm. In the OFF state, the suspended MEMS membrane is away from the SiN ring resonator and the resonant wavelengths are sent to the drop port. On bringing the lossy membrane close to the ring in the ON state, the absorption spoils the resonance, and the resonant wavelengths are transmitted to the through port. The actuation of the MEMS requires 30 V. This device has an average insertion loss of 11 dB – 15 dB (Han et al., 2018). Our device can provide switching over a wider wavelength range with broadband operation at a lower insertion loss of 2.2 dB – 7.5 dB across five switching channels.

Another demonstration reported a rotational MEMS based silicon nitride optical switch operating at a much higher switching voltage of 180 V in comparison to this work. The air gap between the suspended and fixed MEMS Si layer in this rotational MEMS optical switch could only be closed down to 500 nm (Sattari et al., 2021). In this work, we can close the air gap completely between the suspended and fixed Si layer (with a residual gap between the waveguides as previously discussed), as in our previous 1 x 3 optical switch (Sharma et al., 2022). However, our previous device had only 3 switching positions with digital control. Thus, it was prone to higher optical losses due to microfabrication variations in the mechanical stopper gaps. In this work, we improved insertion losses in the three central channels thanks to the analog control on their position. Moreover, we demonstrated a wider operational wavelength range. However, the two additional digital switching channels show similar performance to our 1 x 3 optical switch (Sharma et al., 2022).

A 1 x 4 broadband SiN photonic switch reported recently has a large displacement of 12 µm at just 10 V operational voltage (Barazani et al., 2023). This optical switch utilizes SiN based optics and SOI based MEMS for the switching motion similar to this work, and has an operational wavelength range of 1520 nm to 1620 nm. However, it uses electrothermal actuation to provide the switching motion in comparison to electrostatic actuation used in this work. Electrothermal actuation consumes more power in comparison to electrostatic actuation. The 1 x 5 optical switch demonstrated in this work shows a lower minimum insertion loss of 2.2 dB in comparison to the 4.0 dB lowest insertion loss of the 1 x 4 optical switch.

Recently, a broadband SiN optical switch has also been demonstrated with wide operational wavelength range of 1250 nm to 1610 nm using electrostatic actuation at 50 V. The switching time reported for this optical switch is 20 µs. The device demonstrated is a simple 1 x 2 switch in ON/OFF configuration with insertion loss of 2.6 dB at 1470 nm and 3.7 dB at 1550 nm (Swain et al., 2023). Time-dependent simulations for our 1 x 5 optical switch in COMSOL Multiphysics v5.6 showed a maximum response time of 165 µs for pull-in using the SW actuators. Similar simulations for the GC actuator showed pull-in with a response time of 100 µs. Thus, total response time for our 1 x 5 optical switch would be in the range of 100 µs to 260 µs between all of the switching positions. Notably, the optical switch demonstrated in this work offers 5 output ports with an average insertion loss of 2.2 dB to 7.5 dB over the entire wavelength range of 1540 nm to 1625 nm.

A MEMS based low power SiN phase shifter has been demonstrated recently that uses suspended SiN MEMS structure fabricated over a fixed SiN MZI arm. Movement of the suspended SiN structure toward the fixed SiN creates a phase shift in the optical signal transmitted through the MZI (McNulty et al., 2022). The MEMS structure relies on electrostatic actuation and needs a low operation voltage of 7 V. However, the device was reported to be mechanically unstable wherein the beam broke within 4 sweeps.

Overall, it can be assessed from the table that the proposed device compares favorably to other works, notably in terms of its insertion loss, while providing a wide operating wavelength range.

8.7 Conclusion

Table 8.6 Silicon nitride optical switches state-of-the-art comparison

Reference	Switch Type	Operation	Operating Bandwidth Experimental Wavelength Range (nm)	Power Required (mW)	Switching Voltage (V)	Switching Time (µs)	Insertion Loss (dB)
Nielson et al. 2005	MEMS based wavelength selective switch using ring resonator	Aluminum based electrostatic actuation	1545 – 1585	0.001	30	60	11 – 15
Sattari et al. 2021	MEMS based crossbar switch	SOI based electrostatic actuation	1550	No DC power due to electrostatic actuation	Up to 180	300	12.2 – 14.8
Barazani et al. 2023	MEMS based 1x4 optical switch	SOI based electrother mal and electrostatic actuation	1520 – 1620	-	0 - 10	-	4.0 – 4.9
Swain et al. 2023	MEMS based ON/OFF optical switch	SOI based electrostatic actuation	1250 – 1610	No DC power due to electrostatic actuation	50	10	2.6 – 9.7
Sharma et al. 2022	MEMS based 1x3 optical switch	SOI based electrostatic actuation	1530 – 1580	No DC Power due to electrostatic actuation	80 – 120	50 – 150	4.45 – 6.64
McNulty et al. 2022	MEMS based SiN pi phase shifter	SiN based electrostatic actuation	1450 – 1500	No DC power due to electrostatic actuation	7	-	NA
This work	MEMS based 1x5 optical switch	SOI Based Electrostati c Actuation	1540 – 1625	No DC power due to electrostatic actuation	40 – 120	100 – 260	2.2 – 7.5

A novel 1 x 5 planar MEMS optical switch with integrated SiN channel waveguides was fabricated and tested. The samples characterized required a switching voltage between 40 V and 90 V with a gap closing voltage of 120 V. The optical switch had analog control over the

C, L1 and R1 channels where the input and output waveguides could be fine aligned using the switching actuators. The L2 and R2 switching channels relied upon electrostatic pull-in for digital switching. The average insertion loss in analog channels was between 2.2 dB – 4.7 dB for the two samples tested. The digital switching channels had an average insertion loss between 5.4 dB – 7.5 dB for the two samples. The average insertion loss was measured over the wavelength range of 1540 nm – 1625 nm. The results obtained in this work are a significant improvement over our previous 1 x 3 optical switch that had digital control over all switching channels and higher optical losses. In this work, we demonstrated lower optical losses over the three switching channels actuated in an analog fashion. We also demonstrated two additional digitally actuated switching channels to achieve a 1 x 5 configuration. The demonstrated operating wavelength range is also wider than our previous work (Sharma et al., 2022).

Passive optical networks based upon the NG-PON2 standard require receivers able to select between 4 to 8 wavelength channels (Iovanna et al., 2020; Beyranvand et al., 2019). Our broadband switch can be used in such networks to increase their energy efficiency at low cost. Further optimization of the fabrication process and the use of input/output edge couplers instead of grating couplers can increase the operational bandwidth across all five switching channels. Since these prototypes were fabricated as part of a multiple project wafer (MPW) run, surface grating couplers were used to interface with the devices in order to maximize the number of devices per unit area. Also, our platform enables control over the design and fabrication of SiN based optical components independently of the SOI based MEMS. Such MEMS integration with optics can allow wavelength channel selection systems where each output waveguide can be integrated with different optical filters such as ring resonators, micro disk resonators or Bragg gratings to filter out desired wavelengths. Each output waveguide can be integrated with an optical filter designed for specific wavelengths. The demonstrated wavelength range can be used for a low power MEMS tunable transceiver operating in the C-band and L-band of the telecommunication spectrum. In the future, we aim to provide analog control over all five switching positions and minimize fabrication variations through further process flow optimizations.

CONCLUSION

A methodology for SOI-based MEMS integration with SiN waveguides for broadband optical switching solutions was successfully validated in this thesis. This methodology used a unique design approach to develop SOI-based MEMS device prototypes through commercially available multi-user microfabrication process like PiezoMUMPs, to validate different MEMS designs before integration with SiN waveguides in a more complex fabrication process.

First, in chapter 5 of this thesis, a translational MEMS platform design was fabricated using the PiezoMUMPs process. The design validation process resulted in a better understanding of some key aspects like the impact of fabrication variations in the comb drive structure upon an electrostatic actuator that can limit the maximum uniform translational displacement achieved by the device. Combining such variations with a soft spring structure led to rotational behavior in the device motion. Optical simulations provided an insight into the SiN channel waveguide dimensions and the importance of inverted tapers near the coupling region for optimal transmission between two such waveguides. These simulations also helped in understanding the minimum displacement required to integrate SiN waveguides in a 1 x 3 switching configuration based upon the minimum gap between adjacent waveguides with inverted tapers in the coupling region. The combination of parallel plate electrostatic actuators with single beam spring structures helped us in eliminating the rotational behavior in the next generation of translational MEMS platform devices. Careful implementation of mechanical stoppers for the lateral switching actuator also helped us in achieving the maximum displacement of 3.37 μm at 65 V after pull-in. The impact of air gap upon transmission between two butt-coupled SiN waveguides (one suspended and one fixed) was also investigated through optical simulations. This result led to the implementation of a serpentine spring system to connect the central platform designed for optical waveguides with the switching actuator. The unique design choice of using the platform designed to house suspended waveguides as another actuator, and using the interface designed for butt-coupling between suspended and fixed waveguides as a mechanical stopper enabled closing the air gap completely between the

suspended platform and the fixed substrate in the MEMS devices tested. This gap closing actuator could displace the platform along a direction perpendicular to the displacement direction enabled by the lateral switching actuator. The maximum displacement achieved by the gap closing actuator was 4.26 µm at 50 V.

Second, in chapter 6 of this thesis, an iteration of the translational MEMS platform was successfully integrated with SiN waveguides for broadband optical switching. The digital actuation provided by the MEMS design enabled optical switching in a first of its kind 1 x 3 SiN photonics switch. The microfabrication process developed by AEPONYX Inc. allowed us to integrated SiN waveguides with SOI-based MEMS that use a thick device layer of 59 µm. FEM simulations were used to analyze the impact of Si device layer thickness upon the effect of residual stress from SiN waveguide and SiO_2 cladding integration with SOI-based MEMS. This insight led to the choice of SOI wafers with thick Si device layer. Use of a serpentine spring system for both switching and gap closing actuators allowed us to keep the voltage minimum for our translational MEMS platform design with a 59 µm Si device layer. The gap closing actuator enabled minimizing the air gap between suspended and fixed waveguides in all three switching positions (left, center and right) using an actuation voltage of 80 V. While the center waveguide channel could be used with just the gap closing actuator, left and right waveguide channels could be enabled digitally through electrostatic pull-in while actuating the relevant switching actuator at 170 V. The three samples tested demonstrated an average insertion loss in the range of 4.64 dB to 5.83 dB over the wavelength range of 1530 nm to 1580 nm. Detailed analysis of fabricated samples provided crucial insights into the dependence of optical loss upon misalignment between suspended and fixed waveguides that is caused by fabrication variations in the mechanical stopper gap dimensions. Also, our findings revealed that the etch profile for the optical stack of SiN waveguides and SiO_2 cladding does not allow the air gap to close completely between suspended and fixed waveguides upon actuation of the gap closing actuator. These insights helped in developing the next generation of devices to minimize optical loss while increasing the port count for the optical switch.

The fabrication technology developed by AEPONYX Inc. for integration of SiN optical waveguides with MEMS structures used C-SOI wafers with fixed cavity size. This restricted the space available for MEMS release leading to an alternative MEMS design that could provide large lateral displacement required for potential integration with SiN waveguides with more waveguides while lowering the actuation voltage. This approach led to the development of a new MEMS actuator design presented in chapter 7 of this thesis. The prototype MEMS device was designed and fabricated using the commercially available PiezoMUMPs process. This process allowed us to integrate AlN-based piezoelectric actuation with a translational MEMS platform to provide an out-of-plane displacement of the central platform. A unique combination of cantilever style spring system anchored at one end, and parallel plate actuator provided large displacement with the lateral electrostatic actuators. The central platform could displace 5.9 µm along the positive X-axis, and 5.8 µm along the negative X-axis, with analog control. Electrostatic pull-in phenomena could be used to displace the platform 8.8 µm at 101 V and 8.5 µm at 102 V along the positive and negative X-axis respectively, with digital control. The longitudinal electrostatic actuator could provide displacement of 2.2 µm at 78 V along negative Y-axis while reducing the 600 nm initial misalignment between suspend central platform and the fixed substrate to 50 nm or less beyond 50 V. The initial misalignment due to residual stress was caused by the piezoelectric actuator material deposited on the central platform. This demonstrated the ability of the MEMS design to compensate for a potential misalignment between different optical components when integrated with SiN waveguides in a future implementation of the device. The piezoelectric actuator integration also enabled up to 200 nm of platform displacement along positive Z-axis at -10 V, and 100 nm of vertical displacement along positive Z-axis at +10 V. This integration of electrostatic and piezoelectric actuator using PiezoMUMPs technology for enhanced motional capabilities was the first of its kind demonstration of such a MEMS actuator.

Finally, an enhanced iteration of SiN waveguide integration with SOI-based MEMS was demonstrated as a 1 x 5 optical switch in chapter 8 of this thesis. The enhanced displacement of the switching actuator using the MEMS design validated through PiezoMUMPs technology

earlier helped in getting analog control over switching in three SiN waveguide channels to minimize optical loss. The pull-in phenomena could again be utilized to enable two additional SiN waveguide channels completing the 1 x 5 configuration. Findings from this optical MEMS switch demonstration also allowed insights into the impact of residual stress along different areas of the platform which can impact the device performance through variation in the optical misalignment between suspended and fixed waveguides. Switching actuation voltage could be reduced to a maximum of 90 V in comparison to the 1 x 3 switch demonstration by incorporating the actuator design from the hybrid MEMS protype developed earlier in this thesis. The analog control over three channels enabled an average insertion loss of 2.2 dB to 4.7 dB in the wavelength range of 1540 nm to 1625 nm. The digital channels had an average insertion loss of 5.4 dB to 7.5 dB over the same wavelength range. This was a significant improvement over the capabilities of the previously demonstrated 1 x 3 SiN photonics switch with the same cavity size C-SOI wafer.

Passive optical networks based upon the NG-PON2 standard can benefit from the SiN photonics switch developed in this thesis. Typically, such networks required receivers with 4 to 8 channels. The broadband switch implemented in this thesis can be implemented in such networks for telecommunication applications with low-power operation due to electrostatic actuation. Since the technology demonstration in this thesis allows SiN waveguide integration with SOI-based MEMS, the output SiN waveguides can be modified independently during the design process to develop an energy efficient wavelength channel selection system. Each output waveguide can be configured with different optical filters to realise such a device.

Moreover, this thesis presented a reliable methodology to design and implement MEMS integrated SiN photonics devices through MEMS prototyping using low-cost multi-user processes like PiezoMUMPs. Challenges such as air gap between suspended and fixed waveguides, misalignment due to residual stress between suspended and fixed SiN waveguides, MEMS integrated optical switching with analog control over multiple switching channels were addressed during this thesis to provide efficient MEMS-based SiN photonics

switching solutions with minimum optical loss. Batch processing of devices developed during this thesis can allow low-cost and energy-efficient implementation of broadband SiN photonics switching moving away from thermally tuned energy-intensive existing SiN photonics switching solutions that are restricted over a small wavelength range.

In conclusion, the most significant scientific contributions of this thesis stem from the identification of the key factors that currently limit MEMS integration with SiN-based optics, and successful implementation of MEMS and optical design approaches that help mitigate these limitations. These contributions are:

- Translational motion of a MEMS platform with comb drive based electrostatic actuation can be susceptible to rotational behaviour before pull-in due to fabrication variations in the comb drive fingers. Use of parallel plate actuators can help mitigate this design risk where use of mechanical stoppers can allow large displacement after electrostatic pull-in. Such large displacement can be utilized to integrate the MEMS platform with adjacent SiN waveguides with the required spacing for minimum crosstalk in a digitally controlled SiN optical switch.

- SiN waveguide integration over SOI-based MEMS structures leads to residual stress in the suspended Si. This residual stress increases the optical loss due to misalignment between waveguides. Use of thick Si device layer helps mitigate this residual stress challenge and increases the transmission efficiency of the optical signal between suspended and fixed waveguides.

- MEMS release in a SOI substrate leads to air gaps between suspended and fixed parts of the MEMS structures. These gaps are necessary for mechanical movement of the microstructure upon actuation. However, this intrinsic MEMS design limitation leads to air gap(s) between suspended and fixed waveguides upon integration. Use of the interface between suspended and fixed waveguide in the coupling region as a mechanical stopper

while keeping both the parts grounded during actuation allows closing the air gap to minimize optical loss between coupled waveguides in all switching positions.

- The etch profile of the optical stack that consists of SiN waveguides with SiO_2 cladding creates a residual air gap even when the air gap between the Si MEMS layer underneath the optical stack is closed completely. Use of inverted taper waveguides helps minimize the impact of this residual air gap upon optical loss.

- Increasing the number of waveguides over the suspended MEMS platform can induce, slight yet critical, vertical misalignment between suspended and fixed waveguides even when a thick Si device layer SOI wafer is used for the MEMS part. The electrostatic actuators used for switching and air gap closing motion can also minimize such misalignment by vertical displacement of the misaligned suspended platform inline towards the fixed substrate.

- Microfabrication variations are extremely important for successful implementation of a digitally controlled MEMS optical switch that relies upon electrostatic pull-in for different switching channels. Such losses can be mitigated with analog control over switching channels, with the use of a single beam spring system. Such spring system can be combined with parallel plate actuators for large displacement in a small device footprint in comparison to a similar device footprint with a doubly clamped spring system.

- 3 DOF is important in planar optical switching fabrics for fine alignment of optical components. Integration of piezoelectric actuation with electrostatic actuation using PiezoMUMPs technology allows development of an energy-efficient 3 DOF MEMS device. Such a device can provide large displacement along X-axis and Y-axis through electrostatic actuators. This bi-axial motion can be used to form an integrated SiN optical switch. Piezoelectric actuators can provide the requisite motion along Z-axis for fine alignment of different parts of the device.

- The first of its kind, 1 x 3 and 1 x 5 SiN optical switches that integrate low-power electrostatic actuators with SiN waveguides for broadband optical switching.

- The first of its kind, 3 DOF hybrid MEMS actuator that integrates electrostatic and piezoelectric actuators using the PiezoMUMPs technology.

This thesis led to to four articles (three published and one submitted after major revision) in four different peer-reviewed scientific journals (i.e., Micromachines, Optics Express, Journal of Microelectromechanical Systems, and Journal of Lightwave Technology). Research milestones during this project were also presented and published in two top international conferences in the field of optics (i.e., Optical Fiber Communication (OFC 2022) and European Conference on Optical Communication (ECOC 2022)). Two patent applications also stemmed from this thesis.

The ever-growing demand for optical data centers around the world is increasing faster than ever. The recent surge in generative artificial intelligence further elevates the global power consumption of data centers, creating an urgent need for energy-efficient systems at all levels. Potential implementation of the broadband optical switches developed in this thesis can create an impact towards energy-efficient NG-PON2 access networks with low-cost manufacturing at high volumes. Independent control over SiN-based optical components, and SOI-based MEMS design can allow deployment of wavelength selective devices such as receivers at large scale. SiN-based optical switching in planar optical switching fabrics has largely relied upon thermal tuning of SiN optical components. The optical switches demonstrated in this thesis provide an energy-efficient approach towards the replacement of such components. Integration of low-power electrostatic and piezoelectric actuators with SiN waveguides for efficient optical switching is an important step towards meeting this ever-growing demand.

RECOMMENDATIONS

Based on this work, the following recommendations can be made for future work:

- The microfabrication process to integrate SiN optics with SOI-based MEMS can be optimized to improve the etch profile of the optical stack to achieve a more vertical etch to improve the optical transmission between suspended and fixed waveguides through elimination of the residual air gap limitation.

- The implementation of AlN piezoelectric layer with the integrated photonics device demonstrated in this thesis can allow vertical displacement to compensate any misalignment resulting from residual stress.

- A MEMS design where the input waveguide can be fabricated over the spring structures can allow a 1 x 5 switch with only one air gap instead of the current design limitation of two air gaps between suspended and fixed waveguides. Such MEMS design implementation can reduce the optical loss in half which can catapult the use of such integrated system in the industry.

- Surface grating couplers can be optimised further to reduce the undulations in the transmission spectra thereby increasing the operational wavelength range for the switch.

- Optical filters such as ring resonators and micro disc resonators can be implemented with output waveguides on the fixed substrate to configure an energy-efficient wavelength channel selection system.

- The development of a latch and lock mechanism for the MEMS actuator can allow zero voltage operation in any switching position.

APPENDIX I

MEASURED TRANSMISSION SPECTRA FOR THE THREE SWITCHING POSITIONS OF THE THREE SAMPLES IN CHAPTER 6 'INTEGRATED 1 X 3 MEMS SILICON NITRIDE PHOTONICS SWITCH'

The tunable laser used for optical measurements provides scans covering the wavelength range of 1500 nm to 1630 nm. The transmission power was measured in dBm using the EXFO CT440 optical component tester for the three samples. The spectral response for samples 1, 2, and 3 is shown in Figure-A II-1, Figure-A II-2, and Figure-A II-3, respectively. This includes the transmission power measured for the reference waveguides fabricated alongside each sample on the same die. The crosstalk in the left and right switching channels during transmission in the center channel with the gap closing actuator ON is also shown for each sample in the corresponding figure. Sample 1 and 2 show lower undulations in their wavelength response below 1600 nm whereas sample 3 shows low undulations only between 1560 nm and 1600 nm. Sample 2 also shows larger variations across switching positions, which corresponds to the measured fabrication variation explained in section 6.4 (see Table 6.1).

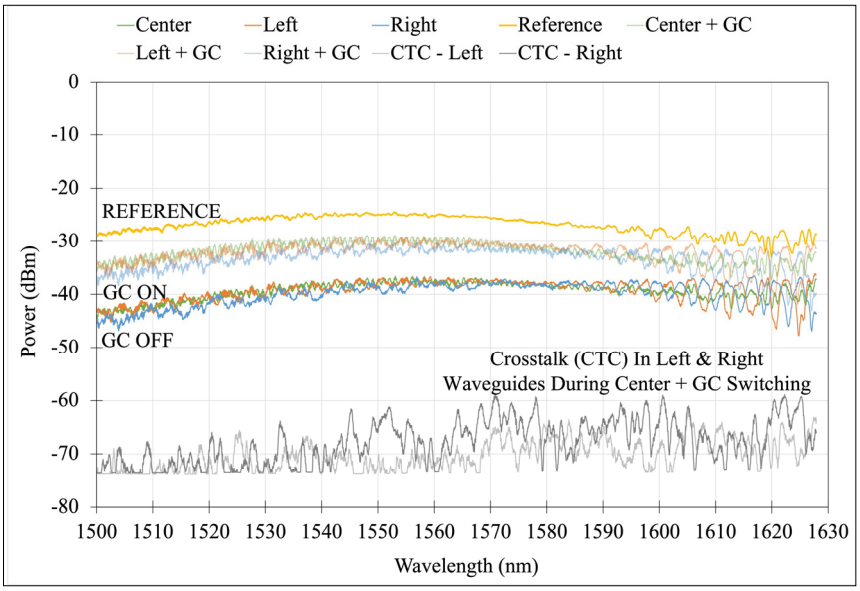

Figure-A I-1 Transmission power for sample 1 across 1500 nm – 1630 nm for in all three switching positions with and without gap closing actuator

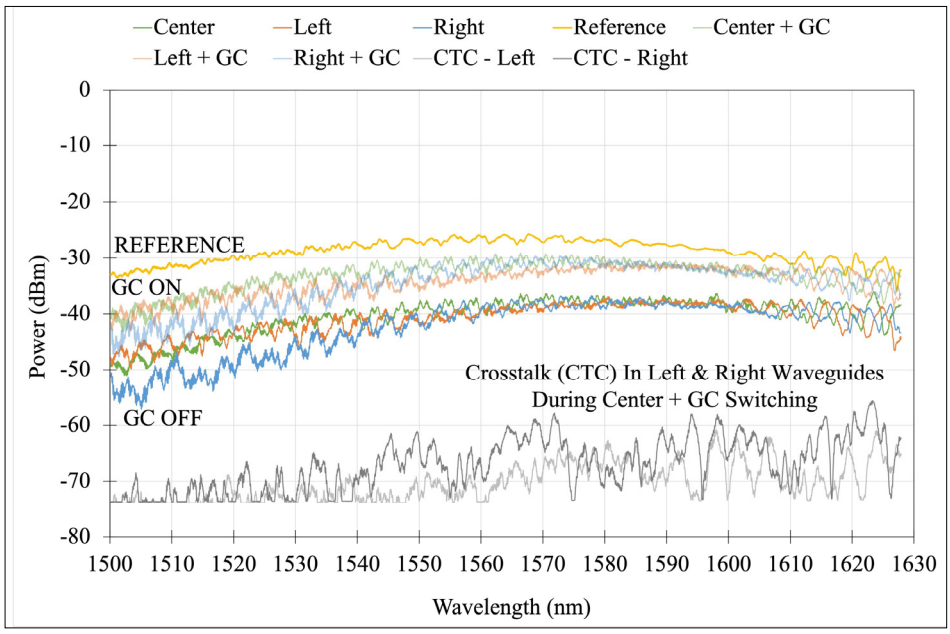

Figure-A I-2 Transmission power for sample 2 across 1500 nm – 1630 nm for in all three switching positions with and without gap closing actuator

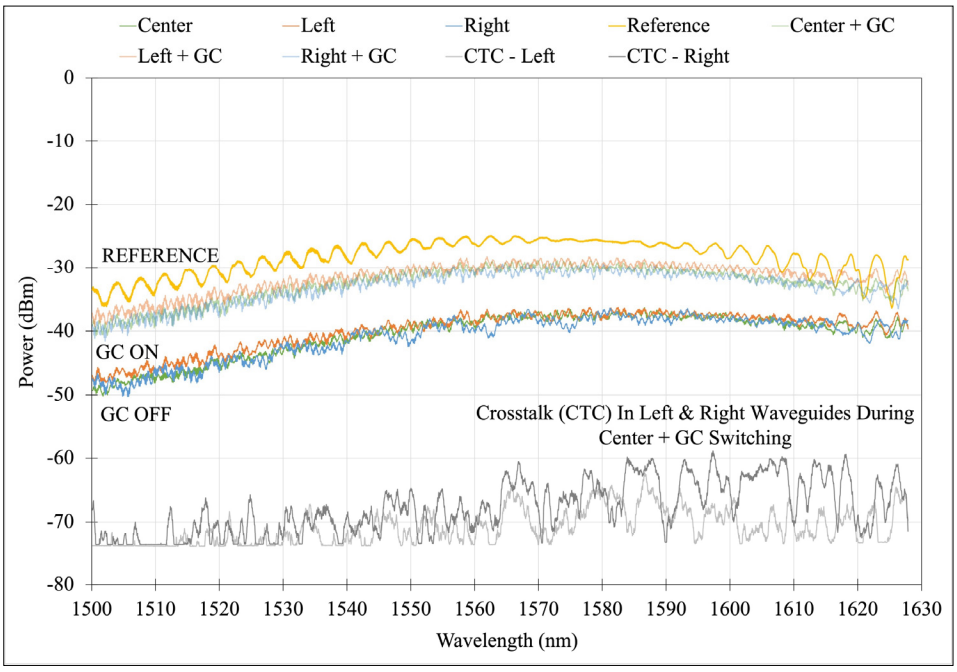

Figure-A I-3 Transmission power for sample 3 across 1500 nm – 1630 nm for in all three switching positions with and without gap closing actuator

APPENDIX II

MEASURED TRANSMISSION SPECTRA FOR THE FIVE SWITCHING POSITIONS OF THE TWO SAMPLES IN CHAPTER 8 'AN INTEGRATED 1 X 5 MEMS SILICON NITRIDE PHOTONICS SWITCH'

The transmitted power measured for the two samples over the wavelength range of 1540 nm to 1625 nm in all five switching positions with and without gap closing actuation is shown in Figure-A II-1. The transmission through the reference waveguides used for normalization is also shown in Figure-A II-1 for both samples.

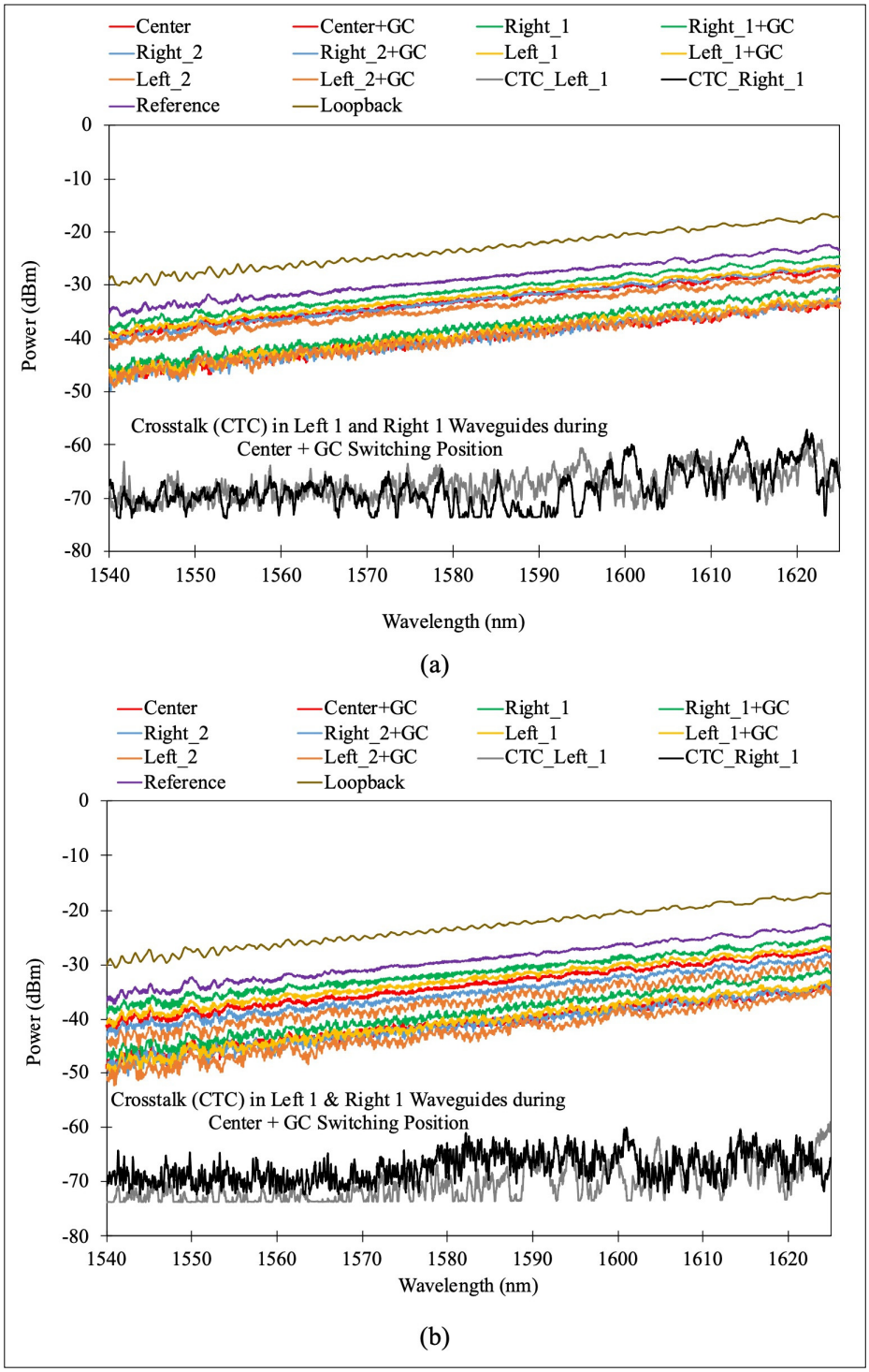

Figure-A II-1 Transmission power between 1540 nm and 1625 nm in the reference waveguide and all of the five switching positions with and without the GC actuator activated for (a) sample 1 and (b) sample 2 when injected with an input optical signal of 10 dBm

APPENDIX III

DIGITALLY CONTROLLED SILICON NITRIDE OPTICAL SWITCH

Suraj Sharma[1], Niharika Kohli[1,2], Jonathan Brière[3], Frederic Nabki[1], and Michaël Ménard[1]

[1]Department of Electrical Engineering, École de Technologie Supérieure, Montreal, Quebec H3C 1K3, Canada

[2]CMC Microsystems, Montreal, Quebec H3C 6M8, Canada

[3]AEPONYX Inc., Montreal, Quebec H3C 2M7, Canada

Conference paper published in 2022 *Optical Fiber Communication Conference and Exhibition (OFC)*, March 2022

Abstract

We report the first 1 x 3 silicon nitride optical switch using silicon electrostatic MEMS actuator with a 4.97 dB average insertion loss over the 1530 nm to 1580 nm wavelength range.

1. Introduction

Previous silicon nitride (SiN) photonic switches relied upon thermo-optic tuning of optical components, such as Mach-Zehnder multi-mode interferometers. (Qiu et al., 2021; Nejadriahi et al., 2020). This tuning method consumes high power in comparison to electrostatically actuated microelectromechanical systems (MEMS) based optical switching solutions. Most of the MEMS based optical switches were designed for integration with silicon (Si) based photonics (Wu et al., 2019). While Si waveguides enable compact photonic circuits with moderate propagation loss, SiN waveguides have a wider operating wavelength range with lower propagation loss (Blumenthal et al., 2018). MEMS integration with SiN waveguides has been limited (Jin et al., 2018; Briere et al., 2017) due to design challenges presented by stress related deformations of suspended silicon structures covered with cladding and waveguide

materials. In this work, we demonstrate experimentally the first 1 x 3 optical switch based upon the integration of SiN waveguides with a bi-axial translational silicon-on-insulator (SOI) MEMS platform.

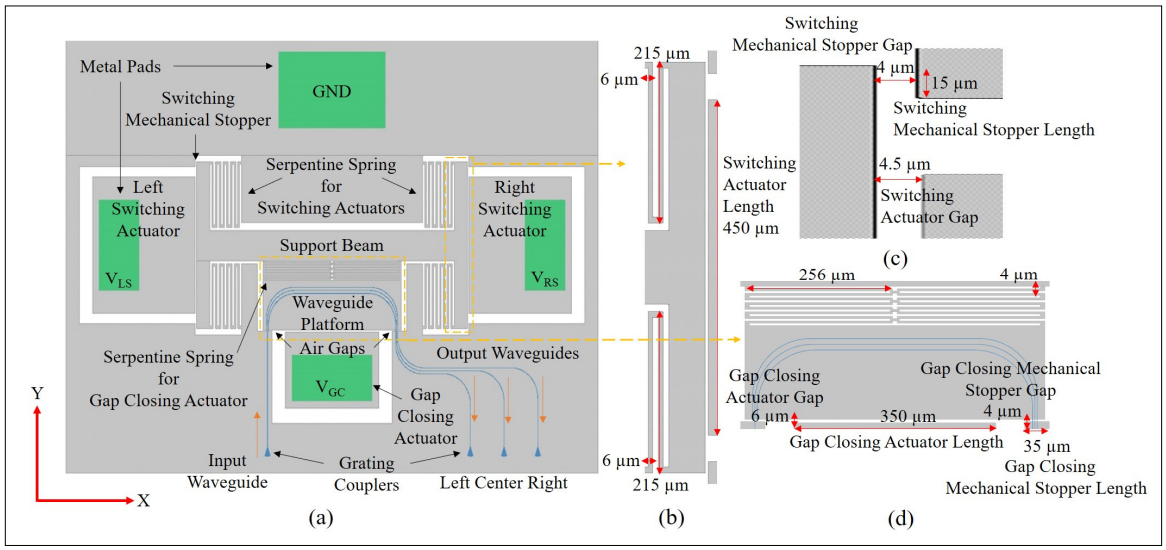

Figure-A III-1 (a) 1 x 3 optical switch with: (b) spring, (c) switching actuator, and (d) gap closing actuator dimensions

2. Device Design

Figure-A III-1 shows a schematic of our translational MEMS switching platform in a 1 x 3 planar switching configuration. The input SiN waveguide is designed over a fixed portion of Si. The three switching waveguides are located over a suspended Si MEMS platform and fixed Si. The suspended waveguide platform can be displaced bidirectionally along the x-axis by actuating the left and right switching actuators. This enables switching in the corresponding left and right output waveguides. The support beam and the independent serpentine spring also enables unidirectional motion of the waveguide platform in the negative y-axis direction. This motion of the suspended platform enables closing of the two air gaps between suspended and fixed waveguides. Hence, we refer to this as the gap closing actuator. If only the gap closing actuator is actuated, the input waveguide is aligned to the center output waveguide. This gap

closing motion can be used in the left and right switching positions as well. Each actuator works based upon the principle of electrostatic pull-in. The parallel plate actuator design enables digital actuation of the waveguide platform in the desired switching positions with minimal optical loss. Figure-A III-1(b) shows the spring and actuator dimensions for the switching actuator. Figures-A III-1(c) and III-1(d) show the actuator gap and mechanical stopper gap dimensions for the switching and gap closing actuators, respectively. The mechanical stopper gap dimension is less than the actuator gap dimensions to prevent any electric shorts between the grounded and high voltage actuator plates upon electrostatic pull-in. The switching and gap closing actuators are designed to operate at 140 V and 62 V, respectively.

3. Microfabrication and Experimental Setup

A 435 nm thick SiN waveguide layer was cladded with 3.2 µm of top and bottom silicon oxide (SiO2). This optical stack was integrated on a silicon-on-insulator (SOI) wafer with a 59 µm thick Si device layer. The microfabrication process followed was similar to our previous work where we integrated SiN waveguides with a rotational MEMS platform (Briere et al., 2017). Simulation results showed that a 59 µm thick device layer produces only 10 nm of stress related deformation upon integration with SiN waveguides and SiO2 cladding. In comparison, a 10 µm device layer would result in 600 nm of deformation of the waveguide platform. The SiN waveguide cores are 450 nm wide and are surrounded by 12.3 µm of cladding on each side. Inverted tapers with a tip-width of 400 nm and a 20 µm length were included at the fixed and suspended waveguide interfaces. This was done to minimize the optical losses. The microfabrication process used requires a minimum gap of 4 µm between the fixed and suspended waveguides for successful release of the MEMS structure underneath. High resolution scanning electron microscope (SEM) images of the fabricated devices are shown in Figure-A III-2. The mechanical stopper gap dimension came out to 4.74 µm as shown in Figure-A III-2(b) instead of the 4 µm designed dimension presented in section 2. Similar variations in fabricated device dimensions were observed for the actuator gap. These variations

increased the operational voltage for both switching and gap closing actuators. The etch profile of the optical stack is shown in Figure-A III-2(c). This etch profile leads to a residual air gap

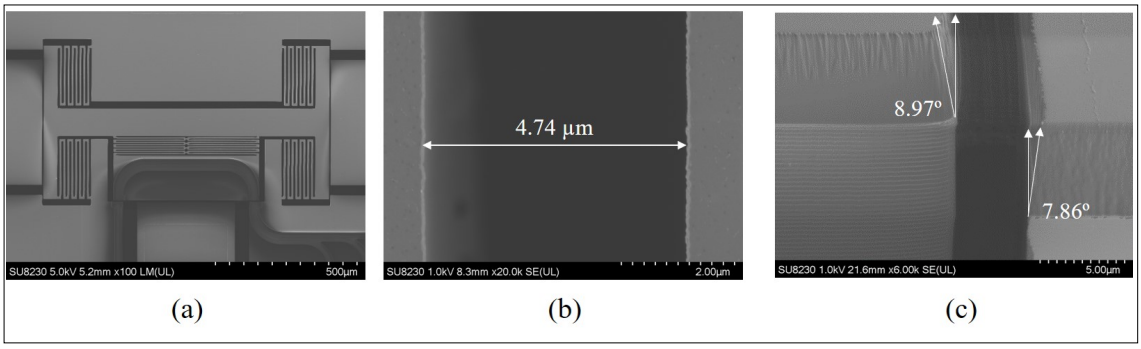

Figure-A III-2 (a) Fabricated 1 x 3 optical switch, (b) switching mechanical stopper gap, and (c) optical stack etch profile

of 1 µm between suspended and fixed SiN waveguides. The impact of these fabrication results is discussed in section 4.

The test setup used for the optical characterization of the device is shown in Figure-A III-3(a). The fabricated device was wirebonded to a custom printed circuit board designed to control actuation during optical measurements. A tunable laser (T100S-HP) and optical component tester (CT440) from EXFO were used for these measurements. The output of the tunable laser was connected to the input of an optical fiber array with a 30º polish angle through the optical component tester. The fiber array was aligned with the surface grating couplers (SGCs) of the input and output waveguides at a vertical distance of 50 µm. Three detector ports on the optical component tester were connected to the output optical fibers from the fiber array. Polarization maintaining fibers were used to maintain the transverse electric (TE) mode during characterization. The SGCs used were optimized for the TE polarization. A microposition controller was used to align the sample to fiber array with 1 µm precision. All three switching positions were characterized with the gap closing actuator in the ON and OFF configurations to demonstrate the impact of the actuator on the optical loss. Only closing the gap actuator by applying 80 V was required for switching in the center output waveguide with minimal optical loss. The left and right switching actuators required 170 V for switching to the left and right

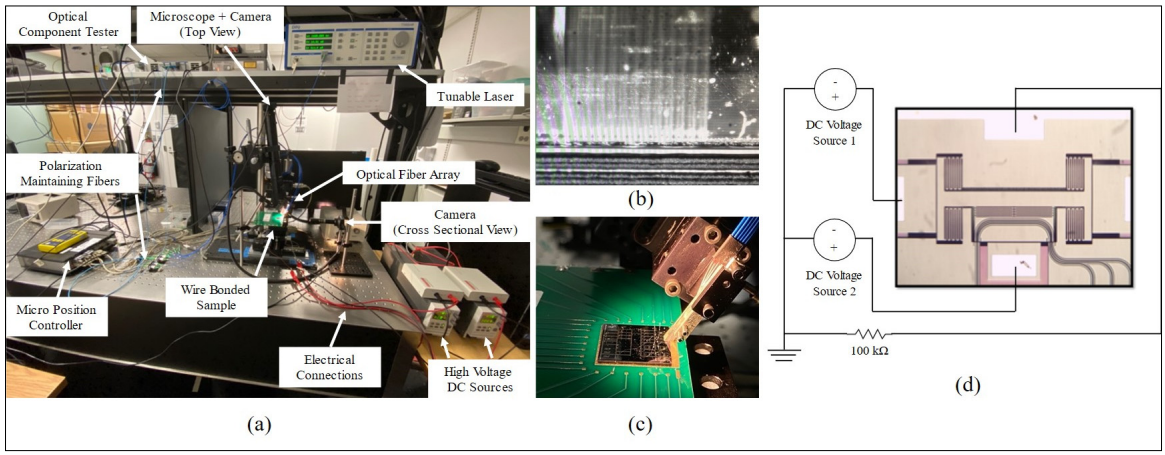

Figure-A III-3 (a) Optical characterization test setup, (b) optical fiber array aligned over the sample, (c) wire bonded sample during measurements, and (d) test circuit used for left channel switching and gap closing actuation

output waveguides, respectively. The gap closing actuator was turned on in these switching positions as well to minimize optical loss. Results from these measurements are presented in section 4.

4. Results and Discussion

Figure-A III-4(a) shows normalized transmission data for a device in three switching positions with the gap closing (GC) actuator ON and OFF. The SGCs used were optimized for a wavelength range of 1530 nm to 1580 nm. The undulations observed in the experimental results come from the SGCs. Similar undulations were observed in our reference waveguide structures. Outside the wavelength range shown, these undulations increase and require further optimization of our SGC. The average insertion loss measured over the wavelength range of 1530 nm – 1580 nm for all switching positions are shown in Figure-A III-4(b). A minimum average insertion loss of 4.97 dB with a maximum loss reduction of 7.74 dB obtained by closing the gap was observed at the center switching position. The loss at the center position is attributed in part to the residual 1 µm distance between the suspended and fixed waveguides once the gap is closed. Moreover, the fabricated switching mechanical stopper gap of 4.74 µm vs the 4 µm originally designed causes misalignment between the suspended and fixed

waveguides in the left and right switching positions, increasing insertion losses. Figure-A III-4(c) shows the impact of the reduction in air gap between suspended and fixed waveguides at

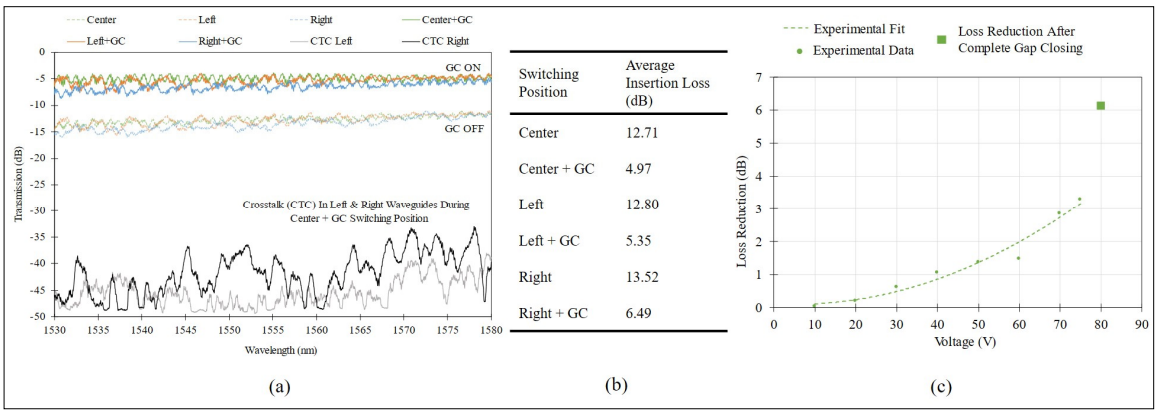

Figure-A III-4 (a) Transmission data in all switching positions with/without gap closing actuator across the 1540 nm – 1580 nm wavelength range, (b) average insertion loss in all switching positions, and (c) optical loss reduction in the center waveguide with increase in gap closing actuator voltage

the center switching position. Measurements in Figure-A III-4(c) were obtained at a wavelength of 1600 nm. The experimental results presented are focused on the C-band and initial L-band of the telecommunication spectrum. The waveguide configuration used in this prototype can be single mode and transparent from 1100 nm to 2200 nm with optimized SGCs.

5. Conclusion

We demonstrated the first digitally controlled SiN 1 x 3 MEMS optical switch. The novel air gap closing mechanism reduces optical losses by up to 7.74 dB providing a minimal optical loss of 4.97 dB in the center switching position. Further optimization of the optical stack etch profile can reduce losses in all switching positions. Analog (i.e., continuous) control of the switching actuator can further minimize losses and allow for an increased number of ports.

APPENDIX IV

1 x 5 SILICON NITRIDE MEMS OPTICAL SWITCH

Suraj Sharma[1], Niharika Kohli[1,2], Michaël Ménard[1], and Frederic Nabki[1]

[1]Department of Electrical Engineering, École de Technologie Supérieure, Montreal, Quebec H3C 1K3, Canada

[2]CMC Microsystems, Montreal, Quebec H3C 6M8, Canada

Conference paper published in *2022 European Conference on Optical Communication (ECOC)*, September 2022

Abstract

We demonstrate the first 1x5 electrostatic MEMS optical switch with silicon nitride waveguides that combines analog and digital control. It achieves average insertion losses between 2.2 dB and 5.39 dB for the five switching channels and operates over a wavelength range of 85 nm.

Introduction

Photonic switching technology has been proposed to implement access networks based on the next generation passive optical networks 2 (NG-PON2) standard with 4 to 8 switching channels (Inoue et al., 2018). Conventional silicon nitride (SiN) photonics based optical switching technology is energy inefficient because it relies on the thermal tuning of optical components, such as ring resonators and Mach-Zehnder interferometers, which consumes high power (Pan et al., 2020; Yong et al., 2022). Microelectromechanical systems (MEMS) based optical switching using electrostatic actuation consumes low power and provides broadband operation. Most MEMS based integrated optical switches are based on silicon (Si) photonics (Seok et al., 2015; Akihama et al., 2011) which complicates design by combining optical and

mechanical constraints. SiN waveguides can provide low propagation loss in comparison to Si waveguides and work over a wider wavelength range (Blumenthal et al., 2018). However, only a few MEMS based optical switches have been developed with integrated SiN photonics (McNulty et al., 2022; Briere et al., 2017). This work is a significant improvement upon our previous device that relied on MEMS based digital switching between SiN waveguides in a 1 x 3 switching configuration (Sharma et al., 2022). Here, our new MEMS based optical switch demonstrates analog control over three switching positions. The device also provides digital switching between 2 additional channel waveguides completing a 1 x 5 switching configuration. The 85 nm operational wavelength range between 1540 nm and 1625 nm is also an improvement on our previous SiN optical switch demonstration (Sharma et al., 2022).

Operating Principle

Our 1 x 5 optical switch relies upon two electrostatic parallel plate actuators on opposite sides of the platform shown in Figure-A IV-1(a). The left switching (LSW) and right switching (RSW) actuators can displace the platform with suspended waveguides by up to 5 μm with analog control, and by up to 8 μm with digital control in the left and right direction respectively, as per the top view of the device design shown in Figure-A IV-1(a). Mechanical stoppers of 10 μm in length on the opposite sides of each switching actuator prevents device shorting during digital switching, which relies upon the pull-in phenomenon of the electrostatic actuators. The unique single beam spring design anchors the device at two points towards the top of the structure. This cantilever like spring structure allows us to achieve large switching displacement with analog control in comparison to our previous work with the same serpentine spring structure allows the displacement of the platform in the downward direction upon actuation of the gap closing (GC) actuator as per the top view of the device design shown in Figure-A IV-1(a). This actuator relies upon the pull-in phenomenon to digitally close the two air gaps. The GC actuator allows closing the two air gaps between the suspended and fixed waveguides shown in the zoomed in views of the device in Figure-A IV-1(a). The reference

waveguide structure (i.e., loopback) shown in Figure-A IV-1(a) is used for the measurement of the coupling losses.

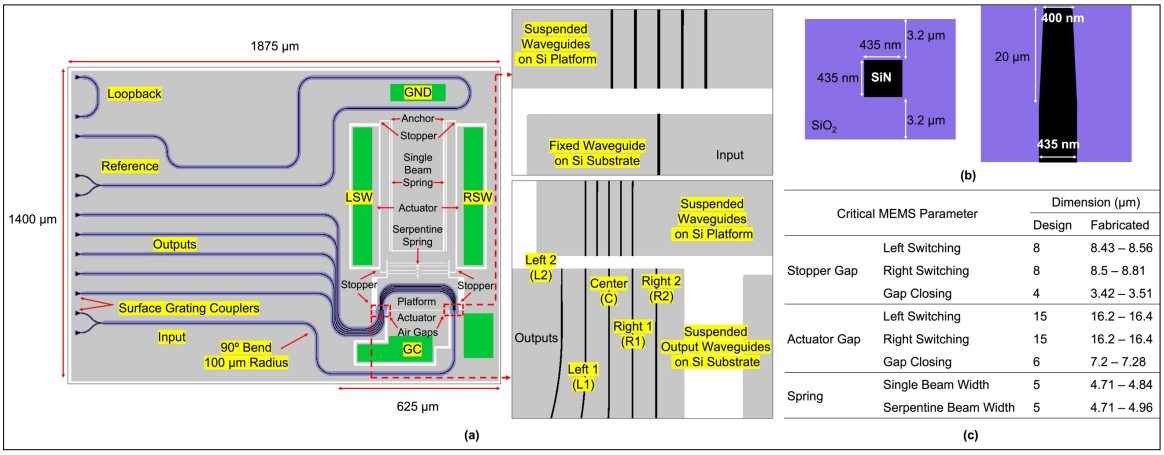

Figure-A IV-1 (a) Schematic of the 1 x 5 optical switch with zoomed in view of the waveguide interface at the edge of the platform, (c) cross-sectional view of the SiN waveguides with dimensions, and top view of the inverted tapers used near the edge of the switching platform, and (c) design vs fabricated dimensions for critical MEMS parameters

During analog actuation, the input waveguide shown in Figure-A IV-1(a) can be aligned to the center (C), left 1 (L1) or right 1 (R1) switching channel. The LSW and RSW actuators can be used for fine alignment between the suspended and fixed waveguides. Digital actuation after electrostatic pull-in of the switching actuators allows us to align the input waveguide to the left 2 (L2) or right 2 (R2) output waveguides. The GC actuator is used in all switching positions for efficient transmission of the optical signal between input and output waveguide channels. The SiN waveguide core dimensions are 435 nm by 435 nm with 3.2 µm thick top and bottom silicon oxide (SiO2) claddings as shown in Figure-A IV-1(b). The inverted taper design of waveguide core also shown in Figure-A IV-1(b) near the air gaps minimizes optical loss during switching. The key MEMS parameters along with the designed and fabricated dimensions are presented in Figure-A IV-1(c). The effects of fabrication variations on the different switching positions and the actuation voltage are discussed below.

Microfabrication and Experimental Setup

The 1 x 5 optical switch was fabricated through a proprietary microfabrication process by AEPONYX Inc., which also used to fabricate our previous 1 x 3 optical switch (Sharma et al., 2022). The layers forming the optical waveguides are grown and patterned over a cavity silicon-on-insulator (CSOI) wafer with a 59 µm thick Si device layer and predefined cavities to facilitate the release of the MEMS. The MEMS are patterned and etched in the device layer after fabrication of the waveguides. Scanning electron microscope (SEM) imaging was used

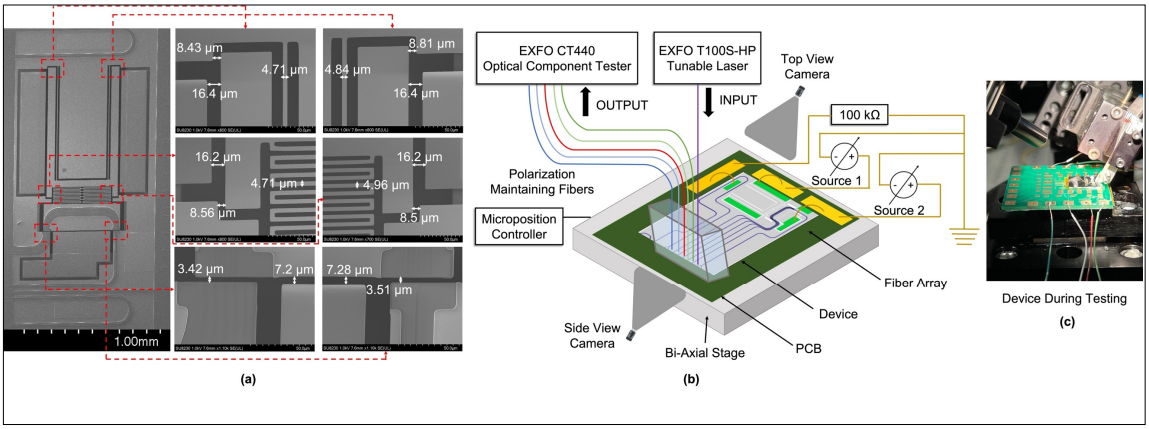

Figure-A IV-2 (a) SEM image of the fabricated 1 x 5 optical switch, (b) schematic of the optical characterization test setup with the test circuit used for MEMS actuation with RSW and GC actuation, and (c) wirebonded sample during measurements

to measure the fabricated dimensions and are shown in Figure-A IV-2(a).

A schematic of the test setup used is shown in Figure-A IV-2(b). The test device was wirebonded to a custom printed circuit board (PCB). The PCB was then placed on a bi-axial stage controlled with a microposition controller that is also used to move the fiber array vertically over the sample for fine alignment. An input optical signal from a T100S- HP laser from EXFO is coupled through the fiber array to the input waveguide using a surface grating coupler (SGC) on the fabricated device. The actuators of the optical switch are connected to two high voltage DC sources as per the test circuit shown in Figure-A IV-1(b). The optical

signal is switched between the different output waveguides in all five switching positions during these measurements. We measured the transmission response in all switching positions with and without the GC actuator. Light from the SGCs on the output waveguides couples to the fiber array and is detected with a CT440 optical component tester from EXFO. Polarization maintaining fibers were used to measure the transmission response of different switching positions for the transverse electric (TE) mode only since our SGCs were optimized for this polarization.

Results and Discussion

Figure-A IV-3(a) shows the normalised transmission data in the five switching positions with the GC actuator in ON and OFF state. The optical switch operates in the wavelength range of 1540 nm to 1625 nm. The range is limited by the bandwidth of the SGCs and not by the switch. The fluctuations in the transmission curve come from the SGCs used for optical coupling between the fiber array and the waveguides. The reference waveguide structure shown earlier in Figure-A IV-1(a) was used for normalization of the transmission data and calculation of the average insertion loss over the wavelength range presented in Figure-A IV-3(a). The average insertion loss in all five switching positions with the GC actuator ON is shown in Table-A IV-

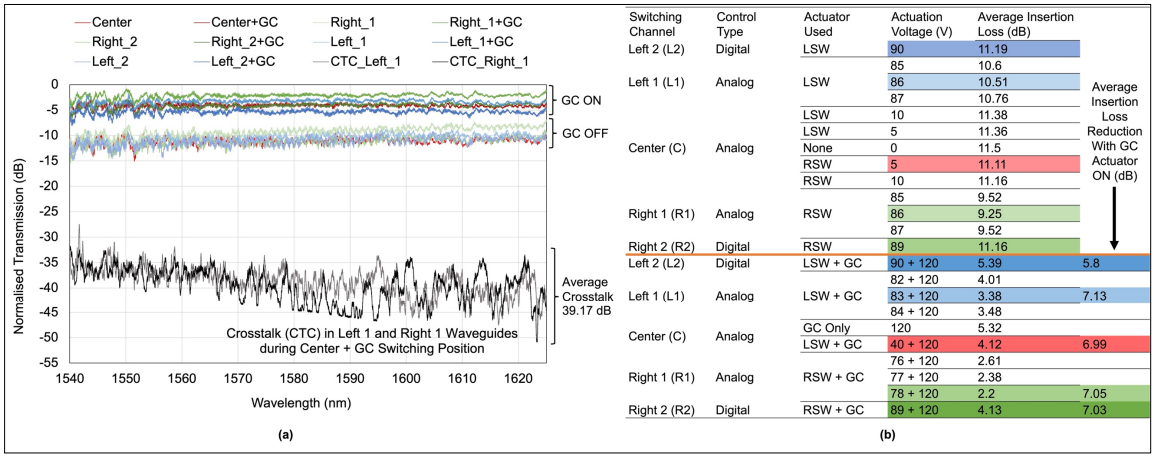

Switching Channel	Control Type	Actuator Used	Actuation Voltage (V)	Average Insertion Loss (dB)	Average Insertion Loss Reduction With GC Actuator ON (dB)
Left 2 (L2)	Digital	LSW	90	11.19	
Left 1 (L1)	Analog	LSW	85	10.6	
			86	10.51	
			87	10.76	
Center (C)	Analog	LSW	10	11.38	
		LSW	5	11.36	
		None	0	11.5	
		RSW	5	11.11	
		RSW	10	11.16	
Right 1 (R1)	Analog	RSW	85	9.52	
			86	9.25	
			87	9.52	
Right 2 (R2)	Digital	RSW	89	11.16	
Left 2 (L2)	Digital	LSW + GC	90 + 120	5.39	5.8
Left 1 (L1)	Analog	LSW + GC	82 + 120	4.01	
			83 + 120	3.38	7.13
			84 + 120	3.48	
Center (C)	Analog	GC Only	120	5.32	
		LSW + GC	40 + 120	4.12	6.99
Right 1 (R1)	Analog	RSW + GC	76 + 120	2.61	
			77 + 120	2.38	
			78 + 120	2.2	7.05
Right 2 (R2)	Digital	RSW + GC	89 + 120	4.13	7.03

Figure-A IV-3 (a) Normalised transmission response of the 1 x 5 optical switch tested in all switching positions with GC actuator in ON and OFF states, (b) fine alignment capability shown by average insertion loss measurements in the wavelength range of 1540 nm to 1625 nm at different actuation voltages, and average insertion loss reduction with the GC actuator in ON state

1. The table also compares the results for this device with our previous digitally controlled 1 x 3 SiN optical switch.

Insertion loss in the three switching positions controlled through analog motion of the switching actuator before electrostatic pull-in allows fine alignment between the suspended and fixed waveguides. Thus, lower losses are observed in the L1, C, and R switching channels compared to other channels. The switching channels at the extremities, L2 and R2, rely on digital control of the switching actuator based on electrostatic pull- in, hence they show similar performance to the 1x3 digital switch in (Sharma et al., 2022). The alignment between the suspended and fixed waveguides for the L2 and R2 switching positions is limited by the precision in the fabrication of the stopper gap, which can vary from of 430 nm to 881 nm as

Table-A IV-1 Device performance comparison

Switch Type	**Average Insertion Loss**				
	L2	**L1**	**C**	**R1**	**R2**
1x5 This work	5.39	3.38	4.12	2.2	4.13
1x3 Sharma et al. 2022	5.35	NA	4.97	NA	6.49

shown in Figure-A IV-1(c). Therefore, higher optical losses are observed in the two outermost channels.

The lowest average insertion loss (2.2 dB) was obtained for the R1 channel with analog control whereas the maximum average insertion loss was 5.39 dB for the L2 channel with digital control. It should be emphasized that this loss includes two air gaps (although closed), thus the per-gap-loss to about half of this value. The variation in optical loss between channels with analog control could be due to the residual stress variation caused by the waveguide and cladding layers across the suspended platform. Such residual stress can cause out-of-plane misalignment between the waveguides. The average crosstalk in adjacent waveguides for all five switching positions with the GC actuator ON was less than 36 dB. The fine alignment capability of the device is shown in Figure-A IV-3(b) with the impact of variations in voltage

on the average insertion loss at different switching positions. The impact of the GC actuator on the optical losses is also shown in Figure-A IV-3(b).

Conclusion

We demonstrated the first 1 x 5 SiN optical switch with analog and digital control through electrostatic MEMS actuation. The novel actuation mechanism allows us to finely align in three switching positions with minimum average insertion loss in the range of 2.2 dB – 4.12 dB. Average insertion loss in the two additional switching positions range between 4.13 dB – 5.39 dB. The demonstrated wavelength range of 85 nm between 1540 nm – 1625 nm is an improvement over our previous optical switch that had a 50 nm operational wavelength range between 1530 nm – 1580 nm (Sharma et al., 2022). Optimization of the residual stress in the optical layers fabricated over suspended Si platform can improve device performance with minimum loss variation between different switching positions.

APPENDIX V

DESIGNING A 1 X 3 MEMS-BASED SIN OPTICAL SWITCH

In this appendix, the methodology for analytical designing of an electrostatic MEMS actuator that can be integrated with SiN waveguides for optical switching is presented in detail. Integration of multiple waveguides with MEMS to realize a 1 x 3 optical switch includes careful consideration of several factors such as degree-of-freedom, targeted displacement, and actuator and spring design. These factors are discussed in detail in this appendix.

Degree-of-freedom

A MEMS-based 1 x 3 optical switch with integrated waveguides would require switching of optical signal from the input waveguide into the 3 output waveguides selectively. In case of butt-coupled SiN waveguides fabricated over SOI-based MEMS, such switching can be achieved by designing, a MEMS platform that can move the output waveguides laterally in-plane, as shown in Figure-A V-1.

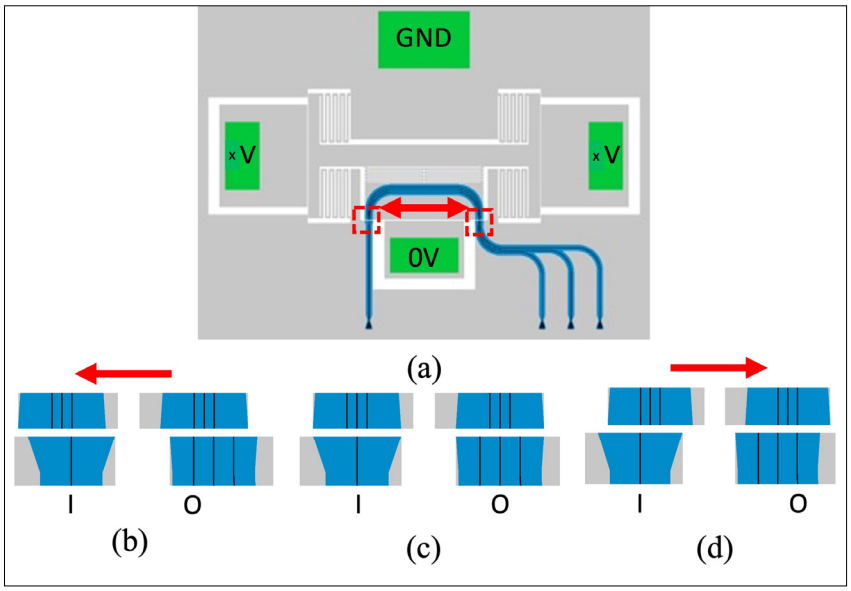

Figure-A V-1 (a) Design illustration of a MEMS platform with lateral bi-directional motion to enable switching from one input to (b, c, d) multiple output waveguides

MEMS integration for switching through mechanical motion requires the release of MEMS structures which would leave an air gap between suspended and fixed waveguide(s) as shown in Figure-A V-2. This would require another lateral motion of the MEMS platform perpendicular to the switching motion to close the air gap between waveguides as shown in Figure-A V-2. This bi-axial motion allows MEMS platform to perform the switching ang gap closing for efficient butt-coupling between multiple waveguides.

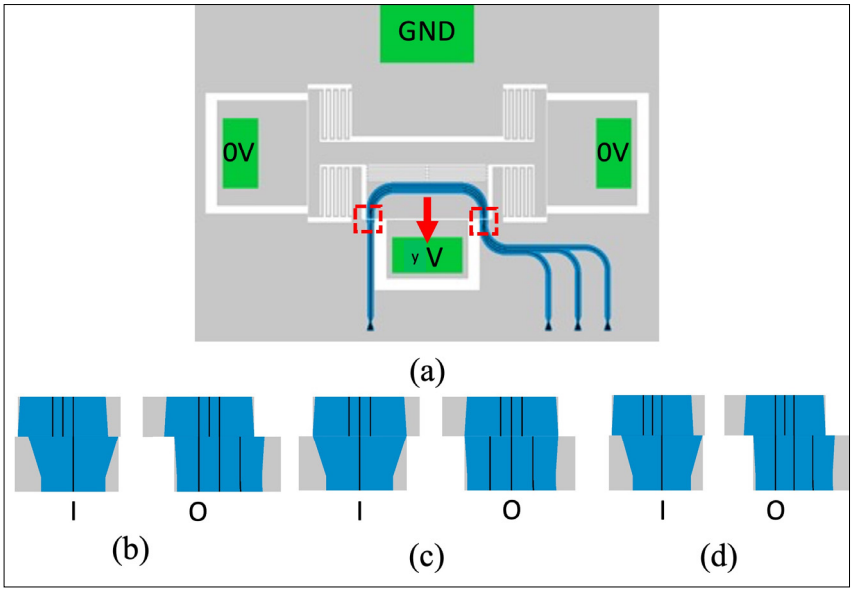

Figure-A V-2 (a) Design illustration of a MEMS platform with lateral motion perpendicular to the switching motion to enable gap closing between suspended and fixed waveguides (b, c, d) in different switching positions

Targeted Displacement

A 1 x 3 optical switch that requires 3 output waveguides needs careful design considerations to analyze the minimum spacing between adjacent output waveguides. This spacing must ensure minimum crosstalk between adjacent waveguides. FDTD simulations can be used to predict the crosstalk between adjacent waveguides at different gaps to ensure efficient coupling in the desired output waveguide during switching. 2.5D FDTD simulation results in Figure-A V-3(b) show that a minimum gap of 3.5 µm is required between adjacent SiN waveguides of

with core dimensions of 435 nm x 435 nm (Sharma et al., 2019). EME analysis using MODE Solutions from Lumerical can be used to predict the impact of air gap between two butt-coupled waveguides. Such analysis of two butt-coupled waveguides with core dimensions of

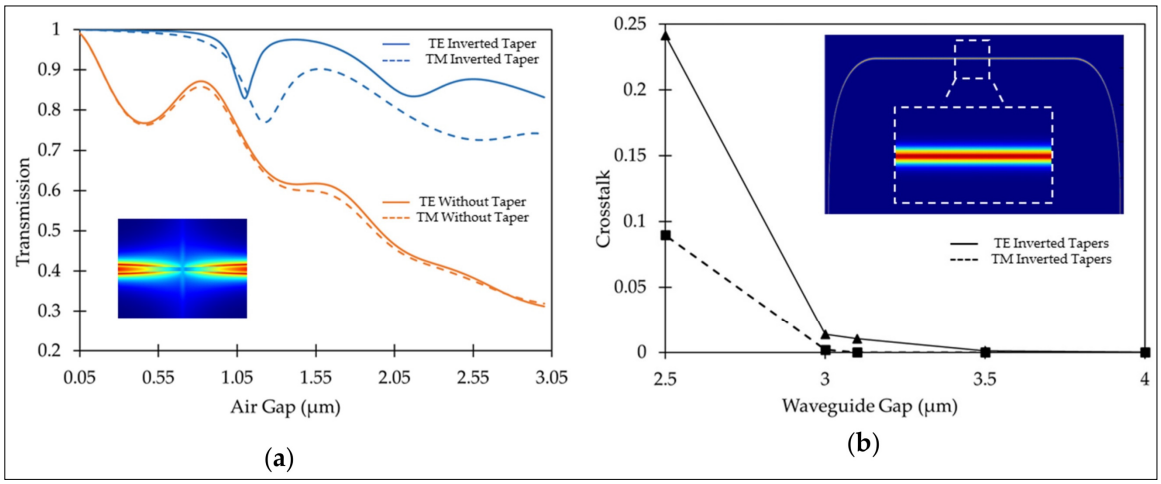

Figure-A V-3 Optical simulation results for: (a) EME analysis showing transmission efficiency for TE and TM modes between two butt-coupled SiN waveguides as a function of air gap with and without inverted tapers. The inset shows the top-view of the magnitude of the electric field of TE mode for butt-coupling with inverted tapers at a gap of 500 nm, (b) 2.5D FDTD analysis showing cross-talk for TE and TM modes as a function of the gap between two SiN waveguides with 90º bends and 75 µm bending radius. Inset shows top-view of the magnitude of electric field of TE mode for the complete optical path with two parallel SiN waveguides at a gap of 3.1 µm. Image shows that the field remains completely confined in the input waveguide Taken from Sharma et al. (2019)

435 nm x 435 nm is also shown in Figure-A V-3(a).

Thus, keeping a gap of 4 µm between the center of two such SiN adjacent waveguide cores would suffice efficient coupling during switching with minimum crosstalk. In this case, a lateral displacement of 4 µm would ensure switching from one waveguide to the other. Designing an actuator with bi-directional motion as shown in Figure-A V-4 would ensure 1 x 3 optical switching capability.

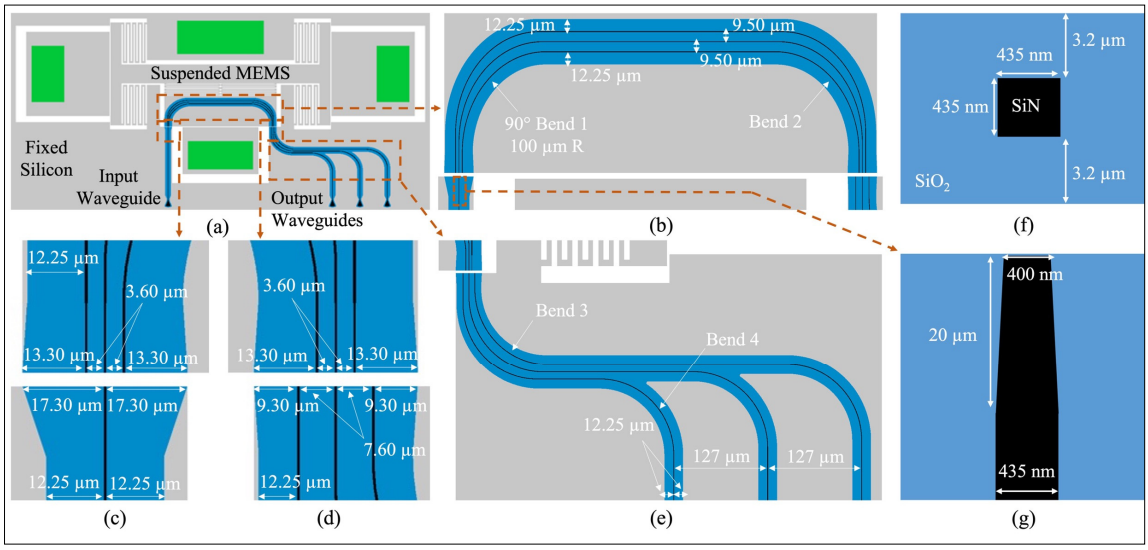

Figure-A V-4 (a) Schematic of the 1 × 3 optical switch. The insets show the waveguide spacing and side cladding dimensions for (b) waveguides on the suspended platform, (c) the input waveguide interface, (d) the output waveguides interface, and (e) the output waveguides over fixed silicon. Cross-sectional view of (f) waveguide core and cladding dimensions. Top view of (g) inverted taper design near air gaps with dimensions
Taken from Sharma et al. (2022)

Actuator

Electrostatic actuators can be design in comb drive and parallel plate configurations. While comb drive actuators are known to produce large linear displacement, parallel plate actuators can be incorporated with mechanical stoppers to leverage the electrostatic pull-in phenomena to achieve large displacement (Sharma et al., 2019). An offset is necessary between the dimensions for the mechanical stopper and the actuator gap as shown in Figure-A V-5. Such offset prevents device shorting after pull-in. In case of such actuator design, the maximum displacement is same as the mechanical stopper gap dimension. This maximum displacement comes with digital control since the actuator relies upon the electrostatic pull-in phenomena.

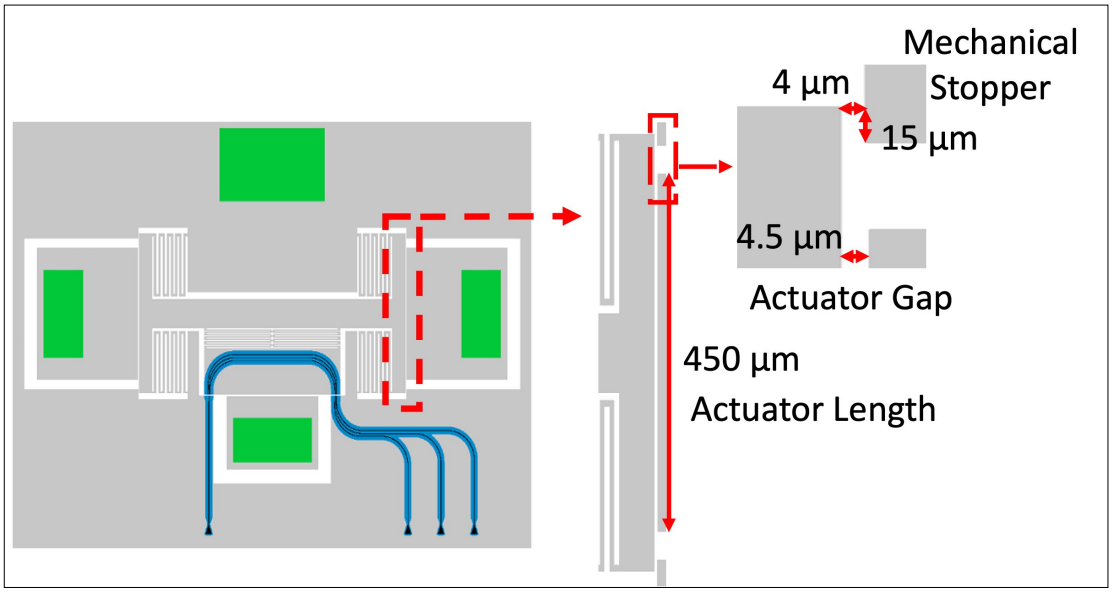

Figure-A V-5 Design illustration of a MEMS platform with lateral motion for switching waveguides showing offset between actuator and mechanical stopper gap

The pull-in voltage (V_p) and pull-in displacement (x_p) of a parallel plate actuator is given as

$$V_p = \sqrt{\frac{8kd^3}{27\varepsilon A}} \tag{A V-1}$$

$$x_p = \frac{d}{3} \tag{A V-2}$$

where k is the spring constant for the spring system connected to the movable actuator plate, d is the initial actuator gap, A is the area of the parallel plate actuator plate, and ε is the permittivity of the dielectric medium between the actuator plates. Through this equation, we can understand that in order the reduce the pull-in voltage, the stiffness of the spring and the gap between the actuator plates would need to be reduced. Increasing the actuator plate area

can also reduce the pull-in voltage. As discussed in the previous section, in case of 435 nm x 435 nm adjacent SiN waveguides, a 4 µm gap between their core center would ensure minimum crosstalk between them. Thus, a 4 µm mechanical stopper gap as shown in Figure-A V-5 can be the targeted displacement for switching between waveguides that are at 4 µm gap between them. Designing a 500 nm offset between the mechanical stopper gap and the actuator gap by keeping the initial actuator gap at 4.5 µm would ensure device operationg during pull-in without any shorting. The thickness of the Si device layer for the technology used for such integration is 59 µm (Sharma et al., 2022). This technology also uses cavity SOI wafers with the cavity size of 1400 µm by 625 µm. For this analytical calculation, we consider an electrostatic actuator of length (l) 450 µm, and initial gap (d) of 4.5 µm as shown in Figure-A V-5. If we consider the Si device layer thickness (t) of 59 µm, the spring constant for the MEMS device can be derived using the pull-in voltage equation described earlier in this section. The spring constant (k) can be given as

$$\mathrm{k} = V_p^2\left(\frac{27\varepsilon \mathrm{A}}{8d^3}\right) = V_p^2\left(\frac{27\varepsilon \mathrm{lt}}{8d^3}\right) \qquad \text{(A V-3)}$$

To design an actuator with the dimensions mentioned earlier, with a pull-in voltage of 110 V, the desired spring constant would be 105 N/m.

Spring

If the actuator described in the previous section is supported by a single beam spring system as shown in Figure-A V-6, the two single beams connected to the actuator can be considered to act as guided beams during horizontal in-plane motion (Kajaakari, 2009). The spring constant (k) for such a beam can be given as

$$\mathrm{k} = \frac{12EI}{L^3} \qquad \text{(A V-4)}$$

where *E* is the Young's modulus, and *L* is the length of the guided single beam. The bending moment (I) of the beam which can be given as

$$\mathrm{I} = \frac{tw^3}{12} \tag{A V-5}$$

where *t* is the thickness of the beam, and *w* is the width of the beam.

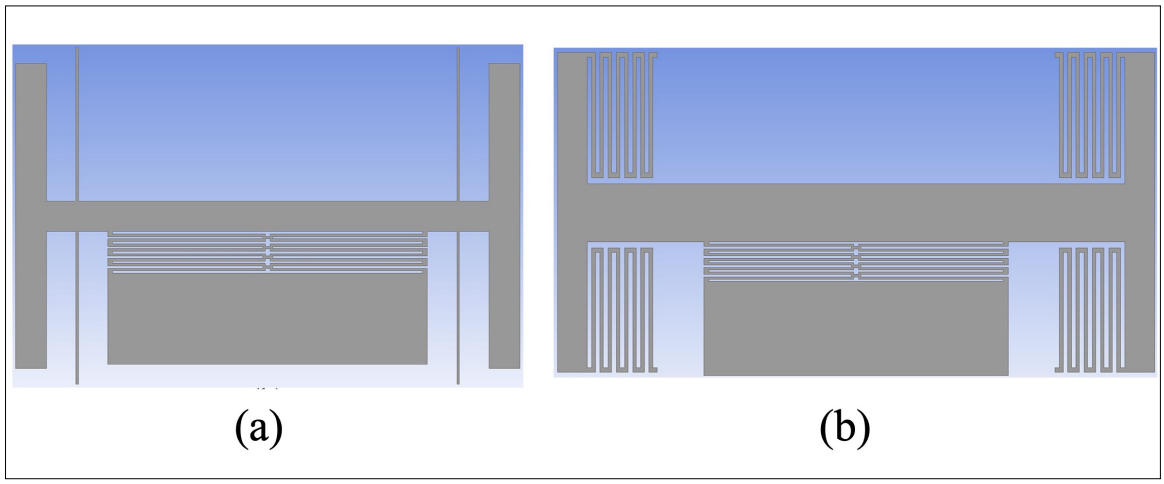

Figure-A V-6 MEMS platform with (a) single beam spring and (b) serpentine spring system for lateral switching motion

For a spring system that uses four such single guided beams in parallel as shown in Figure-A V-6, the total spring constant (K_t) can be given as

$$k_t = 4k = 4\left(\frac{12EI}{L^3}\right) = 4\left(\frac{Etw^3}{L^3}\right) \tag{A V-5}$$

Thus, to design a single beam spring system with total spring constant (k_t) value of 105 N/m derived in the previous section, the spring constant (k) for each beam would need to be 26.25 N/m. For such a single beam, assuming a width of 6 µm and thickness of 59 µm, the length (l) will be 786 µm. Including two such beams on the opposite side of the central support beam as

shown in Figure-A V-6, would require a total length of 1572 µm. Such a system would not be feasible for fabrication using the cavity size of 1400 µm by 625 µm discussed in the previous section. Alternatively, a serpentine spring system with four serpentine springs as shown in Figure-A V-6 can reduce the stiffness of the spring used for lateral actuation. Each beam in the serpentine can be considered a guided beam with spring constant (k) that can be derived using the equation earlier in this section (Kajaakari, 2009). If each serpentine spring consists of eight beams of that are arranged in the configuration shown in Figure-A V-6, the spring constant (k_s) for each serpentine can be given as

$$k_s = \frac{k}{8} = \left(\frac{12EI}{4L^3}\right) = \left(\frac{Etw^3}{8L^3}\right) \quad \text{(A V-6)}$$

and the total spring constant (k_t) of the four serpentine springs can be given as

$$k_t = 4k_s = \left(\frac{Etw^3}{2L^3}\right) \quad \text{(A V-5)}$$

Assuming single beam width of 6 µm, thickness of 59 µm, and length of 215 µm, the total spring constant (k_t) for such a serpentine spring system would be 109 N/m. Such a spring system would fit in the cavity size of 1400 µm by 625 µm and provide an electrostatic pull-in voltage of 112 V for actuator dimensions described in the previous section. Similar design methodology can be used for the gap closing actuator described in the first section of this appendix. A serpentine spring system with two serpentine springs of eight single beams of width 4 µm, thickness 59 µm, and length 256 µm, would result in a total spring constant of 9.5 N/m. A corresponding gap closing actuator with the initial actuator gap of 6 µm, thickness of 59 µm, and length of 350 µm would result in an electrostatic pull-in voltage of 58 V. These analytical pull-in voltages derived here are compared to the pull-in voltages derived from the simulated actuation curves for the switching and gap closing actuators in Figure-A V-7.

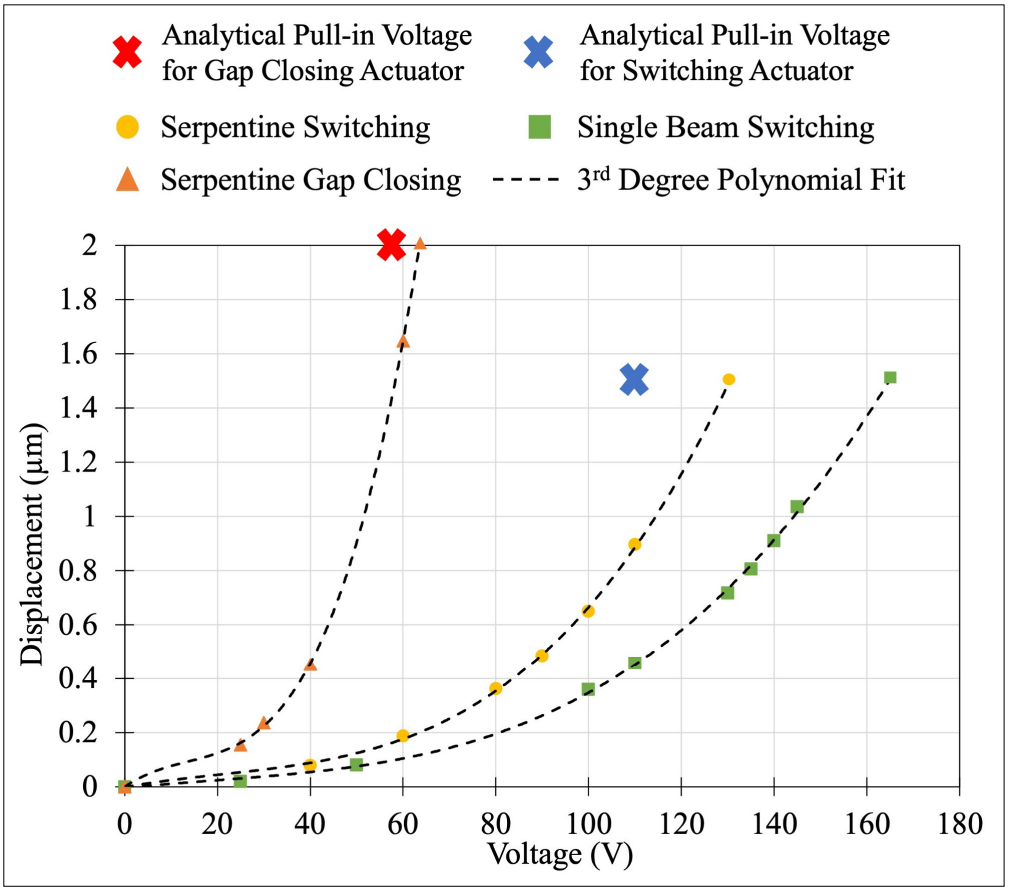

Figure-A V-7 Simulation based displacement vs actuation voltage results for switching and gap closing actuators of single beam spring and serpentine spring-based MEMS structures with 59 µm device layer thickness, analytical pull-in voltage calculated for switching and gap closing actuator with serpentine spring systems Adapted from Sharma et al. (2022)

LIST OF REFERENCES

Abe, S., & Hane, K. (2013). Variable-gap silicon photonic waveguide coupler switch with a Nanolatch mechanism. *IEEE Photonics Technology Letters*, *25*(7), 675-677.

Afsharipour, E., Park, B., Soltanzadeh, R., & Shafai, C. (2018, December). A 3-Degree-of-Freedom MEMS Mirror with Controllable Static and Dynamic Motion for Beam Steering. In *Proceedings* (Vol. 2, No. 13, p. 938). MDPI.

Akihama, Y., Kanamori, Y., & Hane, K. (2011). Ultra-small silicon waveguide coupler switch using gap-variable mechanism. *Optics Express*, *19*(24), 23658-23663.

Aksyuk, V. A., Pardo, F., Bolle, C. A., Arney, S., Giles, C. R., & Bishop, D. J. (2000, August). Lucent Microstar micromirror array technology for large optical crossconnects. In MOEMS and Miniaturized Systems (Vol. 4178, pp. 320-324). SPIE.

Almeida, L., Ramadoss, R., Jackson, R., Ishikawa, K., & Yu, Q. (2006). Study of the electrical contact resistance of multi-contact MEMS relays fabricated using the MetalMUMPs process. *Journal of Micromechanics and Microengineering*, *16*(7), 1189.

Alper, S. E., Azgin, K. I. V. A. N. Ç., & Akin, T. A. Y. F. U. N. (2006, January). High-performance SOI-MEMS gyroscope with decoupled oscillation modes. In *19th IEEE International Conference on Micro Electro Mechanical Systems* (pp. 70-73). IEEE.

An, Y., Sun, B., Wang, P., Xiao, L., Liu, H., & Xie, H. (2021). A 1× 20 MEMS mirror array with large scan angle and low driving voltage for optical wavelength-selective switches. *Sensors and Actuators A: Physical*, *324*, 112689.

Arden, W., Brillouët, M., Cogez, P., Graef, M., Huizing, B., & Mahnkopf, R. (2010). More-than-Moore white paper. *Version*, *2*, 14.

Ba-Tis, F., & Ben-Mrad, R. (2015). A 3-DOF MEMS electrostatic piston-tube actuator. *Journal of Microelectromechanical Systems*, *24*(4), 1173-1184.

Baets, R., Subramanian, A. Z., Clemmen, S., Kuyken, B., Bienstman, P., Le Thomas, N., ... & Severi, S. (2016, March). Silicon photonics: Silicon nitride versus silicon-on-insulator. In *Optical Fiber Communication Conference* (pp. Th3J-1). Optica Publishing Group.

Bai, Y., Yeow, J. T., Constantinou, P., Damaskinos, S., & Wilson, B. C. (2010). A 2-D micromachined SOI MEMS mirror with sidewall electrodes for biomedical imaging. *IEEE/ASME Transactions on Mechatronics*, *15*(4), 501-510.

Barazani, B., Gascon, A., Coia, C., Nabki, F., & Ménard, M. (2023). Broadband 1 x 4 silicon nitride photonic switch fabricated on a hybrid electrothermal and electrostatic MEMS platform. *Journal of Lightwave Technology*, *41*(21), 6710-6722.

Barrett, L. K., Stark, T., Reeves, J., Lally, R., Stange, A., Pollock, C., ... & Bishop, D. J. (2019). A large range of motion 3D MEMS scanner with five degrees of freedom. *Journal of Microelectromechanical Systems*, *28*(1), 170-179.

Barwicz, T., & Haus, H. A. (2005). Three-dimensional analysis of scattering losses due to sidewall roughness in microphotonic waveguides. *Journal of Lightwave Technology*, *23*(9), 2719.

Bauters, J. F., Heck, M. J., John, D., Dai, D., Tien, M. C., Barton, J. S., ... & Bowers, J. E. (2011). Ultra-low-loss high-aspect-ratio Si 3 N 4 waveguides. *Optics express*, *19*(4), 3163-3174.

Bazaz, S. A., Khan, F., & Shakoor, R. I. (2011). Design, simulation and testing of electrostatic SOI MUMPs based microgripper integrated with capacitive contact sensor. *Sensors and Actuators A: Physical*, *167*(1), 44-53.

Ben-Mrad, R., & Pasiliao, D. (2015, April). A MEMS micromirror based head-up display system. In *2015 Symposium on Design, Test, Integration and Packaging of MEMS/MOEMS (DTIP)* (pp. 1-4). IEEE.

Beyranvand, H., Emadi, M. J., Sabouri, S., Jamshidi, K., & Fitzek, F. H. (2019, April). Converged 5G and Fiber-Wireless Access Networks Enhanced with Visible Light Communications and Steerable Infrared Beam. In *2019 2nd West Asian Colloquium on Optical Wireless Communications (WACOWC)* (pp. 152-156). IEEE.

Blumenthal, D. J., Heideman, R., Geuzebroek, D., Leinse, A., & Roeloffzen, C. (2018). Silicon nitride in silicon photonics. *Proceedings of the IEEE*, *106*(12), 2209-2231.

Bose, D., Harrington, M. W., Isichenko, A., Liu, K., Wang, J., Newman, Z. L., & Blumenthal, D. J. (2023). Anneal-free ultra-low loss silicon nitride integrated photonics. *arXiv preprint arXiv:2309.04070*.

Boyd, J. T., & Kuo, C. S. (1976). Composite prism–grating coupler for coupling light into high refractive index thin-film waveguides. *Applied optics*, *15*(7), 1681_1-1683.

Brière, J., Beaulieu, P.-O., Saidani, M., Nabki, F., & Menard, M. (2015). Rotational MEMS mirror with latching arm for silicon photonics (Vol. 9375): SPIE.

Briere, J., Elsayed, M. Y., Saidani, M., Bérard, M., Beaulieu, P. O., Rabbani-Haghighi, H., ... & Ménard, M. (2017). Rotating circular micro-platform with integrated waveguides and latching arm for reconfigurable integrated optics. *Micromachines*, *8*(12), 354.

Bulgan, E., Kanamori, Y., & Hane, K. (2008). Submicron silicon waveguide optical switch driven by microelectromechanical actuator. Applied Physics Letters, 92(10).

Bustillo, J. M., Howe, R. T., & Muller, R. S. (1998). Surface micromachining for microelectromechanical systems. *Proceedings of the IEEE*, *86*(8), 1552-1574.

Cassella, C., Chen, G., Qian, Z., Hummel, G., & Rinaldi, M. (2016). RF passive components based on aluminum nitride cross-sectional Lamé-mode MEMS resonators. IEEE Transactions on Electron Devices, 64(1), 237-243.

Celler, G. K., & Cristoloveanu, S. (2003). Frontiers of silicon-on-insulator. *Journal of Applied Physics*, *93*(9), 4955-4978.

Chen, N., & Tian, C. (2021). Design, modeling and testing of a 3-DOF flexible piezoelectric thin sheet nanopositioner. *Sensors and Actuators A: Physical*, *323*, 112660.

Chen, Wen-Chih., Chu, Chien-Cheng., Hsieh., Jerwei., & Fang, Weilum. (2003). Sensors and Actuators A. P 48-58.

Chiou, J. C., & Lin, Y. J. (2005). A novel large displacement electrostatic actuator: pre-stress comb-drive actuator. *Journal of Micromechanics and Microengineering*, *15*(9), 1641.

Chrostowski, L., & Hochberg, M. (2015). Silicon photonics design: from devices to systems. Cambridge University Press.

Chu, H. M., & Hane, K. (2011). Design, fabrication and vacuum operation characteristics of two-dimensional comb-drive micro-scanner. Sensors and Actuators A: Physical, 165(2), 422-430.

Chu, P. B., Lee, S. S., & Park, S. (2002). MEMS: The path to large optical crossconnects. *IEEE Communications magazine*, *40*(3), 80-87.

Clark, D. (2015). Intel rechisels the tablet on moores law: The last two technology transitions have signaled that our cadence today is closer to two and a half years than two. *Wall Street Journal Digits Tech News and Analysis*.

Cowen, A., Hames, G., Glukh, K., & Hardy, B. (2014). PiezoMUMPsTM 466 design handbook, rev 1.3. MEMSCAP Inc., Tech. Rep.

De Dobbelaere, P., Falta, K., Gloeckner, S., & Patra, S. (2002). Digital MEMS for optical switching. *IEEE Communications magazine*, *40*(3), 88-95.

Delforge, P. (2014) 'America's Data Centers Are Wasting Huge Amounts of Energy', Natural Resources Defense Council (NRDC), IB:14-08-A(August), pp. 1–5.

Dong, B., Tian, H., Zervas, M., Kippenberg, T. J., & Bhave, S. A. (2018, January). PORT: A piezoelectric optical resonance tuner. In *2018 IEEE Micro Electro Mechanical Systems (MEMS)* (pp. 739-742). IEEE.

Du, H., Chau, F. S., & Zhou, G. (2016). Mechanically-tunable photonic devices with on-chip integrated MEMS/NEMS actuators. *Micromachines*, *7*(4), 69.

Dutta, S., & Pandey, A. (2021). Overview of residual stress in MEMS structures: Its origin, measurement, and control. *Journal of Materials Science: Materials in Electronics*, *32*, 6705-6741.

Elsayed, M. Y., Cicek, P. V., Nabki, F., & El-Gamal, M. N. (2016). Bulk mode disk resonator with transverse piezoelectric actuation and electrostatic tuning. *Journal of Microelectromechanical Systems*, *25*(2), 252-261.

Epping, J. P., Hellwig, T., Hoekman, M., Mateman, R., Leinse, A., Heideman, R. G., ... & Boller, K. J. (2015). On-chip visible-to-infrared supercontinuum generation with more than 495 THz spectral bandwidth. *Optics express*, *23*(15), 19596-19604.

Errando-Herranz, C., Niklaus, F., Stemme, G., & Gylfason, K. B. (2015). Low-power microelectromechanically tunable silicon photonic ring resonator add-drop filter. *Optics letters*, *40*(15), 3556-3559.

Fan, L. S., Tai, Y. C., & Muller, R. S. (1988). Integrated movable micromechanical structures for sensors and actuators. *IEEE Transactions on Electron Devices*, *35*(6), 724-730.

Faneca, J., Carrillo, S. G. C., Gemo, E., de Galarreta, C. R., Bucio, T. D., Gardes, F. Y., ... & Baldycheva, A. (2020). Performance characteristics of phase-change integrated silicon nitride photonic devices in the O and C telecommunications bands. *Optical Materials Express*, *10*(8), 1778-1791.

Farrington, N., Porter, G., Radhakrishnan, S., Bazzaz, H. H., Subramanya, V., Fainman, Y., ... & Vahdat, A. (2010, August). Helios: a hybrid electrical/optical switch architecture

for modular data centers. In Proceedings of the ACM SIGCOMM 2010 Conference (pp. 339-350).

Fernandez, A., Staker, B. P., Owens, W. E., Muray, L. P., Spallas, J. P., & Banyai, W. C. (2004, October). Modular MEMS design and fabrication for an 80 x 80 transparent optical cross-connect switch. In Optomechatronic Micro/Nano Components, Devices, and Systems (Vol. 5604, pp. 208-217). SPIE.

Ferraresi, M., & Pozzi, S. (2009). MEMS sensors for non-safety automotive applications. In *Advanced Microsystems for Automotive Applications 2009: Smart Systems for Safety, Sustainability, and Comfort* (pp. 355-367). Berlin, Heidelberg: Springer Berlin Heidelberg.

Ford, J. E., Aksyuk, V. A., Bishop, D. J., & Walker, J. A. (1999). Wavelength add-drop switching using tilting micromirrors. *Journal of lightwave technology*, *17*(5), 904.

Fu, Y., Ye, T., Tang, W., & Chu, T. (2014). Efficient adiabatic silicon-on-insulator waveguide taper. Photonics Research, 2(3), A41-A44.

Fuchs, D. T., Chan, H. B., Stuart, H. R., Baumann, F., Greywall, D., Simon, M. E., & Wong-Foy, A. (2004). Monolithic integration of MEMS-based phase shifters and optical waveguides in silicon-on-insulator. *Electronics Letters*, *40*(2), 1.

Gad-el-Hak, M. (Ed.). (2005). *MEMS: design and fabrication*. CRC press.

Gallagher, D. F., & Felici, T. P. (2003, June). Eigenmode expansion methods for simulation of optical propagation in photonics: pros and cons. In Integrated optics: devices, materials, and technologies VII (Vol. 4987, pp. 69-82). SPIE.

Gaspar, J., Schmidt, M. E., Pedrini, G., Osten, W., & Paul, O. (2010, January). Out-of-plane electrostatic microactuators with tunable stiffness. In *2010 IEEE 23rd International Conference on Micro Electro Mechanical Systems (MEMS)* (pp. 1131-1134). IEEE.

Gerson, Y., Krylov, S., & Ilic, B. (2010). Electrothermal bistability tuning in a large displacement micro actuator. *Journal of Micromechanics and Microengineering*, *20*(11), 112001.

Ghaderi, M., De Graaf, G., & Wolffenbuttel, R. F. (2016). Thermal annealing of thin PECVD silicon-oxide films for airgap-based optical filters. *Journal of Micromechanics and Microengineering*, *26*(8), 084009.

Gondarenko, A., Levy, J. S., & Lipson, M. (2009). High confinement micron-scale silicon nitride high Q ring resonator. Optics express, 17(14), 11366-11370.

Grottke, T., Hartmann, W., Schuck, C., & Pernice, W. H. (2021). Optoelectromechanical phase shifter with low insertion loss and a 13π tuning range. *Optics Express*, *29*(4), 5525-5537.

Grubb, S. G., Welch, D. F., Perkins, D., Liou, C., & Melle, S. (2006, October). OEO versus all-optical networks. In *LEOS 2006-19th Annual Meeting of the IEEE Lasers and Electro-Optics Society* (pp. 221-222). IEEE.

Gu-Stoppel, S., Lisec, T., Fichtner, S., Funck, N., Claus, M., Wagner, B., & Lofink, F. (2020). AlScN based MEMS quasi-static mirror matrix with large tilting angle and high linearity. *Sensors and Actuators A: Physical*, *312*, 112107.

Guan, C., & Zhu, Y. (2010). An electrothermal microactuator with Z-shaped beams. *Journal of Micromechanics and Microengineering*, *20*(8), 085014.

Gyger, S., Zichi, J., Schweickert, L., Elshaari, A. W., Steinhauer, S., Covre da Silva, S. F., ... & Errando-Herranz, C. (2021). Reconfigurable photonics with on-chip single-photon detectors. *Nature communications*, *12*(1), 1408.

Hammadi, A., & Mhamdi, L. (2014). A survey on architectures and energy efficiency in Data Center Networks. *Computer Communications*, *40*, 1-21.

Han, S., Seok, T. J., Quack, N., Yoo, B. W., & Wu, M. C. (2015). Large-scale silicon photonic switches with movable directional couplers. Optica, 2(4), 370-375.

Han, S., Seok, T. J., Yu, K., Quack, N., Muller, R. S., & Wu, M. C. (2018). Large-scale polarization-insensitive silicon photonic MEMS switches. Journal of Lightwave Technology, 36(10), 1824-1830.

Hane, K., Chu, H. M., & Sasaki, T. (2016, July). Silicon photonic waveguide devices tunable by in-plane actuation. In *2016 International Conference on Optical MEMS and Nanophotonics (OMN)* (pp. 1-2). IEEE.

Hettrick, S. J., Wang, J., Li, C., Wilkinson, J. S., & Shepherd, D. P. (2004). An experimental comparison of linear and parabolic tapered waveguide lasers and a demonstration of broad-stripe diode pumping. Journal of lightwave technology, 22(3), 845.

Hoffmann, M., & Voges, E. (2002). Bulk silicon micromachining for MEMS in optical communication systems. *Journal of Micromechanics and Microengineering*, *12*(4), 349.

Holmström, S. T., Baran, U., & Urey, H. (2014). MEMS laser scanners: a review. *Journal of Microelectromechanical Systems*, *23*(2), 259-275.

Hopcroft, M. A., Nix, W. D., & Kenny, T. W. (2010). What is the Young's Modulus of Silicon?. *Journal of microelectromechanical systems*, *19*(2), 229-238.

Hu, F., Yao, J., Qiu, C., & Ren, H. (2010). A MEMS micromirror driven by electrostatic force. *Journal of Electrostatics*, *68*(3), 237-242.

Huffman, T. A., Brodnik, G. M., Pinho, C., Gundavarapu, S., Baney, D., & Blumenthal, D. J. (2018). Integrated resonators in an ultralow loss Si 3 N 4/SiO 2 platform for multifunction applications. *IEEE Journal of selected topics in quantum electronics*, *24*(4), 1-9.

Hung, A. C. L., Lai, H. Y. H., Lin, T. W., Fu, S. G., & Lu, M. S. C. (2015). An electrostatically driven 2D micro-scanning mirror with capacitive sensing for projection display. *Sensors and Actuators A: Physical*, *222*, 122-129.

Hung, E. S., & Senturia, S. D. (1999). Extending the travel range of analog-tuned electrostatic actuators. *Journal of microelectromechanical systems*, *8*(4), 497-505.

Iborra, E., Olivares, J., Clement, M., Vergara, L., Sanz-Hervás, A., & Sangrador, J. (2004). Piezoelectric properties and residual stress of sputtered AlN thin films for MEMS applications. *Sensors and Actuators A: Physical*, *115*(2-3), 501-507.

Inoue, S., Nishimura, S., Nakahama, M., Matsutani, A., Sakaguchi, T., & Koyama, F. (2018). High-speed wavelength switching of tunable MEMS vertical cavity surface emitting laser by ringing suppression. *Japanese Journal of Applied Physics*, *57*(4), 040308.

Iovanna, P., Cavaliere, F., Stracca, S., Giorgi, L., & Ubaldi, F. (2020). 5G Xhaul and service convergence: transmission, switching and automation enabling technologies. *Journal of Lightwave Technology*, *38*(10), 2799-2806.

Ji, Y., Zhang, J., Zhao, Y., Li, H., Yang, Q., Ge, C., ... & Qiu, S. (2014). All optical switching networks with energy-efficient technologies from components level to network level. IEEE Journal on Selected Areas in Communications, 32(8), 1600-1614.

Jia, S., Peng, J., Bian, J., Zhang, S., Xu, S., & Zhang, B. (2021). Design and fabrication of a MEMS electromagnetic swing-type actuator for optical switch. *Micromachines*, *12*(2), 221.

Jin, W., Polcawich, R. G., Morton, P. A., & Bowers, J. E. (2018). Piezoelectrically tuned silicon nitride ring resonator. *Optics Express*, *26*(3), 3174-3187.

Johnston. (1974). Capacitive Pressure Transducer

Jones, A. M., DeRose, C. T., Lentine, A. L., Trotter, D. C., Starbuck, A. L., & Norwood, R. A. (2013). Ultra-low crosstalk, CMOS compatible waveguide crossings for densely integrated photonic interconnection networks. *Optics express*, *21*(10), 12002-12013.

Joo, J., Park, J., & Kim, G. (2018). Cost-Effective 2 x 2 Silicon Nitride Mach-Zehnder Interferometric (MZI) Thermo-Optic Switch. *IEEE Photonics Technology Letters*, *30*(8), 740-743.

Kaajakari, V. (2009). Practical MEMS: Small Gear Publishing: Las Vegas, NV, USA.

Kaykisiz, M., & Bulgan, E. (2011, August). Low-loss optical switch using Brewster angle. In *16th International Conference on Optical MEMS and Nanophotonics* (pp. 215-216). IEEE.

Khan, F., Bazaz, S. A., & Sohail, M. (2010). Design, implementation and testing of electrostatic SOI MUMPs based microgripper. *Microsystem technologies*, *16*, 1957-1965.

Kim, J., Christensen, D., & Lin, L. (2006). Micro vertical comb actuators by selective stiction process. *Sensors and Actuators A: Physical*, *127*(2), 248-254.

Kim, J., Nuzman, C. J., Kumar, B., Lieuwen, D. F., Kraus, J. S., Weiss, A., ... & Gates, J. V. (2003). 1100 x 1100 port MEMS-based optical crossconnect with 4-dB maximum loss. *IEEE Photonics Technology Letters*, *15*(11), 1537-1539.

Kim, S. J., Cho, Y. H., Nam, H. J., & Bu, J. U. (2008). Piezoelectrically pushed rotational micromirrors using detached PZT actuators for wide-angle optical switch applications. *Journal of Micromechanics and Microengineering*, *18*(12), 125022.

Kim, T., & Gorman, J. J. (2022, January). A 3-DOF MEMS motion stage for scanning tunneling microscopy. In *2022 IEEE 35th International Conference on Micro Electro Mechanical Systems Conference (MEMS)* (pp. 470-472). IEEE.

Koh, K. H., Kobayashi, T., & Lee, C. (2012). Investigation of piezoelectric driven MEMS mirrors based on single and double S-shaped PZT actuator for 2-D scanning applications. *Sensors and Actuators A: Physical*, *184*, 149-159.

Koh, K. H., Lee, C., & Kobayashi, T. (2010). A piezoelectric-driven three-dimensional MEMS VOA using attenuation mechanism with combination of rotational and translational effects. *Journal of microelectromechanical systems*, *19*(6), 1370-1379.

Kondo, Y., Murai, T., Shoji, Y., & Mizumoto, T. (2020). All-Optical Switch by Light-to-Heat Conversion in Metal Deposited Si Ring Resonator. *IEEE Photonics Technology Letters*, *32*(13), 807-810.

Kovacs, G. T., Maluf, N. I., & Petersen, K. E. (1998). Bulk micromachining of silicon. *Proceedings of the IEEE*, *86*(8), 1536-1551.

Kress, B. C. (2014). Field Guide to Digital Micro-Optics. SPIE.

Kurth, R. H. (1979). United States Patent 1191

Kwan, A. M. H., Song, S., Lu, X., Lu, L., Teh, Y. K., Teh, Y. F., ... & Tabata, O. (2012). Improved designs for an electrothermal in-plane microactuator. *Journal of Microelectromechanical Systems*, *21*(3), 586-595.

Kwon, S., Milanovic, V., & Lee, L. P. (2004). Vertical combdrive based 2-D gimbaled micromirrors with large static rotation by backside island isolation. *IEEE Journal of Selected Topics in Quantum Electronics*, *10*(3), 498-504.

Laszczyk, K., Bargiel, S., Gorecki, C., Krężel, J., Dziuban, P., Kujawińska, M., ... & Frank, S. (2010). A two directional electrostatic comb-drive X–Y micro-stage for MOEMS applications. *Sensors and Actuators A: Physical*, *163*(1), 255-265.

Lee, D., Krishnamoorthy, U., Yu, K., & Solgaard, O. (2004). Single-crystalline silicon micromirrors actuated by self-aligned vertical electrostatic combdrives with piston-motion and rotation capability. *Sensors and Actuators A: Physical*, *114*(2-3), 423-428.

Lee, M., Chen, Y. C., Chang, C., Hou, M., & Chen, R. (2011, June). A hybrid vertical comb-drive actuator supported by flexible PDMS suspensions. In *2011 16th International Solid-State Sensors, Actuators and Microsystems Conference* (pp. 1476-1479). IEEE.

Lee, S., Park, S., & Cho, D. I. (1999). The surface/bulk micromachining (SBM) process: a new method for fabricating released MEMS in single crystal silicon. *Journal of Microelectromechanical Systems*, *8*(4), 409-416.

Legtenberg, R., Groeneveld, A. W., & Elwenspoek, M. (1996). Comb-drive actuators for large displacements. *Journal of Micromechanics and microengineering*, *6*(3), 320.

Li, H., Oldham, K. R., & Wang, T. D. (2019). 3 degree-of-freedom resonant scanner with full-circumferential range and large out-of-plane displacement. *Optics Express*, *27*(11), 16296-16307.

Li, J., Zhang, Q. X., & Liu, A. Q. (2003). Advanced fiber optical switches using deep RIE (DRIE) fabrication. *Sensors and Actuators A: physical*, *102*(3), 286-295.

Li, S., Xu, J., Zhong, S., & Wu, Y. (2011). Design, fabrication and characterization of a high fill-factor micromirror array for wavelength selective switch applications. *Sensors and Actuators A: Physical*, *171*(2), 274-282.

Liao, W., Liu, W., Zhu, Y., Tang, Y., Wang, B., & Xie, H. (2013). A tip-tilt-piston micromirror with symmetrical lateral-shift-free piezoelectric actuators. *IEEE Sensors Journal*, *13*(8), 2873-2881.

Lin, D., Shi, S., Cheng, W., Liu, P., Lu, M., Lin, T., ... & Cui, Y. (2022). A High Performance Silicon Nitride Optical Delay Line With Good Expansibility. *Journal of Lightwave Technology*, *41*(1), 209-217.

Lin, D., Shi, S., Liu, P., Cheng, W., Lu, M., Lin, T., ... & Cui, Y. (2022). Low loss silicon nitride 1× 4 microwave photonic beamforming chip. *Optics Express*, *30*(17), 30672-30683.

Lin, L. Y., Lee, S. S., Pister, K. S. J., & Wu, M. C. (1994). Micro-machined three-dimensional micro-optics for integrated free-space optical system. *IEEE Photonics Technology Letters*, *6*(12), 1445-1447.

Liu, H. B., & Chollet, F. (2009). Moving Polymer Waveguides and Latching Actuator for 2 x 2 MEMS Optical Switch. *Journal of microelectromechanical systems*, *18*(3), 715-724.

Liu, J. M. (2009). Photonic devices. Cambridge University Press.

Liu, L. (2013). *Large-scan-range Electrothermal MEMS Micromirrors and Microlenses and Their Biomedical Imaging Applications* (Doctoral dissertation, University of Florida).

Liu, L., Pal, S., & Xie, H. (2012). MEMS mirrors based on a curved concentric electrothermal actuator. *Sensors and Actuators A: Physical*, *188*, 349-358.

Liu, T., Pagliano, F., van Veldhoven, R., Pogoretskiy, V., Jiao, Y., & Fiore, A. (2019). Low-voltage MEMS optical phase modulators and switches on a indium phosphide membrane on silicon. *Applied Physics Letters*, *115*(25).

Liu, Y., Wichman, A., Isaac, B., Kalkavage, J., Adles, E. J., Clark, T. R., & Klamkin, J. (2017). Tuning optimization of ring resonator delays for integrated optical beam forming networks. *Journal of Lightwave Technology*, *35*(22), 4954-4960.

Liu, Y., Xu, J., Zhong, S., & Wu, Y. (2013). Large size MEMS scanning mirror with vertical comb drive for tunable optical filter. *Optics and Lasers in Engineering*, *51*(1), 54-60.

Livermore, C. (2007). Design choices: MEMS actuators. *Massachusetts Institute of Technology, course material for*, *6*, 1-50.

Madou, M. J. (2018). *Fundamentals of microfabrication and nanotechnology, three-volume set*. CRC Press.

Maier, M. (2008). Optical switching networks. Cambridge University Press.

Marxer, C., & De Rooij, N. F. (1999). Micro-opto-mechanical switch for single-mode fibers based on plasma-etched silicon mirror and electrostatic actuation. Journal of Lightwave Technology, 17(1), 2–6. http://doi.org/10.1109/50.737413

Mashayekh, A. T., Klos, T., Geuzebroek, D., Klein, E., Veenstra, T., Büscher, M., ... & Witzens, J. (2021). Silicon nitride PIC-based multi-color laser engines for life science applications. *Optics Express*, *29*(6), 8635-8653.

McNulty, K., van Niekerk, M., Deenadayalan, V., Errando-Herranz, C., Pruessner, M. W., Fanto, M. L., & Preble, S. F. (2022, March). Wafer scale fabrication of silicon nitride MEMS phase shifters with XeF2 dry vapor release etch process. In *Silicon Photonics XVII* (Vol. 12006, pp. 74-79). SPIE.

Ménard, F. D., Bérard, M., & Prescott, R. (2015, April). Scaled Out Optically Switched (SOOS) network architecture for Web Scale Data Centers. In *2015 IEEE Optical Interconnects Conference (OI)* (pp. 90-91). IEEE.

Ménard, M., Elsayed, M. Y., Brière, J., Rabbani-Haghighi, H., Saidani, M., Bérard, M., ... & Nabki, F. (2017, July). Integrated optical switch controlled with a MEMS rotational electrostatic actuator. In *Photonics in Switching* (pp. PM4D-4). Optica Publishing Group.

Micó, G., Bru, L. A., Pastor, D., Doménech, D., Fernández, J., Sánchez, A., ... & Muñoz, P. (2018, February). Silicon nitride photonics: from visible to mid-infrared wavelengths. In *Silicon Photonics XIII* (Vol. 10537, pp. 33-41). SPIE.

Milanovic, V., Matus, G. A., & McCormick, D. T. (2004). Gimbal-less monolithic silicon actuators for tip-tilt-piston micromirror applications. *IEEE journal of selected topics in quantum electronics*, *10*(3), 462-471.3

Mimoun, B., Henneken, V., van der Horst, A., & Dekker, R. (2013). Flex-to-rigid (F2R): A generic platform for the fabrication and assembly of flexible sensors for minimally invasive instruments. *IEEE Sensors Journal*, *13*(10), 3873-3882.

Monk, D. W., & Gale, R. O. (1995). The digital micromirror device for projection display. *Microelectronic Engineering*, *27*(1-4), 489-493.

Moore, G. E. (2006). Cramming more components onto integrated circuits, Reprinted from Electronics, volume 38, number 8, April 19, 1965, pp. 114 ff. *IEEE solid-state circuits society newsletter*, *11*(3), 33-35.

Morichetti, F., Melloni, A., Martinelli, M., Heideman, R. G., Leinse, A., Geuzebroek, D. H., & Borreman, A. (2007). Box-shaped dielectric waveguides: A new concept in integrated optics?. *Journal of Lightwave technology*, *25*(9), 2579-2589.

Mousavi, M., Alzgool, M., Lopez, D., & Towfighian, S. (2022). Open-loop control of electrostatic levitation actuators to enhance the travel-range of optical switches. *Sensors and Actuators A: Physical*, *338*, 113453.

Mousharraf, A. (2012). Is PZT an environment friendly piezoelectric material. *Materials Today*.

Mu, X., Wu, S., Cheng, L., & Fu, H. Y. (2020). Edge couplers in silicon photonic integrated circuits: A review. Applied Sciences, 10(4), 1538.

Munemasa, Y., & Hane, K. (2013). A compact 1× 3 silicon photonic waveguide switch based on precise investigation of coupling characteristics of variable-gap coupler. *Japanese journal of applied physics*, *52*(6S), 06GL15.

Nakamura, S., Yanagimachi, S., Takeshita, H., Tajima, A., Hino, T., & Fukuchi, K. (2016). Optical switches based on silicon photonics for ROADM application. *IEEE Journal of Selected Topics in Quantum Electronics*, *22*(6), 185-193.

Nathanson, H. C., Newell, W. E., Wickstrom, R. A., & Davis, J. R. (1967). The resonant gate transistor. *IEEE Transactions on Electron Devices*, *14*(3), 117-133.

Nejadriahi, H., Friedman, A., Sharma, R., Pappert, S., Fainman, Y., & Yu, P. (2020). Thermo-optic properties of silicon-rich silicon nitride for on-chip applications. *Optics Express*, *28*(17), 24951-24960.

Nielson, G. N., Seneviratne, D., Lopez-Royo, F., Rakich, P. T., Avrahami, Y., Watts, M. R., ... & Barbastathis, G. (2005). Integrated wavelength-selective optical MEMS switching using ring resonator filters. *IEEE Photonics Technology Letters*, *17*(6), 1190-1192.

Okamoto, K. (2021). Fundamentals of optical waveguides. Elsevier.

Ollier, E. (2002). Optical MEMS devices based on moving waveguides. IEEE Journal of selected topics in quantum electronics, 8(1), 155-162.

Omran, H., Sabry, Y. M., Sadek, M., Hassan, K., Shalaby, M. Y., & Khalil, D. (2013). Deeply-etched optical MEMS tunable filter for swept laser source applications. *IEEE Photonics Technology Letters*, *26*(1), 37-39.

Pakazad, S. K., Savov, A., Braam, S. R., & Dekker, R. (2012). A platform for manufacturable stretchable micro-electrode arrays. *Procedia Engineering*, *47*, 817-820.

Pallay, M., & Towfighian, S. (2018). A reliable MEMS switch using electrostatic levitation. *Applied Physics Letters*, *113*(21).

Pan, J., Zhai, S., Feng, J., Shi, M., Zhou, L., Cong, G., ... & Zeng, H. (2020). Double-layer cross-coupled silicon nitride multi-ring resonator systems. *IEEE Photonics Technology Letters*, *32*(5), 227-230.

Panda, P. K., & Sahoo, B. (2015). PZT to lead free piezo ceramics: a review. *Ferroelectrics*, *474*(1), 128-143.

Park, S., Kim, B., Kim, J., Paik, S., Choi, B. D., Jung, I., & Chun, K. (2002). A novel 3D process for single-crystal silicon micro-probe structures. *Journal of micromechanics and microengineering*, *12*(5), 650.

Peters, T. J., & Tichem, M. (2016). Electrothermal actuators for SiO2 photonic MEMS. *Micromachines*, *7*(11), 200.

Petersen, K. E. (1980). Silicon torsional scanning mirror. *IBM Journal of Research and Development*, *24*(5), 631-637.

Pfeiffer, M. H., Kordts, A., Brasch, V., Zervas, M., Geiselmann, M., Jost, J. D., & Kippenberg, T. J. (2016). Photonic Damascene process for integrated high-Q microresonator based nonlinear photonics. *Optica*, *3*(1), 20-25.

Pinho, C., Rodrigues, F., Tavares, A. M., Rodrigues, C., Rodrigues, C. E., & Teixeira, A. (2020). Photonic Integrated Circuits for NGPON2 ONU Transceivers. *Applied Sciences*, *10*(11), 4024.

Plander, I., & Stepanovsky, M. (2016). MEMS optical switch: Switching time reduction. *Open Computer Science*, *6*(1), 116-125.

Poulin, A., St-Gelais, R., Goulamhoussen, N., Zhu, G., Boudoux, C., & Peter, Y. A. (2012). In-plane MEMS-based Fabry-Pérot filter for high-speed wavelength-swept semiconductor laser. In *Solid State Sensors, Actuators and Microsystems Workshop, California*.

Prajzler, V., Neruda, M., Nekvindova, P., & Mikulík, P. (2017). Properties of multimode optical epoxy polymer waveguides deposited on silicon and TOPAS substrate. Radioengineering, 26(1), 10-15.

Pruessner, M. W., Park, D., Stievater, T. H., Kozak, D. A., & Rabinovich, W. S. (2016). Broadband opto-electro-mechanical effective refractive index tuning on a chip. *Optics express*, *24*(13), 13917-13930.

Puder, J. M., Bedair, S. S., Pulskamp, J. S., Rudy, R. Q., Polcawich, R. G., & Bhave, S. A. (2015, June). Higher dimensional flexure mode for enhanced effective electromechanical coupling in PZT-on-silicon MEMS resonators. In *2015 Transducers-2015 18th International Conference on Solid-State Sensors, Actuators and Microsystems (TRANSDUCERS)* (pp. 2017-2020). IEEE.

Qiao, Q., Yazici, M. S., Dong, B., Liu, X., Lee, C., & Zhou, G. (2020). Multifunctional mid-infrared photonic switch using a MEMS-based tunable waveguide coupler. *Optics Letters*, *45*(19), 5620-5623.

Qiu, C., Zhang, C., Zeng, H., & Guo, T. (2020). High-performance graphene-on-silicon nitride all-optical switch based on a Mach–Zehnder interferometer. *Journal of Lightwave Technology*, *39*(7), 2099-2105.

Quack, N., Seok, T. J., Han, S., Muller, R. S., & Wu, M. C. (2016). Scalable row/column addressing of silicon photonic MEMS switches. *IEEE Photonics Technology Letters*, *28*(5), 561-564.

Quack, N., Takabayashi, A. Y., Sattari, H., Edinger, P., Jo, G., Bleiker, S. J., ... & Bogaerts, W. (2023). Integrated silicon photonic MEMS. *Microsystems & Nanoengineering*, *9*(1), 27.

Rahim, M., Akkary, P., Jamaleddine, N., Nabki, F., & Menard, M. (2013, August). An integrated silicon-on-insulator continually tunable optical delay line for optical coherence tomography. In *2013 IEEE 56th International Midwest Symposium on Circuits and Systems (MWSCAS)* (pp. 709-712). IEEE.

Ramesh, P., Krishnamoorthy, S., Rajan, S., & Washington, G. N. (2012). Fabrication and characterization of a piezoelectric gallium nitride switch for optical MEMS applications. *Smart materials and Structures*, *21*(9), 094003.

Rangelow, I. W. (2001). Dry etching-based silicon micro-machining for MEMS. *Vacuum*, *62*(2-3), 279-291.

Ren, G., Chen, S., Cheng, Y., & Zhai, Y. (2011). Study on inverse taper based mode transformer for low loss coupling between silicon wire waveguide and lensed fiber. Optics Communications, 284(19), 4782-4788.

Rivlin, B., Shmulevich, S., Hotzen, I., & Elata, D. (2013, June). A gap-closing electrostatic actuator with a linear extended range. In *2013 Transducers & Eurosensors XXVII: The 17th International Conference on Solid-State Sensors, Actuators and Microsystems (TRANSDUCERS & EUROSENSORS XXVII)* (pp. 582-585). IEEE.

Rivlin, B., Shmulevich, S., Joffe, A., & Elata, D. (2015, April). Nonlinear mechanical springs for counteracting nonlinearities in gap-closing electrostatic actuators. In *2015 16th International Conference on Thermal, Mechanical and Multi-Physics Simulation and Experiments in Microelectronics and Microsystems* (pp. 1-6). IEEE.

Robinson, S. D. (2001, May). MEMS technology-micromachines enabling the" all optical network". In 2001 Proceedings. 51st Electronic Components and Technology Conference (Cat. No. 01CH37220) (pp. 423-428). IEEE.

RRA, S. (2004). Scalable electrothermal MEMS actuator for optical fibre alignment.

Saba, N., Soin, N., & Khamil, K. N. (2015, May). Simulation and analysis of actuation voltage of electrostatically actuated RF MEMS cantilever switch. In *2015*

International Conference on Smart Sensors and Application (ICSSA) (pp. 106-110). IEEE.

Sabry, Y. M., Eltagoury, Y. M., Shebl, A., Soliman, M., Sadek, M., & Khalil, D. (2015). In-plane deeply-etched optical MEMS notch filter with high-speed tunability. *Journal of Optics*, *17*(12), 125703.

Sachs, D., Nasiri, S., & Goehl, D. (2006). Image Stabilization Technology Overview, 95054(408), 1–18.

Sattari, H., Graziosi, T., Kiss, M., Seok, T. J., Han, S., Wu, M. C., & Quack, N. (2019). Silicon photonic MEMS phase-shifter. *Optics Express*, *27*(13), 18959-18969.

Sattari, H., Takabayashi, A. Y., Zhang, Y., Verheyen, P., Bogaerts, W., & Quack, N. (2020). Compact broadband suspended silicon photonic directional coupler. Optics Letters, 45(11), 2997-3000.

Sattari, H., Takabayashi, A. Y., Edinger, P., Verheyen, P., Gylfason, K. B., Bogaerts, W., & Quack, N. (2021, January). Low-voltage silicon photonic MEMS switch with vertical actuation. In *2021 IEEE 34th International Conference on Micro Electro Mechanical Systems (MEMS)* (pp. 298-301). IEEE.

Seok, T. J., Quack, N., Han, S., Muller, R. S., & Wu, M. C. (2016). Large-scale broadband digital silicon photonic switches with vertical adiabatic couplers. *Optica*, *3*(1), 64-70.

Seok, T. J., Quack, N., Han, S., Muller, R. S., & Wu, M. C. (2016). Highly scalable digital silicon photonic MEMS switches. *Journal of Lightwave Technology*, *34*(2), 365-371.

Shakoor, R. I. (2010). Design, Fabrication And Characterization Of Metalmumps Based Mems Gyroscopes. In *PhD, Chemical and Materials Engineering*. Pakistan Institute Of Engineering And Applied Sciences.

Sharma, S., Kohli, N., Brière, J., Ménard, M., & Nabki, F. (2019). Translational MEMS platform for planar optical switching fabrics. *Micromachines*, *10*(7), 435.

Sharma, S., Kohli, N., Brière, J., Nabki, F., & Ménard, M. (2022, March). Digitally controlled silicon nitride optical switch. In *2022 Optical Fiber Communications Conference and Exhibition (OFC)* (pp. 1-3). IEEE.

Sharma, S., Kohli, N., Brière, J., Nabki, F., & Ménard, M. (2022). Integrated 1× 3 MEMS silicon nitride photonics switch. *Optics Express*, *30*(12), 22200-22220.

Sharma, S., Kohli, N., Ménard, M., & Nabki, F. (2022, September). 1× 5 silicon nitride MEMS optical switch. In *2022 European Conference on Optical Communication (ECOC)* (pp. 1-4). IEEE.

Sharma, S., Nabavi, S., Rabih, A. A. S., Ménard, M., & Nabki, F. (2023). Hybrid MEMS actuator with 3 degrees-of-freedom for efficient planar optical switching. *Journal of Microelectromechanical Systems*.

Shaw, M. J., Guo, J., Vawter, G. A., Habermehl, S., & Sullivan, C. T. (2005, January). Fabrication techniques for low-loss silicon nitride waveguides. In *Micromachining Technology for Micro-Optics and Nano-Optics III* (Vol. 5720, pp. 109-118). SPIE.

Sinha, N., Wabiszewski, G. E., Mahameed, R., Felmetsger, V. V., Tanner, S. M., Carpick, R. W., & Piazza, G. (2009). Piezoelectric aluminum nitride nanoelectromechanical actuators. *Applied Physics Letters*, *95*(5).

Song, Y. H., Han, C. H., Kim, M. W., Lee, J. O., & Yoon, J. B. (2012). An electrostatically actuated stacked-electrode MEMS relay with a levering and torsional spring for power applications. *Journal of microelectromechanical systems*, *21*(5), 1209-1217.

Srinivasan, P., Gollasch, C. O., & Kraft, M. (2010). Three dimensional electrostatic actuators for tunable optical micro cavities. *Sensors and Actuators A: Physical*, *161*(1-2), 191-198.

Strasser, T. A., & Wagener, J. L. (2010). Wavelength-selective switches for ROADM applications. *IEEE journal of selected topics in quantum electronics*, *16*(5), 1150-1157.

Stutius, W., & Streifer, W. (1977). Silicon nitride films on silicon for optical waveguides. *Applied Optics*, *16*(12), 3218-3222.

Su, S. X., Yang, H. S., & Agogino, A. M. (2005). A resonant accelerometer with two-stage microleverage mechanisms fabricated by SOI-MEMS technology. *IEEE Sensors Journal*, *5*(6), 1214-1223.

Subramanian, A. Z., Ryckeboer, E., Dhakal, A., Peyskens, F., Malik, A., Kuyken, B., ... & Baets, R. (2015). Silicon and silicon nitride photonic circuits for spectroscopic sensing on-a-chip. *Photonics Research*, *3*(5), B47-B59.

Sun, D. M., Dong, W., Wang, G. D., Liu, C. X., Yan, X., Xu, B. K., & Chen, W. Y. (2005). Study of a 2× 2 MOEMS optical switch with electrostatic actuating. *Sensors and Actuators A: Physical*, *120*(1), 249-256.

Sun, X., Feng, J., Zhong, L., Lu, H., Han, W., Zhang, F., ... & Zeng, H. (2019). Silicon nitride based polarization-independent 4× 4 optical matrix switch. *Optics & Laser Technology*, *119*, 105641.

Swain, S., Zawierta, M., Gurusamy, J., Martyniuk, M., Keating, A., Putrino, G., ... & Silva, D. (2024). Broadband Microelectromechanical Systems-Based Silicon Nitride Photonic Switch. *Advanced Photonics Research, 5(1)*, 2300213.

Syms, R. R., & Lohmann, A. (2003). MOEMS tuning element for a Littrow external cavity laser. *Journal of Microelectromechanical Systems*, *12*(6), 921-928.

Tabti, B., Nabki, F., & Ménard, M. (2017, July). Polarization insensitive Bragg gratings in Si3N4 waveguides. In *Integrated Photonics Research, Silicon and Nanophotonics* (pp. IW2A-5). Optica Publishing Group.

Takabayashi, A. Y., Sattari, H., Edinger, P., Verheyen, P., Gylfason, K. B., Bogaerts, W., & Quack, N. (2021). Broadband compact single-pole double-throw silicon photonic MEMS switch. *Journal of Microelectromechanical Systems*, *30*(2), 322-329.

Takahashi, K., Kanamori, Y., Kokubun, Y., & Hane, K. (2008). A wavelength-selective add-drop switch using silicon microring resonator with a submicron-comb electrostatic actuator. *Optics express*, *16*(19), 14421-14428.

Tas, N., Sonnenberg, T., Jansen, H., Legtenberg, R., & Elwenspoek, M. (1996). Stiction in surface micromachining. *Journal of Micromechanics and Microengineering*, *6*(4), 385.

Tian, H., Dong, B., Zervas, M., Kippenberg, T. J., & Bhave, S. A. (2018, May). An unreleased MEMS actuated silicon nitride resonator with bidirectional tuning. In *CLEO: Science and Innovations* (pp. SW4B-3). Optica Publishing Group.

Tonisch, K., Cimalla, V., Foerster, C., Romanus, H., Ambacher, O., & Dontsov, D. (2006). Piezoelectric properties of polycrystalline AlN thin films for MEMS application. *Sensors and Actuators A: Physical*, *132*(2), 658-663.

Toshiyoshi, H., Piyawattanametha, W., Chan, C. T., & Wu, M. C. (2001). Linearization of electrostatically actuated surface micromachined 2-D optical scanner. *Journal of microelectromechanical systems*, *10*(2), 205-214.

Truex, T., Bent, A. A., & Hagood, N. W. (2003). Beam steering optical switch fabric utilizing piezoelectric actuation technology. In *Proc. NFOEC*.

Tu, C., & Lee, J. E. (2015). A semi-analytical modeling approach for laterally-vibrating thin-film piezoelectric-on-silicon micromechanical resonators. *Journal of Micromechanics and Microengineering*, *25*(11), 115020.

Uren, R. (2019). Developments in the generation and measurement of vortex modes in solid-state lasers (Doctoral dissertation, University of Southampton).

Walker, J. A. (2000). The future of MEMS in telecommunications networks. *Journal of Micromechanics and Microengineering*, *10*(3), R1.

Wang, F., Li, X., & Feng, S. (2008). A MEMS probe card with 2D dense-arrayed 'hoe'-shaped metal tips. *Journal of Micromechanics and Microengineering*, *18*(5), 055008.

Wang, J., Yang, Z., & Yan, G. (2012). Silicon-on-insulator out-of-plane electrostatic actuator with in situ capacitive position sensing. *Journal of Micro/Nanolithography, MEMS, and MOEMS*, *11*(3), 033006-033006.

Wang, L., Wang, C., Wang, Y., Quan, A., Keshavarz, M., Madeira, B. P., ... & Kraft, M. (2022). A review on coupled bulk acoustic wave mems resonators. *Sensors, 22(10)*, 3857.

Warren, S. J. D. (2010). Motion Sensing in iPhone 4 MEMS Journal.

Wörhoff, K., Heideman, R. G., Leinse, A., & Hoekman, M. (2015). TriPleX: a versatile dielectric photonic platform. *Advanced Optical Technologies*, *4*(2), 189-207.

Wu, M. C., Seok, T. J., Kwon, K., Henriksson, J., & Luo, J. (2019, March). Large scale silicon photonics switches based on MEMS technology. In *Optical Fiber Communication Conference* (pp. Th1E-1). Optica Publishing Group.

Xue, G., Toda, M., & Ono, T. (2015, January). Assembled comb-drive XYZ-microstage with large displacements for low temperature measurement systems. In *2015 28th IEEE International Conference on Micro Electro Mechanical Systems (MEMS)* (pp. 14-17). IEEE.

Yang, C., & Pham, J. (2018). Characteristic study of silicon nitride films deposited by LPCVD and PECVD. *Silicon*, *10*, 2561-2567.

Yong, Z., Chen, H., Luo, X., Govdeli, A., Chua, H., Azadeh, S. S., ... & Sacher, W. D. (2022). Power-efficient silicon nitride thermo-optic phase shifters for visible light. *Optics express*, *30*(5), 7225-7237.

You, K. Y. (Ed.). (2018). Emerging Waveguide Technology. BoD–Books on Demand.

Yunjia, L. (2014). *Vertical comb-drive actuators for millimeter waveguide applications* (Doctoral dissertation, ETH Zurich).

Zandi, K., Bélanger, J. A., & Peter, Y. A. (2012). Design and demonstration of an in-plane silicon-on-insulator optical MEMS Fabry–Pérot-based accelerometer integrated with channel waveguides. *Journal of Microelectromechanical systems*, *21*(6), 1464-1470.

Zhang, C., Guo, T., & Qiu, C. Y. (2019, December). All-optical Mach-Zehnder Switch on a Graphene-on-silicon Nitride Chip. In *2019 Photonics & Electromagnetics Research Symposium-Fall (PIERS-Fall)* (pp. 582-585). IEEE.

Zhang, W., Li, P., Zhang, X., Wang, Y., & Hu, F. (2018). InGaN/GaN micro mirror with electrostatic comb drive actuation integrated on a patterned silicon-on-insulator wafer. *Optics Express*, *26*(6), 7672-7682.

Zhang, X. M., Liu, A. Q., Lu, C., & Tang, D. Y. (2007). A real pivot structure for MEMS tunable lasers. *Journal of microelectromechanical systems*, *16*(2), 269-278.

Zhao, R., Qiao, D., Song, X., & You, Q. (2017). The exploration for an appropriate vacuum level for performance enhancement of a comb-drive microscanner. *Micromachines*, *8*(4), 126.

Zhou, L., Kahn, J. M., & Pister, K. S. (2006). Scanning micromirrors fabricated by an SOI/SOI wafer-bonding process. *Journal of microelectromechanical systems*, *15*(1), 24-32.